Factors Influencing Magnetic Reconnection at the Magnetopause

Brigid Margaret Anne Cooling

Thesis submitted for the degree of
Doctor of Philosophy (Ph.D.)
of the University of London

Queen Mary, University of London
2003

Certificate of thesis as own work

I, **Brigid Margaret Anne Cooling** of **Queen Mary, University of London**, do hereby certify that this thesis is my own work.

Work forming part of chapters 3 and 4 has been published jointly with Dr C. J. Owen and Prof. S. J. Schwartz, my Ph.D. supervisors. The subject matter was suggested by Dr Owen, and general advice and discussion was provided by both Dr Owen and Prof. Schwartz. I confirm that development of the model, application of relevant physics, writing of the software and interpretation of the results was my own work.

The data analysis and interpretation in chapters 6 and 7 is my own work (with general advice and discussion with Prof. Schwartz).

Minor amendments and clarifications have been made in accordance with the examiners' requests.

Signed: .....

Date: .....

Abstract

We used existing models for magnetosheath flow, density and magnetic field strength to construct a model which predicts whether (steady-state) reconnection may occur for given input solar wind conditions. The subsequent motion of reconnected flux tubes along the magnetopause and into the magnetotail is determined. Results are shown for a range of cases. The model has applications for hypothesis testing, predicting likely sites for the location of reconnection events on the dayside or near-nightside magnetopause, IMF B_Y effects and so forth. In particular, the rôle of sub-Alfvénic flow and the orientation of the reconnection line in allowing steady-state reconnection poleward of the cusps for northward IMF is highlighted.

Next, we carried out a broad survey of magnetosheath parameters using Geotail and Wind data. We compared our results with the predictions of existing numerical models and found general agreement, though lower values, for velocity and number density. We analysed our data for a range of effects and found some evidence for a dawn-dusk effect for velocity and density ratios, and an Alfvén Mach number influence on the magnetic field. We also found evidence of an aberrated stagnation area in the sub-solar region.

We constructed empirical models for the magnetosheath parameters and compared predictions for the extent of sub-Alfvénic flow using the existing and our empirical models. We found that there are solar wind conditions under which the existing models will predict sub-Alfvénic flows extending poleward and tailward of the cusps. The empirical models predict a wider range of conditions, including higher velocities, at which extensive sub-Alfvénic flow may be present.

Our data samples are in the ecliptic plane. If we further assume cylindrical symmetry, then we may broaden our conclusions to say that a range of solar wind conditions exists in which the existing numerical models predict steady-state reconnection poleward of the cusps. Our empirical models predict a wider range of conditions under which such reconnection may occur.

Acknowledgements

With special thanks to a cast of thousands in particular:

Steve Schwartz for keeping faith and all his continuing help, support and advice in getting me this far.

Chris Owen for introducing me to space plasma, magnetic reconnection and guiding me through the first nine months. David Burgess, Rob Lowe, Janet Barnes, Tony Allen, Markus Fraenz, Vincent Genot and all other members of the Space Plasma Group and Astronomy Unit at Queen Mary and the wider space plasma community.

PPARC for three years' funding, and those scientists more particularly mentioned in the text for publishing their work and data, especially the Geotail and Wind teams.

Colleagues past and present: Those from UCLH - especially Tony Young, Henry Stanley, Brian MacInerney, and Rolf Meyer - you know the way in which you helped me along this path! Those at Railtrack East Anglia in the year before I started, and those at Network Rail (Sussex) and other rail companies in the two years since my studentship expired, especially Jane Galvin, David Wilks, Mark Langman, Steve Westwood, Colin Morris, Richard Dean, Hagit Slonimsky, Sue Greetham, Mike Conn, Jannene Osborne, Simon Smith, Mary Collins and the rest of the 'Holiday Camp', for continued encouragement, comradeship and support through a very difficult year. The similarities between the railways and space plasma continue to amaze me! Special thanks to Conrad Ward for reading the finished work and attempting to give me a mock viva!

Friends and family especially Sue Morgan, Sarah Lowe, Paul & Liz Dembina, Nick & Helen Burnikell, Pam Harris, Ade Awoyinka, Moira Adrain, Mike McCarthy, Tessie & Huw, Chezzie, Mike, Nick & Kim, - including those members of the "not written up club" and those of you who told me it would be quicker to buy one off the internet "who'd know?" - you know who you are!

Marla the Flylady, organizedhome.com and the wonderful Payroll SHEs yahoo group, especially Silvia Straka, whose "baby-steps" approach to life not only helped me overcome the chaos engulfing my abode but also helped keep me chipping away through some very dark days.

The small, black shadows, Cat-a-strophe (the Indisputable) and Cat-a-clysm (Destructimo), for their furry presence and little presents which kept my feet firmly on the ground.

Most importantly, Poppy the wanna-be nun and Cuthbert the novice monk for becoming the Rev^2 Cooling - i.e. my mum Margaret for encouraging me in my ambition to study physics at a time when girls "didn't" and from whom I inherited my "don't tell me I can't" attitude, and my dad, Derrick, for introducing me to C.S.Lewis, Isaac Asimov and other worlds at a tender age and whose sermons often include references to the greatest philosophical question facing humanity, the impossible and unknowable nature of the solution to the quadratic equation - what can I say Dad, this one's gone cubic!!!

Trying

It's hard to start something,
you mean to do
you make a plan
write a line
then put down your pen
and start again.
You pace the room.
It keeps you sane
inviting endless words
into your brain.
You sit down
try again,
no
nothing
only the strain.
You walk the room
and want to shout
maybe later
you'll write something out.

Claire, Brighton,
Big Issue July 1-7 2002

Contents

List of Figures

List of Tables

Chapter 1

Introduction

Magnetic reconnection is a process which, to date, has proved to be the most successful paradigm for the transfer of the majority of that proportion of solar wind plasma and its energy, momentum and mass, which enters the Earth's magnetosphere. In Chapter 2 of this thesis, we discuss this process in some detail. However, before doing so, it is first necessary to place it in the context of space plasmas in the near-Earth environment.

In this chapter we begin with a short historical overview of how awareness of the interaction of the solar wind with the Earth's environment came about and some personal motivations for its study. Next, we review some basic features of collisionless plasma dynamics, in particular the magnetohydrodynamic (MHD) description, ideal MHD and the frozen-in-flux theorem. We then consider the discontinuities which may exist between two separate plasma regimes. This is followed by a brief overview of the near-Earth environment in the context of these discontinuities. Lastly, we give an overview of the remainder of our thesis.

1.1 Interaction between the solar wind and the Earth

1.1.1 Historical overview

The eleventh century Chinese are the earliest people known to have deduced the existence of a magnetic field surrounding the Earth. It was not until the seventeenth century that Gilbert first proposed that the field may be analogous to that of a bar magnet, though the magnetic poles are not directly opposite each other, nor are they aligned with the Earth's spin axis. In modern times, we believe that the geomagnetic field reverses its polarity every few hundred thousand years. Evidence in support of this theory comes from the study of magnetic fields trapped in igneous and sedimentary rocks (e.g. Fuller *et al.* [1996]).

In the eighteenth century, small disturbances in the Earth's magnetic field known as 'magnetic storms' were detected. In 1859, Carrington's observations of a solar flare followed within hours by fluctuations in the geomagnetic field and auroral displays led to the notion that solar and

geomagnetic activity were somehow linked.

Birkeland proposed that beams of electrons were emitted from the Sun during solar flares and that these were responsible for the interaction. It was not until the 1950s that Biermann's observations of cometary tails, together with other work on the relationships between solar and geomagnetic activity and models of the solar corona lead to the conclusion that there is a continuous stream of quasi-neutral plasma from the Sun, named the 'solar wind' by Parker [1958].

The first measurements of solar wind plasma were made by Explorer 10 in 1961, and measurements made by Mariner 2 established the continuous nature of the solar wind [Snyder *et al.*, 1963].

1.1.2 Motivations for Study

Laboratory for the Study of Space Plasma

Probably the main reason for studying the interaction of the solar wind with the Earth is that it forms a fantastic laboratory for the study of space plasmas. Collisionless plasmas (Section 1.2.1) are believed to be the most common form of visible matter throughout the Universe, yet it is impossible on Earth to duplicate the conditions under which such plasmas exist. This is because the density of the space plasmas is often much lower than that of the best 'vacuums' achievable on Earth giving a much longer mean free path between particle collisions.

The solar wind is formed at extremely hot temperatures in the base of the solar corona. It expands out through the Solar System, accelerating from subsonic to supersonic speeds, passing into the extremely cool regions of the outer planets. The density and pressure reduce until the solar wind encounters the termination shock separating the Solar System from the interstellar medium. Along the way it meets and adjusts to the various obstacles to its flow caused by the magnetized and unmagnetized planets, asteroids and comets.

With the development of spacecraft, we are now able study the solar wind in the vicinity of some of these obstacles and to observe how it changes; thus the near-Earth environment acts as a laboratory for observation and measurement of plasma under conditions not attainable on Earth. The solar wind also carries with it the influences of solar activity and thus a second reason for its study is to assist in understanding more about stellar processes.

Affects of Solar Activity on Human Life

In addition to the increased understanding about astrophysical plasmas which can be gained from a study of the solar wind, the solar wind also has a more direct impact on human activity, most noticeably in the field of communications, particularly with our rising dependence on satellite technology. There is also increasing evidence of its impact on the environment, medical and psychological behaviours.

NASA and NOAA both attempt to track solar activity in order to predict magnetic storms

and radio blackouts which may disturb high frequency radio communications causing problems for air and sea navigation devices. Magnetic storms may also be of sufficient strength to cause failure of satellites and other communication systems, and may also cause current surges and failure in electrical transmission systems. The most well-known example of such a storm occurred in 1989 causing the Hydro-Quebec electrical power system to fail leaving six million Canadians and North Americans without electricity for over nine hours. This storm also caused the LDEF satellite to drop into a lower orbit earlier than had been planned (e.g. NASA [1996]). High cost systems are at risk and already space storms cause averaged annual losses estimated to exceed $100M [Maynard, 1995].

Problems may be caused during peaks in solar flare activity. In particular, electrostatic discharge caused by the build up of ionization on the spacecraft, or protons or heavier particles passing through the spacecraft may cause damage and disruption to subsystem electronic components (e.g. Dorman [2001]). Today, companies operating satellites use, for example, shielding technology to take into account the variable conditions in space [Maxwell, 2003].

While the effects of solar activity on communications systems are accepted, a much more controversial area is how solar activity may affect human physiology and behaviour [Durand-Manterola & Mendoza, 2001]. A number of scientists are looking at the implications of interdisciplinary aspects of such research, for example Roederer [1988], and the accumulated evidence across these disciplines led to the formation of the informal Biosphere and the Cosmos (BIOCOS) project in the late 1990s. The international project is attempting to align a range of geophysical data with medical information and encouraging a systematic approach across a range of geomagnetic and geographic sites [Halberg *et al.*, 2000].

A number of links between geomagnetic activity and the behaviour of birds, physiological changes in mice, changes in human blood composition, psychopathalogical disturbances, and so forth have been made (Davydov [1995], Durand-Manterola & Mendoza [2001] and references therein). If links between solar activity and the geomagnetic field can be made, then a further relationship between solar activity and these conditions may be inferred. Research has also been carried out on relationships between solar activity, in particular persistence of southward IMF component on myocardial infarctions [Villoresi *et al.*, 1994a, Mendoza & Diaz-Sandoval, 2001], strokes [Feigin *et al.*, 1997] and on a range of clinically important pathologies [Villoresi *et al.*, 1994b]. Durand-Manterola & Mendoza [2001] have proposed a physical mechanism by which solar activity may act to induce currents in cells thereby causing damage.

Various economic and financial models have been developed which postulate a relationship between the cycle of sunspot activity and cycles in commercial activity via the direct impact of solar change on important economic factors. For example, W.S. Jevons, the nineteenth century economist, explained commercial crises as being caused by the effects of periodic sunspots on crops and consequently the economy [Cameron, 1997] and Burns & Mitchell [1946] believed that business cycles would follow essentially the same pattern as sunspots.

Some firms incorporate sunspot activity modelling [Lattice Financial, 2001] into stochastic scenario generation systems allowing financial institutions to forecast satellite outages. This is important when insuring those companies that depend on satellites. An element of weather derivatives in the the area of financial modelling is often incorporated.

1.2 Plasma

The term 'plasma' was introduced by Tonks and Langmuir (1929) when investigating arc-type discharges [Sturrock, 1994, p.6]. A plasma is a quasi-neutral, ionized gas consisting of free positive and negative charges which not only move under the influence of electric and magnetic fields, but can also produce them. These fields are, therefore an important part of the description of plasma behaviour.

1.2.1 Collisionless plasma

In the near-Earth environment, we normally deal with extremely low density plasma, where the mean free paths of the particles may be of the order of $1AU$ and collisions extremely rare. Equilibrium between the various particles is highly unlikely to be reached and thus their properties may be preserved for enormous distances. In these plasmas, the electric and magnetic fields are of key importance in determining the behaviour of the ions. The solar wind is an example of a collisionless plasma (Section 1.4.1).

The calculation of the forces acting on the particles can be complicated but need only be considered in an average sense [Kivelson, 1995a]. Because of this, and because the magnetic field links distant regions, it is possible to use a fluid description for many aspects of space plasma behaviour, despite the absence of particle-particle collisions.

1.2.2 Magnetohydrodynamics

Magnetohydrodynamics is the name given to the fluid model of a plasma. Because there are at least two species of particle (electrons and protons) in a plasma, then two sets of fluid equations are needed to describe the plasma behaviour. However, a set of one-fluid equations may be used to describe basic features of the system. We also assume that the system changes in which we are interested occur over a temporal and spatial scales much greater than those of the individual particle motions. If temporal scales are long enough, we can ignore the displacement current $\partial\mathbf{E}/\partial t$ which is approximately inversely proportional to the characteristic time of the system.

On a simple level, if we consider a fluid whose motion is governed only by the electric and magnetic fields permeating it, then if we take Maxwell's equations:

$$\nabla \wedge \mathbf{E} + \frac{\partial \mathbf{B}}{\partial t} = 0\,, \tag{1.1}$$

$$\nabla \cdot \mathbf{B} = 0\,, \tag{1.2}$$

$$\nabla \wedge \mathbf{B} = \mu_0 \mathbf{j}\,, \tag{1.3}$$

and Ohm's Law:

$$\mathbf{j} = \sigma(\mathbf{E} + \mathbf{V} \wedge \mathbf{B}) \tag{1.4}$$

where σ is the conductivity of the plasma. In a collisionless plasma σ is usually very high. Combining Equations 1.3 and 1.4, inserting the result into Equation 1.1, and making use of Equation 1.2 leads to:

$$\frac{\partial \mathbf{B}}{\partial t} = \nabla \wedge (\mathbf{V} \wedge \mathbf{B}) + \frac{1}{\sigma\mu_0}\nabla^2\mathbf{B}\,. \tag{1.5}$$

This equation is known as the Induction Equation and describes the evolution of the magnetic field over time. The first term on the right hand side is the convective term and the second term is the diffusive term and represents the extent to which the magnetic field lines will diffuse across the plasma.

We define a term R_M known as the 'magnetic Reynolds number':

$$R_M = \frac{|\text{convective term}|}{|\text{diffusive term}|} = \frac{L^{-1}VB}{\{1/\sigma\mu_0\}L^{-2}B}\,, \tag{1.6}$$

so that

$$R_M = \sigma\mu_0 LV\,, \tag{1.7}$$

where L is a length characteristic of the spatial variation of the magnetic field and $1/(\sigma\mu_0)$ is a diffusion coefficient. In astrophysical plasmas, R_M is normally very high.

The form of the Induction Equation is identical to the hydrodynamic equation describing vorticity in incompressible flow [Parks, 1991, p.157], and some analogies may be drawn. (The vorticity ω is analogous to $\mathbf{B}$, and kinematic viscosity analogous to $1/(\sigma\mu_0)$ which we call 'magnetic viscosity').

1.2.3 Ideal MHD and the frozen in flux theorem

The 'frozen-in-flux theorem' is a key element in the explanation of plasma behaviour in the interplanetary environment. It arises in regions of very high conductivity, σ, so that the diffusion term on the right hand side of the Induction Equation(1.5) becomes negligible. Thus, Equation 1.5 becomes:

$$\frac{\partial \mathbf{B}}{\partial t} - \nabla \wedge (\mathbf{V} \wedge \mathbf{B}) = 0 \tag{1.8}$$

The theorem shows that the magnetic flux threading a surface remains constant as the surface moves with the fluid, or alternatively, that the magnetic fields lines are frozen into the plasma. One consequence of this theorem is that plasmas of high conductivity organized by different magnetic field regimes do not mix.

Equation 1.4 is equivalent to:

$$\mathbf{E} = -\mathbf{V} \wedge \mathbf{B}. \tag{1.9}$$

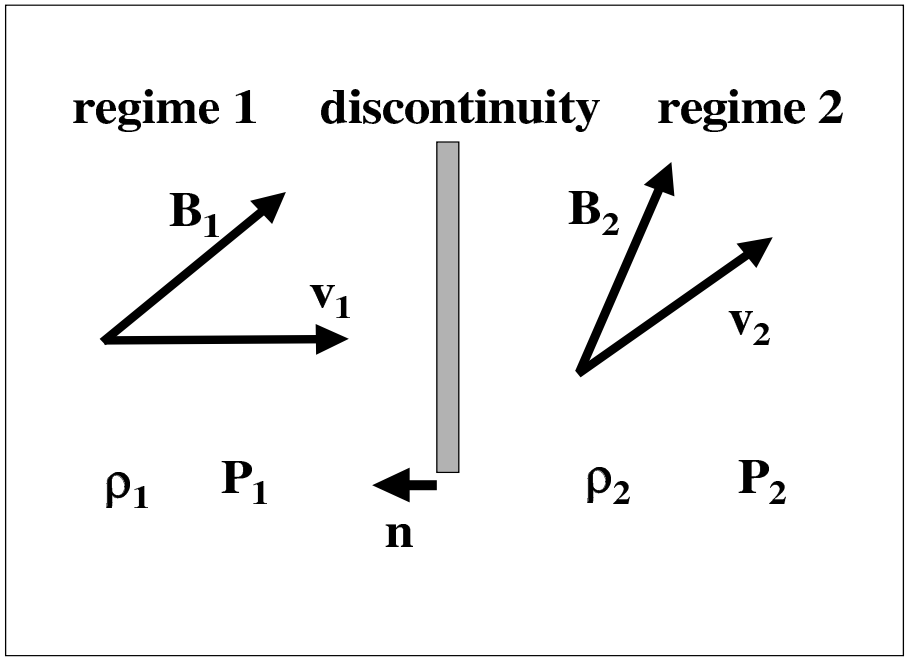

Figure 1.1: Discontinuities: Shows a discontinuity with parameters from two different regimes (based on figure from Burgess [1995])

from whence

$$\mathbf{V} = \frac{\mathbf{E} \wedge \mathbf{B}}{|\mathbf{B}^2|} \tag{1.10}$$

Thus, for a fluid in motion, we may also say that there is an electric field in the rest frame given by Equation 1.9 or, alternatively, if there is an electric field in the rest frame, then this is the equivalent of saying that the fluid is moving with a velocity given by Equation 1.10.

1.3 Discontinuities

Two separate highly conductive plasma regimes will not normally mix and hence there must be a discontinuity between them. The plasma parameters across the discontinuity change according to its nature. Figure 1.1 represents a discontinuity and the parameters of the plasma regimes on either side. If the normal component of velocity V_n is non-zero, then the discontinuity takes the form of a shock or a rotational discontinuity and plasma may pass through. A rotational discontinuity is similar to the intermediate shock and plasma may cross the boundary at the normal Alfvén speed of the plasma. If V_n is zero, then we have either a tangential or contact discontinuity across which plasma does not pass. Table 1.1 lists these discontinuities together with the main parameter changes associated with them. The subscripts n and t refer to 'normal' and 'tangential' components respectively.

The tangential and rotational discontinuities are of most relevance to this thesis and so are explored in more detail using the work of Hudson [1970].

Discontinuity	$\mathbf{V}$, $\mathbf{B}$	Summary of changes
Shocks	$V_n \neq 0$	
parallel shock	$B_t = 0$	magnetic field unchanged
perpendicular shock	$B_n = 0$	plasma pressure and field strength increase at the shock
oblique shock	$B_t \neq 0$, $B_n \neq 0$	plasma pressure, field strength and orientation change at shock depending on whether it is fast, slow or intermediate
contact discontinuity	$V_n = 0, B_n \neq 0$	arbitrary density jump, all other quantities continuous
tangential discontinuity	$V_n = 0, B_n = 0$	plasma pressure and field change while maintaining pressure balance
rotational discontinuity	$V_n = \frac{B_n}{\sqrt{\mu_0 \rho}}$	large amplitude intermediate wave, in isotropic plasma, field and flow change direction but not magnitude

Table 1.1: Discontinuities in plasmas: Shows how plasma parameters change across various discontinuities. Based on Burgess [1995].

1.3.1 Tangential Discontinuity

In the case of the tangential discontinuity, V_n and $B_n = 0$. The consequence of this is that the field and flow are tangential to the boundary as no plasma can cross it, nor magnetic field permeate it. The normal, $\mathbf{n}$, to the boundary can thus be determined from the equation:

$$\mathbf{n} = \frac{\mathbf{B}_1 \wedge \mathbf{B}_2}{|\mathbf{B}_1 \wedge \mathbf{B}_2|}, \tag{1.11}$$

In the rest frame of the tangential discontinuity, the normal component of the flow, $V_n = (\mathbf{V}_1 - \mathbf{U}) \cdot \mathbf{n}$, should be zero, thus the speed of the discontinuity, $\mathbf{U}$, in the measurement rest frame may be deduced from:

$$\mathbf{U} \cdot \mathbf{n} = \mathbf{V}_1 \cdot \frac{\mathbf{B}_1 \wedge \mathbf{B}_2}{|\mathbf{B}_1 \wedge \mathbf{B}_2|}, \tag{1.12}$$

Lastly, from pressure balance:

$$P_{\perp 1} - P_{\perp 2} + \frac{{B_1}^2 - {B_2}^2}{2\mu_0} = 0. \tag{1.13}$$

These equations say nothing about how other dynamical parameters or magnetic field direction may change across the boundary thus Hudson warns that it would be easy to mistake a tangential discontinuity for some other kind.

1.3.2 Rotational Discontinuity

In the case of the rotational discontinuity, the normal component of velocity at the discontinuity is the Alfvén speed for the plasma. A component of the magnetic field threads the boundary and plasma can mix across it. For anisotropic plasma, we define a modified Alfvén speed:

$$\mathbf{V}_{Amod} = \frac{\mathbf{B}}{\sqrt{\mu_0 \rho}} \left(1 - \frac{(P_\parallel - P_\perp)\mu_0}{B^2}\right)^{\frac{1}{2}} \tag{1.14}$$

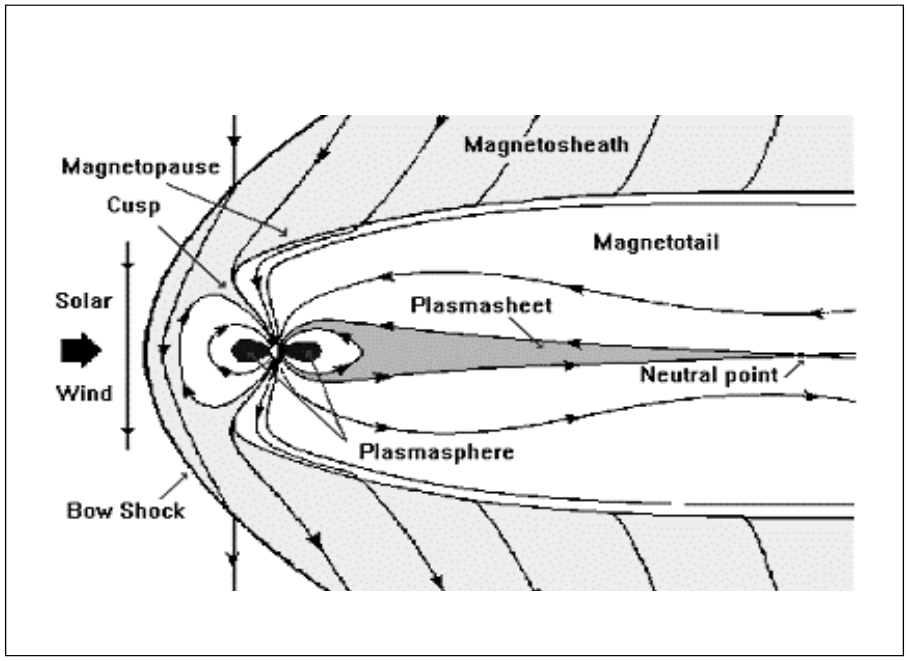

Figure 1.2: Near-Earth Environment: Shows major features of the near-Earth environment (based on figure from Oulu [1998])

In the frame of the discontinuity, continuity of mass through the boundary leads to the result that:

$$\rho_1 \mathbf{V}_{Amod1} \cdot \mathbf{n} = \rho_2 \mathbf{V}_{Amod2} \cdot \mathbf{n} \tag{1.15}$$

Hudson also shows that a rotational discontinuity can only occur if the so called 'firehose instability' condition is not reached, that is:

$$P_{\|1} - P_{\perp 1} < {B_1}^2/\mu_0 \tag{1.16}$$

$$P_{\|2} - P_{\perp 2} < {B_2}^2/\mu_0 \tag{1.17}$$

and that $\mathbf{V}_1 - \mathbf{V}_2$ is parallel to $\mathbf{B}_1/\rho_1 - \mathbf{B}_2/\rho_2$.

For isotropic plasma, $P_{\|} - P_{\perp} = 0$, Equation (1.14) becomes the simple Alfvén velocity, $\mathbf{V_A} = \mathbf{B}/\sqrt{(\mu_0 \rho)}$. Putting this together with the mass continuity equation leads to the result that B_n, ρ and hence all other thermodynamic quantities and $|\mathbf{B}|$ are continuous across the boundary. The rotational discontinuity, therefore, acts to rotate the magnetic field through an angle about the normal but does not alter its magnitude. These aspects of the rotational discontinuity in an isotropic plasma are derived in Section 3.3.

1.4 Near-Earth Environment

1.4.1 The solar wind and the interplanetary magnetic field

Figure 1.2 shows the major features of the near-Earth environment. In our work, we are not concerned with the features shown within the magnetopause, other than the geomagnetic field.

The flow of plasma in the inner corona is channelled by the magnetic field lines to the surface. At the base of the corona the flow is subsonic and almost stationary, however at some distance from the Sun it becomes supersonic. For an isothermal corona, this occurs at a distance of several solar radii [Cravens, 1997].

The supersonic solar wind then expands from the solar corona throughout the Solar System. The thermal energies of the particles at the surface are sufficient for them to escape the gravitational field of the Sun [Illingworth, 1994]. There is also a pressure difference between the coronal and the interstellar medium [Hundhausen, 1995] which drives the expansion.

Solar wind plasma consists of ionized particles, principally protons and electrons, but with around 5% ionized helium and a smaller percentage of other heavier elements [Hundhausen, 1995]. The protons carry the majority of the momentum and energy of the flow. Most solar wind parameters vary with distance from the Sun, but at a distance of $1AU$ (i.e. at Earth distance), it has a number density of $\sim 10cm^{-3}$, a flow speed of $\sim 400kms^{-1}$ with a sonic Mach number of $\sim 5-10$ and a temperature of $\sim 30000K$. Some key parameters of the solar wind at a distance of $1AU$ are summarised in Table 1.2.

The solar wind plasma is organized by the Sun, carrying with it the imprint of the solar magnetic field, known as the interplanetary magnetic field (IMF). Its strength is $\sim 5nT$ [Cravens, 1997] and its usual direction in the ecliptic plane near $1AU$ is at an orientation of 45^o to the solar wind velocity direction. Parker was the first to explain the structure and hence this orientation is known as the 'Parker spiral'.

1.4.2 Parker spiral

One consequence of the frozen-in flux theorem is to explain the Archimedean spiral form of the average IMF.

Figure 1.3 shows the 'ballerina skirt' view of the IMF. As noted in Section 1.2.3, plasmas organized by two different magnetic fields do not mix. At their boundaries, they are separated from each other by current sheets. The ballerina skirt represents the current sheet which arises because the magnetic field in the Sun's northern hemisphere is of opposite polarity to that in the southern, thus the plasma originating from each hemisphere is differently organized. The white spiral arrows visible on the diagram represent the magnetic field carried by the plasma in the plane of the ecliptic, the plane in which the planets of the Solar System lie, and hence represents the IMF orientation most likely to be encountered by the planets as obstacles in the IMF.

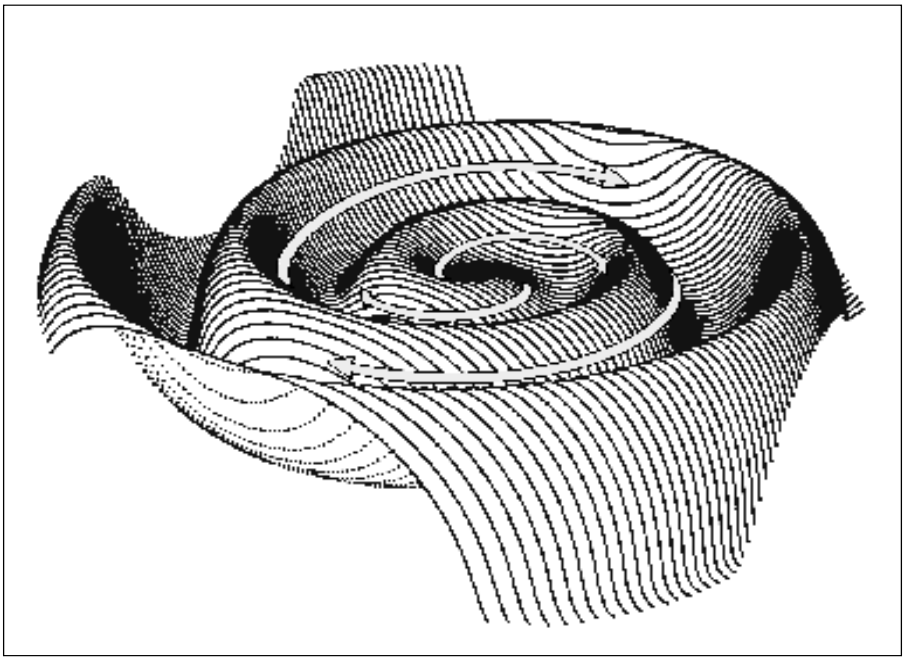

Figure 1.3: Parker spiral: 'Ballerina skirt' view of Parker Spiral (taken from Jokipii [1997]). The white spiral arrows indicate the magnetic field carried by the plasma in the plane of the ecliptic and hence the IMF most likely to be encountered by the planets of the solar system.

If fluid parcels are emitted at a constant speed from a fixed source on the Sun, then by the frozen-in flux theorem, the fluid parcels remain linked by the particular magnetic field traced out from that source. Thus as the source rotates and parcels continue to be emitted along the field line, the magnetic field line winds into the form of an Archimedean spiral which, in the plane of the ecliptic, approaches an angle of 45^o to the solar wind velocity vector at a distance of $1AU$, facing either 'toward' or 'away' from the Sun. An additional North-South component may also be present.

1.5 Discontinuities and the near-Earth environment

Two major features of the near-Earth environment take the form of discontinuities; the bow shock and the magnetopause. These arise between the plasma organized by the IMF and that of the Earth's magnetosphere which is organized by the geomagnetic field.

1.5.1 The magnetosphere

The magnetosphere is a highly structured region, bounded by the magnetopause, immediately surrounding the Earth and extending out from the ionosphere. While the geomagnetic field immediately around the Earth is similar to that of a bar magnet, as we move out, the shape becomes more distorted, compressed on the dayside and expanded on the nightside. The shape

and magnetic field of the magnetosphere are also discussed later in this thesis (Chapter 3.6.2).

1.5.2 The bow shock

The bow shock is the first discontinuity encountered by the solar wind as it approaches the Earth. It takes the form of a quasi-steady state collisionless shock standing in the solar wind sunward of the Earth's magnetosphere [Burgess, 1995]. It results from the magnetized plasma of the solar wind encountering the geomagnetic field as an obstacle in its flow causing the plasma to slow and heat. The modified subsonic plasma forms the magnetosheath which surrounds the magnetosphere.

Because of its collisionless nature, few people expected the formation of a shock since these normally arise from particle interactions. However, Axford [1962] and Kellogg [1962] independently predicted the existence of such a shock wave, and spacecraft observations in 1963 confirmed it [Parks, 1991, p.413]. Results from the OGO missions in 1964 provided data with which it was possible to study bow shock structure [Russell, 1995]. Observations of the bow shocks of the Earth and of other planets with magnetospheres and ionosphere, and also of interplanetary shocks, have shown that electric and magnetic fields in a plasma can provide the dissipation necessary to enable shock formation [Russell, 1995, Parks, 1991].

The shape and position of the bow shock have been the subject of many investigations and Formisano [1979] carried out the first three dimensional study. The results of the investigations were that the shape and position of the bow shock showed only minor variations with solar cycle and an element of dependency on the sonic Mach number of the solar wind. In general, they were found to be in good agreement with gas dynamic theory. No dependency on the IMF was found [Slavin & Holzer, 1981].

The bow shock has an almost paraboloid shape with cylindrical symmetry about the Sun-Earth axis, and its sub-solar location is at about $14R_e$ from the Earth's centre, though its exact position depends on the dynamic pressure of the solar wind. The dynamic pressure is important because almost all of the mass flux crossing the bow shock must flow around the obstacle formed by the Earth's magnetosphere and the bow shock must therefore form a shape which allows this flow (see 5.3.4).

While the shape and location are only mildly dependent on plasma conditions, the structure itself is very sensitive to parameters such as the Mach number, the plasma beta and the IMF direction. If the IMF is almost aligned with the direction of propagation of the shock (the shock normal), the shock is said to be quasi-parallel. If the field is more nearly perpendicular to the normal, it is said to be quasi-perpendicular.

1.5.3 The magnetosheath

The magnetosheath is the region between the bow shock and the magnetopause. The plasma in the magnetosheath is the shocked solar wind. Near the Earth-Sun axis, the solar wind downstream

Region	Solar Wind $\sim 1AU$	Magnetosheath $\sim 1AU$	Magnetosphere (at magnetopause)
Proton No. Density (cm^{-3})	7	15	8
Proton Temp. (K)	10^5	2 x 10^6	10^7
Gas Dynamic Pressure (pPa)	30	590	450
Magnetic Pressure (pPa)	15	960	880
Magnetic Field Strength (nT)	5	50	50

Table 1.2: Some typical plasma parameter values in various regimes: derived from Hundhausen [1995], Parks [1991, p.339] and NSSDC Omniweb data.

of the bow shock is subsonic [Cravens, 1997]. The flow near the flanks is supersonic, though the component of the downstream flow normal to the shock surface is subsonic. Within the magnetosheath, the plasma is hot, turbulent, and compared to that of the magnetosphere and the solar wind, dense. Table 1.2 compares the major features of the three different plasma regimes. On passing through the magnetosheath the shocked solar wind plasma must be changed so that by the time it reaches the magnetopause, the magnetic field and the velocity are tangential to the magnetopause. The character of the magnetosheath is explored in more detail in Chapter 5.

1.5.4 The magnetopause

The magnetopause is the seond major discontinuity found between the solar wind and the Earth. At this point in its journey, the shocked solar wind plasma of the IMF cannot normally mix with the plasma of the magnetosphere which is organized by the geomagnetic field. The magnetopause, therefore, forms a tangential discontinuity. However, under certain conditions, the magnetopause opens, possibly forming a rotational discontinuity, and magnetosheath plasma can cross into the magnetosphere (and the reverse process can also occur). Chapter 2 deals with some of the ways in which this may happen. Other features of the magnetopause are discussed as appropriate throughout this thesis.

1.6 Overview of thesis

In Chapter 2, we examine more closely the entry of solar wind plasma to the magnetosphere and possible mechanisms for this process. In particular, magnetic reconnection is explored in some detail.

An important manifestation of magnetic reconnection at the magnetopause is the formation of open flux tubes linking the IMF with the geomagnetic field along which solar wind and magnetosphere plasma may mix.

The resulting motion of the flux tubes along the magnetopause can help us to link observations with theoretical models of magnetopause processes, and thus can be be very useful. In Chapter 3,

we describe the development of a semi-analytical model for the motion of open flux tubes which combines a number of existing models in a new way, and in Chapter 4, we present a range of results obtained from the model.

The results reveal the importance of certain solar wind plasma parameters in determining the motion of the flux tubes. In Chapters 5, 6 and 7 we describe a broad brush survey of those parameters within the magnetosheath which we carried out using Geotail and Wind data, and compare those results with other models.

Our concluding chapter draws together the results of our model runs with the data from our survey.

Acronyms, symbols and subscripts used throughout are listed in Appendix A.

Chapter 2

Magnetic reconnection at the magnetopause

In this chapter, we review our understanding of the way in which the energy, momentum and plasma of the solar wind enter the magnetosphere and the consequences of that entry.

The chapter is divided into five sections. In the first, we discuss evidence for the entry of solar wind plasma to the magnetosphere. There are, broadly, two major mechanisms by which the transfer of plasma, energy and momentum may occur: Viscous processes and the process of magnetic reconnection. These are described in the second section. In the third section we describe the development of models of magnetic reconnection and discuss its manifestation at the magnetopause as either a quasi-steady state or transient process.

Factors causing the onset of reconnection at the magnetopause are the subject of some debate and a number of these are outlined in the fourth section. The parameters of the magnetosheath itself form an important part of this subject, and are described in some detail in Chapter 5. Magnetic reconnection poleward of the cusps under northward IMF is a hot topic of current research and is considered in the fifth section. Lastly, we discuss how an understanding of the motion of open flux tubes formed by the magnetic reconnection process assists explanation of a number of phenomena observed in the near-Earth environment.

2.1 Entry of solar wind plasma to the magnetosphere

2.1.1 Evidence for entry of solar wind plasma to the magnetosphere

In Chapter 1.1.1, we briefly outlined the origins of the understanding that there was an interplay between solar activity and disturbances in the geomagnetic field. There was, however, little indication of how this interaction may be mediated. Chapman & Ferraro [1931] were first to suggest the existence of the magnetopause boundary. Originally, they believed that the boundary

would only appear during periods of solar activity. The plasma emanating from the Sun would compress the geomagnetic field giving rise to the disturbances which had been seen to correlate with solar activity [Hughes, 1995]. Biermann's [1951] observations of comet tails showed that the solar wind was continuously present and thus the magnetopause was predicted to be a permanent feature by Dungey [1954a, 1954b].

Observational evidence demonstrating the existence of the magnetopause was obtained in 1961 from the Explorer 12 mission. Cahill & Amazeen [1963] looked at the measurements of particles and fields moving outwards from the Earth. The changes in the features at the outer edges demonstrated the existence of a discontinuity. Energetic particles were no longer trapped, and beyond the boundary the particles were of a lower energy than inside it, as would be expected from shocked solar wind plasma.

The discovery of the low latitude boundary layer (LLBL) followed within a few years, after studies of the output from the Vela 4B, 5 and 6 missions. The LLBL is located just inside the magnetopause. While it was initially observed in the near-Earth tail region, we now know that it stretches right across the magnetopause being thinnest and slowest at the sub-solar point, thickening and gaining speed as we move tailward. The LLBL itself is also a layered structure, normally, but not always, containing magnetosheath ions [Eastman & Christon, 1995, Fuselier *et al.*, 1989a].

There are a range of phenomena arising from the entry of solar wind plasma to the magnetosphere. The most spectacular of all are the aurorae. The aurorae form in ovals around the magnetic poles in both hemispheres and are normally seen during winter nights at very high latitudes. They are produced by energetic particles travelling down magnetic field lines from the magnetosphere, injected via a variety of processes including pitch angle scattering and reconnection. Collisions with ionospheric particles cause a release of energy thus generating the visible light displays.

Poleward moving auroral forms (PMAFs) have been observed as the polar cap expands with the motion depending on the North-South (B_Z) component of the IMF, moving equatorward for negative B_Z and poleward for positive B_Z. Under northward IMF, the auroral oval contracts and the auroral displays are weak. During southward IMF, the oval expands and the auroral display increases in intensity. The appearance of the display also depends on the local atmospheric composition. Aurorae may also occur on the dayside, but study of daytime aurorae is relatively recent.

A number of field aligned current systems have been identified. They form in a 6^o band of latitude coincident with the auroral oval [Kennel, 1995] and have proved to be a major coupling mechanism between the ionosphere and space [Lysack *et al.*, 1995].

The currents are commonly divided into two (or three) regions. Those of Region 1 lie on the poleward side of the band. On the morning side they flow into the ionosphere, and on the evening side flow out. Region 2 currents form on the equatorward side of the band and flow in

the opposite directions. The Region 1 currents arise from stresses which originate in the solar wind and which generate ionospheric convection. The Region 2 currents relate to closure of the ring current system [Peymirat & Fontaine, 1994]. The current system pattern changes in line with geomagnetic activity which is itself driven by the solar wind conditions. A third current system, sometimes known as Region 0, may also form poleward of the Region 1/2 system and shows a dependency on IMF B_Y [Lysack *et al.*, 1995].

Currents may be generated in several different ways: dynamic pressure pulses of the solar wind which cause the magnetopause to move in and out and this may generate compressional fast mode Alfvén waves [Southwood & Kivelson, 1990], a Kelvin-Helmholtz instability due to the flow shear across the magnetopause, or by localized magnetic reconnection at the magnetopause or in the tail.

2.1.2 Sources of plasma in the magnetosphere

The two main sources of plasma within the magnetosphere are the solar wind and the ionosphere. During quiet times, most of the plasma originates from the solar wind. In times of greater activity, the ionosphere may become the principal source.

Direct evidence for the entry of solar flare electrons into the magnetosphere was found by Lin & Anderson [1966] and Winningham & Heikkila [1974], for example. The latter showed that the solar wind electrons were transported from the tail lobes to the polar cap ionosphere in the form of 'polar rain'. Morfill & Scholer [1973] and Fennell [1973] showed that solar wind protons were also entering the polar caps directly.

There are two sources of ionospheric plasma, the 'polar wind' and the auroral zones, illustrated in Figure 2.1. The polar wind, in analogy with the solar wind, occurs because gravity cannot contain the ionospheric pressure and consists of 1-10 eV H^+ and electrons of very low density 0.1 - 1 cm^{-3} and low speeds of order tens of kms^{-1}. The second ionospheric source occurs above the auroral zones. The plasma is of higher energy, $100eV$ to a few keV and with speeds of order hundreds of kms^{-1}.

A number of plasma populations form within the magnetosphere: the solar wind plasma in the LLBL, polar rain, plasma mantle, outer plasma sheet and ring current, while the ionospheric plasma gives rise to the polar wind, and inner plasma sheet and ring currents.

The polar cusp is the only region where solar wind plasma has been observed to enter the magnetosphere directly. It precipitates into the ionosphere along cusp field lines. The energy carried down can heat the ionospheric plasma giving rise to a phenomenon known as the 'cleft ion fountain' [Lockwood *et al.*, 1985]. Figure 2.2 shows the interaction between the magnetosheath and ionospheric plasmas in the cusp/cleft region.

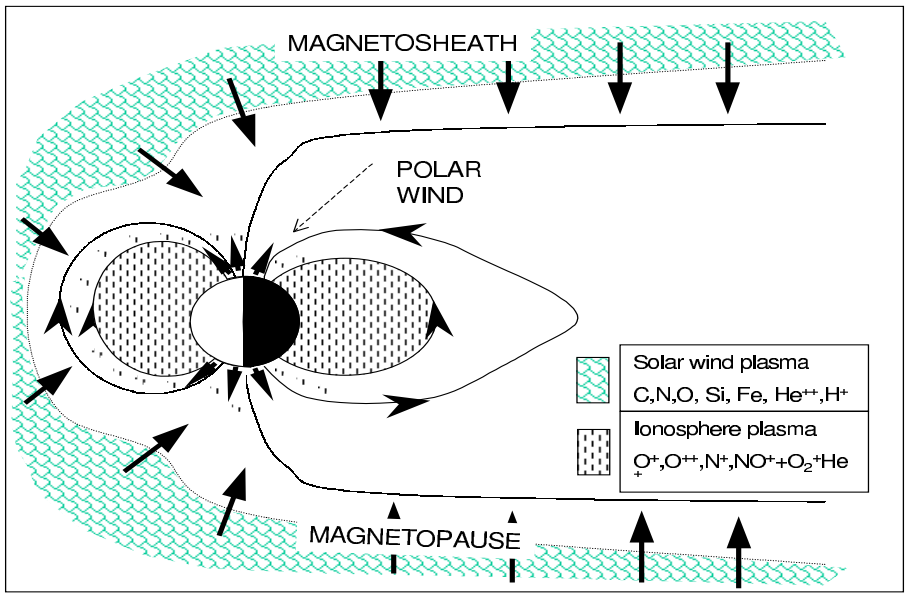

Figure 2.1: Showing the two basic sources of magnetospheric plasma. Based on Saunders [1991]

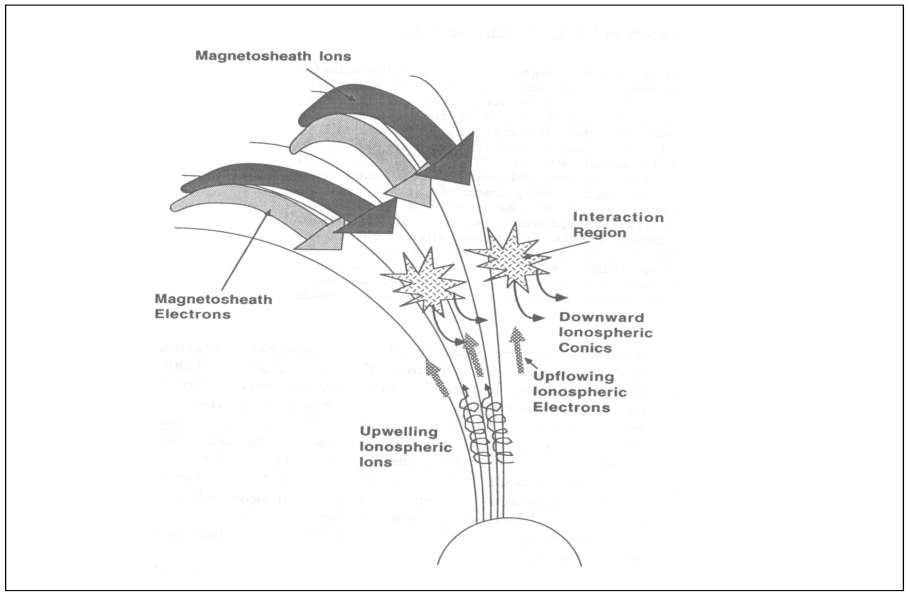

Figure 2.2: Schematic diagram showing the interaction between the magnetosheath and ionospheric plasmas in the cusp/cleft region. From Winglee *et al.* [1994]

2.1.3 Identification of plasma from different regimes

In order to investigate the transfer of plasma from one regime to another, we need to be able to identify characteristics peculiar to each. Solar wind plasma tends to contain about 95% H^+ ions, but also He^{++} and the higher charge state groups of C, N, O, and also Si and Fe ions [Eastman & Christon, 1995]. Ionospheric plasma on the other hand tends to comprise He^+ and O^+ ions.

The different characteristics of the particles making up the plasma populations within the

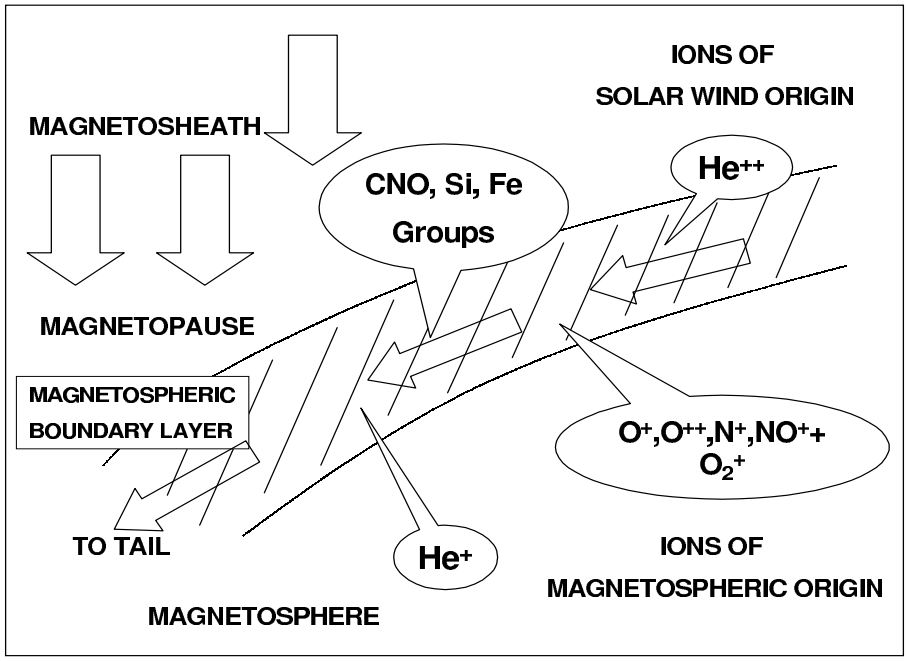

Figure 2.3: Ions of solar wind and ionospheric origin come together in the boundary layer region and are convected tailward as illustrated here. Based on Eastman & Christon [1995]

magnetosphere allow the separation of ion species and their occurrence probabilities to be used for tracing the originating regime of the plasma under observation (e.g. Stubbs *et al.* [2001]). Figure 2.3 shows the coming together of the ions of solar wind and ionospheric origin into the boundary layer and subsequent convection down tail.

2.2 Transport mechanisms for solar wind plasma entry to the magnetosphere

Having established that solar wind plasma, energy and momentum do pass through the magnetopause and enter the magnetosphere, we need to consider further the mechanisms which may allow this to happen. Transport mechanisms fall into two main categories: viscous processes and magnetic reconnection. Classic papers on both processes were published in 1961, Axford & Hines [1961] proposing a viscous process as a driver of the convection cycle, and Dungey [1961] introduced the idea of magnetic reconnection as a mechanism for magnetospheric convection. Figure 2.4 compares the two models.

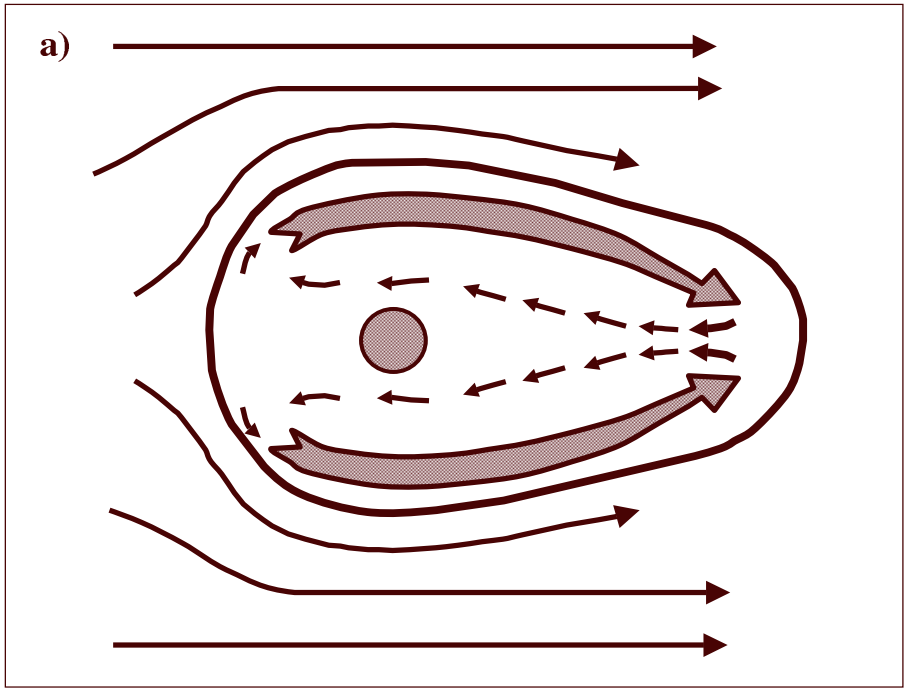

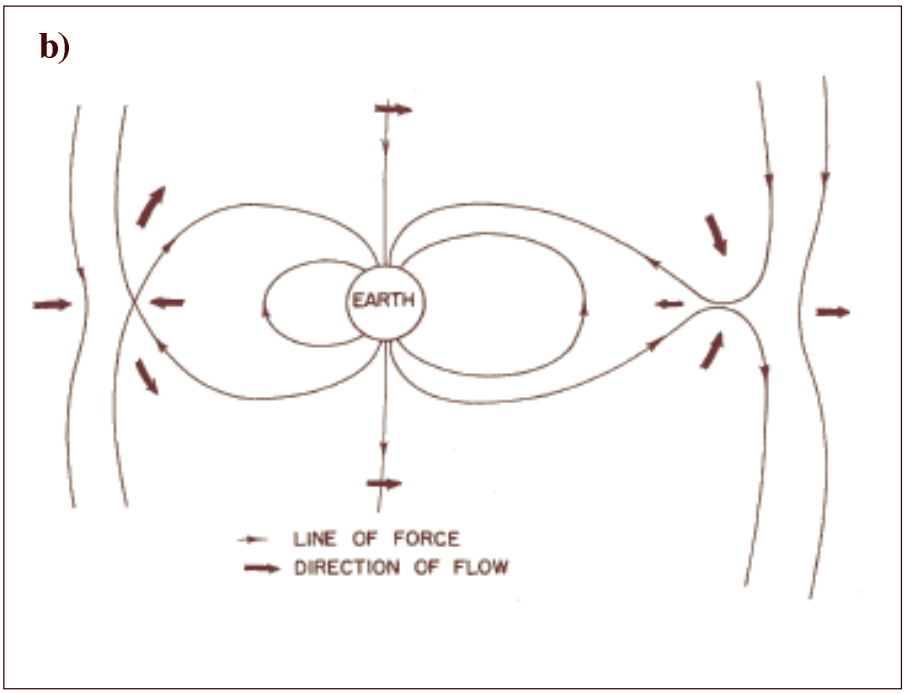

Figure 2.4: Comparing (a) Axford & Hines [1961] viscous model and (b) Dungey [1961] reconnection model for interaction at the magnetopause.

2.2.1 Viscous processes

Axford and Hines model

Axford & Hines proposed that a single causal mechanism could explain the observed phenomena of the magnetosphere, e.g. aurorae, distribution of ionosphere electrons, steady-state of the magnetosphere and the production of trapped particles in the Van Allen belts. They proposed a viscous-like mechanism between the solar wind and the magnetosphere. Compression arising from convection in an inhomogeneous field would explain the increase in energy of particles trapped in the geomagnetic tail and of solar wind particles from the boundary. Figure 2.4(a) shows an equatorial section of the magnetosphere with the solar wind coming in from the left. Force tubes near the surface of the magnetosphere are pulled tailward as indicated by the large arrows, with a return flow indicated by the smaller arrows within the interior of the magnetosphere.

Impulsive penetration

The impulsive penetration model has been developed in two ways, the Lemaire and Roth Model [Lemaire & Roth, 1978] and the Heikkila Model [Heikkila, 1982]. These models emphasize the kinetic energy of the solar wind and localized inhomogeneities in the interaction between the solar wind and the magnetosphere (e.g. the development of small scale inhomogeneities in plasma density ('plasmoids') formed by the continuously changing IMF vector [Bostik, 1956, Burlaga *et al.*, 1977]).

In the Lemaire and Roth model, (as described in Roth [1995]), when a plasmoid moves towards the magnetopause with the solar wind speed, it reaches the average position of the magnetopause with an excess of momentum and kinetic energy. As its motion may be described in the guiding centre approximation [Schmidt, 1991], there is an electric drift parallel to $\mathbf{E} \wedge \mathbf{B}$ arising from the charge separation electric field, a gradient-$\mathbf{B}$ drift and a polarization drift. A plasmoid penetrating the magnetopause gains a normal polarization electric field related to the inhomogeneity of the surface charge density. Such a plasmoid decelerates (accelerates) adiabatically when the magnetic field intensity inside the magnetosphere is greater (smaller) than that in the magnetosheath. The maximum distance to which a plasmoid may penetrate is the position x at which the magnetic field intensity in the magnetosphere is given by:

$$B(x) = B_0 \left[1 + \frac{m{V_{ex}}^2}{2k({T_{\perp o}}^+ + {T_{\perp o}}^-)}\right] \tag{2.1}$$

$$= B_0 \left[1 + {M_s}^2\right] \tag{2.2}$$

where B_0 is the magnetic field strength at the point of impact at the magnetopause and M_s is the sonic Mach number in the magnetosheath. Penetration distance x increases with increasing B_0 and M_s.

Heikkila [1982] proposed a somewhat different mechanism for impulsive penetration which placed greater stress on the rôle of induced electric fields. A magnetosheath plasma cloud with

excess momentum may distort the magnetopause and its associated currents thereby inducing an electric field. If there is no B_n component, then the plasma flow follows the moving magnetopause. However, if $B_n \neq 0$, then the inductive electric field gains a normal component causing plasma to polarize along B_n allowing the cloud to move through the moving magnetopause. Owen & Cowley [1991] showed that the Heikkila version of the impulsive penetration theory using ideal MHD did not work as it violates Faraday's law.

Various observations offer support to Lemaire and Roth's mechanism including magnetosheath plasma injection events at the dayside magnetopause in the LLBL and their auroral and ionospheric signatures, e.g. Lundin & Dubinin [1985], Heikkila *et al.* [1989]. More recently, observational evidence from the Cluster Ion Spectrometer experiment of 'Plasma Transfer Events' [Lundin *et al.*, 2003], lends further support to the impulsive penetration mechanism.

Kelvin Helmholtz Instability

The Kelvin Helmholtz instability (KHI) is generated by a strong velocity shear at the LLBL. This creates surface waves which compress the magnetosphere, further generating compressional waves [Kivelson, 1995b]. Growth times for the KHI are comparable to the time it takes for Alfvén waves to reach the ionosphere from the magnetopause, and hence the ionosphere has a rôle to play in analysis of the KHI [Lysack *et al.*, 1995].

The KHI is more important at the flanks of the magnetopause than on the dayside [Treumann *et al.*, 1995] and can transport momentum but was not thought to be able to transmit mass (and hence plasma). Recent work by Nykyri & Otto [2001] suggests that in fact the KHI may be able to transport mass by twisting the surface in such a way that magnetic reconnection may occur (though this is not classical KHI). Smets *et al.* [2002] also claim that the KHI may allow some mass transfer. They suggest a crossing rate of order of 10% from test-particle calculations, through the magnetopause at the flanks.

Particle diffusion and wave-particle interactions

In order to maintain the LLBL under northward IMF, a diffusion rate of $\sim 10^{13} cm^2 s^{-1}$ is needed [Fu *et al.*, 1995]. Several theories on the rôle wave-particle interactions may play in providing diffusion of the required rate have been put forward. For example: Tsurutani & Thorne [1982] suggest that the diffusion arising from electric and magnetic turbulence levels near the ion cyclotron frequency may be sufficient. Haerendel & Paschmann [1982] put forward the notion that low frequency eddy currents may be able to transport large plasma blobs into the magnetosphere so that continuous microscopic diffusion processes are not required. Pu *et al.* [1986] and Fu *et al.* [1995] developed the idea of drift kinetic Alfvén wave (DKAW) instabilities which have magnetic field perturbations normal to the magnetopause. Sufficiently large amplitude waves cause the onset of turbulence and phenomena similar to magnetic percolation (Section 2.3.3) may take place.

Evidence for viscous processes

- Existence of the LLBL under northward IMF: the existence of the LLBL with its population of magnetosheath ions is difficult to explain under northward IMF. The reasons for this will become apparent in Section 2.4. Viscous processes may offer an explanation for the introduction of magnetosheath ions into the LLBL. Recent work, however, suggests that it may be possible to invoke magnetic reconnection to explain this (Section 2.5)

- Mozer [1984] studied the electromotive force (e.m.f.) across the LLBL for 28 ISEE1 encounters with the magnetopause. His conclusions were that the average e.m.f. attributable to the viscous interaction is around 5kV. There appeared to be no relationship with the B_Z component of the IMF and hence it is not related to magnetic reconnection.

- Papitashvili *et al.* [2001] report persistence of field aligned Region 1 and 2 currents through a full range of IMF orientations, including a near-zero IMF.

- Evidence from Viking: Magnetosheath plasma intrusion events [Woch & Lundin, 1991] which are best explained by impulsive plasmoid entry into the magnetosphere through the magnetopause.

2.2.2 Magnetic reconnection

Dungey model

Magnetic reconnection was originally developed during the 1950s as an explanation for solar flares and Dungey produced an exposition of this idea in Dungey [1958]. In 1961, he proposed that magnetic reconnection could be used to explain the convection patterns seen within the magnetosphere. The underlying concept of magnetic reconnection (discussed in more detail in Section 2.3) is that when two plasma regimes are driven together, a current sheet develops between them. A local breakdown in the 'frozen-in-flux theorem' allows magnetic field lines from the different regimes to link across the current sheet. The release of magnetic energy causes the plasma to heat and accelerate along the reconnected field lines resulting in an exchange of mass, energy and momentum between the two plasmas. Dungey's idea for a steady-state model was that, under southward IMF, reconnection would occur in two places, in the sub-solar region and at a location in the geomagnetic tail. Figure 2.4b shows this process.

When reconnection occurs at the magnetopause, we now have three types of field lines. There are field lines with both ends in the IMF, closed geomagnetic field lines stretching from pole to pole, and a third, open, type with one end stretching to one of Earth's poles and the other in the IMF. Upon reconnection in the sub-solar region, the open reconnected field lines convect anti-sunward along the magnetopause as shown in Figure 2.5.

Dungey's theory took many years to gain acceptance but today is believed to explain most of the transfer of solar wind plasma to the magnetosphere. Sections 2.3.2 and 2.4 are devoted

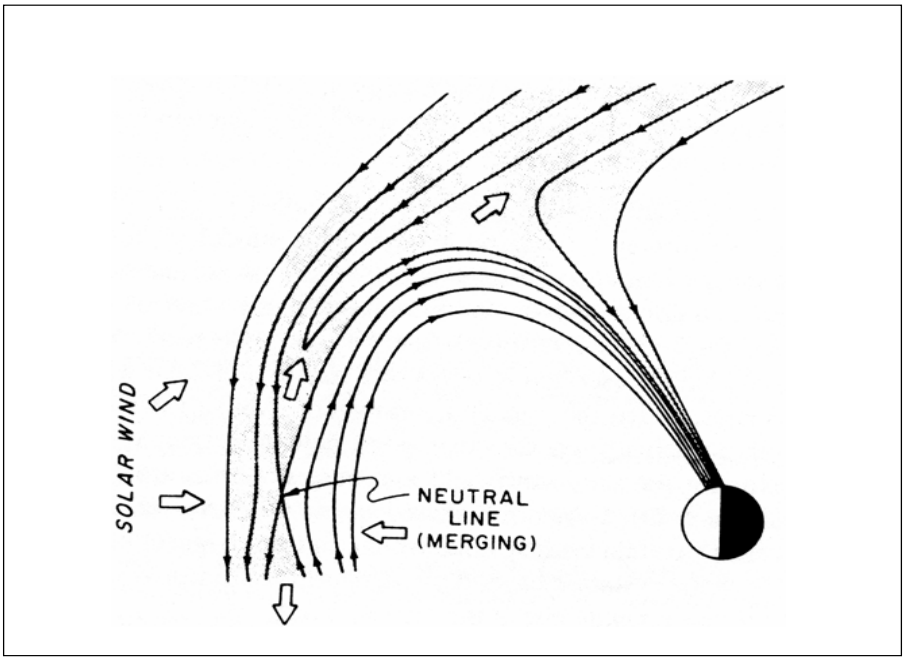

Figure 2.5: The classical picture of the convection of a flux tube following reconnection at the sub-solar point under southward IMF (source: unknown)

to setting out more detailed models of magnetic reconnection, the forms it may take at the magnetopause and the conditions required for its onset.

Evidence for Reconnection Models

- Dependence on B_Z: Fairfield & Cahill, Jr. [1966] were the first to demonstrate that geomagnetic activity was modulated by the IMF B_Z component. Viscous mechanisms do not explain why this should be so.
- Non-zero normal magnetic field component, B_n, at the magnetopause [Sonnerup & Ledley, 1979]. (See Sections 1.3 and 2.3.3).
- Polar rain (see Section 2.1.2):. Electrons carrying distinctive solar spectra are found in polar cap field lines but only in the cap which is connected to the IMF. That is, the northern cap for 'away' and the southern cap for 'toward' IMF [Winningham & Heikkila, 1974].
- Accelerated flows: many researchers have observed accelerated plasma flows or jets consisting of magnetosheath plasma just inside the magnetopause. The first of these was Paschmann *et al.* [1979], also giving the first direct evidence of magnetic reconnection .
- Existence of tail neutral line: ISEE3 data showed the existence of the tail neutral line [Slavin *et al.*, 1985].

- Substorms (see below): The substorm phenomenon is most readily explained using a magnetic reconnection description such as the near-Earth neutral line theory (e.g. McPherron *et al.* [1973], Russell & McPherron [1973]).

A number of these phenomena are described more fully below.

Non zero magnetic field component normal to the magnetopause

The clearest theoretical signature for magnetic reconnection is the existence of a rotational discontinuity characterized by a non-zero normal component for the magnetic field at the magnetopause. The normal direction is difficult to identify experimentally. This is due to the continuous motion of the magnetopause making the definition of the normal vector at any given time very tricky. Experimentalists have devised a number of ways of getting around this problem (see, for example, Paschmann & Daly [1998]), but they are not discussed here as they do not contribute to this work.

Plasma jets and high speed flows

From simple stress balance (Section 3.3) under southward IMF, reconnection at the sub-solar point with anti-parallel magnetic fields, leads to the expectation that plasma jets in the magnetopause boundary layer will be found with speeds $\sim 2V_A$ [Sonnerup, 1979, Cowley, 1979, 1981]. However, an arbitrary magnetic flux component in the direction of the reconnection line may be added without changing the validity of the analysis. For example, pure north/south jetting of the earlier simple models is modified in the presence of IMF B_Y (dawn-dusk) components. A range of B_Y asymmetries have been identified e.g. Svalgaard [1968], Mansurov [1969], Heppner [1972], Cowley [1981], Cowley *et al.* [1983].

Paschmann *et al.* [1979], studying ISEE data, made the first detailed observation of accelerated plasma flows just inside the dayside magnetopause field rotation consistent with a magnetosheath source. This was the first direct observational evidence in support of Dungey's theory. Later, Sonnerup *et al.* [1981] made a systematic survey of eleven passes of the ISEE satellites through the dayside magnetopause and found that ten out of the eleven events concurred with the expectations for magnetic reconnection. The characteristics of the detected plasma were consistent with a magnetosheath source. The best indicator of magnetic reconnection would be oppositely directed plasma jets, on either side of the x-line. Phan *et al.* [2001] claim that such jets had never been unambiguously seen prior to their reported observations in Phan *et al.* [2000] in which in situ dual-spacecraft observations of such plasma jets were made.

Tail structure

The structure of the magnetotail is a signature of magnetic reconnection. The open field lines stretch out into a long, low density, magnetic field. The tail is divided into two lobes representing plasma connection to the northern and southern polar caps respectively. The two lobes are

separated by a central current sheet. Finally, a site for magnetic reconnection in the central plasma sheet is found.

Convection and Substorms in the Magnetosphere

Ground-based observations of the ionosphere show a convection pattern coincident with the auroral zone. At high latitudes, plasma flows from noon toward midnight and returns via the dayside at lower latitudes. Heppner & Maynard [1987] used electric field measurements from the Dynamics Explorer 2 satellite to construct global representations of characteristic equipotential, or plasma flow, patterns. More recently, studies using data from the SuperDARN/CUTLASS radar arrays coupled with data from Polar (UVI instrument), DMSP, IMP 8 and Geotail satellites, have looked at various aspects of ionospheric convection and its dependence on the orientation of the IMF. For example, Kozlovsky *et al.* [2002] show how for negative B_Y the convection is colocated with the maximum of auroral luminosity, while for positive B_Y it is poleward of the auroral oval. Senior *et al.* [2002] found that convection in the morning sector reacts with intermediate delay to a turning of B_Y from negative to positive, and Lu *et al.* [2002] demonstrated that there is a two stage response of the convection pattern when the IMF turns southward. The flow pattern is analogous to that of a thermal process, hence it is named 'convection'. However, there are no thermal processes involved in this flow.

The magnetosphere evolves through different phases over time. Under northward IMF, the magnetosphere is in a relatively quiet phase there is very little interaction between the IMF and the Earth's field and magnetic flux is not being added to the magnetotail. After the IMF turns southward, dayside reconnection produces open magnetic flux which convects over the pole into the tail. When enough flux has entered the tail, it becomes unstable and a substorm develops. Substorms occur at night, in particular around local midnight. They are characterized by a sharp disturbance in the geomagnetic field of up to a few hours in duration. Associated phenomena include auroral displays, an increase in ionospheric electron density and emissions of x-rays and vlf radio waves. These phenomena always occur simultaneously in the northern and southern hemispheres. (See, for example, McPherron [1995]).

There are a number of explanations for the phenomena of substorms, the most successful of which invoke magnetic reconnection. The near-Earth neutral line model (e.g. McPherron *et al.* [1973], Russell & McPherron [1973]) explains this phenomenon as follows. The interaction between the IMF and the Earth's magnetic field intensifies and magnetic flux from the dayside magnetosphere erodes as it passes into the tail lobes, storing up energy in the tail. This increases pressure on the plasma sheet which separates the two tail lobes causing it to compress and move inward, extending the neutral current sheet and causing the onset of reconnection in the near-Earth tail at 20-30R_e downtail. A plasma bubble known as a plasmoid forms and is ejected away from the Earth, meanwhile excess flux in the lobes passes back to the Earth's dayside. The returning energetic particles may be captured by the Van Allen belts and the x-line retreats tailward.

2.2.3 Competing or Parallel Theories?

The discussion above has presented the two mechanisms of the viscous interaction and magnetic reconnection processes as though they are competing alternatives. In fact we now believe that both mechanisms have a rôle to play in the transfer of solar wind plasma and its attendant energy, mass and momentum to the magnetosphere. The two processes are not mutually exclusive. The magnetosphere is a dynamic, constantly changing region of space and thus as conditions change, so may one process be favoured over the other at a given instant. While we now believe magnetic reconnection to be the predominant process, responsible for the transfer of the majority of the plasma from the magnetosheath to the magnetosphere, viscous processes are by no means a negligible part of this system.

The relative contributions of each process to the energy input to the magnetosphere from the magnetosheath may be measured using the Perreault-Akasofu [1978] energy input rate, $\epsilon = V_{sw}B^2L^2sin^4(\theta/2)$ where ϵ is the energy input rate, V_{sw} is the solar wind speed, B is the magnetic field strength, L the effective length of the reconnection 'line' (usually taken to be $7R_e$ [Kennel, 1995, p.93]) and $\theta = B_Y/B_Z$ is the clock angle of the IMF in GSM coordinates. Kennel (and references therein) states that the Perreault-Akasofu function shows that reconnection can provide 100-1000 GW of power for southward IMF on the dayside magnetopause, while that due to the KHI under similar conditions is around 100 GW.

2.3 Magnetic reconnection

In this section we first define magnetic reconnection and the reconnection rate. Next, we describe the development of the main models of magnetic reconnection. Lastly, we describe manifestations of magnetic reconnection at the magnetopause as either a (quasi)-steady or transient phenomenon.

2.3.1 Definitions of Magnetic Reconnection

Lee [1995, p148] sets out three definitions for 2D magnetic reconnection, also neatly summarised by Scudder [1997]:

- Where field energy is transferred to plasma energy when crossing a topological boundary, alternatively where plasma flows across separatrices [Vasyliunas, 1975].
- Where a parallel electric field is collocated with field aligned currents, alternatively, where there is a non-zero electric field component along all or part of the magnetic x-line or separator [Baum & Bratenahl, 1980, Sonnerup, 1984].
- Where the frozen field approximation; $\mathbf{E} = -\mathbf{V} \wedge \mathbf{B}$ is violated, alternatively, a process in which magnetic flux connection is changed due to localized violation of the frozen-in-flux condition [Axford, 1984].

Reconnection Rate

An important concept in models of reconnection is that of reconnection rate. This is a measure of the amount of plasma which is accelerated to the inflow Alfvén speed per unit time [Cowley, 1985, p.133], $E = V_i B_i$ where V_i, B_i are the velocity and magnetic field intensity in the inflow region, i.e. the electric field along the reconnection line [Sonnerup *et al.*, 1995].

When analyzing experimental data, it is more common to use the local Alfvén Mach number, M_{An} of the plasma flow into the magnetopause as a proxy for the reconnection rate providing that the distance from the location of the observations to the reconnection line is not too great. This is because in a rotational discontinuity, normal flow velocity $|V_n| \approx |V_{An}|$ and we may then write

$$M_{An} \equiv |V_n|/|V_A| \approx |B_n|/B. \tag{2.3}$$

(Also refer to Equation 1.14 for V_A in an anisotropic plasma). Thus the size of the normal magnetic field component (or the normal flow component) serves to measure the reconnection rate.

The reconnection rate appears to be independent of the mechanisms causing the onset of reconnection [Shay *et al.*, 2001].

2.3.2 Models of Reconnection

Fluid versus Kinetic Theories

The basic idea of magnetic reconnection was discussed in secion 2.2.2. The underlying microphysics of the process is, however, not well understood. This has not prevented the successful application of the theory to various problems in space plasmas. In this section, the development of models of magnetic reconnection over a period of several decades is reviewed. Fluid MHD models developed from Alfvén's 1942 concept of moving flux tubes. Others (e.g. Hill [1975]) have developed particle models which use the same conservation laws as the fluid models and which can model totally collisionless behaviour. It can be shown (e.g. Cowley [1985], Hughes [1995]) that reconnection rates similar to those of MHD and flow patterns similar to those of the Petschek model are obtained. For this reason, a particle description of magnetic reconnection will not be given in this thesis.

Sweet and Parker Model

Sweet [1958] and Parker [1957] first proposed an MHD model of magnetic reconnection which used a basic x-line structure as shown in Figure 2.6.

In this model, symmetric inflow and outflow regions with a diffusion region of size 2L x 2l are assumed (Figure 2.6). The model also assumes incompressible flow and conservation of mass. It is also assumed that the electromagnetic energy flowing into the diffusion region may be equated directly to the gain in kinetic energy of the outflowing plasma. This leads to an inflow plasma speed, V_i of

$$V_i = V_{Ai}(2^{\frac{1}{2}}/R_M)^{\frac{1}{2}} \tag{2.4}$$

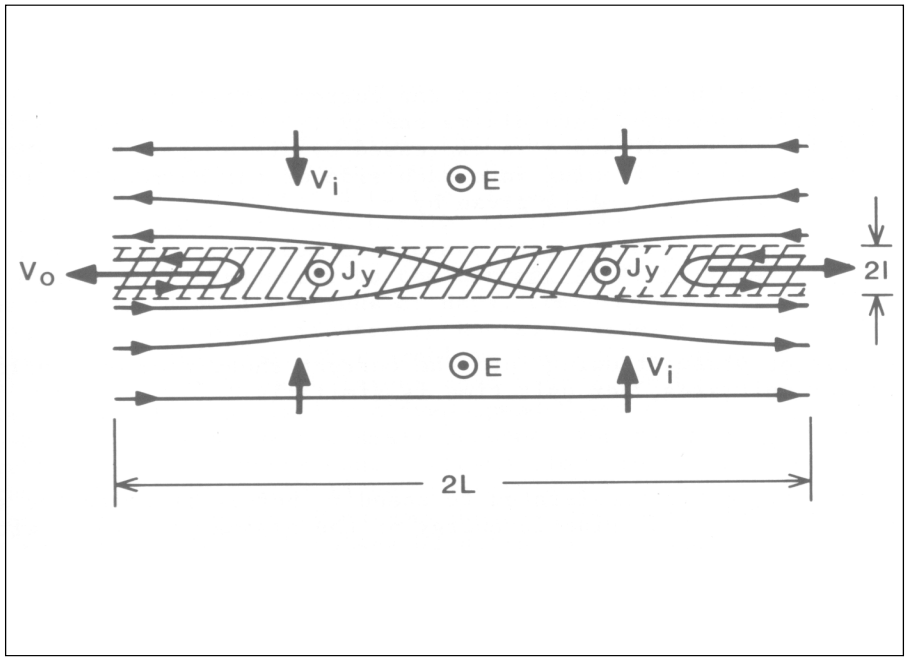

Figure 2.6: Field (solid lines) and flow (arrows) assumed in the Sweet-Parker model. The current sheet (diffusion region) shown hatched, small half-width l set by the scale of diffusion over its whole half-length L, the latter length is equal to the scale size of the system. [Cowley, 1985]

where

$$R_M = \mu_0 \sigma V_{Ai} L \tag{2.5}$$

For solar system plasmas where R_M (the magnetic Reynolds number) is very large, this gives an inflow speed which is much too slow for magnetic reconnection to be seriously considered as a mechanism for transfer of energy and momentum. For example, solar flares are observed to grow in a few minutes, but using the Sweet-Parker model, this would take many days.

Petschek Model

Petschek [1995], drawing on a number of concurrent developments in fusion physics and his background in turbulence in fluid dynamics, refined the Sweet and Parker model by adding the notion of shock waves as a means of increasing the diffusion rate [Petschek, 1964]. He suggested that magnetic energy could be dissipated by the propagation of Alfvén waves. As the inflow plasma speed is always supersonic with respect to the slow wave speed, slow MHD shocks emanating from the diffusion region will be the result [Jardine, 1991]. As a result, the diffusion region becomes extremely small. Four slow mode shock waves radiate from it which serve to change the strength and direction of the plasma flow and cause the magnetic field strength to drop.

A detailed analysis of the system shows that in the steady state, the inflow speed is less than $0.1V_{Ai}$ but this is still sufficiently fast for magnetic reconnection to be considered a suitable candidate for the dissipation of magnetic energy.

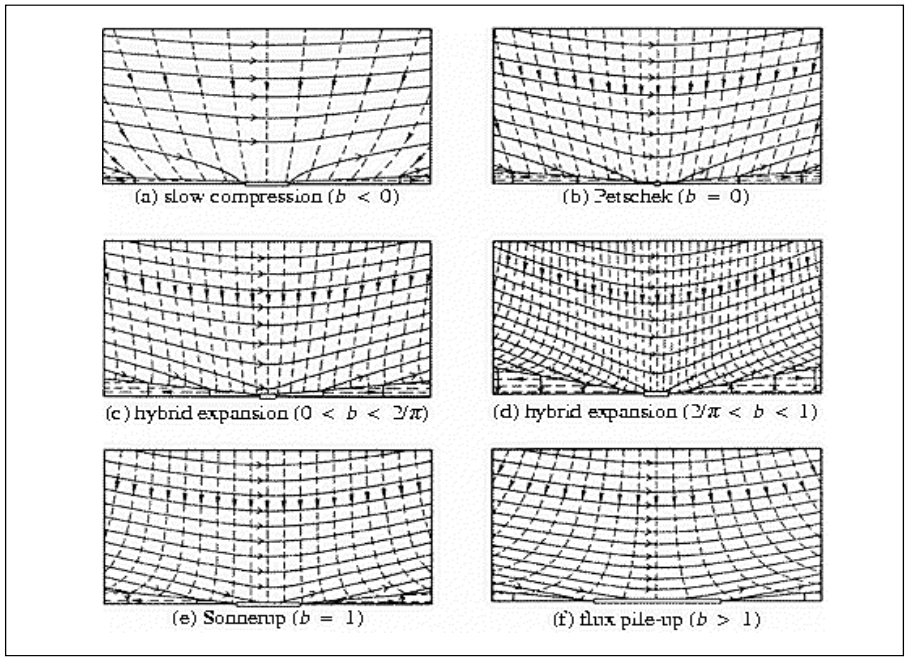

Figure 2.7: Priest & Forbes [1986] model showing magnetic-field lines (left to right) and streamlines(vertical) for several regions of the unified theory of almost-uniform steady reconnection, indicated by different values of the parameter b. (Taken from Priest & Forbes [2001])

Sonnerup

In 1970, Sonnerup [1970] introduced a set of fast-mode shocks which act to compress the magnetic field and plasma in the inflow region and start the change in flow direction. The positions of the shocks are determined by external boundary conditions, and in some cases occur gradually throughout the inflow region rather than as discrete shocks. Sonnerup's solution gives reconnection rates of the order of the Alfvén speed.

Priest and Forbes

In the mid 1980s, Priest & Forbes [1986] (and Forbes & Priest [1987]) presented a new unified family of models. The conditions imposed upon the inflow boundary determine whether Petschek-like or Sonnerup-like reconnection occurs. Priest and Forbes built on the suggestion by Vasyliunas [1975] that differences in models could be explained by considering the MHD interactions taking place in the inflow region and characterised their family of solutions by the parameter b, where b is a measure of the transverse velocity on the inflow boundary. Figure 2.7 shows results for different values of b.

$b = 0$ gives Petschek-like solutions and $b = 1$ Sonnerup-like. The Petschek result is a special case, where inflow current $\mathbf{j} = 0$. For the case where b is very large, there is a strong transverse component to the inflow. The solution seems to be the limiting case of a flux-pile-up regime. It has the form of a slow mode expansion close to the diffusion region and a fast-mode expansion

further away.

Numerical Experiments

A number of numerical simulations have been carried out on magnetic reconnection which do not necessarily support the more analytical approaches above [Jardine, 1991]. Some of these differences are, for example:

- Biskamp's 1982, 1984b, 1984a, 1986 results show that as the reconnection rate increases, the width and length of the diffusion region also increase, contrary to the expection from Petschek-like reconnection where $l \sim R_M^{-1}$ and $L \sim R_M^{-2}$. Forbes & Priest [1987] argue that as the reconnection rate increases, transverse velocity on inflow changes, therefore the reconnection regime changes hence these results would not apply.
- Lee & Fu [1986b], Fu & Lee [1986] found that the diffusion region length increases with reconnection rate, but that expansion changes from fast to slow mode.
- Scholer [1989] found that Petscheck reconnection can only be obtained if resistivity is localized.
- Numerical experiments predict the presence at the outflow of the diffusion region of a spike of reverse current acting to deflect plasma jets along the separatrices (e.g. Soward & Priest [1986], Schindler & Birn [1987]).

Much other work has been carried out in looking at aspects of reconnection both in the laboratory, e.g. Swarthmore Spheromax and Princeton's MRX experiments, and simulations but will only be discussed further in this work where relevant. A review of laboratory experiments can be found in Yamada [1999].

Limitations of Models

The analytical models make a number of assumptions about the plasma regimes either side of the current sheet. These often include assuming that the plasma regimes either side of the current sheet are symmetrical with antiparallel magnetic fields. One example with asymmetrical inflow regions is that of Levy *et al.* [1964]. Another major assumption is that time steady conditions prevail both with regard to the inflow plasma and to the stability of the current sheet. Various commentators have addressed these issues which will be discussed later where necessary.

2.3.3 Steady or non-steady magnetic reconnection

Magnetic reconnection at the magnetopause may occur as either a steady (or quasi-steady) process, or, more commonly, as a transient phenomenon typified by 'flux transfer events'.

Quasi-Steady Reconnection

Saunders [1991] defines dayside quasi-steady reconnection (QSR) as events where the reconnection rate is constant for at least one minute. Development of the theory of the sandwich-like structure of the reconnection layer enabled more observations to be compared against theory [Heyn *et al.*, 1988, Biernat *et al.*, 1989]. The structure may consist of two Alfvén waves on each of the outer 'surfaces', one adjacent to the magnetosheath and the other to the magnetosphere. Inside each of the Alfvén waves there may be two slow shocks. These, in turn, may be separated by a contact discontinuity. By adapting Petschek's model to take into account plasmas of different density and arbitrary magnetic field direction, Rijnbeek *et al.* [1989] showed that a particular magnetopause crossing event could be interpreted as QSR. However, as mentioned in Section 2.2.2, Phan *et al.* [2001] claim to provide the first unambiguous observation of reconnection. Recent results from Cluster II taken in early 2001 may also provide evidence of continuous reconnection [Owen *et al.*, 2001].

Flux Transfer Events

Flux transfer events (FTEs) are an important manifestation of non-time steady reconnection at the magnetopause and are its most commonly observed form. The overall contribution of FTEs to the global transfer of magnetic flux from the magnetosheath to the magnetosphere is not known and work on assessing this is ongoing.

FTEs were discovered in the early ISEE1 and 2 data by Russell & Elphic [1978]. At the same time, Haerendel *et al.* [1978] also used Heos 2 data to deduce that magnetic reconnection was probably occuring as a transient process in the cusp region. Russell & Elphic [1978] had developed a local boundary normal coordinate system (LMN) for plotting magnetopause magnetometer data (see Appendix B), where N is perpendicular to the local magnetopause. When the magnetic field data were organized using this system, a bipolar signature was found in the data. An example of this signature is shown in Figure 2.8. This signature is found to be characteristic of FTEs. A northward (southward) moving event produces a positive (negative) perturbation in B_N. Other features of FTEs are an increase in field strength and some repetition of events.

In the Russell and Elphic model, flux tubes reconnect over a narrow segment forming a hole in the magnetopause. A pair of elbow-shaped flux tubes, one linked to the northern cap and the other to the southern cap are formed. This is illustrated in Figure 3.2.

A number of theoretical models of FTEs have been put forward depending on whether reconnection is believed to occur at a single x-line or across multiple x-lines (see Section 2.4.2 for further discussion on reconnection lines). Other models invoke a combination of the KHI and a tearing mode instability. An example is the percolation model described by Kuznetsova *et al.* [1995]. This can cause magnetic islands to grow and for magnetic field lines to wander from one side to the other, crossing the current layer via an irregular path thus 'percolating' through the layer.

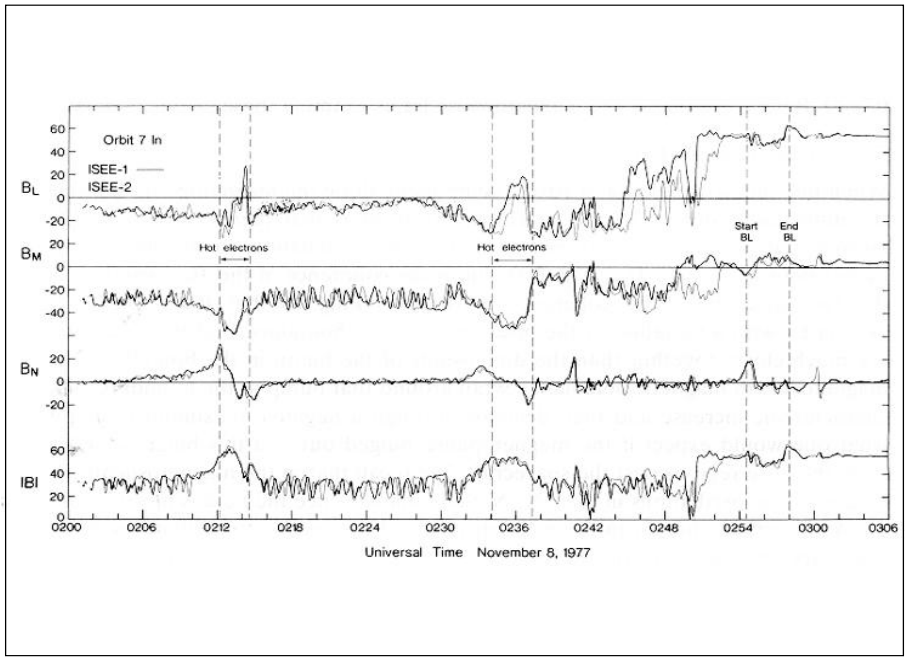

Figure 2.8: An example of the B_N bipolar signature of FTEs [Russell & Elphic, 1978].

Single x-line bursty reconnection was proposed independently by Scholer [1988] and Southwood *et al.* [1988]. In this model FTEs are created when either an increased reconnection rate or sudden onset of reconnection leads to the creation of a pair of bulges in the magnetopause. These bulges have a large longitudinal dawn-dusk orientation and are transported to the north and south cusps at the Alfvén speed.

Multiple x-line reconnection was suggested by Lee & Fu [1985, 1986a], Fu & Lee [1986] who proposed that when a magnetized plasma is continously injected toward a 1D current sheet, the tearing mode causes the growth of magnetic islands which become flux tubes embedded in the magnetopause. They propose also that the neutral line will extend over a large longitudinal segment of the dayside. Lee & Fu [1986a] carried out various simulations showing that as the ratio of system length to system width increases, steady state single x-line reconnection can no longer be maintained and multiple x-line reconnection commences, with magnetic reconnection occuring in multiple sites simultaneously.

Some observers, e.g. Sibeck [1990, 1992], Sibeck & Smith [1992], have put forward the view that a range of transient ($\sim 1min$) phenomena, including FTEs, may explained by alternative, non-reconnection, mechanisms such as the KHI, impulsive penetration and pressure pulse driven riplets on the magnetopause. Sibeck [1995] concludes that, for example, the pressure pulse model can predict certain features of the occurence of transient events, and in particular, does not support a view that such events would occur mainly during periods of southward IMF.

A wide range of observations of FTEs have been recorded in the literature investigating a number of aspects. Lockwood & Wild [1993], Berchem & Russell [1984], Rijnbeek *et al.* [1984],

Jacob & Cattell [1993], Kawano *et al.* [1992] investigated the dependence of FTE activity on IMF orientation, the first finding evidence that it increases with southward IMF, and the remainder having a mixed view. Daly *et al.* [1981], Daly & Keppler [1983] and Thomsen *et al.* [1987] investigated ion and electron distributions and abundances and found FTEs had a mixture of magnetosphere and magnetosheath populations.

Events with LLBL plasma were shown to have a 'crater' signature, i.e. a decrease in the magnitude of the magnetic field at the centre of an FTE by Lühr & Klocker [1987] and Labelle *et al.* [1987], while Berchem & Russell [1984]and Rijnbeek *et al.* [1984] concluded that magnetosphere FTEs exhibited a layered structure, particularly in the plasma β. Lately, observations from the Cluster II PEACE mission show that FTEs may have a substructure on a scale of the order of the spacecraft separation distance of $\sim 600km$ [Owen *et al.*, 2001].

2.4 Onset of magnetic reconnection at the magnetopause

A range of factors, both local and global, may be important in provoking the onset of reconnection. The conditions under which these factors occur and the locations at which these may occur on the magnetopause are the subject of continued debate.

2.4.1 Factors Contributing to the Onset of Reconnection

Magnetic reconnection may be either 'driven' by factors external to the current sheet such as the direction of the IMF, velocity and density of the solar wind, or 'spontaneous', caused by instabilities at the current sheet [Hughes, 1995]. In order to allow the field line topology to change, the onset of reconnection requires a breakdown in the frozen-in-flux theorem (see Chapter 1.2.3).

Local Factors

Many commentators invoke anomalous resistivity as the mechanism responsible for local breakdown, e.g. Coroniti & Eviatar [1977], Huba *et al.* [1977]. Semenov & Pudovkin [1985] in their review of magnetic reconnection state that reconnection may occur if the mean current density is great enough to cause anomalous resistivity. Recent simulation work by Watt *et al.* [2002] suggests that much higher values of ion-acoustic resistivity may be obtained at the magnetopause than previously expected from analytical considerations and thus be of great importance at the magnetopause.

Drake [1995] points out that Ohm's Law (Equation 1.4) is an electron equation of motion and that some important terms have been neglected in our description of ideal MHD. Ohm's Law also contains terms representing electron inertia, electron pressure and the Hall ($\mathbf{j} \wedge \mathbf{B}$) effect. These terms have scale lengths of the electron skin depth, ion Larmor radius and ion skin depth respectively and, depending on the resistivity scale length, should be included in the description of local breakdown.

Global Factors

Hughes [1995] lists three external factors which are believed to influence the onset of magnetic reconnection: magnetosheath flow speed, plasma beta and the magnetic shear.

In order for the local factors listed above to have time to develop, reconnection is more likely to occur where the magnetosheath flow is slowest. This is at the stagnation point of the flow, which is in the vicinity of the sub-solar point, but slightly offset to allow for the Earth's orbital motion and asymmetries in the system. In particular, steady-state reconnection requires sub-Alfvénic magnetosheath flow. Again, the dayside magnetopause is favoured. The rôle of the magnetosheath flow is discussed in more detail in Chapters 3 and 4.

There is some evidence to suggest that magnetic reconnection favours low plasma beta (e.g. Paschmann *et al.* [1986]). Plasma β is likely to be lowest near the sub-solar point and a plasma depletion layer may form there. Sonnerup *et al.* [1995] suggest that the dependence on β may not be direct, but possibly results from the affect of plasma beta on the location and position of the magnetopause boundary.

The dependence on magnetic shear is one of the most controversial areas today. While it is generally acknowledged that reconnection will take place more easily for anti-parallel fields, there are two schools of thought, one which believes that it will only take place where fields are (nearly) anti-parallel, say within 10^o, e.g. Crooker [1979], Luhmann *et al.* [1984b], and the other which believes that reconnection may occur for any orientation of the magnetic fields where the components perpendicular to the merging line are anti-parallel, e.g. Gonzalez & Mozer [1974], Cowley [1976].

There is observational evidence for both theories: Šafránková *et al.* [1998] considered two-point spacecraft observations which seem to support the anti-parallel hypothesis, while recent observations by Kim *et al.* [2002] support component merging theory. Coleman *et al.* [2001] believe that they have developed a conclusive test based on ionospheric convection patterns which supports the anti-parallel merging hypothesis rather than the sub-solar component merging theory. This test has, however, been the subject of recent debate [Petrinec & Fuselier, 2003, Coleman *et al.*, 2003]. Recent work by Moore *et al.* [2002] also concludes that there is stronger evidence for reconnection across a wide range of IMF clock angles.

In Appendix C we show the shears at the magnetopause for the magnetosheath and geomagnetic field models used in Chapter 3. Under the anti-parallel hypothesis, magnetic reconnection would be confined to the white and palest yellow regions of the magnetopause. Under component merging, there is greater potential for magnetic reconnection elsewhere. This is discussed later in this work. In the next section we consider the most likely locations for magnetic reconnection.

2.4.2 Location of magnetic reconnection

The preceding section set out a number of factors which are believed to have some influence on the onset of magnetic reconnection. In this section, we consider which locations on the magnetopause are most likely to be favoured by these factors.

Of the factors described above, the stagnation point of the flow, which is near the sub-solar point, and the dependence on low plasma β both favour the sub-solar region of the dayside magnetopause. Under conditions of pure southward IMF, the magnetic shear in the sub-solar region is almost exactly anti-parallel and this, combined with the other factors, weighs heavily on the side of the sub-solar point as the preferred site for magnetic reconnection.

One of the most controversial issues around reconnection at the magnetopause is the existence and form of the reconnection line, otherwise known as the merging line, neutral line or x-line. A number of theories have been proposed. Gonzalez & Mozer [1974] propose a merging line lying along the direction in which the magnetosheath and geomagnetic fields have equal parallel components (in effect the magnetopause current direction) and extending globally along the magnetopause, not necessarily passing through the sub-solar point [Gonzalez, 1991]. Crooker has developed various models, one insisting that the merging line passes through the cusps, e.g. Crooker [1979] and another through the sub-solar point, e.g. Crooker *et al.* [1990]. A further model [Crooker, 1985] suggests a split-separator merging line derived from Stern [1973] who proposed that a separator line in a uniform field plus dipole (modelling the geomagnetic field) will split into two separate lines in the presence of surface currents.

It is possible that there are not competing theories but patterns which depend on the system conditions. Shi *et al.* [1991] show that the magnetic Reynolds number, R_M, of the plasma is very important in determining the pattern reconnection takes at the magnetopause. In Equation 1.7, we represented R_M by LV/D where L is a characteristic length of the spatial variation of the magnetic field, say $1R_e$, V is the bulk flow of the plasma and D a diffusion coefficient. Shi *et al.* [1991] find that for $R_M < 100$, reconnection at a single x-line passing through the stagnation point occurs. For $R_M > 200$, multiple x-line reconnection occurs.

Some have argued for patchy reconnection, e.g. Kan [1988], Nishida [1989] have proposed that reconnection may occur in patches at the magnetopause.

There are also questions concerning the length of the merging line. Some recent results from Pinnock *et al.* [2003] utilising the SuperDARN radar data set from Phan *et al.* [2000] under a steady period of southward IMF indicate a magnetopause reconnection line of length $\sim 39R_e$.

Magnetic reconnection under northward IMF is an extensive area of current research and is discussed in Section 2.5.

2.5 Magnetic reconnection under northward IMF

There is little argument that for magnetic reconnection to occur under northward IMF, it would be favoured poleward of the cusps where the geomagnetic field points equatorward, hence providing anti-parallel fields. Such reconnection was proposed by Dungey [1963] in an extension of his original work [Dungey, 1961]. Evidence of reconnection at such latitudes has been seen by, for example, Kessel *et al.* [1996] who used Hawkeye data to demonstrate high-latitude reconnection under northward IMF from the motion of sunward flowing protons. It is also commonly accepted that steady-state reconnection can only occur in regions of sub-Alfvénic magnetosheath flow, i.e. where $V_{sh} < V_A$. In Sections 3.3 and 3.4 we develop the theory which leads to the conclusion that steady-state reconnection cannot occur in regions of super-Alfvénic magnetosheath flow. Our conclusion is actually more subtle than this. However in the case of exactly anti-parallel magnetic fields it is the same. Generally in this work, we will use the statements 'sub-' and 'super-' Alfvénic flow as a loose shorthand. Gas-dynamic models of magnetosheath flow generally predict that the flow becomes super-Alfvénic at a distance of around $5R_e$ from the sub-solar point. This mitigates against steady-state reconnection occurring poleward (tailward) of this distance, hence the prevailing view that steady-state reconnection poleward of the cusps for northward IMF is not possible.

The controversial aspects of reconnection under a northward IMF are (a) whether in these high-latitude locations, poleward of the cusps, it can occur in a (quasi)-steady state or whether it is of necessity a transient phenomenon, and (b) whether it can occur equatorward of the cusps.

In recent years, a number of observations have been made which are interpreted as demonstrating that steady-state reconnection has in fact taken place at these high latitudes. For example, Polar/TIMAS observations reported by Fuselier *et al.* [2000b] showed stable reconnection sites for four events, three of which were well within the region normally expected to be super-Alfvénic. Avanov *et al.* [2001] reported observations from the Interball Tail spacecraft which showed quasi-steady reconnection and a relatively stable reconnection site at a high-latitude under northward IMF. Again, the location was expected to be super-Alfvénic but the spacecraft observed sub-Alfvénic flow which would allow for steady-state reconnection in this area. Lately, Phan *et al.* [2003] report Cluster observations consistent with reconnection poleward of the cusp under northward IMF. Once more, the Cluster observations demonstrated sub-Alfvénic flow in an area where super-Alfvénic flow was predicted.

In a second paper, Fuselier *et al.* [2000a], using Polar/TIMAS data, postulate that reconnection equatorward of the cusp for northward IMF has been observed under conditions of high solar wind dynamic pressure which they believe causes strong plasma depletion allowing component merging at very small angles. However, their interpretation of the events used is questioned by Russell *et al.* [2000] who propose an alternative explanation which does not require reconnection equatorward of the cusp. The event of May 29 1996 is a second example of the difficulties in interpretation of

data which may arise. Avanov *et al.* [2001] and Russell *et al.* [1998] amongst others both interpret this event as evidence of reconnection poleward of the cusp while the same event is interpreted as evidence for reconnection equatorward of the cusp by Chandler *et al.* [1999].

The originating site for the reconnection event is inferred from observations of ion and electron velocity distributions, how these are modified by the reconnection process, and the motion of the rotational discontinuity. This is discussed in the next section.

2.6 Open flux tube motion

Observationally, it is highly unlikely that a spacecraft will actually take measurements precisely at a reconnection site, though at least one report has been received: Øieroset *et al.* [2001] report an event on 1 April 1999 when the Wind spacecraft actually flew through a reconnection event while travelling down tail. Usually, therefore, inferences will almost certainly have to be made as to the locations of the underlying processes giving rise to the observed features. This would be achieved by projecting observations back using a model or theory of what happens at a reconnection site.

In Section 2.2.2, the idea of an open flux tube was introduced. An open flux tube is formed following magnetic reconnection and contains reconnected field lines joining the magnetic field of the IMF to that of the Earth. Particles from the plasmas on both sides of the rotational discontinuity which forms the site of reconnection at the magnetopause can mix along the tube. The flux tube moves along the magnetopause under the action of both the magnetic tension forces on the open tubes and the magnetosheath flow.

As discussed in the preceding sections, attention in recent years has been focused on reconnection other than at the subsolar dayside magnetopause, in particular for cases of northward IMF poleward of the cusps. In an attempt to address some of these issues theoretically, Cowley & Owen [1989] (hereafter CO89) developed a simple model to illustrate the initial motion of flux tubes created by reconnection between magnetic fields of equal strength but arbitrary orientation across a planar magnetopause.

The CO89 model makes a number of assumptions as follows:

- Following reconnection at an arbitrary location, there are uniform fields and densities on either side of the magnetopause but at arbitrary relative orientation. These conditions follow from stress-balance considerations (see Section 3.3).
- The dayside magnetopause may be modelled as a plane. This assumption is not unreasonable at the sub-solar dayside magnetopause, but is less valid as we move tailwards.
- Magnetosheath flow has a stagnation-point in the vicinity of the sub-solar point.
- The flow expands radially outwards from the stagnation point with a linearly increasing speed.

- Divergence of the flow is accommodated by inflow of magnetosheath plasma towards the magnetopause.

This study has been useful in investigating a number of aspects of dayside reconnection where a qualitative and quantitative framework is needed. For example, Lockwood [1997] used CO89 to model the energy and pitch angle dispersions of low-latitude boundary layer (LLBL) /cusp ions and estimated from such kinetic observations the Alfvén speed and field-aligned flow at the magnetopause reconnection site [Lockwood, 1995]. The model has been used to demonstrate that both the acceleration of cold ion beams [Gosling *et al.*, 1990] and the spectra of particles crossing the magnetopause and in the cusp/cleft region (Lockwood & Smith [1994], Onsager *et al.* [1995]) may be accounted for in terms of reconnection events.

CO89 has also been used in looking at global flow patterns and currents. Predictions based on this model have been compared to observations of inflow and outflow (boundary layer) velocities of particles following reconnection events (Song & Russell [1992], Mei *et al.* [1995], Chen *et al.* [1997], Siscoe *et al.* [2000]). The model supports the view that low and high latitude cleft currents are not extensions of Region 1 and Region 2 current systems but arise from newly reconnected field lines on the dayside magnetopause [Taguchi *et al.*, 1993]. Korotova & Sibeck [1995], Rodger *et al.* [2000] and Coleman *et al.* [2000] have made use of the model in determining whether reconnection events are steady-state or transient. Lockwood & Smith [1994] and Lockwood & Davis [1995]) have used it to demonstrate that neither the spectra of particles crossing the magnetopause nor flux line evolution are significantly affected by the reconnection rate.

A third area in which the CO89 model has proved useful is in considering mechanisms by which mass, energy and momentum enter the magnetosphere. For example, Owen & Cowley [1991] used it to evaluate the Heikkila [1982] impulsive transport mechanism. Konik *et al.* [1994] investigated how the orientation of the IMF affects magnetic impulse events [Konik *et al.*, 1994]. Drakou *et al.* [1994] used the model to explain the assimilation of reconnected flux tubes under northward IMF into the magnetosphere.

The CO89 model is, however, too restrictive for many applications. It deals with a planar magnetopause and employs simplified representations of the magnetic fields and sheath flow. Some studies have addressed these points by using, for example, a Tsyganenko [1995] magnetopause description, e.g. Rodger *et al.* [2000], or by using some form of magnetosheath field draping, e.g. Lockwood [1997], Lockwood [1995], Rodger *et al.* [2000].

In Chapter 3 we build upon the CO89 model by using a paraboloid representation of the magnetopause and existing models for the magnetosheath flow and density at the magnetopause. Additionally, we use an analytical model of the magnetosheath magnetic field and a simple model of the geomagnetic field in order to attempt to assess likely sites where reconnection may occur.

2.7 Summary

In this chapter we have reviewed the entry of solar wind energy, momentum and plasma into the Earth's magnetosphere. The predominant transfer mechanism is believed to be magnetic reconnection. There are a number of hotly debated topics surrounding reconnection at the magnetopause:

- Does magnetic reconnection occur only where fields are anti-parallel or can it take place if there are anti-parallel components perpendicular to the merging line?
- What is the length, form and path of the reconnection line itself?
- Can reconnection under northward IMF take place in the steady-state poleward of the cusps?
- Can reconnection under northward IMF take place equatorward of the cusps?

These issues may be explored from data observations. In order to understand whether the observations result from reconnection at particular locations, it is necessary to be able to track back from the observation by inferences about the motion of flux tubes and the acceleration of particles following reconnection. The CO89 model of flux tube motion has been used to review a number of the issues relating to reconnection, however it is limited. In this thesis, therefore, we seek to develop a more realistic, but still simple, semi-analytical model to improve understanding. In Chapter 3 we set out the model and in Chapter 4 a selection of our results.

Chapter 3

Model Development

3.1 Introduction

In this chapter, we first outline the scheme of our model and its component parts. Next we discuss those parts of our model directly derived from CO89, i.e. the stress-balance of two reconnecting field lines and the instantaneous motion of the open flux tubes. We then describe how we integrate that motion to determine trajectories of reconnected flux tubes over the magnetopause surface. We develop the models which we have used for the magnetosheath [Kobel & Flückiger, 1994] and geomagnetic fields, the sheath flow speed and density immediately adjacent to the magnetopause [Spreiter *et al.*, 1966]. Lastly, we formulate our initial reconnection test and how we establish a merging line, and the steady-state reconnection test which we apply. Much of the work in Chapters 3 and 4 has been described in our paper Cooling *et al.* [2001].

3.2 Scheme

Figure 3.1 shows the flow diagram of our model. We specify the solar wind velocity and the IMF strength and direction, the bow shock and magnetopause stand-off distances, and a location for reconnection. This information feeds through to the magnetosheath flow and density models and to the magnetopause magnetic field models. The sheath flow speed, density and components of the magnetic field on either side of the magnetopause at the proposed location are then calculated. Next, a test for the possibility of initial reconnection is carried out. If the test is satisfied, the length and orientation of a merging line are determined. Initial velocities of reconnected field lines are calculated from the balance of field and plasma stresses on these field lines, and a test for steady-state reconnection is applied. The velocities of a number of representative flux tubes in the Earth frame are calculated and their positions incremented over a short time interval. The new locations are fed back into the model and the magnetosheath flow, the density, the fields and the stress-balance conditions at the new points are calculated. The locations of the intersection of

these open flux tubes with the magnetopause may thus be determined over a desired time interval.

In essence, we are quantifying the process illustrated by Crooker [1979], and elements of this approach are similar to those described by Lockwood [1997]. In Figure 3 of the first of these papers, Crooker shows the qualitative evolution of a single field line following merger with the IMF near the cusp. Magnetosheath flow is directed radially away from the sub-solar point. The flow velocity imparted from the reconnection process is assumed to be $2V_A$ and the resultant flow velocities for the reconnected field lines are $\mathbf{V_{R1}} = \mathbf{V}_{sh} + 2\mathbf{V_A}$ and $\mathbf{V_{R2}} = \mathbf{V}_{sh} - 2\mathbf{V_A}$ where $\mathbf{V}_{sh}$ is the magnetosheath flow velocity. In the second paper (and references therein), a model for investigation of sheath ion dispersion is developed which draws on the predictions of Spreiter *et al.* [1966] and the method of CO89 to predict the evolution of a newly-opened field line over the dayside magnetopause.

3.3 Stress Balance

At the magnetopause, we define a local orthogonal boundary normal coordinate system $\hat{\mathbf{q}}$, $\hat{\mathbf{j}}$, $\hat{\mathbf{n}}$ such that: $\hat{\mathbf{q}}$ is tangential to the current sheet and parallel to the direction $\mathbf{B}_{ms} - \mathbf{B}_{gm}$ where $\mathbf{B}_{ms}$ and $\mathbf{B}_{gm}$ are respectively the draped magnetosheath and geomagnetic fields either side of the magnetopause; $\hat{\mathbf{j}}$ is also tangential to the local magnetopause current sheet and parallel to the current, i.e. in the direction $\nabla \wedge \mathbf{B}$; and $\hat{\mathbf{n}}$ is the outward normal to the local current sheet.

In this system, magnetic fields $\mathbf{B}_{ms}$ and $\mathbf{B}_{gm}$ either side of the sheet may be written as (B_{msq}, B_j, B_n) and (B_{gmq}, B_j, B_n), so both the $\hat{\mathbf{j}}$ and $\hat{\mathbf{n}}$ components of the field remain constant across the magnetopause. Here, $B_n \neq 0$ for a rotational discontinuity, or open magnetopause. We can find a de Hoffmann & Teller [1950] frame (henceforth dHT) in which the local convection electric field is transformed away, such that in this frame, the plasma flows along the field direction, i.e. $\mathbf{V} \wedge \mathbf{B} = \mathbf{0}$.

The dHT is a frame in which the upstream flow and magnetic field are parallel and the discontinuity is stationary. This may be found by adding a transformation velocity tangential to the discontinuity. In the dHT frame, upstream particles move parallel to the magnetic field and gyrate around it. As $\mathbf{E} = 0$, the energy of the particles is constant. Additionally, as the dHT velocity, $\mathbf{V_{HT}}$, depends on the normal component of the magnetic field and tangential component of the upstream velocity, and as these components are constant across the discontinuity, then $\mathbf{V_{HT}}$ is the same both upstream and downstream [Burgess, 1995].

We make the additional assumption that the flow is dominated by the magnetosheath plasma moving into the magnetosphere. While some plasma does flow in the opposite direction, the density and pressure of the magnetospheric plasma is much lower than that of magnetosheath plasma and thus is negligible for our work.

In Chapter 1.3.2 we set out the properties of a range of discontinuities. Here, we assume that we are working with a rotational discontinuity in an isotropic MHD plasma. Alternatively, if we

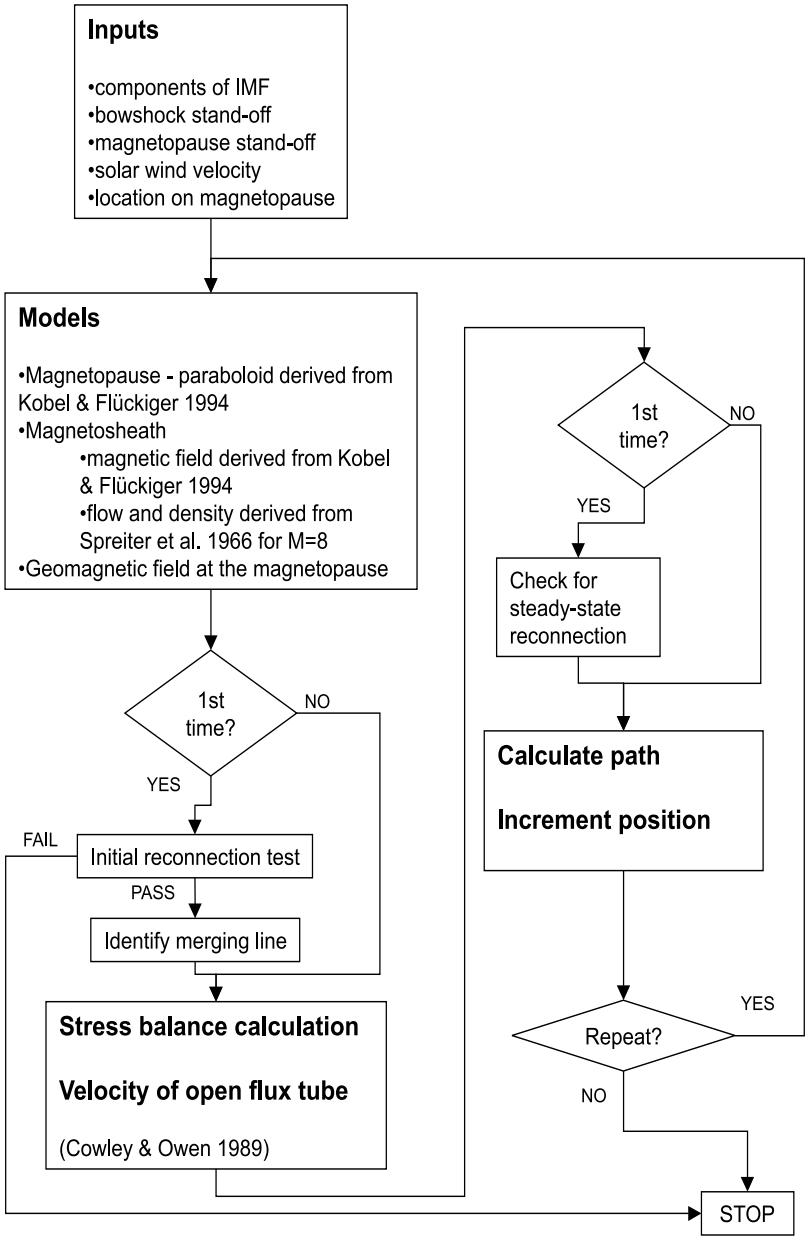

Figure 3.1: Scheme: Flow diagram of the model operations developed in the study. We input the solar wind velocity, the IMF, bow shock and magnetopause stand-off distances and a location to attempt to initiate reconnection. Initial reconnection tests are carried out, and if successful the model calculates the relevant plasma parameters, calculates the flux tube velocity and increments the position. Calculations are repeated at the new location and the process repeated for the desired time interval. The trace of the intersection of the open flux tube with the magnetopause is plotted over the desired time interval.

assume that thermal pressures are negligible, then we need not assume isotropic plasma. These assumptions are justified by the outcome of the analysis which follows.

In the following analysis, we use the method of Parks [1991, p.331] and Cowley & Owen [1989]. We call on the conservation of mass flux and energy flux across the current sheet in the dHT frame and balance the change in momentum flux with the magnetic forces in the current sheet to deduce the inflow and outflow speed. For clarification $\mathbf{V_{ms}}$ is the magnetosheath flow parallel to $\mathbf{B_{ms}}$ in the dHT frame. $\mathbf{V_{sh}}$ refers to the magnetosheath flow in the Earth rest frame.

Mass flux is conserved across the current sheet, thus:

$$\rho_{ms} V_{msn} = \rho_{gm} V_{gmn}. \tag{3.1}$$

where the subscript ms indicates magnetosheath parameters, gm indicates the magnetosphere parameters and n indicates the normal component. Then the energy flux in the dHT frame reduces to the flux of bulk flow kinetic energy, which is conserved, such that:

$$\frac{1}{2}\,\rho_{ms} V_{msn} {V_{ms}}^2 = \frac{1}{2}\,\rho_{gm} V_{gmn} {V_{gm}}^2. \tag{3.2}$$

We deduce from these two equations that the inflow and outflow speeds are the same, and will be denoted V. Thus we can write the flow velocities $\mathbf{V}_{ms}$ and $\mathbf{V}_{gm}$ in the dHT frame as:

$$\mathbf{V}_{ms} = V\mathbf{b}_{ms} = \frac{V}{|\mathbf{B}_{ms}|}(B_{msq}, B_j, B_n) \tag{3.3}$$

and

$$\mathbf{V}_{gm} = V\mathbf{b}_{gm} = \frac{V}{|\mathbf{B}_{gm}|}(B_{gmq}, B_j, B_n) \tag{3.4}$$

where $\mathbf{b}_{gm}$ is a unit vector in the direction of the geomagnetic field and $\mathbf{b}_{ms}$ is a unit vector in the direction of the magnetosheath field.

The change in momentum flux across the sheet, $\mathbf{\Delta M}$, is given by:

$$\mathbf{\Delta M} = \rho_{gm} V_{gmn} \mathbf{V}_{gm} - \rho_{ms} V_{msn} \mathbf{V}_{ms} \tag{3.5}$$

while the magnetic forces within the current sheet may be written as:

$$\mathbf{j} \wedge \mathbf{B} = \frac{B_n}{\mu_0}\frac{\partial B_q}{\partial n}\,\hat{\mathbf{q}} - \frac{1}{2\mu_0}\frac{\partial ({B_q}^2)}{\partial n}\,\hat{\mathbf{n}}. \tag{3.6}$$

Integrating these magnetic forces through the layer balances the change in momentum flux such that in the dHT frame:

$$\begin{aligned} &\rho_{gm} V_{gmn} \mathbf{V}_{gm} - \rho_{ms} V_{msn} \mathbf{V}_{ms} = \\ &\quad \frac{B_n}{\mu_0}(B_{gmq} - B_{msq})\,\hat{\mathbf{q}} - \frac{1}{2\mu_0}({B_{gmq}}^2 - {B_{msq}}^2)\,\hat{\mathbf{n}} \end{aligned} \tag{3.7}$$

The $\hat{\mathbf{j}}$ component together with Equation 3.1 immediately leads to $V_{msj} = V_{gmj}$. Then equations 3.3 and 3.4 show that $|\mathbf{B}_{ms}| = |\mathbf{B}_{gm}|$, and will be denoted B. From this it follows that $B_{gmq} = \pm B_{msq} \equiv \pm B_q$ (the upper sign corresponds to the trivial case in which the current is

zero). Now the $\hat{\mathbf{n}}$ component of Equation 3.7 results in $V_{gmn} = V_{msn}$ from which Equation 3.1 implies $\rho_{gm} = \rho_{ms} \equiv \rho$.

Hence, we may now write:

$$\mathbf{V}_{ms} = \frac{V}{B}(B_q, B_j, B_n) \tag{3.8}$$

and

$$\mathbf{V}_{gm} = \frac{V}{B}(-B_q, B_j, B_n) \tag{3.9}$$

Finally, the $\hat{\mathbf{q}}$ component of Equation 3.7 is:

$$\rho V_n(V_{gmq} - V_{msq}) = \frac{B_n}{\mu_0}(B_{gmq} - B_{msq}) \tag{3.10}$$

which, together with the previous results reduces to:

$$V^2 = \frac{B^2}{\mu_0 \rho} = {V_A}^2 \tag{3.11}$$

where V_A is the Alfvén speed of the system.

The sheath and boundary layer plasmas have the same density and field strength as a consequence of the assumption that the plasma is isotropic and that there is a pure rotational discontinuity across a simple, single-layered, thin current sheet. It is much more likely, however, that the magnetopause is comprised of multiple layers and is possibly better described as a standing wave structure [Cowley, 1995]. Here, we consider the changes encountered by plasma entering the magnetosphere via a reconnection mechanism only across the outermost layer of the magnetopause consisting of an Alfvén wave (or rotational discontinuity). The Alfvén wave acts only to rotate the magnetic field direction and accelerate the particles in this model. It does not affect the thermodynamic properties of the plasma [Cowley, 1995].

3.4 Flux Tube Motion

3.4.1 Instantaneous flux tube velocity along the magnetopause

Following reconnection, the reconfigured magnetic fields divide into two separate open flux tubes. The cartoon Figure 3.2 illustrates the formation of an open flux tube.

The velocities calculated from stress-balance in Section 3.3 are those in the dHT or field-line rest frame. The velocity space diagram in Figure 3.3 illustrates the relationship between the velocity vectors in the dHT frame and those in the Earth frame.

The frame transformation velocities described in the figure caption are simply the differences between the flow velocities as measured in the two frames, i.e.

$$\mathbf{V}_{HTN} = \mathbf{V}_{sh} - V_A \mathbf{b}_{ms} \tag{3.12}$$

$$\mathbf{V}_{HTS} = \mathbf{V}_{sh} + V_A \mathbf{b}_{ms} \tag{3.13}$$

where $\mathbf{V}_{sh}$ is the magnetosheath flow velocity in the earth frame.

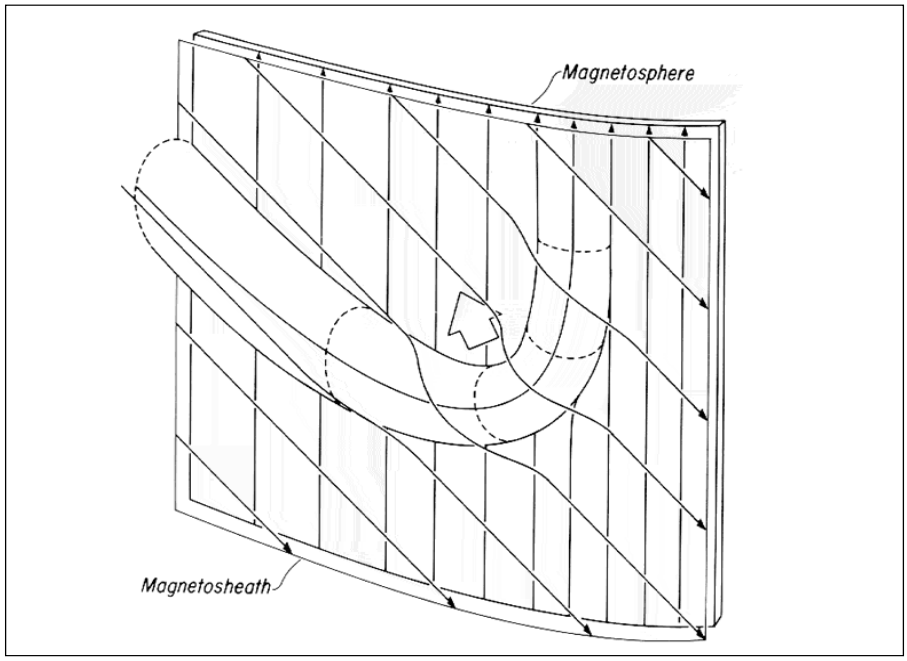

Figure 3.2: Reconnected flux tubes: This sketch from Russell & Elphic [1978] of a flux transfer event shows the formation of the open flux tube which is carried in the direction of the large arrow by the magnetosheath flow. The stressed field at the bend relaxes, shortening the flux tube and straightening up.

The boundary layer (outflow) velocities on the magnetospheric side are:

$$\mathbf{V}_{gmN} = \mathbf{V}_{HTN} + V_A \mathbf{b}_{gm} \tag{3.14}$$

$$\mathbf{V}_{gmS} = \mathbf{V}_{HTS} - V_A \mathbf{b}_{gm} \tag{3.15}$$

which become:

$$\mathbf{V}_{gmN} = \mathbf{V}_{sh} + V_A(\mathbf{b}_{gm} - \mathbf{b}_{ms}) \tag{3.16}$$

$$\mathbf{V}_{gmS} = \mathbf{V}_{sh} - V_A(\mathbf{b}_{gm} - \mathbf{b}_{ms}) \tag{3.17}$$

At the sub-solar point where $V_{sh} = 0$, these give boundary layer outflow speeds of just $2V_A$ for anti-parallel fields as expected [Crooker, 1979].

3.4.2 Integrated flux tube motion

Once we have calculated the velocity $\mathbf{V}_{HT}$ of a particular tube along the magnetopause, we then increment the position vector by $\mathbf{V}_{HT}\Delta T$ where ΔT is a short time interval. The new position is constrained to lie on the magnetopause by projection along the local normal. In order to calculate this, we construct the equation for the normal to the paraboloid passing through the new position and the intersection of this line with the surface. This is a cubic equation and is solved using the Cardan-Tartaglia method as shown in, for example, Heard & Martin [1978]. If there is more

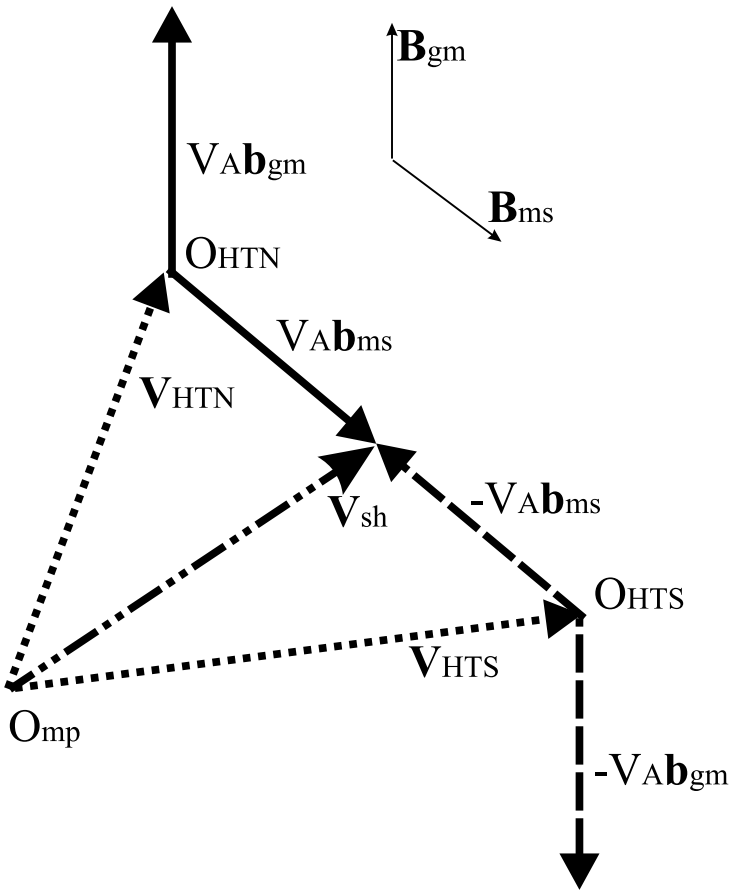

Figure 3.3: Velocity space diagram: Illustrating the relationship between the various velocity vectors following reconnection at an arbitrary point. The magnetosheath and geomagnetic field vectors, labelled $\mathbf{B}_{ms}$ and $\mathbf{B}_{gm}$ respectively, are shown in the top right of the figure. The dot-dash line labelled $\mathbf{V}_{sh}$ shows the magnetosheath flow in the Earth rest frame. Following reconnection, a pair of open flux tubes is formed connected to the northern and southern cusps respectively. In the reconnected field line rest frame (dHT) for each tube, which have origins O_{HTN} and O_{HTS}, the sheath flow appears as a field-aligned flow at the Alfvén speed. This is indicated by the thick solid arrow marked $V_A\mathbf{b}_{ms}$ for the flux tube connected to the northern cusp, and by the thick dashed line marked $-V_A\mathbf{b}_{ms}$ for the flux tube connected to the southern cusp. Consequently, the instantaneous flux tube motions can be constructed and are indicated by the dotted vectors marked $\mathbf{V}_{HTN}$ and $\mathbf{V}_{HTS}$ respectively. Plasma in the magnetospheric boundary layer is also moving at the Alfvén speed along the geomagnetic field line in the dHT frame, represented by vectors marked $V_A\mathbf{b}_{gm}$ and $-V_A\mathbf{b}_{gm}$ respectively.

than one real solution to the equation, then we choose the intersection point giving the shortest distance to the new position.

The plasma and field parameters at the new location are determined in order to calculate the new flux tube velocity and perform a second incrementation of flux tube position. This process is repeated as required in order to determine the trajectory of each flux tube along the magnetopause surface.

In our model we assume that the path followed by the flux tube moves only under the magnetic tension $\mathbf{j} \wedge \mathbf{B}$ forces. However, in addition to the rotational discontinuity there may be, for example, fast (or, less common, slow) mode waves which reduce the pressure gradients and which could cause shocks to build up in the flow. There may also be other disturbances, for example solar wind pressure pulses, surface waves, Kelvin-Helmholtz instabilities, which influence motion, especially far from the reconnection site, which we ignore.

3.5 Coordinate System

In defining the global aspects of the model, such as the magnetic fields and sheath flow parameters, we use a right-handed orthogonal system, X, Y, Z, based on GSM coordinates. The origin is based at the centre of the Earth; the X axis lies along the Sun-Earth axis (positive X is toward the Sun); positive Y points toward dusk, and the Z axis, representing the dipole axis, is aligned South to North. In this study, we neglect the effects of dipole tilting.

3.6 Magnetic Field Models

3.6.1 The Magnetosheath Field

On passing through the bow shock, the solar wind plasma is slowed and deflected in order to pass around the magnetosphere. As a consequence of the frozen-in flux theorem, the magnetic field in the magnetosheath initially drapes around the geomagnetic field forming a tangential discontinuity at the magnetopause (e.g. Crooker *et al.* [1985]). We require an analytical model which can be applied over the day and near-nightside magnetopause which takes draping into account and can be used for any IMF. We use, therefore, the analytical model of Kobel & Flückiger [1994] (henceforth KF94) as the basis for deriving the magnetosheath field just outside the magnetopause.

The KF94 model requires only three inputs: The stand-off distances of the bow shock, R_{bs}, and magnetopause, R_{mp}, from the Earth's centre, and the IMF components B_{imfX}, B_{imfY}, B_{imfZ}.

The bow shock and the magnetopause are each described as paraboloids of revolution about the X-axis with foci midway between the Earth and the sub-solar point. In our coordinate system, the magnetopause surface is defined as:

$$Y^2 + Z^2 = 2R_{mp}(R_{mp} - X) \tag{3.18}$$

This model compares well with others (see Elsen & Winglee [1997]) out to $X \sim -20$ to $-30R_e$ where the radius of the magnetopause is about $25R_e$. Other models tend to become more cylindrical down tail, reaching a radius of $25R_e$ at $X \sim -100R_e$.

The field within the magnetosheath is assumed to be current-free (e.g. Fairfield [1979]) except at the outer and inner boundaries. Potentials are then matched at the boundaries to arrive at a description of the steady-state field at any point within the magnetosheath.

In the KF94 paper, the z axis is defined along the Sun-Earth line with origin (and focus of the paraboloids) halfway between the Earth and the nose of the magnetopause with positive z pointing tailwards. The x axis corresponds to Z_{GSM} with the y axis corresponding to Y_{GSM}. In paraboloidal (or parabolic) coordinates, a parameter $\nu = constant$ uniquely defines a paraboloid surface. For further details, see Appendix B. KF94 define the bow shock by ν_{bs} and the magnetopause by ν_{mp} where $\nu_{bs} = \sqrt{2R_{bs} - R_{mp}}$ and $\nu_{mp} = \sqrt{R_{mp}}$.

$$\mathbf{B^{ms}}(x,y,z) = \mathbf{B^{imf}}\left(1 + \frac{{\nu^2}_{mp}}{\nu_{bs}^2 - \nu_{mp}^2}\right) + \mathbf{B^{dis}}\left(\frac{\nu_{mp}^2 \nu_{bs}^2}{\nu_{bs}^2 - \nu_{mp}^2}\right) \tag{3.19}$$

where

$$B_x^{dis} = \frac{1}{r(r-z)}\left[B_x^{imf}\left(r - \frac{x^2}{r-z}\right) - B_y^{imf}\frac{xy}{r-z} + B_z^{imf}\frac{x}{2}\right] \tag{3.20}$$

$$B_y^{dis} = \frac{1}{r(r-z)}\left[-B_x^{imf}\frac{xy}{r-z} + B_y^{imf}\left(r - \frac{y^2}{r-z}\right) + B_z^{imf}\frac{y}{2}\right] \tag{3.21}$$

$$B_z^{dis} = \frac{\frac{z}{r} - 1}{(r-z)^2}\left[-B_x^{imf}x - B_y^{imf}y + B_z^{imf}\frac{r-z}{2}\right] \tag{3.22}$$

and ${\nu^2}_{mp} \leq (r-z) \leq {\nu^2}_{bs}$. In these equations r is the distance from the focus to a point on the paraboloid defined by constant ν, not the distance from the centre of the Earth to such a point.

As we are only interested in the value of the magnetosheath field at the outer magnetopause boundary, we can make the substitution $r - z = const = R_{mp}$ and transform to GSM coordinates using $x_{KF} \rightarrow Z_{GSM}$, $y_{KF} \rightarrow Y_{GSM}$ and $z_{KF} \rightarrow \frac{R_{mp}}{2} - X_{GSM}$

We applied this model to determine the components B_{msX}, B_{msY} and B_{msZ} of the magnetosheath field at a given location (X,Y,Z) immediately outside the magnetopause boundary. These are given by

$$B_{msX} = -A[-B_{imfX}(1 - \frac{R_{mp}}{2l}) + B_{imfY}(\frac{Y}{l}) + B_{imfZ}(\frac{Z}{l})], \tag{3.23}$$

$$B_{msY} = A[-B_{imfX}(\frac{Y}{2l}) + B_{imfY}(2 - \frac{Y^2}{lR_{mp}}) - B_{imfZ}(\frac{YZ}{lR_{mp}})], \tag{3.24}$$

$$B_{msZ} = A[-B_{imfX}(\frac{Z}{2l}) - B_{imfY}(\frac{YZ}{lR_{mp}}) + B_{imfZ}(2 - \frac{Z^2}{lR_{mp}})] \tag{3.25}$$

where

$$A = \frac{2R_{bs} - R_{mp}}{2(R_{bs} - R_{mp})} \tag{3.26}$$

where typically, A=2, and l is the distance from the focus ($X = R_{mp}/2$) to the magnetopause surface:

$$l = \frac{3R_{mp}}{2} - X \tag{3.27}$$

Equations 3.23 to 3.25 above are valid only on the paraboloid surface defined by l. The general equations from which they are derived are curl free. The normal component of the curl of the above equations is also zero satisfying the requirement that outside of the boundaries, the magnetosheath is current free. Tangential to the magnetopause boundary, the above equations have a non-zero curl component as expected for a current sheet.

Apart from its analytical nature, a major feature of this model is that, unlike other models (e.g. Alksne [1967]) based on gas-dynamic considerations, it does not give an infinite magnitude for the magnetosheath field at the sub-solar point. Methods of avoiding an infinite magnitude in such models have been proposed including: replacing the stagnation point with a stagnation line extending along the magnetic field direction either side of the gas dynamic stagnation point (e.g. Pudovkin & Semenov [1977], Sonnerup [1979]) and plasma depletion (e.g. Zwan & Wolf [1976]). These methods produce different deflections in the flow, the first perpendicular to the magnetic field direction, and the second parallel to it. A third model predicts displacement of the stagnation point (e.g. Zhuang & Russell [1981]). Crooker *et al.* [1984] essentially showed that none of these theories applied all of the time. A simple empirical model devised by Crooker *et al.* [1982] fits the magnetosheath field at the dayside magnetopause, B_{sh}, by the relation $B_{sh} = 2^{5/4}\sqrt{{M_A}^t}{B_{sw}}^t$ where B_{sw} is the magnetic field strength of the solar wind and claim that it is valid over a wide range of solar wind conditions.

The KF94 model also allows for draping in three-dimensions. Figure 3.4 shows the YZ plane projection of the draped magnetosheath field just outside the magnetopause for a pure southward IMF prior to reconnection. As we move away from the Y=0 and Z=0 axes, draping in the Y direction can be clearly seen in the figure, becoming more pronounced as Y increases. Draping in the X direction also occurs. The clock angle of the IMF is clearly not preserved as we move anti-sunwards. However, throughout the dayside, deviation from the clock angle is modest, and thus the assumption that it is preserved, often used in theoretical studies, (e.g. Rodger *et al.* [2000]) is reasonable.

Crooker *et al.* [1985] used the magnetic field model derived from gas dynamic considerations [Spreiter *et al.*, 1966, Alksne, 1967] to model the magnetosheath magnetic field near the magnetopause. The IMF was rotated into GIPM coordinates (where the coordinate system is rotated about the X axis so that the magnetic field vector lies in the XY plane, and where the X and Y coordinates are always of opposite sign). The gas dynamic models were then used to convect the magnetic field to the vicinity of the magnetopause and the resulting field draping patterns for a range of cone angles are given in the left hand panel of Figure 3.5. As a comparison, in the right hand panel we show the equivalent results for the same cone angles and using input IMF with positive B_X and negative B_Y when using the KF94 model. The patterns obtained for

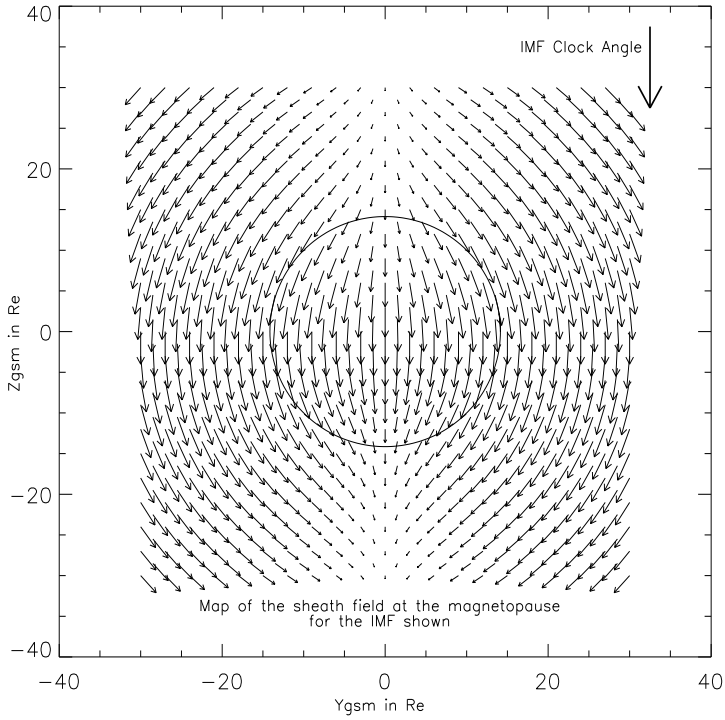

Figure 3.4: Draped field southward IMF: The projection of the unreconnected draped magnetosheath field resulting from pure southward IMF just outside the magnetopause. The figure is drawn looking down the X axis from the Sun with the Y (dawn-dusk) coordinate along the horizontal axis and the Z (South-North) coordinate along the vertical axis. The large arrow in the top right hand corner indicates the projection of the IMF direction and is not to the same scale as the vectors representing the magnetosheath magnetic field. The short arrows show the Y, Z components of the magnetosheath field vector calculated from the KF94 model. The superimposed circle has the radius of $\sim 15\ R_e$, the radius of the magnetopause at X=0. Draping of the field in the $\pm$Y - direction as we move away from the origin is clearly seen. Draping in the X direction also occurs.

negative B_X and positive B_Y are the same but with arrow directions reversed.

The application of the two models differs slightly; in both cases, a model magnetopause of $R_{mp} = 10R_e$ has been used. However, the figures given by Crooker *et al.* [1985] represent draping on a surface of $R_{mp} = 11R_e$ while those of the KF94 model as applied, are at the outer surface of a $10R_e$ paraboloid. This notwithstanding, there is a good match between the two models within the dayside, indicated by the circle on the right-hand figures. The biggest difference is in the 15^o case where the magnetic field null lies more to the west in the left-hand figure than in the right.

Further, the magnetic shear patterns at the magnetopause obtained from the KF94 model (see Appendix C.1) compare very well with those given by others, for example Luhmann *et al.* [1984a] and Rodger *et al.* [2000].

Since developing our model, a new analytical model has been developed [Kallio & Koskinen, 2000] which again assumes paraboloid bow shock and magnetopause. However, the magnetic field at the magnetopause, B_{mp}, is an input to the model in the form $B_{mp} = \sqrt{4B^t{}_{imf}B_{st}}$ where B_{st}

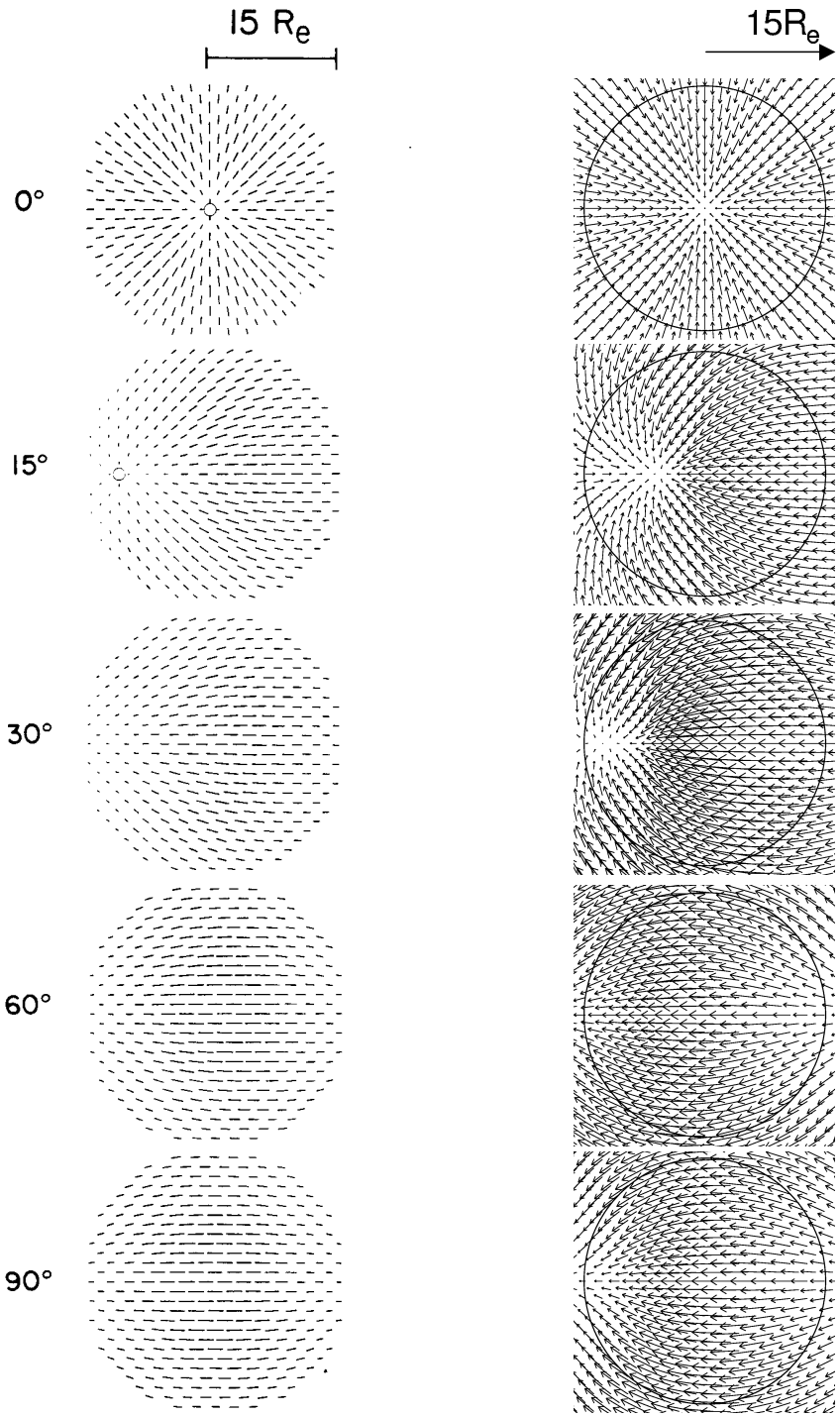

Figure 3.5: Comparison of draping patterns: The left-hand side of the figure shows the draping patterns for a range of IMF cone angles as modelled by Crooker *et al.* [1985] for $R_{mp} = 10R_e$, but at a surface of $R = 11R_e$, and the right-hand side shows those obtained from the KF94 model for $R_{bs} = 15R_e$ and $R_{mp} = 10R_e$. It can be seen that there is good qualitative agreement between the two models over the dayside (as indicated by the circle on the right-hand figures).

is the stagnation field strength determined by Stern's [1973] magnetosphere model and $B^t{}_{imf}$ is the transverse component of the IMF. The resulting magnetic shears at the magnetopause, while broadly agreeing with those obtained by us (for example, for northward dawn IMF, the highest shears are shown in the northern pre-dawn and southern post-dusk quadrants), do differ in contour shape.

3.6.2 The Geomagnetic Field at the Magnetopause Boundary

From the simplifying assumptions of our stress balance calculations, we obtain the result that the magnetic field strength of the reconnected field line is equal on both sides of the current sheet during all stages. For this reason we require only the direction of the magnetospheric field just inside the magnetopause boundary. Additionally, we are constrained to use a paraboloid model by our choice of the KF94 magnetosheath field model. Tsyganenko [1995] developed a widely-used model which uses many satellite observations to contribute towards a semi-empirical best-fit representation for the geomagnetic field. The models are revised from time to time as more data becomes available. However, many parameters are required to utilise the model effectively and we consider therefore that the use of a more detailed geomagnetic field model, such as that of Tsyganenko [1995] is not warranted at this stage of our work.

We have modelled the unperturbed geomagnetic field at the inner edge of the magnetopause boundary very simply, based on the following assumptions: The direction of the field prior to reconnection is everywhere tangential to the magnetopause. We place the cusps on the magnetopause at the locations $(\frac{1}{2}R_{mp}, 0, \pm R_{mp})$. All field lines map from the southern to the northern cusp over the surface of the paraboloid. In XY projection, the field lines map in straight lines from any point on the surface toward the Northern cusp and away from the Southern cusp (see Figure 3.6). Figure 3.7 shows the mapping of the assumed geomagnetic field onto the YZ plane prior to reconnection. Note that special treatment is required if the fields at the singular cusp points are needed. In this case, the geomagnetic field vector is pointed directly toward or away from the relevant geographical pole and the field strength is zero. The positioning of the cusps implies that we are near-equinoctal as dipole tilting causes the cusps to move either sunward, tailward and from side to side depending on the time of year. We do not attempt to address this in our model.

3.6.3 Sheath Flow and Density

In order to calculate the flux tube motion, we also require a model for the magnetosheath flow velocity at locations adjacent to the magnetopause. One of the most commonly used models in this area, (e.g. Mei *et al.* [1995] and Lockwood [1997]), is that of Spreiter *et al.* [1966], based on simulation studies of gas-dynamic flow around an obstacle. Magnetosheath flow models are discussed in more detail in Chapter 5.3. Assuming cylindrical symmetry about the X-axis, we

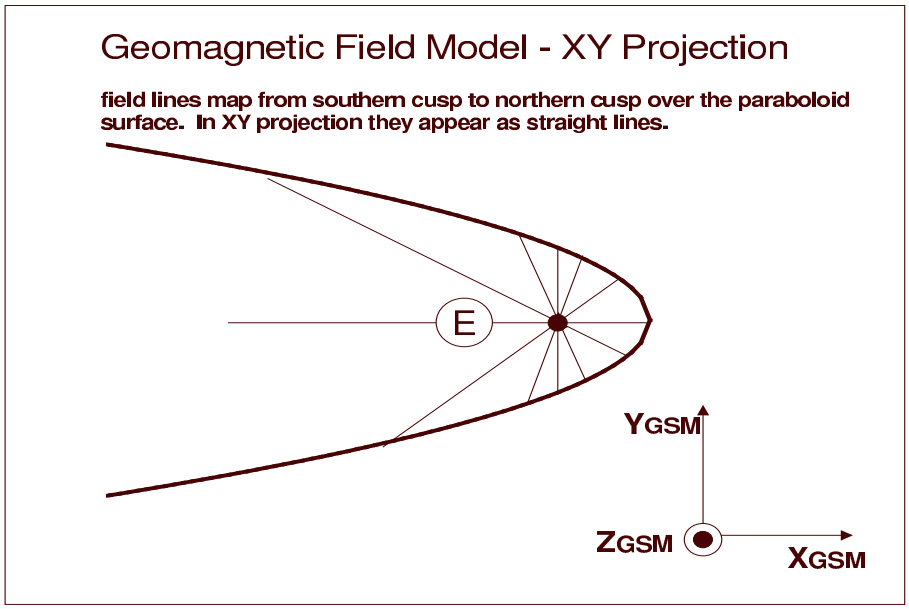

Figure 3.6: Geomagnetic field: Shows the XY projection of the geomagnetic field used in our model. The field lines map from the Southern to the Northern cusp over the paraboloid magnetopause in straight lines.

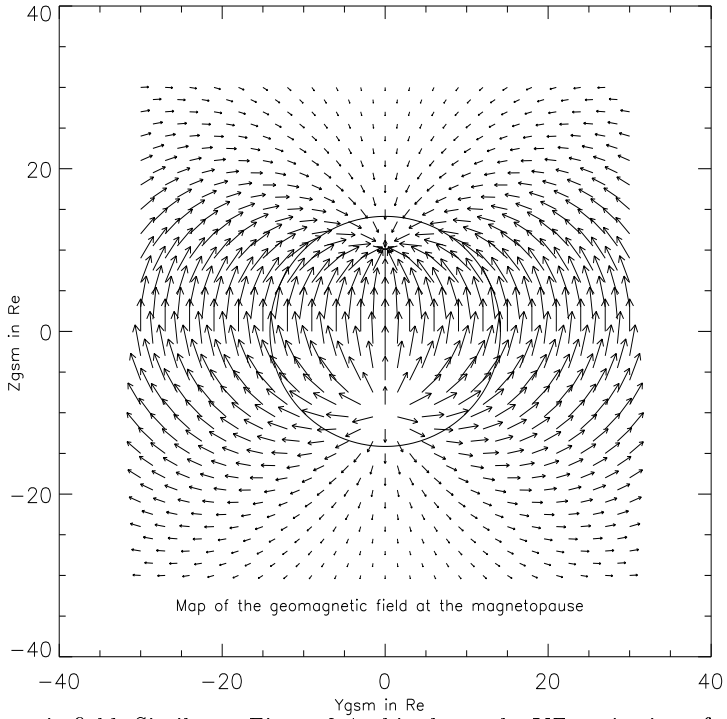

Figure 3.7: Geomagnetic field: Similar to Figure 3.4, this shows the YZ projection of the unreconnected geomagnetic field just inside the magnetopause boundary. The southern cusp at $(5, 0, -10)R_e$ shows clearly as a 'source' and the northern cusp at $(5, 0, 10)R_e$ as a 'sink' for the magnetic field lines in this model.

have fitted a magnetosheath flow speed variation at the magnetopause, $V(X)$, to the Spreiter *et al.* [1966] result for solar wind with fast magnetosonic Mach number 8 and $\gamma = \frac{5}{3}$ by the curve:

$$\frac{V(X)}{V_{sw}} = 0.784 \ln(1 + \sqrt{\frac{2(R_{mp} - X)}{R_{mp}}}) \tag{3.28}$$

where V_{sw} is the velocity of the unshocked solar-wind. The projection of this flow vector on the YZ plane (not shown) is directed radially away from the stagnation point. This ratio reaches 1 for $X \sim -23R_e$.

The density at the magnetopause was also derived from Spreiter *et al.* [1966] and fitted by:

$$\frac{\rho(X)}{\rho_{sw}} = 1.509 \exp(\frac{X}{R_{mp}}) + 0.1285 \tag{3.29}$$

where ρ_{sw} is the density of the unshocked solar-wind. This ratio has a maximum value of 4.23 at the sub-solar point. Once more, the simplifying assumptions of Section 3.3 imply that the densities of the reconnecting plasmas immediately either side of the magnetopause on a given pair of reconnected field lines are the same in this model.

While the geometry of the Spreiter *et al.* [1966] magnetopause model differs from that of KF94, the latter claim good qualitative agreement between the streamline patterns found in the two models. Comparison by eye of KF94 Figures 2 and 3 with Figures 9a and 10 of Spreiter & Stahara [1980] supports this view. The individual components of our model are all representative and allow easy manipulation. Additionally, the high degree of symmetry in the model field and flow configuration enables the control by the IMF to be unambiguously defined. An example of this may be seen in Chapter 4.1.4 where the results obtained for 'toward' and 'away' Parker spiral are not symmetric, and this can be attributed directly to the IMF as all other components of the model show cylindrical symmetry.

3.7 Reconnection Conditions

Many aspects of reconnection remain the subject of debate. In particular, the conditions leading to the occurrence of reconnection at a given point are unknown, as are the parameters controlling the length and orientation of the merging line. Moreover, it appears that reconnection may occur as a quasi-steady state process, or a sporadic, time-dependent process, e.g. flux transfer events (Russell & Elphic [1979], Korotova & Sibeck [1995], Onsager *et al.* [1995]). In this work, we make a number of ad hoc assumptions concerning these factors. Our model includes an initial reconnection test, an algorithm to put limits on the length of a merging line, and a test of whether reconnection can proceed in a steady-state manner. Each of these tests is described below.

3.7.1 Initial reconnection test

There are various hypotheses as to where and under what conditions reconnection may occur and these are discussed more fully in Chapter 2. Reconnection may simply occur if there are anti-

parallel components perpendicular to the merging line (e.g. Gonzalez & Mozer [1974], Luhmann *et al.* [1984b]). Alternatively, reconnection may be restricted to occur only where the magnetosheath and geomagnetic fields are exactly anti-parallel (e.g. Crooker [1979]). Other hypotheses assume that reconnection may occur if the mean current density is great enough to cause anomalous resistivity (e.g. Pudovkin & Semenov [1985]).

In our model, we input a location for reconnection. We check that the draped magnetosheath and geomagnetic fields are not exactly parallel and apply the threshold criterion to the magnitude of the difference in components perpendicular to the current direction (i.e. $|\Delta B_q|$) above which reconnection is allowed to occur (where $|\Delta B_q|$ serves as a proxy for the mean current density in the sheet).

In practice, this test will allow reconnection for any shear angle provided that the strength of the components is great enough. For lower field strengths, a larger shear angle is required before reconnection may proceed. Even if the shear angle is 180°, reconnection may not proceed if the strengths of the perpendicular field components are too weak. This is illustrated in Figure 3.8 in which shaded contours represent shear angle resulting from a typical Parker spiral IMF with a moderately strong southward B_Z component of $6nT$. Threshold values of $35nT$ and $50nT$ corresponding to magnetopause currents of $28mAm^{-1}$ and $40mAm^{-1}$ respectively, are overplotted. Reconnection will occur provided the threshold test is satisfied at the chosen location. So for example, in Figure 3.8, for a threshold of $50nT$, reconnection may occur if the selected position is within the central band stretching from the top left of the figure to the bottom right. Figures similar to Figure 3.8 may be produced for any IMF and used as an aid for selection of an appropriate location for initial reconnection. In this figure, for example, we would therefore favour initial locations in the two white bands between the $50nT$ contours. In Chapter 4.3 we show how our model may be used to identify appropriate locations for a range of IMFs.

In our examples, we use a threshold of $35nT$. This is an arbitrary choice, designed to allow reconnection at the sub-solar point for a pure southward IMF of $\gtrsim 5nT$.

3.7.2 The merging line

The existence or otherwise of a merging line and its orientation are also open questions and are discussed in 2.4.2.

In our model, we calculate the direction of the reconnection current at a location and assign this as the merging line. Using, say, a Tsyganenko [1995] model for the geomagnetic field would change the direction slightly but would not be consistent with the reconnection model employed here. The model increments along the local current direction until the threshold test described in Section 3.7.1 fails, up to an arbitrary maximum length.

Determining the length and orientation of the merging line is not a key feature of our model. In our examples we have used a maximum length of $8R_e$ though in fact the merging line may be much longer.

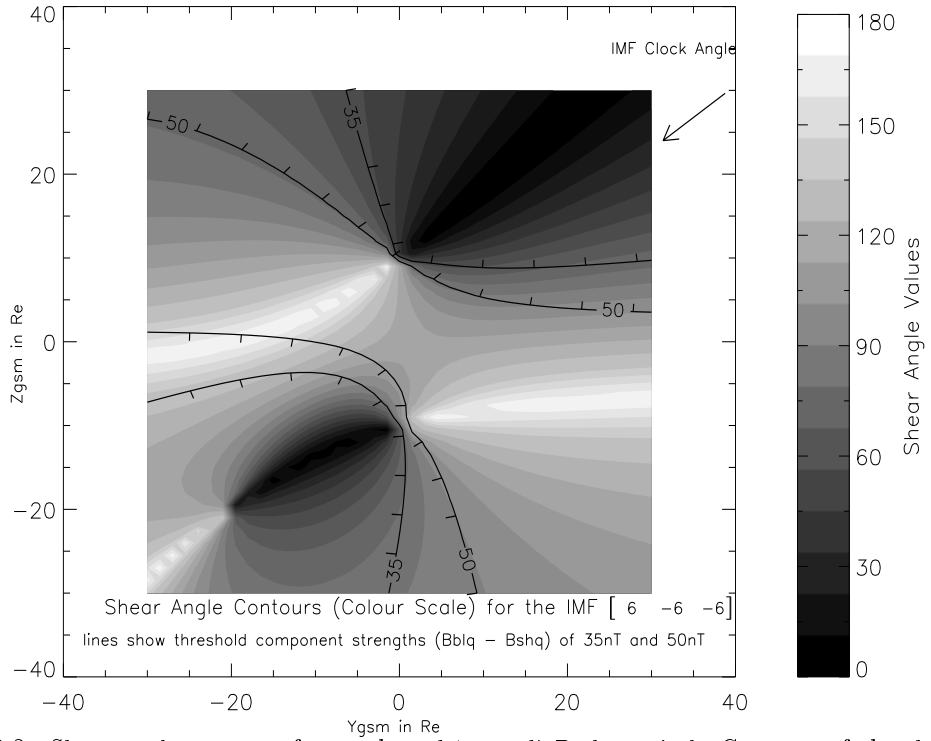

Figure 3.8: Shear angle contours for southward 'toward' Parker spiral: Contours of the shear angle between the magnetosheath and magnetosphere fields at the magnetopause are shown in greyscale for the Parker spiral IMF with $-B_Z$ $(6, -6, -6)nT$. Lines showing thresholds ($|\Delta B_q|$ as described in the text) of $35nT$ and $50nT$ are overplotted. Note that in practice, there are areas where even with anti-parallel magnetic fields, the threshold test may fail for weak field strengths, and that there are areas of lower shear angle where it may succeed for strong fields.

3.8 Steady-state reconnection

When magnetic fields reconnect, two flux tubes are formed which must peel away from the merging line on opposite sides (CO89). If this is not the case, the tubes would have to cross back over the merging line, which implies a temporal evolution at the reconnection site. We therefore test that the components of the two flux tube velocities perpendicular to the merging line are in opposite directions. Using Equations 3.12 and 3.13, we note that the $\hat{\mathbf{q}}$ components (i.e. those perpendicular to the merging line) of V_{HTN} and V_{HTS} need to be in opposite directions. So, either $(\mathbf{V_{sh}} - V_A\mathbf{b_{ms}}) \cdot \hat{\mathbf{q}} > 0$ and $(\mathbf{V_{sh}} + V_A\mathbf{b_{ms}}) \cdot \hat{\mathbf{q}} < 0$, which leads to a contradiction (i.e. that $\mathbf{V_{sh}} \cdot \hat{\mathbf{q}}$ is both greater than and less than $V_A\mathbf{b_{ms}} \cdot \hat{\mathbf{q}}$), or $(\mathbf{V_{sh}} - V_A\mathbf{b_{ms}}) \cdot \hat{\mathbf{q}} < 0$ and $(\mathbf{V_{sh}} + V_A\mathbf{b_{ms}}) \cdot \hat{\mathbf{q}} > 0$ which leads to the condition:

$$| \mathbf{V}_{sh} . \hat{\mathbf{q}} | < | V_A \mathbf{b}_{ms} . \hat{\mathbf{q}} | \tag{3.30}$$

from which it may be seen that the ratio of the magnetosheath flow speed to the Alfvén speed (CO89) is particularly important. In Chapter 4.1.5 we show a range of results demonstrating how this varies under different conditions.

Provided that the initial reconnection test is passed, the model will run. A merging line will be determined and flux tubes initiated along that line. Should the steady-state test fail, then the model can be set up to indicate this on the plot. We believe that in this case, the paths shown will be those of flux transfer events.

In the following chapter, we show a range of results achieved from our model for a number of classical test cases. We also catalogue some of the output for a range of IMFs. In particular, we also discuss the implications of our model for steady-state reconnection under northward IMF.

Chapter 4

Model Results & Discussion

4.1 Results

In this section we describe a number of representative examples of the output from our model.

We ran each of the examples using the parameters: $R_{bs} = 15R_e$, $R_{mp} = 10R_e$, $V_{sw} = 400kms^{-1}$, $N_{sw} = 10cm^{-3}$ and assume the ion population is composed entirely of protons. We impose an initial reconnection threshold magnetic field strength of $35nT$ (see Chapter 3.7.1), and a maximum merging line length of $8R_e$ (see Chapter 3.7.2). We iterate reconnected flux tube motion over a timestep $\Delta T = 0.5s$ for a total duration of $500s$.

4.1.1 Southward IMF

In the example shown in Figure 4.1, we first examine the classical case of reconnection on the subsolar magnetopause for pure southward IMF of $(0, 0, -10)nT$, and impose an initial reconnection location at the sub-solar point itself. At this point the sheath flow velocity is zero as it is the stagnation point of the gas dynamic flow. The draped magnetosheath field at this point remains purely southward and the geomagnetic field purely northward.

Considering first the pair of flux tubes formed by reconnection at the subsolar point itself, we find that the initial flux tube velocity is directly northward (southward) with a speed equal to that of the Alfvén speed. As these tubes move cuspward away from the sub-solar point, the Alfvén speed changes, and the sheath flow increases. However, the sheath flow vector is also directly cuspward, thus the flux tubes accelerate toward the relevant cusps. This accords directly with the classical expectations for the motion of open flux tubes formed by the reconnection of a purely southward IMF at the sub-solar point (e.g. Dungey [1961]).

Consider now a pair of open flux tubes formed by reconnection at a point on the merging line dawnward of the sub-solar point. In this case the sheath flow will be non-zero and directed dawnward along the merging line. The initial motion of the flux tubes is thus northward (southward) away from the merging line and dawnward. As they recede from the merging line, they move

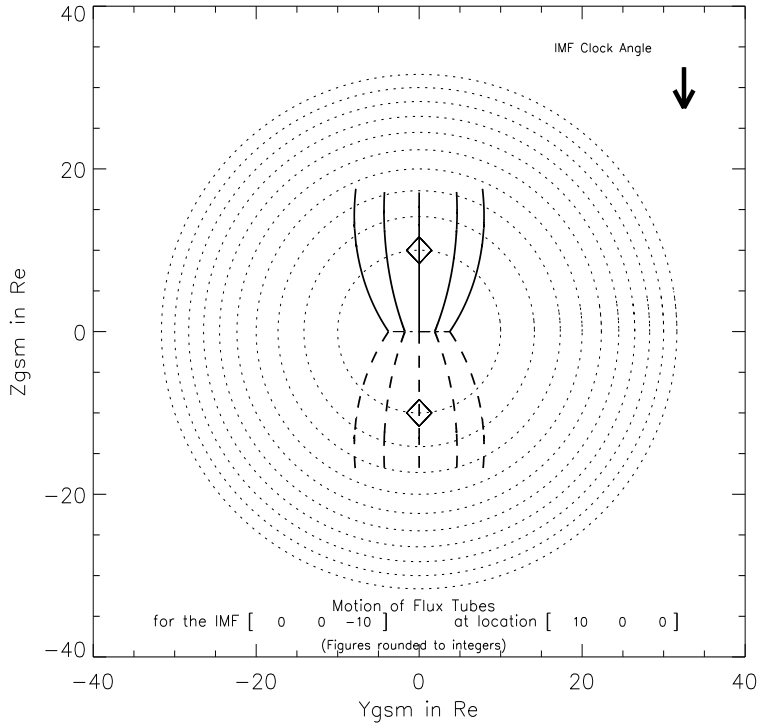

Figure 4.1: Motion of flux tubes under southward IMF: The figure is projected in the YZ plane, looking Earthward from the Sun. The dotted circles indicate the radius of the magnetopause at X coordinate intervals of $5R_e$. The innermost circle represents X=$5R_e$, which contains the position of the cusps (diamonds) for a magnetopause stand-off distance of $10R_e$. The reconnection conditions are satisfied along a merging line lying parallel to the ecliptic plane, the projection of which is indicated by the horizontal (dot-dash) line. In this case, the merging line length is limited to the arbitrary maximum of $8R_e$. Pairs of open reconnected flux tubes are initiated along the merging line (the central pair being at the originally selected location) and the motion of each tube is calculated as described in the text. The points of intersection of each tube with the magnetopause over a period of 500s are plotted. The solid lines indicate the trajectories of tubes which connect to the northern cusp, and the dashed lines to the southern cusp.

into regions in which the sheath flow has an increasing poleward component. Additionally, the draped magnetosheath field has a dawnward (duskward) component in the northern (southern) hemisphere. Changes in field strength and density also result in the flux tubes moving into regions of increased Alfvén speed. The overall effect is these flux tubes accelerate into a more tailward direction as they unwind. In this case, there is a dawn-dusk, North-South symmetry in the motion of reconnected flux tubes. Thus open windows develop over the magnetopause intially with the merging line width, but expanding to a dawn-dusk width of around 15-20R_e by the time the flux tubes have moved tailward to X=-5R_e.

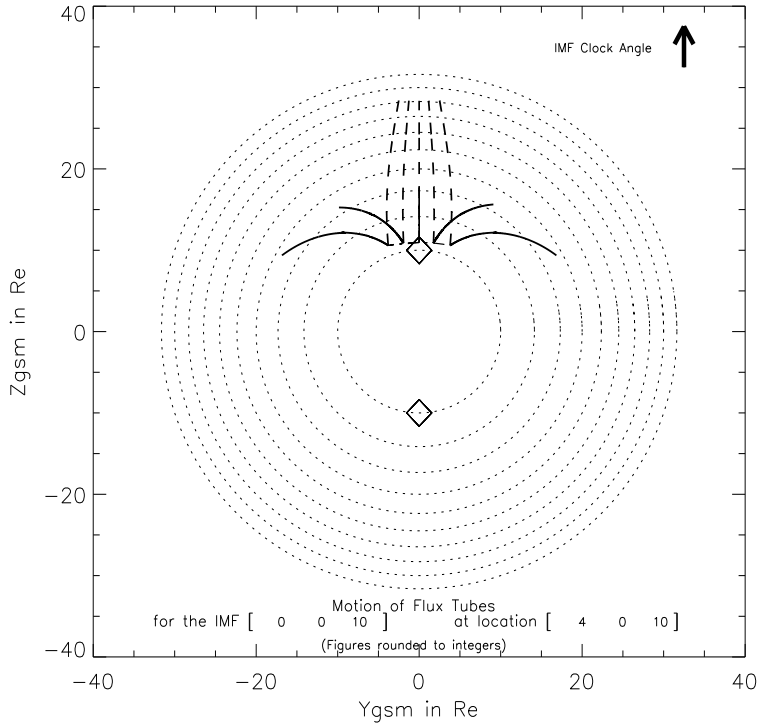

Figure 4.2: Motion of flux tubes under northward IMF: As in Figure 4.1 but for northward IMF. Flux tubes connected to the northern cusp (solid lines) move back over the merging line and also cross the path of reconnected flux tubes with both ends in the solar wind (dashed lines). Hence a steady state cannot be maintained in such a case.

4.1.2 Northward IMF

We now present the results of two model runs for a pure northward IMF $(0, 0, 10)nT$. We show that if we use the standard velocity and density parameters in our calculations, then steady-state reconnection poleward of the cusp under northward IMF is not predicted. We then show that if we reduce the density calculated in our model, then we can find steady-state reconnection under these conditions.

We impose an initial reconnection location just poleward of the northern cusp where the magnetosheath and geomagnetic fields for pure northward IMF are exactly anti-parallel, thus the current direction is dusk-dawn. In the first case, shown in Figure 4.2, the model is able to calculate flux tube paths for a reconnection event at this location, but the steady-state test is not satisfied. It would be interesting to consider whether this is the case for any x-line orientation. However, this is beyond the scope of this thesis. The paths of the flux tubes connected to the northern cusp (solid lines) move back over the merging line. They also cross the path of reconnected flux tubes with both ends in the solar wind (dashed lines) in this configuration. This is a consequence of the strong magnetosheath flow which is super-Alfvénic and directed tailward and parallel to the magnetosheath field in these regions. Since this result implies either a motion of the merging line, or cessation of reconnection, this is impossible under steady state conditions. However, a transient burst of reconnection may occur at this point, since all other criteria are satisfied. The

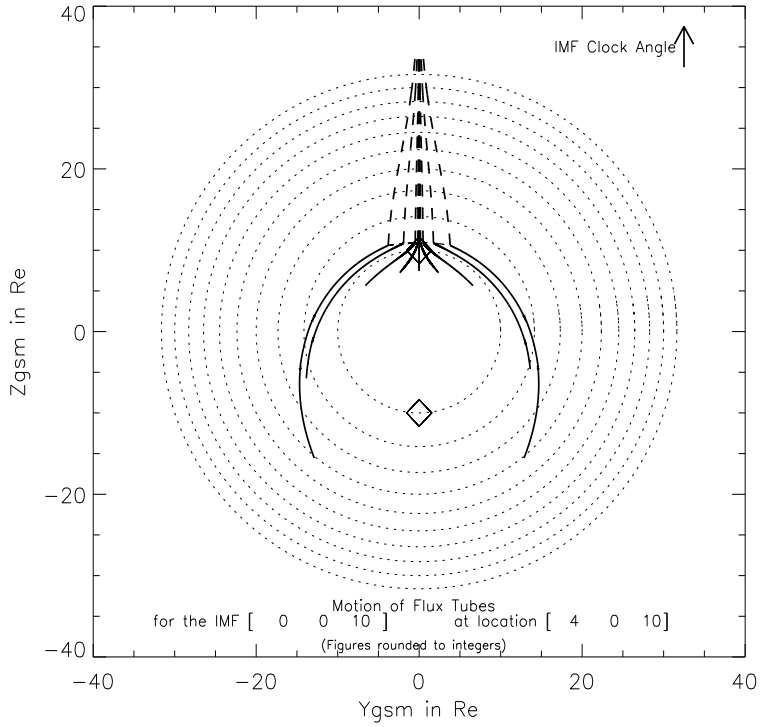

Figure 4.3: Motion of flux tubes under northward IMF with reduced density: As Figure 4.2 but with an arbitrary reduction in magnetosheath density to 20% of the value derived from the Spreiter gas dynamic model. The steady-state condition is now satisfied. Note the very slow movement equatorward of the central North-connected tube.

trajectories shown in Figure 4.2 then represent the paths that flux tubes formed in this manner are expected to follow.

In the example shown in Figure 4.3, we use the same IMF and reconnection location as above. However, we have arbitrarily reduced the density to 20% of the value arrived at from our Spreiter-derived model in Section 3.6.3. The effect of reducing the density in this manner is to increase the Alfvén speed, such that the magnetosheath flow at the reconnection site is now just sub-Alfvénic. A similar effect may be achieved by increasing the IMF strength or by reducing the speed derived from the Spreiter model. The steady-state condition is now satisfied and accords with recent observations which suggest that a plasma depletion layer effect may allow quasi-steady reconnection tailward of the cusp under northward IMF (e.g. Fuselier *et al.* [2000b]).

In particular we note that the central tube connected to the northern cusp moves sunward very slowly under these conditions, $\sim 3R_e$ in around $500s$, as indicated by the short solid line. The motion of this central tube may be an artefact of our treatment of the cusp in the model, however the tubes immediately adjacent to the cusp exhibit similar motion. The outermost North-cusp connected open flux tubes move sharply southward down the flanks. The resulting open flux window, bound by the outermost tubes is very broad and covers a large part of the dayside. The tailward window is quite narrow and extends directly anti-Sunward. The reconnected flux tubes which map out into solar wind at both ends (dashed lines), now move tailward at around $2V_A$,

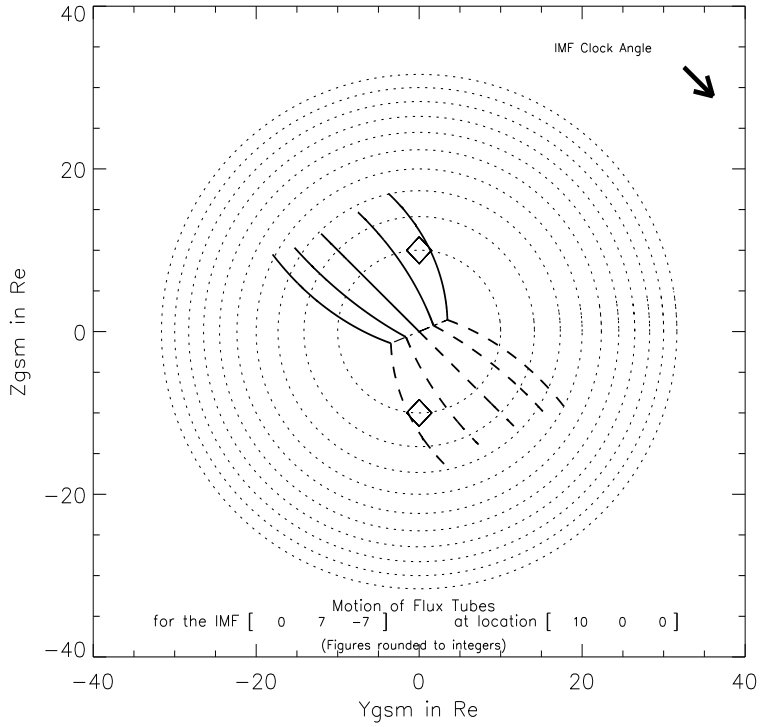

Figure 4.4: Motion of flux tubes for southward IMF with B_Y component: Flux tube motion following reconnection for an IMF of clock angle 135°. The tubes have a distinct dawn-dusk asymmetry to their motion. The tubes connected to the northern cusp (solid) move dawnward and behind the cusp and those connected to the southern cusp (dashed) move duskward.

double the sheath flow velocity. One consequence of this is that the boundary layer flows for these flux tubes are almost $3V_A$ in the Earth frame. These flows may correspond to the accelerated plasma flows on the magnetosheath side of the magnetopause observed by e.g. Gosling *et al.* [1986].

4.1.3 Southward IMF with non-zero B_Y

In Figure 4.4 we show the flux tube motion for an IMF of clock-angle 135°, (0,7,-7)nT with initial reconnection point again located at the sub-solar point. The conditions for initial and steady-state reconnection are once more met. The merging line passes through the sub-solar point, but is tilted out of the ecliptic plane. The draped magnetic field crossing the sub-solar point retains its IMF orientation, and the central tubes move radially away from the sub-solar point, parallel to the sheath flow, with the northern tube heading over to the dawn side, and the southern tube toward dusk.

The outermost (dawn-side) North-connected tube forms just below the ecliptic plane. Here the sheath flow is directed tailward and southward, however its speed is still quite slow. The draped field has gained a slight duskward component and the resulting initial motion of the tube is thus dominated by the velocity component anti-parallel to the magnetosheath field. As the tube moves tailward, it moves into a region of greater radial sheath flow speed which, combined with the draping, begins to pull the tube toward and parallel to the central tube. The open window

connected to the northern (southern) cusp broadens out over the dawn (dusk) sectors at high latitudes before narrowing off downtail. In this configuration, magnetic flux is added to the tail lobes in an asymmetrical manner.

4.1.4 The Parker spiral fields with northward B_Z

Here we show open flux tube motion for the two Parker spiral field directions with northward B_Z. We used the reduced density version of the model and initiated reconnection poleward of the northern cusp.

In Figure 4.5 we show the 'away' sector configuration with the duskward B_Y component $(-6, 6, 6)nT$. The model returns a merging line running from high latitudes at the dawnward end to lower latitudes at the duskward extreme. The North cusp-connected open window (solid lines) is quite narrow and stretches down and round the dawn flank. The flux tubes connected downtail (ultimately to interplanetary space) (dashed lines) move faster, tailward and duskward, forming an open window over the dusk quadrant of the northern lobe of the magnetotail.

The 'toward' sector Parker spiral configuration with dawnward B_Y component $(6, -6, 6)nT$ is shown in Figure 4.6. In this case, the steady-state condition is only just satisfied. The flux tubes connected to interplanetary space now move tailwards over the dawn flank of the magnetopause, while the North-cusp connected tubes move around the southern dusk flank. Note that this motion is not symmetric with the 'away' sector case shown in the previous figure. The velocities of the IMF-connected flux tubes (dashed lines) are somewhat slower than in the 'away' spiral case, and the tubes connected to the northern cusp (solid lines) are much faster, as evidenced by the relative length (distance travelled in 500s) of the respective trajectories. The window formed by the latter flux tubes is extremely narrow.

4.1.5 The structure of the sheath flow

The results presented above emphasize the importance of the sheath flow in determining the motion of open-flux tubes along the magnetopause. In particular, the value of the sheath flow Alfvén Mach number is critical in determining whether steady-state reconnection may occur. To investigate this further, we have mapped the ratio $|\mathbf{V}_{sh}.\hat{\mathbf{q}}|/|V_A\mathbf{b}_{ms}.\hat{\mathbf{q}}|$ (see Section 3.8) over the surface of the magnetopause. By way of example, consider the case of the 'away' sector Parker spiral direction with northward B_Z component, i.e. $B_{imf} = (-6, 6, 6)nT$ shown in Figure 4.7, which uses the standard density model. We find that there is a band $\sim 3R_e$ (1 hour) wide stretching from cusp to cusp and centred on MLT noon where the ratio is less than 1 and hence the steady-state condition is satisfied. There is a dawn-dusk asymmetry visible at both the cusps, with sub-Alfvénic flows only on the dusk (dawn) side of the northern (southern) cusp. The region of sub-Alfvénic flow also extends to slightly higher latitudes in the northern hemisphere than it does in the southern hemisphere and has a broader duskward extension than the dawnward

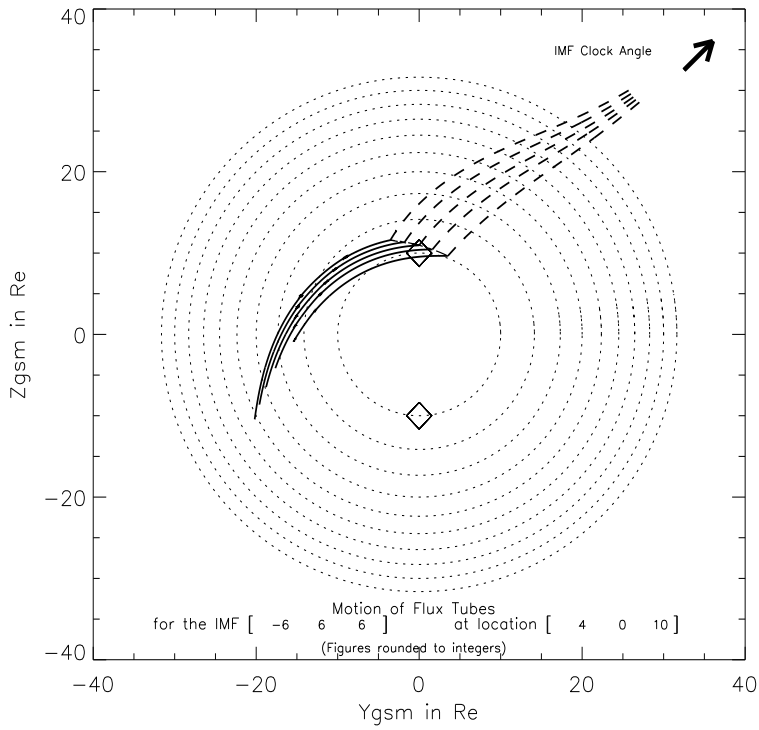

Figure 4.5: Flux tube motion for 'away' Parker spiral with northward IMF: IMF of (-6,6,6)nT using a reduced density of 20%. The result satisfies the steady-state reconnection conditions.

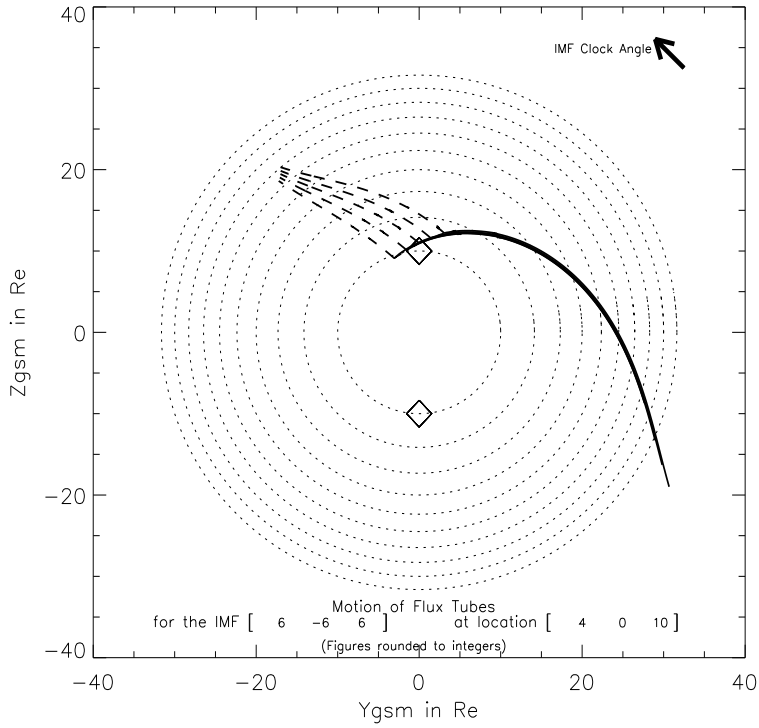

Figure 4.6: Flux tube motion for 'toward' Parker spiral with northward IMF: IMF of (6,-6,6)nT, also with reduced density. In this case, the result only just satisfies the steady-state reconnection condition. Note that this is not a reflection of Figure 4.5.

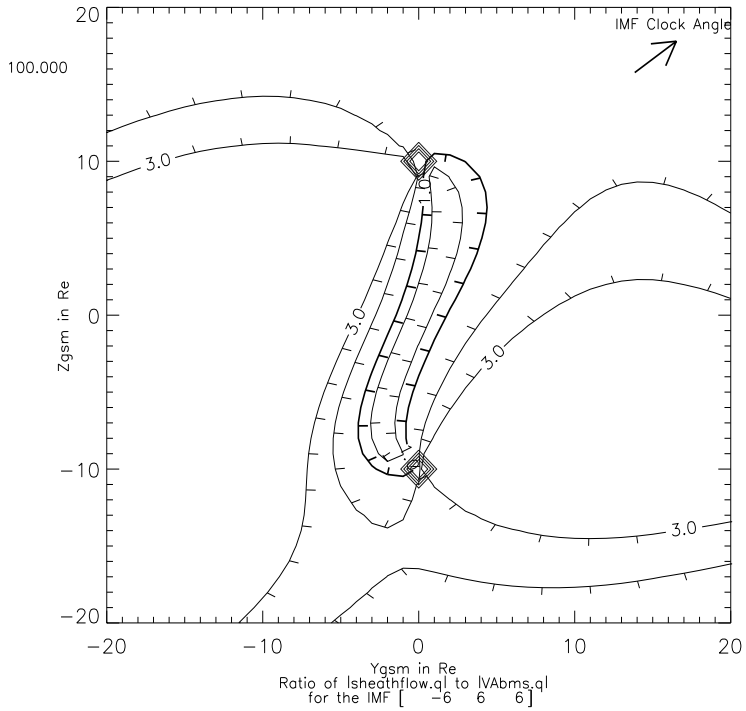

Figure 4.7: Locations for steady-state reconnection for northward 'away' Parker spiral at full density: Contours showing the ratio $|\mathbf{V}_{sh}.\hat{\mathbf{q}}|/|V_A\mathbf{b}_{ms}.\hat{\mathbf{q}}|$ on a YZ projection of the magnetopause for an 'away' Parker spiral with northward B_Z component (-6,6,6)nT and with standard density. The two light grey diamonds represent the cusps. The heavy contour shows the locations where the ratio is 1 and the short lines illustrate the decreasing edge of the contour. The elongated North-South sausage shaped contour stretching between the cusps is the region where steady-state reconnection for this IMF at 100% density may occur in our model.

extension at the southern cusp. This effect becomes more marked when a reduced magnetosheath density is used. In this example, the asymmetry is due to the different symmetries of the draped magnetosheath and the geomagnetic field, where the directional vector is symmetrical about the line Y=0. We would expect, therefore, to see asymmetries in the convection patterns at the opposing polar caps.

Figure 4.7 is quite different from the usual assumption that steady-state reconnection can only occur for the condition that the magnetosheath flow speed is sub-Alfvénic, i.e. $V_{sh}/V_A < 1$ (e.g. Gosling *et al.* [1991]) and Figure 4.8 shows what that would be for the same IMF.

4.2 Discussion

Our model represents a substantial extension to that of CO89. In particular, unlike CO89, who considered only the initial motion, we follow the evolution of the reconnected flux tube motion into the tail. To achieve this we use a more realistic paraboloid shape to represent the magnetopause, rather than a plane. Additionally, we use a more realistic model of the draped magnetosheath field, together with a simple representation of the geomagnetic field. We also utilise the Spreiter

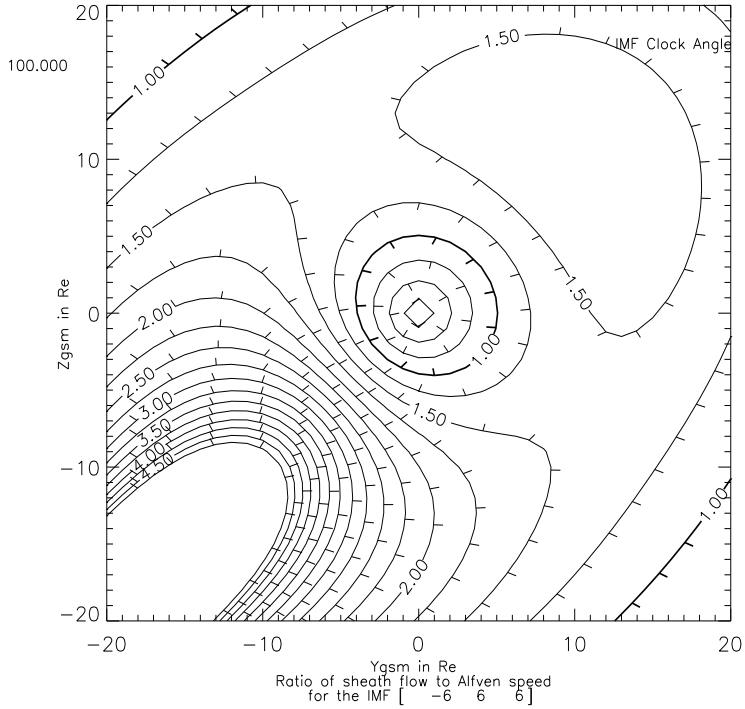

Figure 4.8: Regions of sub-Alfvénic flow for 'away' northward Parker spiral: Contours showing the ratio $|\mathbf{V}_{sh}|/|V_A\mathbf{b}_{ms}|$ on a YZ projection of the magnetopause for an 'away' Parker spiral with northward B_Z component (-6,6,6)nT and with standard density. The region where the magnetosheath flow speed is sub-Alfvénic is more oval in shape, and does not extend as far in the North-South direction as the q-component variation shown in Figure 4.7 and has a greater East-West extension.

et al. [1966] gas dynamic sheath flow model. While each component on its own is not new, the way in which we have put the parts together is.

There are a number of assumptions both implicit and explicit in our model. However, these are reasonably representative of the real magnetopause, adequately reproducing, for example, expectations from the classical southward B_Z picture (Figure 4.1). The results can be regarded as semi-quantitative while maintaining the advantage of not requiring large amounts of computing time. The model is suited therefore to rapid hypothesis testing.

Our model gives a clear picture of how the open flux windows may spread over the magnetopause and thus where magnetic flux is added to the magnetotail. Asymmetrical loading of flux (Figure 4.4) may, for example, give rise to net torques being applied to the magnetotail which may in turn cause tail-twisting (Cowley [1982], Owen *et al.* [1995]), or asymmetries in the plasma populations in the two tail lobes (Gosling *et al.* [1982], Gosling *et al.* [1986]).

The asymmetry between the two Parker spiral orientations shown in Figures 4.5 and 4.6 will translate into the magnetosphere and down to the flux tube footpoints in the auroral ionosphere. Thus the ionospheric flow patterns should also show as a statistical asymmetry when sorted by IMF B_Y. This is characteristic of the Svalgaard-Mansurov effect (Svalgaard [1968], Mansurov [1969]). These authors independently discovered a correlation between the vertical components of the geomagnetic field and the B_Y component of the IMF, later suggesting [Svalgaard, 1973] that

that this may be caused by a narrow current circulating clockwise (anticlockwise) at the North pole for negative (positive) B_Y, and in the opposite direction at the South pole. Heppner [1972] also observed correlations between B_Y and the dawn-dusk asymmetries of the polar electric field. These characteristics are consistent with the motion of open flux tubes across the magnetopause shown in Figures 4.4, 4.5 and 4.6.

We have not explicitly considered the effects of dipole tilting in this thesis. However, assuming that the magnetosheath flow and magnetic field parameters are unchanged by tilting, the example shown in Figure 4.7 and the results of Section 4.1.5, show that very little, if any, sunward tilting of the dipole (northern summer) would be necessary to bring an initial reconnection site poleward of the northern cusp into the region of sub-Alfvénic flow, and hence to satisfy the steady-state condition. Anti-sunward tilting (northern winter) could bring the southern cusp into a sub-Alfvénic region provided that the initial reconnection site was offset to the dawn-side. Seasonal asymmetries of polar cap convection currents have been seen by some observers (see Kennel [1995, p.184] and references therein) and this work may contribute to an understanding of these phenomena.

Our results show the sensitivity of the model's predictions as to whether the magnetosheath flow is sub- or super-Alfvénic at the reconnection site. This is particularly important poleward of the cusps under northward IMF conditions. If the Spreiter-model for magnetosheath flow is correct and flows poleward of the cusp are super-Alfvénic then steady-state reconnection under northward IMF is not possible in this region. The standard Spreiter model gives super-Alfvénic flow within 5 - 10 R_e of the sub-solar point [Cowley, 1995], i.e. well equatorward of the cusp. Moreover, Figures 4.7 and 4.8 show the importance of replacing the simple sub- or super-Alfvénic flow criterion by one which takes acount of the importance of the vector orientations.

In order to achieve steady-state reconnection poleward of the cusps, a mechanism for producing sub-Alfvénic flow must be found. In our northward IMF examples (e.g. Figures 4.2 and 4.3) we achieved this by arbitrarily reducing the density to 20% of the value predicted by the Spreiter model in order to modify the Alfvén Mach number within the magnetosheath. Similar effects may be achieved by increasing the magnetosheath field strength at the magnetopause, by reducing the magnetosheath flow speed predicted by the Spreiter model, or a combination of all three.

A study of 20 events by Crooker *et al.* [1984] showed that only about half of the magnetosheath flows followed the gas-dynamic predictions. A recent study by Siscoe *et al.* [2000] also shows deviation from the gas-dynamic predictions. In addition, it was reported by Alexeev *et al.* [1998] that using the magnetosheath model of KF94 without a density depletion overestimated field magnitude. The density predicted by the Spreiter models may be too high, and a physical mechanism which reduces the plasma density in the vicinity of the magnetopause may be in operation (e.g. Zwan & Wolf [1976], Le *et al.* [1996]).

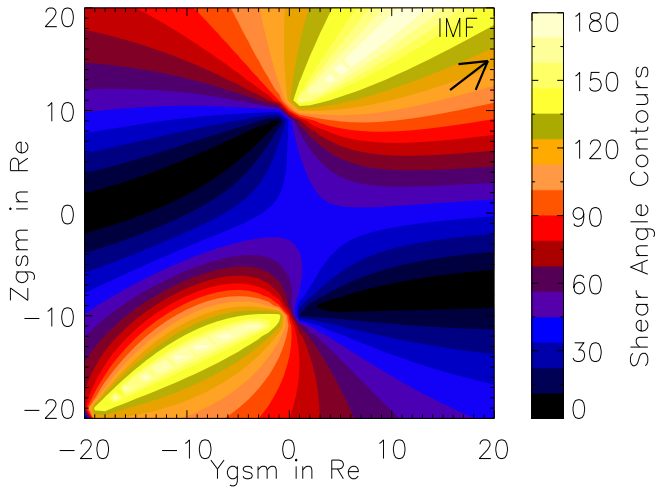

Figure 4.9: Shear angle contours for northward 'away' IMF: Showing the shear angle between the magnetosheath and magnetosphere magnetic field on a YZ projection of the magnetopause for northward 'away' Parker spiral (-6,6,6)nT. The white regions show virtually anti-parallel magnetic fields, and the black regions parallel fields.

4.3 Location of Initial Reconnection

In this section we show how our model may be used to identify the most likely sites for steady-state reconnection. First, we plot the shear angle contours for the required IMF (Figure 4.9), in this case an 'away' Parker spiral with a northward B_Z component (-6,6,6).

Next, we overplot the current threshold contours for the required IMF, Figure 4.10. Reconnection is more likely for regions of higher current.

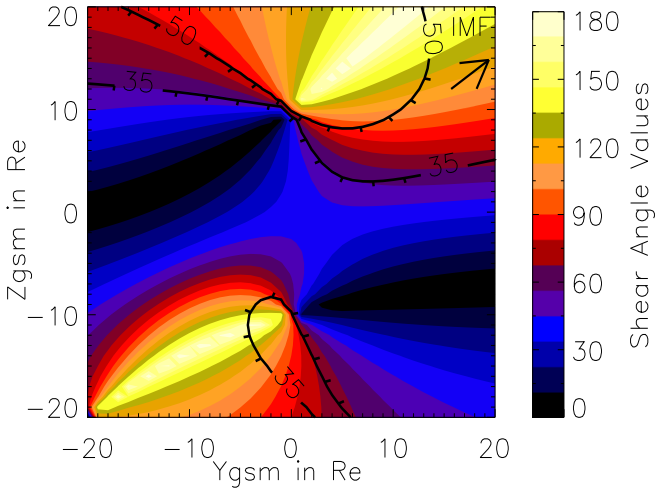

Figure 4.10: Current contours for northward 'away' IMF: Overplots the current contour thresholds (in this case 35nT and 50nT are plotted) for the given IMF.

And lastly, in Figure 4.11, we overplot the sheath flow q component to Alfvén velocity q component ratio at the required density reduction (see Figure 4.7). In this case, no density reduction has been applied. Steady-state reconnection can only occur in the region where this

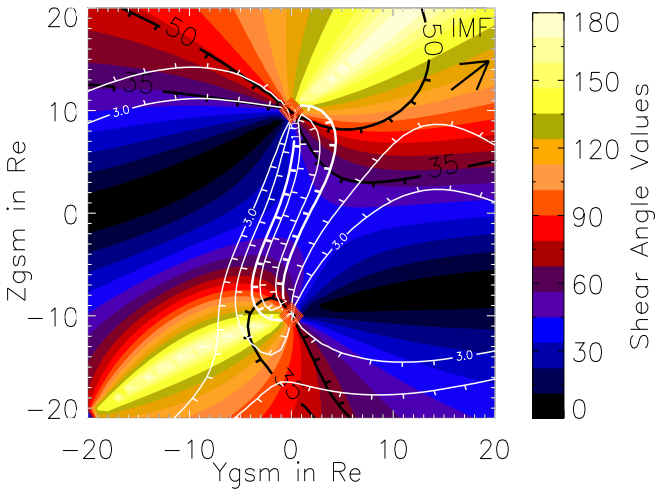

Figure 4.11: Overplot of velocity q component ratio: Overplots the velocity ratio contours for the given IMF.

ratio is less than 1.

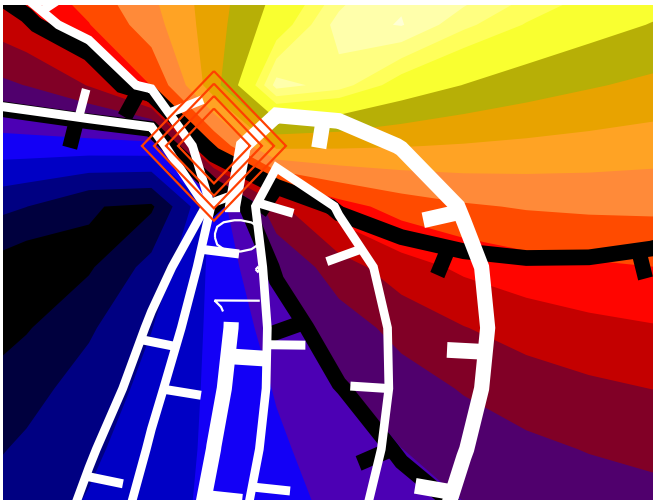

Figure 4.12: Enlargement of overlayed region: This figure is an enlargement of the northern cusp (indicated by the orange diamonds) region from Figure 4.11. For the northward 'away' IMF, steady-state reconnection is most likely to occur in the top part of the region beneath the thickest white contour which represents velocity ratio of 1. This is just on the post-noon side of the northern cusp.

Figure 4.12 shows an enlargement of the northern cusp region showing all the overlays. For this example of northward 'away' IMF, with no density reduction, steady-state reconnection is most likely to occur on the post-noon side of the northern cusp, just below the thick white contour representing the $V_{shq}/V_{Aq} = 1$ but where the shear angle and currents are highest. Inspection of Figure 4.11 also shows a smaller region just pre-noon of the southern cusp where steady-state reconnection may also occur for this IMF.

If density reduction is applied, then the steady-state region expands. The upper plot in Figure 4.13 shows the same as Figure 4.11 but with the density reduced to 50% of the standard

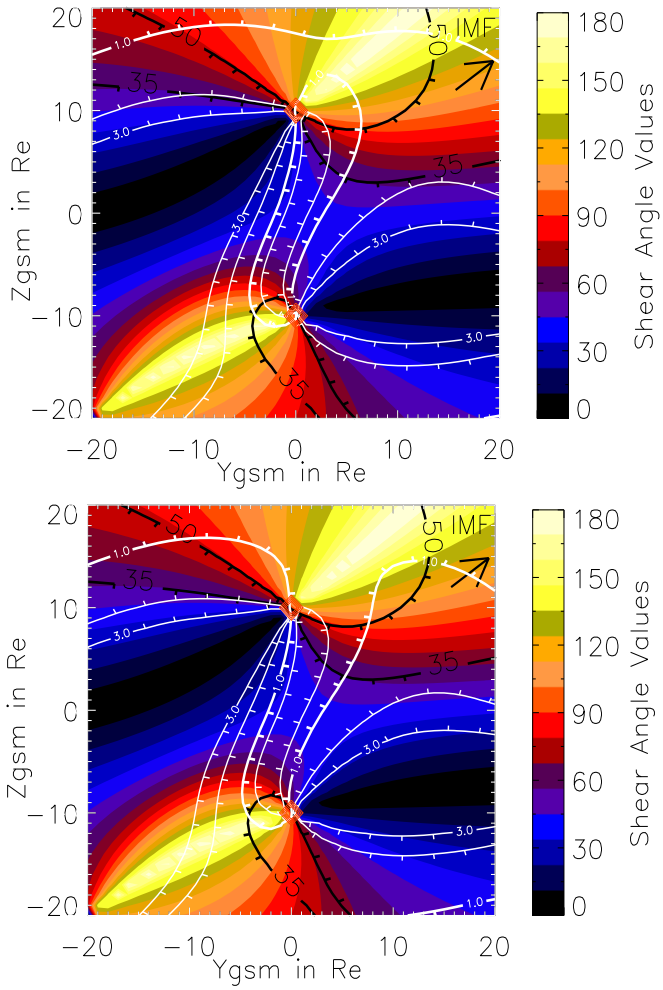

Figure 4.13: Location for steady-state reconnection under northward IMF at reduced density: As in Figure 4.11 but, in the top figure, with the density reduced to 50% and in the bottom figure reduced to 40%. In the top figure, at the northern cusp, the steady-state region has expanded duskward and poleward. A sub-Alfvénic region is also encroaching from the tail regions. In the bottom figure, the steady-state region has opened up across the poleward regions.

density and the lower plot with density further reduced to 40%. In the latter case,the difference is much more dramatic. In this case, the poleward and tail regions open right up to the possibility of steady-state reconnection.

4.4 Summary

We have constructed a model which follows open flux tube motion along the Earth's magnetopause, after reconnection at a given location and for a given set of IMF conditions. We find (i) the model reproduces the expected poleward motions of open field lines for southward B_Z; (ii) for northward B_Z, the model's predictions are very sensitive to whether the flows are sub- or super-Alfvénic for reconnection occuring poleward of the cusp. This indicates that work on comparing flow observations with model predictions would be useful in further investigations into signatures of

reconnection in general and conditions for steady-state reconnection under northward IMF in particular; (iii) B_Y effects can lead to asymmetrical loading of the tail; and (iv) flux tube motions for the two Parker spiral directions are asymmetrical and may thus explain statistical asymmetries in the dayside polar ionosphere convection patterns.

On the basis of northward IMF studies we conclude that steady state reconnection poleward of the cusp will not occur under typical conditions unless one or more of the magnetosheath flow, density and field models is modified or unless dipole tilt is sufficent to bring the cusp into a sub-Alfvénic flow region.

Our model can also assist in identification of possible/most likely sites for steady-state reconnection to occur. Using this method, we showed how an arbitrary reduction in the density, forcing an extension of the sub-Alfvénic flow region, could lead to conditions where steady-state reconnection could occur poleward of the cusps under northward IMF.

In Appendix C we show a range of results from our model.

Following this work, we believed that a broadscale survey of magnetosheath parameters to compare with the models used in constructing our own would be useful. This is described in detail in the remainder of our thesis.

Chapter 5

The Magnetosheath

5.1 Introduction

Following on from the modelling work of Chapters 3 and 4, the importance of the magnetosheath parameters, particularly of flow, density and magnetic field, in predicting flux tube motion became apparent. A search of the literature also revealed that very few surveys of the magnetosheath region have been carried out and we set out, therefore, to attempt such a survey.

In this chapter, we first review the formation of the magnetosheath, and the predictions for the changes in plasma parameters arising therefrom. We then describe a number of models describing the flow and evolution of other parameters within the magnetosheath and a selection of models dealing with the shapes and positions of the bow shock and magnetopause boundaries of the magnetosheath. Following this, we describe surveys of the magnetosheath which have been carried out to date, and, lastly, some joint Geotail and Wind experiments which we believe will justify our choice of data from these two spacecraft as the basis of our survey which will be discussed in the next two chapters.

5.2 Features of the magnetosheath

5.2.1 Formation

The magnetopause behaves as an obstacle in the flow of the solar wind, separating plasma emanating from the Sun from that organized by the geomagnetic field. Solar wind flow is supersonic. As such, when it encounters an obstacle in the flow, a shock forms upstream of the obstacle. The magnetosheath is the region of shocked solar wind plasma bounded upstream by the bow shock (see Sections 1.5.2, 5.3.4) and downstream by the magnetopause (see Sections 1.5.4, 5.3.4).

The shape of the magnetopause is principally determined by pressure balance. Additionally, it behaves as a tangential discontinuity for most of the time and this acts as an impenetrable barrier. The shock therefore must act to deflect the flow of the solar wind so that it may flow

around the obstacle. The shape of the bow shock is determined by this and approximates a paraboloid of revolution centred on the Sun-Earth axis [Burgess, 1995]. It should be stressed that the environment is constantly in motion due to the continual changes in the solar wind flow, hence these boundaries are not static. Nevertheless, we tend to treat the system as if it were in a steady-state.

5.2.2 Changes in Plasma Parameters

The bow shock changes the character of the solar wind flow by slowing it to subsonic and sub-Alfvénic speeds. In Table 1.1 we summarized various discontinuities and we consider the oblique shock as the general case of the bow shock as plasma flows through this discontinuity, ie $V_n \neq 0$. Essentially, the bow shock slows and compresses the plasma.

The underlying equations governing the changes in the plasma parameters comprise of a set of MHD equations known as the Rankine-Hugoniot relations and Maxwell's equations. For a simple, steady, 1-D discontinuity where plasma flows in from the upstream (u) across the discontinuity and out downstream (d) and assuming isotropic pressure, negligible electric stress, adiabatic changes such that $P\rho^{-\gamma} = const.$, and ideal MHD where $\mathbf{E} = -\mathbf{V} \wedge \mathbf{B}$ and where n and t represent normal and transverse components respectively, ρ is density, $\mathbf{V}$ velocity, P pressure and so forth, the equations may be summarized as follows:

Conservation of mass:

$$[\rho V_n] = 0 \tag{5.1}$$

where $[x_a]$ is known as a jump condition and represents $x_{a_u} - x_{a_d} = 0$.

Conservation of normal momentum:

$$\rho V_n \frac{\partial V_n}{\partial n} + \frac{\partial P}{\partial n} + \frac{\partial}{\partial n}\left(\frac{B^2}{2\mu_0}\right) = 0 \tag{5.2}$$

leading to

$$\left[\rho {V_n}^2 + P + \frac{B^2}{2\mu_0}\right] = 0 \qquad \text{(using } [{B_n}^2] = 0\text{)} \tag{5.3}$$

Conservation of tangential momentum leading to:

$$\left[\rho V_n \mathbf{V_t} - \frac{B_n}{\mu_0}\mathbf{B_t}\right] = 0. \tag{5.4}$$

Conservation of energy:

$$\left[\rho V_n \left(\frac{1}{2}V^2 + \frac{\gamma}{\gamma - 1}\frac{P}{\rho}\right) + V_n \frac{B^2}{\mu_0} - \mathbf{V}\cdot\mathbf{B}\frac{B_n}{\mu_0}\right] = 0 \tag{5.5}$$

Conservation of the tangential component of the electric field leading to:

$$[V_n \mathbf{B_t} - B_n \mathbf{V_t}] = 0 \tag{5.6}$$

The consequences of these changes for the magnetosheath are that the bow shock slows the solar wind leading to an increase in the plasma density (from the conservation of mass). Thus the

plasma is compressed which leads to an increase in the temperature, an increase in $|\mathbf{B}|$ (though for a slow shock it decreases), and changes in $\mathbf{B}$ and in $\mathbf{V}$. Burgess [1995] points out that for high-Mach number, the maximum jump for a collisionless, monatomic gas of $\gamma = 5/3$ is a factor of 4.

Generally, the magnetopause forms a tangential discontinuity (except as discussed in Chapter 2). Plasma does not, therefore, cross this boundary. Hence at this boundary we expect to see tangential vector quantities, i.e. $B_n = 0$ and $V_n = 0$. In the sub-solar region, therefore, we should see $V_X \approx 0$ and $B_X \approx 0$. We should also see changes in V_Y, V_Z, B_Y and B_Z consistent with the flow of the plasma around the obstacle.

At the magnetopause boundary, pressure balance is maintained. The magnetospheric side consists almost entirely of a quasi-steady magnetic pressure from the geomagnetic field. The magnetosheath side consists of mainly thermal pressure, but with a magnetic pressure contribution. As a result of the deflection of plasma around the magnetospheric boundary, plasma at the dayside is forced out along the field lines. Additionally, compressional stresses on flux tubes very near the boundary in the sub-solar region cause further squeezing out of plasma along the field lines. We expect to see, therefore, a drop in the density and the formation of a plasma depletion layer (e.g. Zwan & Wolf [1976], Southwood & Kivelson [1995]). This has consequences for the shape of the density profile within the magnetosheath which should show an initial increase on passing the bow shock and a decrease at the magnetopause. For higher shear (or southward-B_Z), magnetic reconnection, or other possible mechanisms (see Chapter 2), may act to destroy the local tangential discontinuity allowing transmission of plasma through the magnetopause.

On passing the magnetopause, the density profile within the magnetosphere should show a drop. This is not because of 'action' at the tangential discontinuity but because the magnetopause separates two plasma regimes. Magnetospheric plasma is extremely rarefied, and is also much hotter. However, just inside the magnetosphere side of the magnetopause, we also expect to see tangential flow and magnetic field components. Again, in the sub-solar region, we expect $V_X \approx 0$ and $B_X \approx 0$. Inside the magnetopause, the geomagnetic field is steadily northward and significantly stronger than that of the magnetosheath.

5.2.3 Phenomena

As the magnetosheath plasma is simply shocked solar wind, its particle composition will be the same. Various solar wind phenomena such as waves, discontinuities and shocks may also be found. Additionally, the bow shock interaction generates a number of wave phenomena including mirror and Alfvén ion cyclotron waves driven by shock-induced temperature anisotropies [Schwartz *et al.*, 1996]. A relatively current-free magnetic field inside the magnetosheath is also predicted [Fairfield, 1979, Kobel & Flückiger, 1994].

5.3 Models of the magnetosheath

Models of the magnetosheath may be divided into two main, albeit overlapping, groups: those dealing with the size, shape and motion of the boundaries and those dealing with the plasma parameters within the magnetosheath such as the flow, density and magnetic field. In this section we first review in some detail the work of Spreiter *et al.* [1966] and some developments of their work. Next we review some other work on magnetosheath flow. Lastly, we review a number of models relating to the size and shape of the magnetosheath boundaries. It should be noted that we do not attempt to address localised variations in flow at the magnetopause which may arise from magnetic reconnection considerations.

5.3.1 Hydromagnetic flow around the magnetosphere - Spreiter, Summers and Alksne 1966

A key paper in the development of our understanding of flow and other plasma parameters in the magnetosheath is the work of Spreiter *et al.* [1966], henceforth known as S66, we therefore choose to outline it in some detail. In this paper, an MHD model for the interaction of the solar wind and geomagnetic field is described. The magnetosphere boundary (which we would now call the magnetopause) and distant tail are treated as tangential and contact discontinuities respectively. The bow shock is treated as a fast MHD shock. However, the application of the model to the near-Earth system ignores the contributions from the magnetic field because of their smallness, and thus the treatment is essentially hydrodynamic. The paper gives detailed results for the location of the bow shock, density, velocity and temperature in the magnetosheath for a range of different Mach numbers and γs. The paper also shows the modification of the magnetic field within the magnetosheath as it convects with the magnetosheath flow for incident IMF of 45° and 90°.

The paper discusses (i) the application of fundamental MHD to hypersonic plasma flow, (ii) the degree to which it may be approximated by gas dynamics and (iii) numerical results.

Starting with the MHD equations (see Chapter 1.2.2) and the Rankine-Hugoniot relations (see Section 5.2.2), the authors obtain a range of results for mass flux which may be interpreted as various discontinuities (see Chapter 1.3). From this discussion it is deduced that the bow shock must be a fast shock, though this does not preclude other shocks from forming downstream of the fast shock.

These results are then considered in the light of the geophysical environment and a number of important parameters defined: Mach number $M = V/C_s$ and Alfvénic Mach number $M_A = V/V_A$ where V is the fluid speed, $C_s = (\gamma P/\rho)^{\frac{1}{2}}$, the speed of sound, and $V_A = \left(B^2/\mu_0\rho\right)^{\frac{1}{2}}$, the Alfvén speed. Generally, M_∞ and $M_{A_\infty} >> 1$ where the subscript ∞ indicates the values in the solar wind stream.

Knowledge of M_∞, M_{A_∞}, $\mathbf{V}_\infty$ and $\mathbf{B}_\infty$ (the paper actually uses $\mathbf{H}$, the magnetic field strength, but we will use $\mathbf{B}$ in this description) coupled with use of a Friedrich's diagram can give the

asymptotic directions of the shock waves and wake. If $\mathbf{B} = 0$ then $(C_s/V_A)_\infty >> 1$ leading to the gasdynamic approximation. Where $V_A >> C_s$, then the result approachs a gasdynamic approximation for the case where $M_\infty = M_{A_\infty}$. For more general combinations of $\mathbf{V}_\infty$ and $\mathbf{B}_\infty$, hydromagnetic flow bears little resemblance to gasdynamic flow.

In the case where the velocity and magnetic field are aligned, then the use of 'pseudoquantities', e.g. setting $\mathbf{V}^* = \mathbf{V}(1 - {M_A}^2)$ and so forth leads to the gasdynamic equations.

In calculating their results, the authors give the location of the bow shock and the conditions applying across it. The magnetic field vector is set to zero because of the smallness of terms in the equations containing it. The flow field and the body shape (of the magnetopause) are found as part of the solution. The solution for the desired body shape is found by iterating from trial bow shock shapes. The paper gives a range of contours for $M_\infty = 8$ and $\gamma = 5/3$ or 2 including density, velocity, temperature, mass flux together with streamlines and wave patterns and position of bow shock wave for various M_∞ and γ. A number of shadowgraphs from experiments with a magnetosphere-shaped object fired into argon are given in support of their work. Generally, they find that the size and shape of the magnetosphere is insensitive to variations in Mach number and γ.

Lastly, the authors deal with the distortion of the interplanetary field throughout the magnetosheath. The calculation of the flow field is separated from that of the magnetic field which is a subsequent step. In order to calculate the magnetic field vector, the 'frozen-in flux' theorem (see Section 1.2.3) is assumed to hold. Attention is also confined to the plane containing both the incident $\mathbf{V}$ and $\mathbf{B}$. Because of the assumption of axial symmetry, the distorted field lines are confined to the same plane. Two results are given for $M = 8$ and $\gamma = 5/3$, with the incident magnetic field set at 45° and 90°. The results show that the magnetic field lines bend discontinously through the bow shock at any angle except 90° and then curve in a continous manner throughout the magnetosheath. The bend at the bow shock is in a direction that preserves the sign of the tangential component of $\mathbf{B}_t$. Draping at the nose is predicted. The authors do state, however, that because the draping may take place in three-dimensions, then the bending of the field lines may be much less than that shown in their figures.

Subsequent modifications to S66

Spreiter & Stahara [1980]'s paper made advances but mainly with improvements in computation methods. Solar wind parameters were introduced as input to the model to assist with the choice of boundary shapes. The main change was in the calculation of the magnetic field. The gas dynamic calculations are the same as for S66. One component of the magnetic field is calculated using the frozen-in flux theorem. The remaining components are determined using a decomposition method proposed by Alksne & Webster [1970].

Further advances in their method were not made until 1999 [Song *et al.*, 1999a]. They used a method known as 'Gasdynamic Convected Field Model' (GDCFM). A simplified description

of the magnetosheath with high spatial and temporal resolution is used. The basic equations assume that the solar wind is an ideal gas, and also assume the frozen-in flux theorem. There are three main approximations: First, from the ideal MHD equations, combine the magnetic forces in the momentum equation with the thermal pressure force and set it as the pressure force in the GDCFM equations. Next, replace the sonic Mach number with $M_f = V/C_f$ (where C_f is the magnetosonic fast mode speed). This approximation is good for high β plasma, i.e. downstream of the sub-solar bow shock. Thirdly, assume a steady state exists. Temporal variations longer than 5 minutes are adequately represented by the model. Lastly, make the adiabatic assumption that $P = \alpha\rho^{\gamma}$ where α is a constant, but changes across the bow shock.

The upstream boundary is the plane perpendicular to the solar wind flow, and its direction is aberrated from the Sun-Earth line by $30kms^{-1}$. Quantities in the GDCFM system were obtained by intergrating along the flow vector. The shape of the magnetopause is obtained by pressure balance.

In GDCFM, the location and shape of the magnetopause change in unison as upstream pressure varies. It is also assumed that the magnetopause changes instantly in response to changes in solar wind values. A number of normalizations were also made.

The new scheme was tested in Song *et al.* [1999b] with a certain success. The density profile at the stagnation stream line is in accord with models of the modified plasma depletion model. This model, though, like other MHD models predicts a gradual slowing of the magnetosheath solar wind speed along the stagnation streamline from bow shock to magnetopause. Observational evidence suggests that in reality, the speed remains relatively constant along the streamline until very near the magnetopause [Song *et al.*, 1990].

5.3.2 Other magnetosheath flow models

Wu [1992] developed an MHD model based on ideal MHD and a conducting sphere as the obstacle. He assumed a southward IMF and an initial $\mathbf{B} = \mathbf{B}_{imf}$, and additionally that $M_s = 4$ and $M_A = 10.3$. Results include prediction of a plasma depletion layer. Wu's results show that as we move from the bow shock along the Sun-Earth line, the density initially increases rather than decreases. The density then falls as we approach the magnetopause. A shift in the stagnation point is also predicted.

A number of models dealing with anistropic plasma have also appeared recently. Erkaev *et al.* [2000] (and the very similar paper, Erkaev *et al.* [1999]) describe an ideal MHD model which they have developed which accounts for anisotropic pressure. Starting with the basic ideal MHD equations, they consider, as a general case, the relation between perpendicular and parallel pressures as $P_{\perp} = P_{\parallel}F(\rho, B, P_{\parallel})$ where the function F has different values depending on the relationship between the two pressures as follows:

- Isotropic MHD model: $F = 1$.

- Anisotropic adiabatic model: $F = const B^3/\rho^2$.
- Mirror instability criterion: $F = 0.5(1 + \sqrt{1 + 4/\beta_{\|}})$.
- Empirical relation: $F = 1 + A/\sqrt{\beta_{\|}}$ and $A = 0.848$.

The authors use isotropic Rankine-Hugoniot relations. The obstacle is a paraboloid of revolution and the shock front a hyperboloid. A range of stagnation streamline profiles are given for each of the closure relations.

Samsonov *et al.* [2001] also propose an MHD model for large scale flow for the case where the IMF and solar wind velocity are at an angle of 45°. Besser *et al.* [2000] deal with an anisotropic plasma model using the second assumption of the Erkaev *et al.* model described above (the Chew-Goldberger-Low approximation) as does Besser *et al.* [2000].

Are gasdynamic and MHD models successful predictors?

A number of surveys, some of which are described in Section 5.4, have been carried out. Observational support for gasdynamic and MHD theories is mixed. Crooker *et al.* [1984] found agreement in 50% of cases tested. Němeček *et al.* [2000b] found some differences as did Zastenker *et al.* [2002], Samsonova & Hubert [2002] and Paularena *et al.* [2001]. Siscoe *et al.* [2000] found substantial disagreement. In particular, and as mentioned above, Song *et al.* [1999b] found the magnetosheath flow profile at the stagnation line quite different to that predicted by existing models.

In summary, the models do predict some general features of the magnetosheath region: the existence of a stagnation point in the flow in the vicinity (albeit offset) of the sub-solar point of the magnetopause. A density maximum near the nose of the magnetopause is also predicted, and all but the S66 model show a drop in density immediately at the magnetopause, as expected from plasma depletion theories. However, when comparing predictions to observations, the profile of the magnetosheath flow along the sub-solar stagnation line is predicted by all models to be steadily slowing, contrary to observations. The density profile along the sub-solar stagnation line varies with models. S66 predicts a steadily increasing density, Wu [1992] predicts a 'bump' and those of Erkaev *et al.* [2000] vary with the model assumptions. Song *et al.* [1990] found evidence that the density profile along the stagnation line is relatively constant through the magnetosheath until near the magnetopause. In over half of their cases, they found a density enhancement in front of the magnetopause not predicted by models, and found mixed evidence of a plasma depletion layer.

As a dynamic, turbulent region, the magnetosheath is difficult to model as demonstrated by the mixed success of the gas dynamic and MHD models in predicting observations. The S66 model has been found to be a successful predictor in a number of cases and is widely used. It also lends itself readily to comparisons throughout the magnetosheath. We choose, therefore, to use this as the comparator for the results of our survey to be described in Chapters 6 and 7.

5.3.3 Magnetic Field Models

The majority of models dealing with the magnetic field within the magnetosheath are derived from gasdynamic or MHD models. One weakness in all the models concerns the evolution of the magnetic field throughout the magnetosheath. In most of these models it is dealt with by first calculating the flow, and then, assuming frozen-in flux theorem, integrating the magnetic field along the flow streamlines.

The KF94 model was described in some detail earlier in this work (see Section 3.6.1) and takes a very different approach to that mentioned above using the method of potentials to calculate the magnetic field throughout the sheath. KF94 give two examples of good qualitative agreement between their model and Spreiter & Stahara [1980]. Our reasons for choosing this model are given in that section.

5.3.4 Models dealing with size, shape and motion

A brief overview of the bow shock and magnetopause were given in Section 1.5. In this section we discuss these models in a little more depth.

The bow shock

According to Song [2000], our ability to predict the bow shock location is still very limited. Generally speaking, it is assumed that the two most important factors in predicting bow shock location are the dynamic pressure of the solar wind and the north-south component of the IMF [Elsen & Winglee, 1997].

One of the most widely used models of the bow shock is that of Fairfield [1971]. The model is hyperbolic and has a fixed R_{bs}/R_{mp} ratio of 1.3. There are two basic models for the magnetosheath thickness along the stagnation line: the ratio of thickness to stand-off distance of the magnetopause $\propto \rho_u/\rho_d$ which is good at high Mach number [Petrinec & Russell, 1997], and the more general

$$\frac{R_{bs}}{R_{mp}} = 1 + 1.1\frac{(\gamma-1){M_\infty}^2+2}{(\gamma+1){M_\infty}^2-1} \tag{5.7}$$

where R_{bs} and R_{mp} are the distance from the focus of the ellipsoid object (which is at the Earth's centre) and M_∞ is an upstream Mach number. There is some dispute about which Mach number is most appropriate here. It is usual to use the sonic Mach number [Peredo *et al.*, 1995]. However, Petrinec & Russell [1997] believe the magnetosonic Mach number is most appropriate. We calculated the ratio using all of sonic, magnetosonic and Alfvénic Mach number versions for a few typical values and found a difference of around 1% which we did not feel was significant for our purpose and hence used the sonic Mach number in our survey.

Peredo *et al.* [1995] used a large data set of 1392 bow shock crossings from 17 different spacecraft to investigate the dependence of the bow shock on the solar wind and IMF and deviations from gasdynamic and MHD theory. The data were normalised to aberrated GSE coordinates and further

normalised to a standard pressure (the average pressure of their data set). The data were binned in a number of ways using the different Mach numbers (sonic, magnetosonic and Alfvénic). Their conclusion was that the Alfvénic Mach number organised the results best, predicting a thicker magnetosheath more in line with observations.

The magnetopause

Numerous studies have been carried out on the magnetopause boundary, e.g. Sibeck *et al.* [1991], Roelof & Sibeck [1993, 1994]. The boundary is normally found from Newtonian pressure balance considerations where the pressure on the boundary from the magnetosheath side may be given by, for example, $k\rho_\infty {V_\infty}^2 cos^2\psi$ where ψ is the angle between the upstream flow and the normal to the obstacle. The resulting equation for the location of the magnetopause stand-off distance from the Earth's centre, R_{mp} in R_e is:

$$R_{mp}(R_e) = 107.4(N_\infty {V_\infty}^2)^{\frac{-1}{6}} \tag{5.8}$$

where N_∞ is the solar wind proton number density adjusted for helium content in cm^{-3} and V_∞ is the solar wind bulk velocity in kms^{-1} [Walker & Russell, 1995].

The usual pressure balance model, however, does not predict well the observed asymptotic behaviour of the magnetopause downtail for low Mach number. It also breaks down as ψ approaches 90°. Petrinec & Russell [1997] propose a formula which they claim predicts both the behaviour in the stagnation region and the more realistic asymptotic nature of the far downtail magnetopause. This is given by: $k\rho_\infty {V_\infty}^2 cos^2\psi + P_\infty sin^2\psi$. Here, k is a measure of how the divergence of the flow diminishes the pressure and, for $\gamma = 5/3$ and $M_\infty = \infty$, has a value of around 0.881 [Walker & Russell, 1995].

Elsen & Winglee [1997] developed a predictive model of the magnetopause using 30 3-D MHD simulations for a range of solar wind pressures and IMF directions. Using ideal MHD as the basis, the magnetopause was modelled as an ellipsoid with one focus at the Earth's centre. Their model shows general agreement with empirical axisymmetric magnetopause models but is, in fact, asymmetrical between the equatorial and noon-midnight meridian planes. Their model also included a feature missing from almost all other MHD models [Pulkkinen *et al.*, 1995], the ring current. Inclusion of the ring current increased the magnetopause position to a value more consistent with observations. MHD models without this underestimate the sub-solar distance by about $1R_e$.

5.4 Surveys of the magnetosheath

There are remarkably few surveys of the magnetosheath reported in the literature. None of these attempted the kind of broad-scale survey which we have carried out. This position has begun to change recently, and in particular two papers published after we carried out our survey and which address some similar issues have appeared [Zastenker *et al.*, 2002, Paularena *et al.*, 2001] and are

discussed in greater detail in Section 5.4.1. In this section, we first review some of the older work in the field, and this is followed by a review of more recent work.

A number of surveys in the magnetosheath region were carried out in the 1980s and early 1990s reviewing different aspects of the region. Several of these concentrated on investigations of the dayside. For example, Crooker and co-workers published a range of results considering the source and location of energetic ions within the magnetosheath and its relationship to the IMF [Crooker *et al.*, 1981]. Another paper investigated the relationship of magnetic field compression and the IMF at the dayside magnetopause [Crooker *et al.*, 1982]. Research was also carried out on observations of large-scale flow in the dayside magnetosheath [Crooker *et al.*, 1984]. Other dayside work includes observations of the density profile in the magnetosheath near the stagnation streamline [Song *et al.*, 1990].

Examples of work carried out on the flanks or downstream of the Earth are Howe & Binsack [1972]'s survey of magnetosheath flow downstream of earth using Explorer 33 and 35 data, and Chen *et al.* [1993]'s investigation of magnetosheath flow and the shape of the magnetopause at the dawn flank.

More recent work on various aspects of the magnetosheath has been undertaken. The Interball teams have been quite active in this area. For example: Němeček *et al.* [2000b] used Interball-1 measurements of ion flux on the dusk flank of the magnetosheath, with Wind acting as the solar wind monitor to compare the radial magnetosheath profile with gasdynamic model predictions. Němeček *et al.* [2000a] used Interball measurements in conjunction with Wind and Geotail spacecraft to examine the magnetosheath ion flux profile and to ascertain the timescale on which it matched gasdynamic predictions. Two further studies [Fuselier *et al.*, 2002, Dubinin *et al.*, 2002] were carried out using Interball in conjunction with POLAR and other spacecraft to investigate the characteristics of plasma at the cusps and again, to compare this with gasdynamic models. Lastly, a survey which bears some comparison with our own and that used multispacecraft measurements of the magnetosheath to test gasdynamic models was carried out [Zastenker *et al.*, 2002] and is discussed separately in Section 5.4.1.

Several studies have been carried out in this region using Geotail data. Matsuoka *et al.* [2002] tested for the existence of a relationship between temporal changes in magnetic field, ΔB and those in plasma velocity, ΔV, comparing it with the expectations of MHD wave theory. They found strong evidence for plasma anistropies, particularly of temperature. This, they believe, may be caused by the adiabatic expansion of magnetic flux tubes in the magnetosheath. Ivchenko *et al.* [2000] performed a statistical survey of numerous dayside magnetopause boundary crossings for comparison with models of magnetopause motion. Their results suggest that pressure pulses generated at a quasi-parallel bow shock drive the boundary motion. Density fluctuations in the flank-side magnetosheath were investigated using Geotail and Wind spacecraft by [Seon *et al.*, 1999]. Anti-correlations between plasma density variations and magnetic field variations were found. The authors propose that convected slow-mode waves play a role in the generation

of density fluctuations. Petrinec *et al.* [1997] utilized the same two spacecraft in the analysis of three intermediate downstream crossings to investigate magnetosheath flow finding that the magnetosheath velocity is slowest when the local magnetic field and velocity vectors are aligned, and largest when they are perpendicular to each other. Lastly, Kessel *et al.* [1999] investigated the local variations of IMF at the Earth's bow shock at the dawn and dusk flanks. Their results suggested that there may be a kink in the magnetic field line near the Sun-Earth line.

A variety of other experiments have been carried out. For instance, Paularena *et al.* [2001] found dawn-dusk asymmetry in Earth's magnetosheath. Again, this paper has some similarity of methodology to our own work and will be discussed in more detail in Section 5.4.1. Pudovkin *et al.* [2001] looked at how southward IMF affected variations of the plasma density and magnetic field intensity across the magnetosheath, particularly in the vicinity of the magnetopause. The results were compared with a magnetosheath model of Pudovkin *et al.* [1995]. Song *et al.* [1999b] devised a new scheme for studying the magnetosheath and their paper uses four case studies to assess its success. In particular they consider the magnetosheath density profile near the stagnation streamline and the magnetosheath flow profile near the stagnation streamline showing that the flow does not slow down towards the stagnation point, but moves rapidly until very near the magnetopause. Two other investigations comparing observations of magnetosheath variations on single crossings with those of MHD calculations [Samsonova & Hubert, 2002, Farrugia *et al.*, 2001] have also been reported.

5.4.1 Two recent surveys

The following two papers were published after we had carried out our survey and address some similar issues.

Paularena *et al.* [2001] used IMP8 data in the magnetosheath flanks from August 1978 - February 1980 with ISEE-1 or ISEE-3 as the solar wind monitor and from November 1994 to October 1997 with Wind as the solar wind monitor. Data at 5 minute averages were used. The team carried out a number of coordinate shifts and normalizations to endeavour to ensure that data from the same relative regions of the magnetosheath were binned together. Time shifting for the solar wind data were done at the solar wind propagation speed and no attempt to compensate for slowing of plasma speed within the magnetosheath was made. Solar wind flow and position were aberrated by 4.5° to compensate for the Earth's motion and the magnetosheath data were also rotated into the same system. The spacecraft position within the magnetosheath was transformed by first calculating the magnetopause and bow shock positions, the former using Sibeck *et al.* [1991] and the latter using Fairfield [1971]. The radial position of the spacecraft was calculated relative to these locations and the X coordinate scaled by the magnetopause stand-off distance. This allowed data to be binned depending on relative location. Points outside the calculated magnetosheath were removed from the data.

The authors found evidence for a significant dawn-dusk asymmetry in the density (with a

greater density on the dawn side) at times of solar maximum. A much less significant asymmetry was found at solar minimum. However, at solar maximum the asymmetry did not depend on the orientation of the IMF, while at solar minimum it did. Comparisons with MHD simulations gave qualitatively similar results. The authors speculate that the origin of this phenomenon may lie in the Earth's magnetosphere.

Zastenker *et al.* [2002] surveyed variations in plasma and magnetic field in the magnetosheath using multispacecraft measurements. Results were also compared with gasdynamic models and motion of the structures. Magnetosheath data were provided by Interball-1, Magion-4, Geotail and IMP8. Solar wind monitoring was provided by IMP8 and Wind. The measurements were made in the flanks of the magnetosheath. One minute averaged data were used as the basis of the survey. Solar wind data were time-shifted at the propagation time to the magnetosheath data points and a comparison was made between the time-shifted solar wind data and relevant magnetosheath data to show that it was a reasonable match. The positions of the spacecraft within the magnetosheath were also adjusted to relative units. The magnetopause stand-off distance was calculated using the Roelof and Sibeck magnetopause model [Roelof & Sibeck, 1993] and all the coordinates scaled relative to that. All plasma and field values are given relative to the solar wind values. As well as comparisons with solar wind values, a number of comparisons between pairs of spacecraft operating in the magnetosheath at the same time were also made. Their conclusions were that while the average behaviour of the magnetosheath parameters was as predicted by gasdynamic models, a number of deviations from the model were observed, perhaps due to internal magnetosheath processes.

In our survey we address the issue of linking solar wind data to magnetosheath measurements and appropriate scaling of data within the magnetosheath in a similar manner, though our time shifting is very slightly different. Both of these surveys are based in the magnetosheath flanks. The first of the two surveys above was concerned with densities, while the second was concerned with a more general comparison of magnetosheath parameters with Spreiter models. Our survey has a broader remit, focusing more on the day and near-nightside data. We seek both to compare observations with (principally) Spreiter models and also to investigate a range of potential effects. In particular, we consider the extent of sub-Alfvénic flow.

5.5 Linked Geotail - Wind experiments

The purpose of this section is to describe a number of occasions where Geotail and Wind data have been linked in order to carry out investigations. This is to demonstrate the suitability of our choice of spacecraft for this survey.

A range of experiments have been carried out using linked data from the Geotail and Wind spacecraft and a selection of these are described below. They include examples where Geotail and Wind were both in the magnetosheath or geomagnetic tail, both upstream of the bow shock, or

where one was in the magnetosheath and the other acting as the solar wind monitor. In a few cases, the spacecraft made simultaneous observations of the same phenomena.

Berdichevsky *et al.* [1999] determined intervals where Geotail and Wind were in magnetic conjunction, i.e. on the same magnetic field line in order to investigate the Earth's ion foreshock. Comparisons were made by Hashimoto *et al.* [1998] of AKR (auroral kilometric radiation) dynamic spectra observed simultaneously by Geotail in near-Earth orbit and Wind both in near-Earth orbit and far upstream. Terasawa *et al.* [1997] studied a large magnetic cloud which was observed by both Wind and Geotail while both were upstream of the bow shock.

Angelopoulos *et al.* [1997] used observations by Geotail and Wind, both of which were in the geomagnetic tail coupled with IMP8 and POLAR data in the solar wind to examine Bursty Bulk Flows. Measurements from both spacecraft were used in the first reported observations of sulphur in anomolous cosmic rays by Takashima *et al.* [1997].

Three examples of studies that have used Wind as the solar wind monitor for Geotail observations. McPherron *et al.* [1997] analysed a number of substorms where Geotail was at the centre of the tail and Wind acted as solar wind monitor. Petrinec *et al.* [1997] examined plasma flow and magnetic fields in the magnetosheath at intermediate downtail distances. Geotail was located in the tail and Wind again acted as the solar wind monitor. Also, Kessel *et al.* [1999] investigated local variations in the IMF at the Earth's bow shock. In this case, Geotail was at the dawn flank and Wind upstream on the duskside. Data from the IMP spacecraft were also used in this experiment.

This range of experiments demonstrates that use of Geotail and Wind for studies of the magnetosheath in our area of interest is not uncommon. In the next chapter we explain our choice of spacecraft further. We describe the data sets used and the method by which we carried out the analysis. In Chapter 7 we set out our results.

Chapter 6

Magnetosheath Parameter Survey

6.1 Introduction

In this chapter, we describe a broadbrush survey of basic density, flow and magnetic field strength parameters in the magnetosheath which we have carried out using one year's worth of Geotail and Wind data.

The motivation for this study arises from the results of the model described in Chapters 3 and 4 of this thesis. Outcomes from the model demonstrated the importance of sub-Alfvénic magnetosheath flow for steady-state reconnection. Usual models show the flow becoming super-Alfvénic within a few R_e of the sub-solar point, so in order to obtain sub-Alfvénic flow poleward and tailward of the sub-solar point one or more parameters in the model need to be modified:

- Decrease the magnetosheath flow speed
- Increase the Alfvén speed by:
  - decreasing plasma density
  - increasing magnetic field strength

The magnetosheath flow and plasma densities used in the model were drawn directly from the common gas dynamic models of Spreiter *et al.* [1966] and the magnetic field model from Kobel & Flückiger [1994], and it is interesting to compare the observational evidence with these models. No large scale survey of these magnetosheath parameters appears to have been carried out as discussed in the previous chapter.

6.2 Acknowledgements for Data Sources

Publicly available data from the Geotail and Wind missions was used as the basis of the survey described in this chapter.

Geotail magnetic field and plasma moment data were provided by S. Kokubun and T. Mukai through DARTS (Data Archive and Transmission System) at the Institute of Space and Astronautical Science (ISAS) in Japan.

Wind magnetic field data were provided by R. Lepping and the plasma moment data for Wind and IMP-8 by A. Lazarus through CDAWeb, the NASA Coordinated Data Analysis Web.

SSCWeb, in particular SSCLocator was also used. SSCWeb is jointly operated by NASA/GSFC Space Physics Data Facility and the National Space Science Data Center (NSSDC).

Some supporting data from NSSDC OMNIWEB, in particular for solar wind temperature and plasma beta was also used.

6.3 Survey of Magnetosheath Using Geotail and Wind data

We are attempting to carry out a broadscale survey of the magnetosheath parameters for X ranging from the bow shock stand-off distance to approximately -25R_e downtail, and for the accompanying width of the magnetosheath for this range of X. The three goals of our survey are (i) to compare observations with existing models, (ii) to suggest, where appropriate, new empirical models based on our results, and (iii) to investigate the locations of sub-Alfvénic flow in our data.

We need to identify, therefore, a plasma data set which is in the dayside and near-nightside magnetosheath and to compare the data with appropriate solar wind measurements. In this section we first discuss why we chose Geotail and Wind data, a brief description of the instrumentation on the spacecraft, and the data sets used. Following this, the two main issues to be addressed are (i) identifying intervals where Geotail is traversing the magnetosheath, and (ii) identifying an appropriate solar wind measurement which requires dealing with the question of time-lagging. Time-lagging is addressed in Section 6.3.3 and interval selection, with a worked example, in Section 6.4.

6.3.1 Geotail

In order to carry out our survey, we required a dataset which would give a consistent set of measurements throughout the area under consideration. We required magnetosheath parameters and associated solar wind information.

We selected Geotail data for the year 1997 because, as shown in Figure 6.1, over the course of that year, its orbit makes a full circuit of the Earth in the ecliptic plane while making repeated traversals of the magnetosheath in the day- and near-night side of geospace. In particular, it visits the sub-solar region allowing for comparison with other work in this area.

The two experiments providing the data which we have used are the Magnetic Field Experiment, from which data at 3-second intervals is obtained from the DARTS site, and the Low Energy Particle Experiment, from which data at 12-second intervals is available.

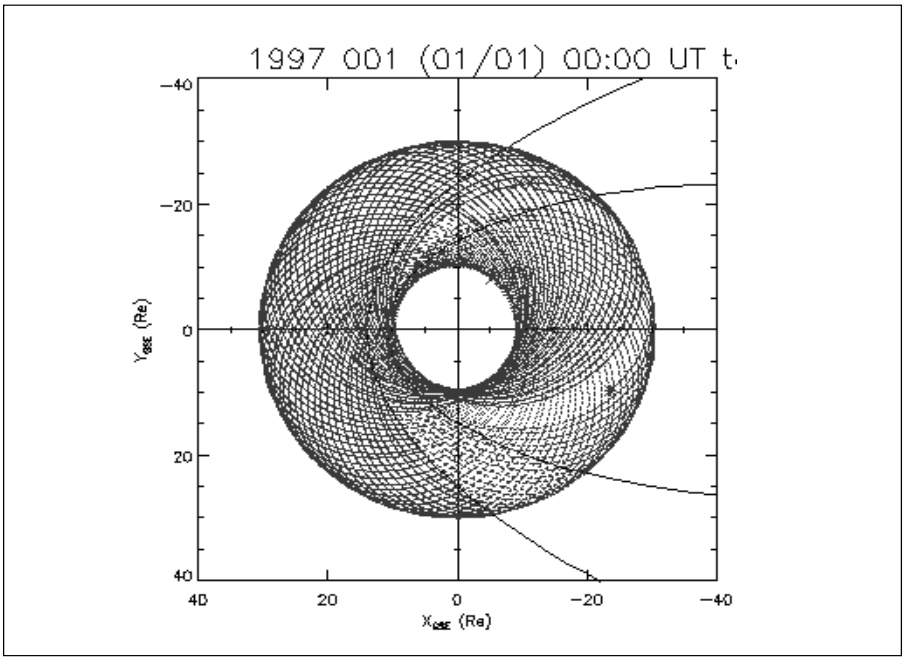

Figure 6.1: Geotail orbit 1997: Plot from CDAWeb showing the orbit of Geotail for the year 1997 in the XY plane. The approximate location of the bow shock and magnetopause are indicated on the plot by the quasi-parabolae.

The site offers the option of choosing between the Editor A and Editor B data sets where Editor A is more reliable. (See the Moment Data subsection below). However, there are many gaps in this data set, and for this reason, and given the broad-brush nature of our survey, we chose the Editor B data sets. Additionally, we selected the GSE Cartesian coordinate system.

Magnetometer data

The Magnetic Field Experiment (MGF) is described in detail in Kokubun *et al.* [1994]. The high-resolution MGF provides magnetic field data in the frequency range below 50 Hz. It consists of two fluxgate magnetometers and a search coil magnetometer. The fluxgate sensors are mounted on an extendable mast so that noise from the spacecraft is reduced. There are seven ranges from $\pm$ 16nT to $\pm$ 65536nT and switching takes place automatically. The fluxgate magnetometers are of a standard design.

The inboard sensor is similar to those used on AMPTE, Voyager and other NASA missions and the outboard sensor also has a similar design. Calibration tests, covering sensor orientation, offsets, sensitivity and noise levels were carried out using the magnetic facilities at Kakioka Magnetic Observatory and at NASA/Goddard, indicate that they are in good agreement with an accuracy of better than 0.1nT and the preflight tests showed that the bias field from the spacecraft would be less than 1nT at the outboard sensor.

The absolute zero levels were determined using various techniques (e.g. Hedgecock [1975]).

However, the magnetometer mast did not deploy exactly as plans resulting in a bias field, which the team state is less than $0.5nT$.

The team report that the data obtained is of excellent quality without significant contamination from the spacecraft. The only issue of note is that the temperatures of the sensors increased slightly resulting in a drift in the zero level of the outboard fluxgate magnetometer of $0.05nT/^{o}C$.

MGF Data is available from the DARTS site at 3-second intervals.

Moment data

The Low Energy Particle Experiment (LEP) is described in detail in Mukai *et al.* [1994]. The LEP instrument makes observations of plasma and energetic particles in geospace. There are three sensor units, LEP-EA, LEP-SW and LEP-MS and common electronics, LEP-E. The LEP-EA are energy-per-charge analyzers (EA) and measure the three dimensional velocity distributions of electrons and ions over the range of several eV/Q to $43keV/Q$. EA are particularly designed to measure the plasma found in the magnetotail. The SW is designed more to measure the solar wind ions. Our results in Chapter 7 use only the data collected by the EA monitor. The MS analyzer is designed to measure ion composition.

In both analyzers, the velocity distributions are obtained over four spins, while the velocity moments are calculated every spin period (about 3 seconds).

There are two separate onboard editors, A and B. Editor A transmits the raw data for the three-dimensional distributions every four spins, while Editor B transmits either two-dimensional data with the same time resolution as Editor A or three-dimensional data with coarser time resolution. The data from Editor B are also continuously recorded. Table 6.1 summarizes the parameters which are measured and derived from the sensors. The major sources for background noise in the data are electrical interference, high energy particle penetration, thermal emission inside some of the detectors and solar EUV radiation. After comparing data on the ground which has background subtracted and that onboard which includes the background, it was decided that background subtraction logic would be incorporated in future.

The team confirm that the LEP instrument is giving high-quality performance. LEP data is available from the DARTS site at 12-second intervals.

6.3.2 Wind

For comparison purposes, a data set giving solar wind parameters during the same period is required. The Wind spacecraft also operated in the ecliptic plane for the year 1997. For about half the time it was located at around 150 - $200R_e$ upstream of Earth, but on several occasions it executed orbits around the Earth passing through the magnetosheath and magnetosphere. The orbit is shown in 6.2.

The two experiments supplying the data sets which we used are the Wind Magnetic Field Instrument and the SWE instrument.

Sensor	Measured Parameters	Derived Parameters
EA SW	electron and ion count rates (*) for 32 energy steps, 16 azimuthal sectors and 7 elevation angles.	3-D velocity distribution functions functions of electrons and ions
	velocity moments for the electron and ion distribution functions up to the third order	no. densities, flow, velocities, pressure tensors and heat flux tensors of electrons and ions
	energy range EA-e: $8eV$ - $38keV$ EA-i: $32eV/Q$ - $39keV/Q$ SW-i: $140eV/Q$ - $8keV/Q$	
MS	count rates (*) at 32 energy steps, 16 azimuthal sectors and 5 elevation angles for selected five ion species energy range 0.1 - $25keV/Q$	3-D velocity distributions and their moments for five ion species (H^+,He^{++},O^{++},O^+)

Table 6.1: LEP experiment: Measured and derived parameters: This table shows the different parameters measured and derived by the sensors comprising the LEP experiment onboard Geotail (taken from Mukai *et al.* [1994])

* Note: The measured count rates can be directly converted into directional, differential energy intensities of electron or ion fluxes.

Magnetometer data

The Wind Magnetic Field Investigation (MFI) is detailed in Lepping *et al.* [1995].

The magnetometers are similar to those used in earlier missions such as Voyager, Ulysses (formerly ISPM) and GIOTTO. They are dual triaxial fluxgate magnetometers which as with Geotail are deployed away from the spacecraft body on a boom. The team state that the magnetometers have a wide measurement range of ± 0.001 to $\pm 65536nT$. The level of noise in the sensors is much lower than recorded fluctuations in the IMF at $1AU$. On board systems clean up the data before onward transmission to the ground.

The data is available at a range of time intervals and we selected the one-minute data set.

Moment data

The Wind Solar Wind Experiment (SWE) is described in Ogilvie *et al.* [1995]. It comprises five integrated sensor/electronics boxes and a data processing unit. There are a pair of Faraday Cup analyzers which measure the velocity distribution measurements of the solar wind ions, two triaxial sets of electrostatic deflection analyzers known as VEIS which measure the velocity distribution

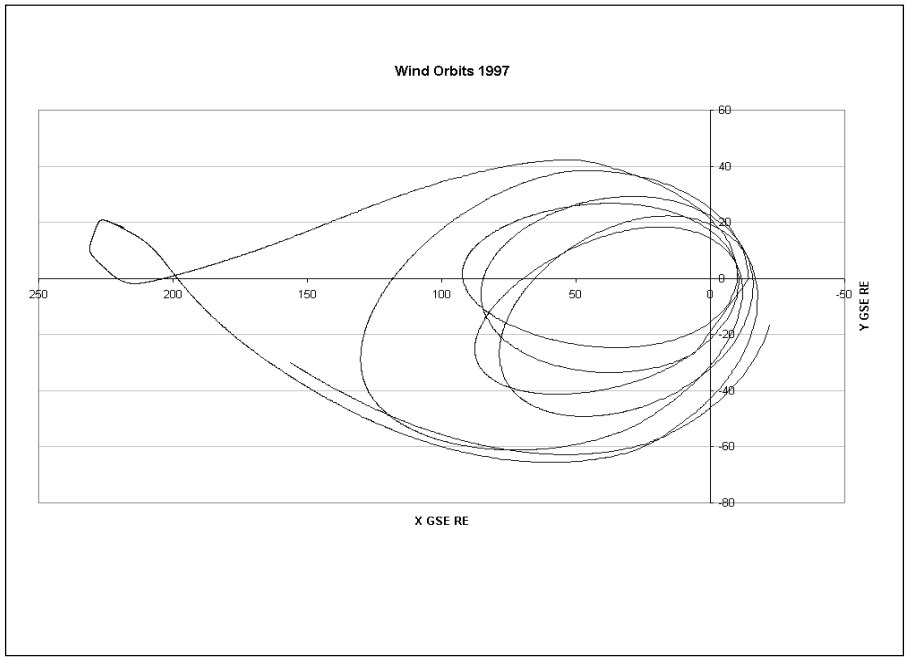

Figure 6.2: Plot constructed from downloaded data from CDAWeb showing the orbit of Wind for the year 1997 in the XY plane.

for ions and electrons in sub-Mach 1 plasmas, and a toroidal electrostatic analyzer functioning as a strahl (field-aligned energetic electrons from the Sun) sensor. The moment data are at irregular intervals of approximately 84 seconds though with quite a wide range.

6.3.3 Linking the Data

Data were downloaded in ASCII format and imported into MS-Access 97 for manipulation.

First, Wind magnetometer and moment data were linked. Next, Geotail moment data were linked to Wind data, and lastly, the Geotail magnetometer data were tied in. The aim was to form a unified set of Geotail and Wind data grouped at one minute intervals. One minute was chosen for two reasons, firstly it was the longest of the time-scales for the four different downloaded data sets, and secondly because this reduces some of the noise in the data. The chosen magnetometer data set was at one minute intervals. The moment data were interpolated to the same times. The linkage methods are described below.

Time Lagging - Linking the Geotail moment and Wind data

The idea behind linking these two data sets is that a way should be found of representing a plasma 'blob' as measured by Geotail within the magnetosheath and the same or an equivalent plasma blob measured at an earlier time upstream. A number of methods were considered, for example:

Petrinec *et al.* [1997] state that they advanced the Wind observation period at the solar wind convection speed in order to match the Geotail time frame. More detail was not given on how precisely this was done, though they also state that the solar wind speed for their time intervals was very steady so it is possible a single propagation speed was used for this.

In their work, Němeček *et al.* [2000b] using INTERBALL-1 measurements compared with Wind, lag Wind measurements of the IMF by propagation time using two-step interpolation. Again, precise details of how this was carried out were not given.

Crooker *et al.* [1981] in their investigations using ISEE-1 and ISEE-3 measurements use a comparison of the magnetic field components and their features in order to link the data. In their method, they adjust the time offset between the two plots in order to maximize the alignment of magnetic features.

However, as we were attempting to automate this process for a large quantity of data, we decided to assume that plasma travelled at the Wind-recorded X-speed (V_X) while in the interplanetary region down to the nearest whole R_e upstream to the Geotail measurement, and from that point to the actual Geotail location at the local X-speed. This is illustrated in Figure 6.3. This method may be a blend of the first two described above, though as neither paper specified precisely how they carried out their propagations it is difficult to be sure.

The detailed linking is as follows:

- Geotail moment data were gridded to the nearest whole R_e upstream in the X direction. E.g. if the X coordinate of the data point was at $9.3R_e$, it was gridded to $10R_e$. If at -$9.3R_e$, then -$9R_e$.
- The time taken for the plasma to travel from the gridded X to its actual X at the locally measured actual V_X was calculated.
- This time was deducted from the actual local time for the majority of cases where local V_X was negative and added for the extremely small number of cases within the useable intervals (see Section 6.4.2) showing positive V_X.
- The resulting time was gridded to the nearest minute.
- All Wind data for days relevant to the useable intervals was progressed from its local X coordinate to a range of gridded X coordinates from $15R_e$ down to -$23R_e$ at its local V_X and the times at the progressed locations were gridded to the nearest minute.
- Matching of the Geotail and Wind moment data on the gridded X coordinate and time at the grid was then carried out.
- This resulting data set was then binned by the Geotail moment measurement minute and the quantities averaged over each bin.

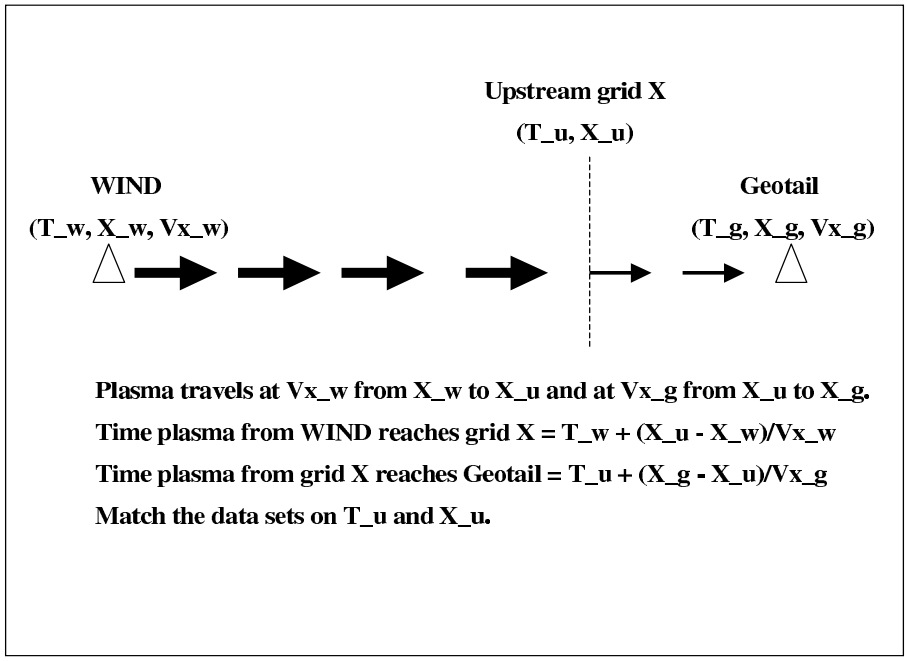

Figure 6.3: Showing how Geotail data are married to Wind data. For a particular Geotail measurement, we take Grid X to be the nearest whole R_e upstream, e.g. for Geotail at $X_g = -9.3R_E$, $X_u = -9R_E$, while if $X_g = +9.3R_E$, $X_u = +10R_E$. We assume that the plasma travels from Wind X_w to Grid X_u at the velocity V_{Xw} measured at Wind. We then assume that it travels at the (normally slower) V_{Xg} measured at Geotail for the last leg of its journey from Grid X_u to Geotail X_g. This is to make some allowance for the fact that generally the flow is slower in the magnetosheath than in the solar wind. Most cases in the literature (cited in the text) simply assume that the plasma travels at the X-component of the solar wind speed from the solar wind monitor to the magnetosheath monitor (here, this would be from X_w to X_g at V_{Xw}) making no allowance for slower speeds in the magnetosheath. We believe our method is a marginal improvement.

In order to demonstrate whether this linking was reasonable, we also linked data using two further methods, a crude linking where the time for plasma to flow from Wind to $15R_e$ at solar wind speed was added to the Wind time, and the time taken from Geotail to $15R_e$ at 85% of the average solar wind speed for the data set ($373kms^{-1}$) was deducted from the Geotail time, and the data binned to the minute at $15R_e$ for linking. The third method was to do nothing, and simply bin the Wind and Geotail data to the nearest minute and link those data sets. We plotted the ion flux (density·velocity) for both the solar wind and the magnetosheath and also correlation graphs between the two functions. Overall, the correlation for the interval data set is low (see Appendix E), with R-Sq (where R-Sq refers to $R^2 = \frac{\text{explained variation}}{\text{total variation}}$ x 100%) ~ 0.29 for the time-lagged data and R-Sq ~ 0.21 for the 'do nothing' data. Numerical correlation may be low because of internal processes in the magnetosheath which may affect the parameter values once the solar wind as passed through the bow shock. However, some qualitative correlation of

features should be visible as described earlier (see Section 6.3.3).

We show in Figure 6.4 the output for the interval of June 22nd to 23rd 1997. Geotail was traversing the dusk flank from bow shock to magnetopause. This interval is one of the highest numerically correlating intervals with the precise and more crude methods. In this particular case it is noted that the correlation is highest for the crude method and lowest for the precise method! A check of a selection of intervals shows that there is little to choose between the precise and crude methods, but that on the whole both are better than doing nothing. We propose to carry out the survey using the precise method as we believe it has a sound basis, though it may be useful to use one or both of the other methods at certain times.

Geotail magnetometer to linked Geotail moment / Wind data set

The Geotail magnetometer data were binned to the minutes and quantities averaged. This data set was then matched to the linked Geotail and Wind data set to form a single final data set grouped to the minute.

6.4 Intervals

In this section, we first discuss identification of boundary crossings at the magnetopause and the bow shock and secondly, the identification of likely interval candidates.

6.4.1 Identification of Crossings

Before suitable intervals for investigation can be chosen, it is necessary to establish how a boundary crossing may be identified within the data. There is no precise method for identifying a crossing, particularly of the magnetopause, as it is a layered structure. However, certain gross features may be noted. Figure 6.5 shows data for the days 5th and 6th March which has a crossing from interplanetary medium, through the bow shock, magnetosheath and magnetopause and into the magnetosphere. On 5th March, Geotail spends a 4 hour period in the interplanetary medium from around 14:30 - 18:30. It enters the magnetosheath at around 18:30 in the evening, traverses the magnetosheath and finally crosses the magnetopause at around 19:30 on the evening of the 6th March.

Magnetic Fields

In Figure 6.5(a), the magnetic field carried by the solar wind within the interplanetary medium varies over time, particularly in the B_Z direction. Once the plasma reaches the bow shock and crosses into the magnetosheath, then the shocked plasma becomes more turbulent and variability becomes much more pronounced. Within the magnetosphere, the B_Z component of the geomagnetic field is steadily northward and all the components of the magnetic field are reasonably steady, showing little variance.

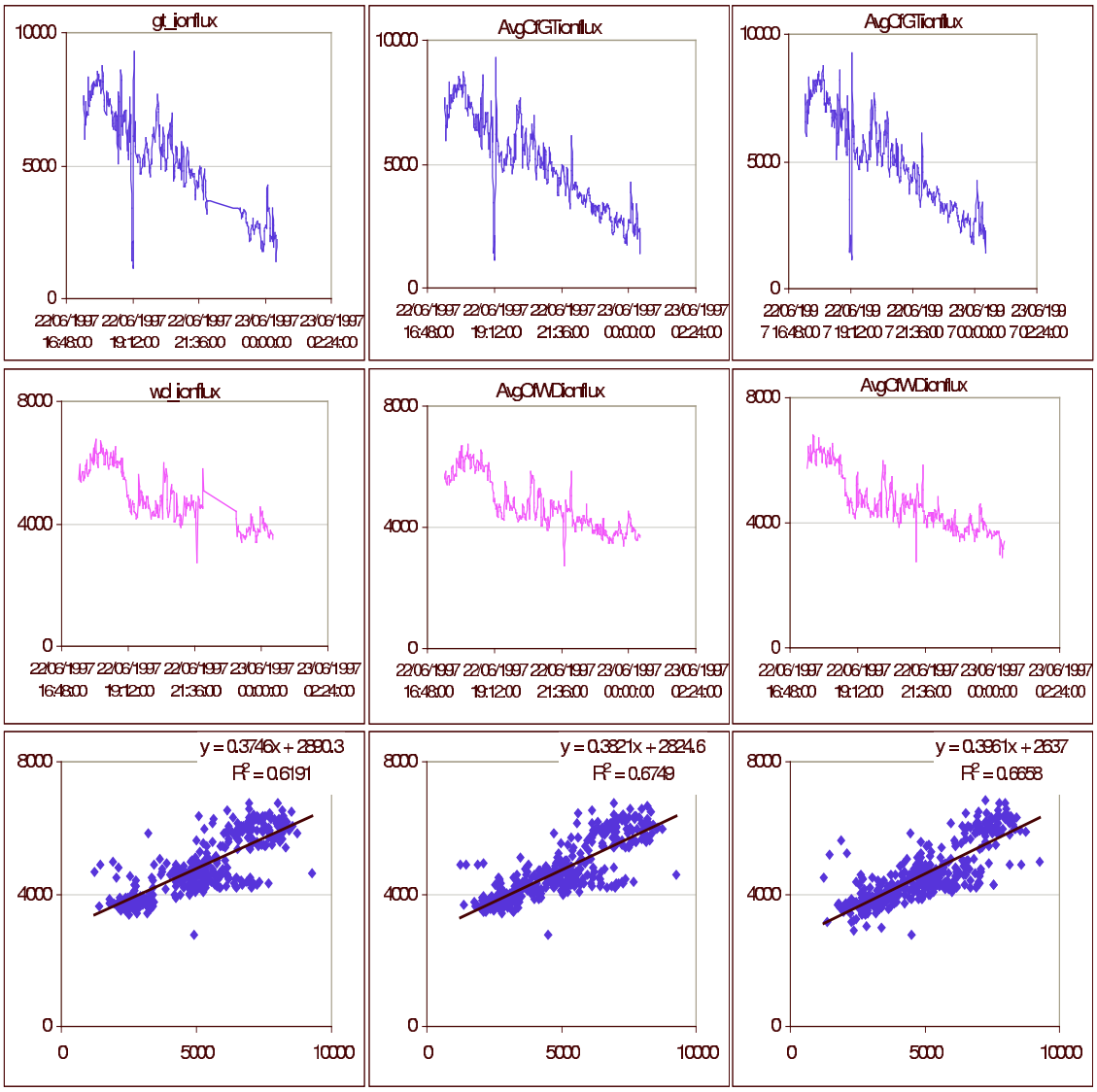

Figure 6.4: Ion flux correlation: Comparing linking methods for ion flux on the interval June 22nd-23rd 1997. The first column is the output from the 'precise' method detailed above. The second column is that from the 'crude' linking based on plasma times at $15R_e$, and the third column the 'do nothing' option where instantaneous transmission is assumed. The top row is the Geotail data, middle row Wind data and the bottom row is the correlation graph of Wind against Geotail data. It can be seen that there is a qualitative correlation between the two data sets.

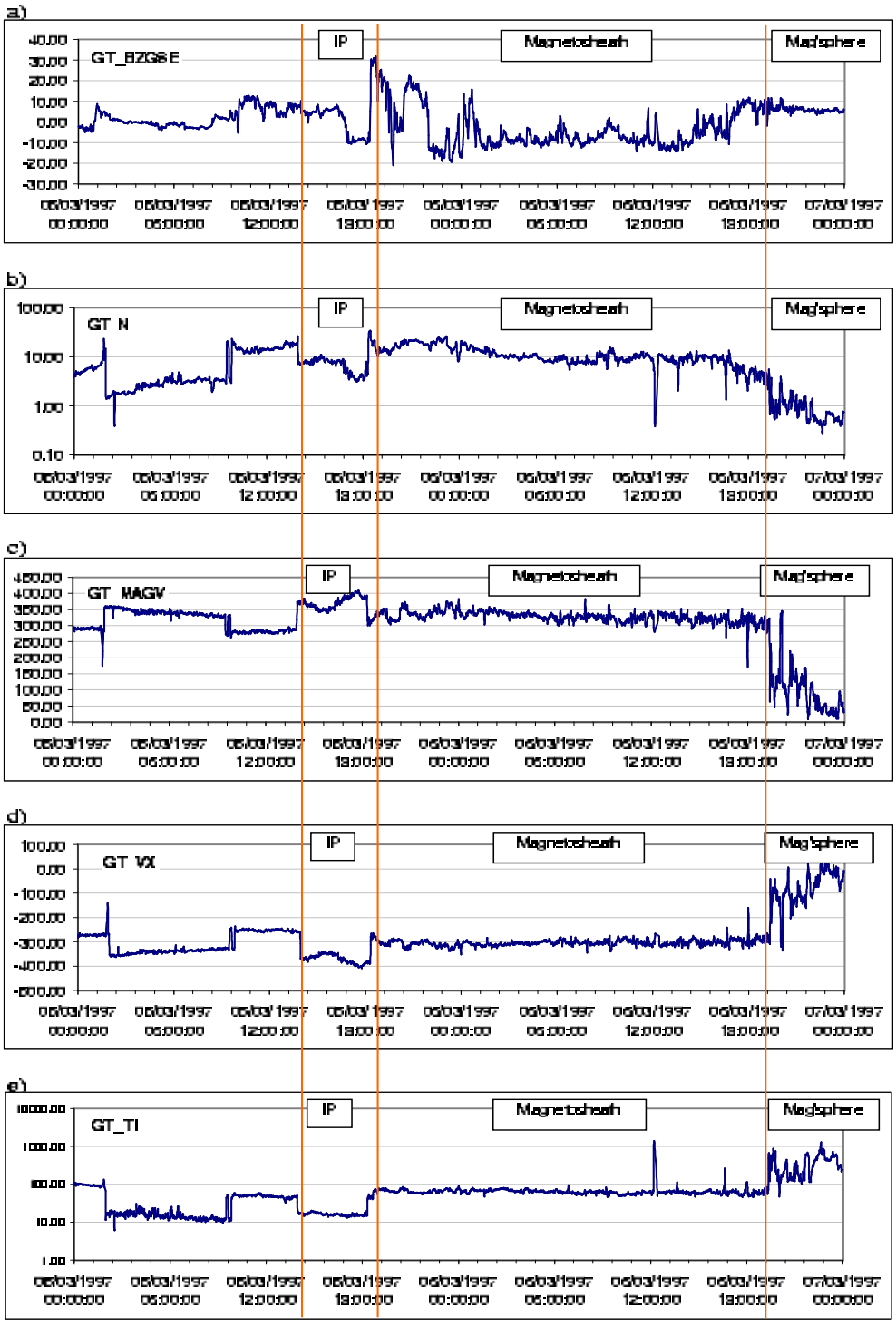

Figure 6.5: Geotail Data: Showing features of crossings of the bow shock and the magnetopause. The three orange vertical lines indicate, from left to right, a magnetosheath to interplanetary medium crossing through the bow shock, a reverse crossing again through the bow shock and lastly, a crossing from the magnetosheath to the magnetosphere across the magnetopause.

Proton Density

In Figure 6.5(b), the proton number density of the interplanetary medium is in the region of 1-10cm^{-3}. On reaching the bow shock, the plasma is compressed and thus the density shows an increase within the magnetosheath. In this example, the density drops through the magnetosheath and in the magnetosphere, plasma is of very low density and so a drop is shown upon crossing into that region.

Speed

The solar wind speed in the interplanetary medium varies continuously. Figure 6.5(c) shows how the speed is slowed by the bow shock but shows somewhat more variation. Within the magnetosphere the speed slows considerably.

V_X Component

Figure 6.5(d) shows how the V_X component varies. Again, within the interplanetary medium it varies continuously. Upon crossing into the magnetosheath the V_X component slows and in this example remains relatively steady until we reach the magnetopause where it drops. In this particular case, and for the dayside magnetopause, there is little difference between the speed and the magnitude of V_X. This is less true on the flanks.

Ion Temperature

The downloaded Geotail data consists of two components, Ti,YY and Ti,ZZ. For these investigations we have taken the average of the two, ie. (Ti,YY + Ti,ZZ)/2, as the ion temperature,Ti. The ion temperature in the interplanetary region, as shown in Figure 6.5(e) is low, of order 10-20eV. Compression at the bow shock leads to an increase in magnetosheath ion temperature to around 60-80eV. In the magnetosphere, ion temperature is still higher at 100s of eV. The temperature shows a clear jump at the bow shock and a more blurred but definite change at the magnetopause.

bow shock crossings

In summary, a crossing from the interplanetary medium through the bow shock to the magnetosheath may be characterized by:

- B_Z - greater variability.
- N - increases.
- V - slows and becomes more variable.
- Ti - increases by roughly order 10.

Magnetopause crossings

The characteristics of a magnetopause crossing from magnetosheath, through magnetopause to magnetosphere are:

- B_Z - becomes steadily northward.
- N - drops substantially.
- V - slows and becomes more variable. In the sub-solar region it should approach zero.
- Ti - increases and becomes more variable.

6.4.2 Interval Selection

We are interested in intervals which show a complete traversal of the magnetosheath, including a magnetopause and a bow shock crossing. Having identified 1997 as a suitable year where Geotail made numerous crossings in the region of interest, more detailed 4-day orbit plots were created on SSCLocator and examined in order to narrow down the time intervals for likely crossings.

Figure 6.6 shows that Geotail crosses the magnetosheath from magnetopause to bow shock in the latter part of the 4th March into the early hours of 5th March, appears to skim the bow shock, and then makes a longer crossing in the reverse direction from 5th March to 6th March. It is not possible to be more precise than this because the bow shock and magnetopause positions marked on the figure are model approximations. Additionally, the boundaries fluctuate continuously, and in particular, in this case, Geotail appears to skim the bow shock and so there are probably several crossings of the bow shock before the continuous traversal of the magnetosheath occurs.

Once likely days had been identified, the DARTS data plots for the relevant days were examined to narrow the time interval further.

In Figure 6.7 we see that the data shows the features of a traversal from magnetosphere through the magnetopause at around 19:00 on March 4th, and a crossing from magnetosheath through bow shock at around 02:00 on March 5th. On 5th March, it can also be seen that Geotail skims back through the bow shock into the magnetosheath between approximately 09:30 and 14:00 before re-entering finally at around 18:30 to complete the next traversal.

Once the broad time-scales of the data are established, it was imported into MS-Excel97 for deeper analysis. The interval can be further refined to try to establish exact times of crossings. As we are interested in magnetosheath plasma, we selected points which we believe represented plasma within the magnetosheath side of the boundaries. Figure 6.8 shows how the data can be refined to point-by-point detail.

In general, the ion temperature was used as the main selection criterion as it gave the cleanest distinction between regions. The other features were used for support and clarification where necessary.

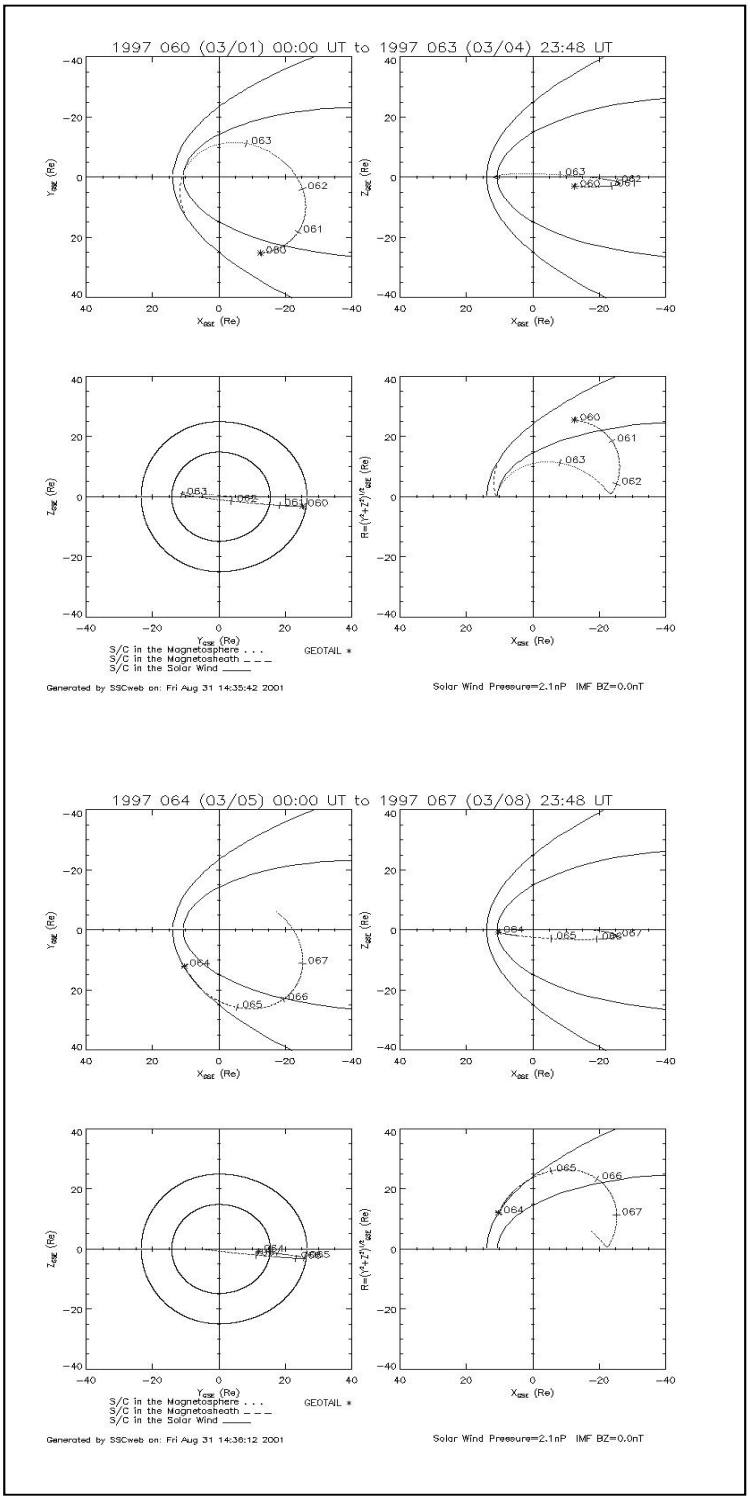

Figure 6.6: Two SSC Locator 4-day plots showing Geotail orbit for March 1st to 8th 1997. Geotail crosses the magnetopause sometime late on March 4th and traverses the magnetosheath, crossing the bow shock at around midnight. It then skims the bow shock before making a somewhat longer crossing back through the magnetosheath and through the magnetopause late on the 6th March.

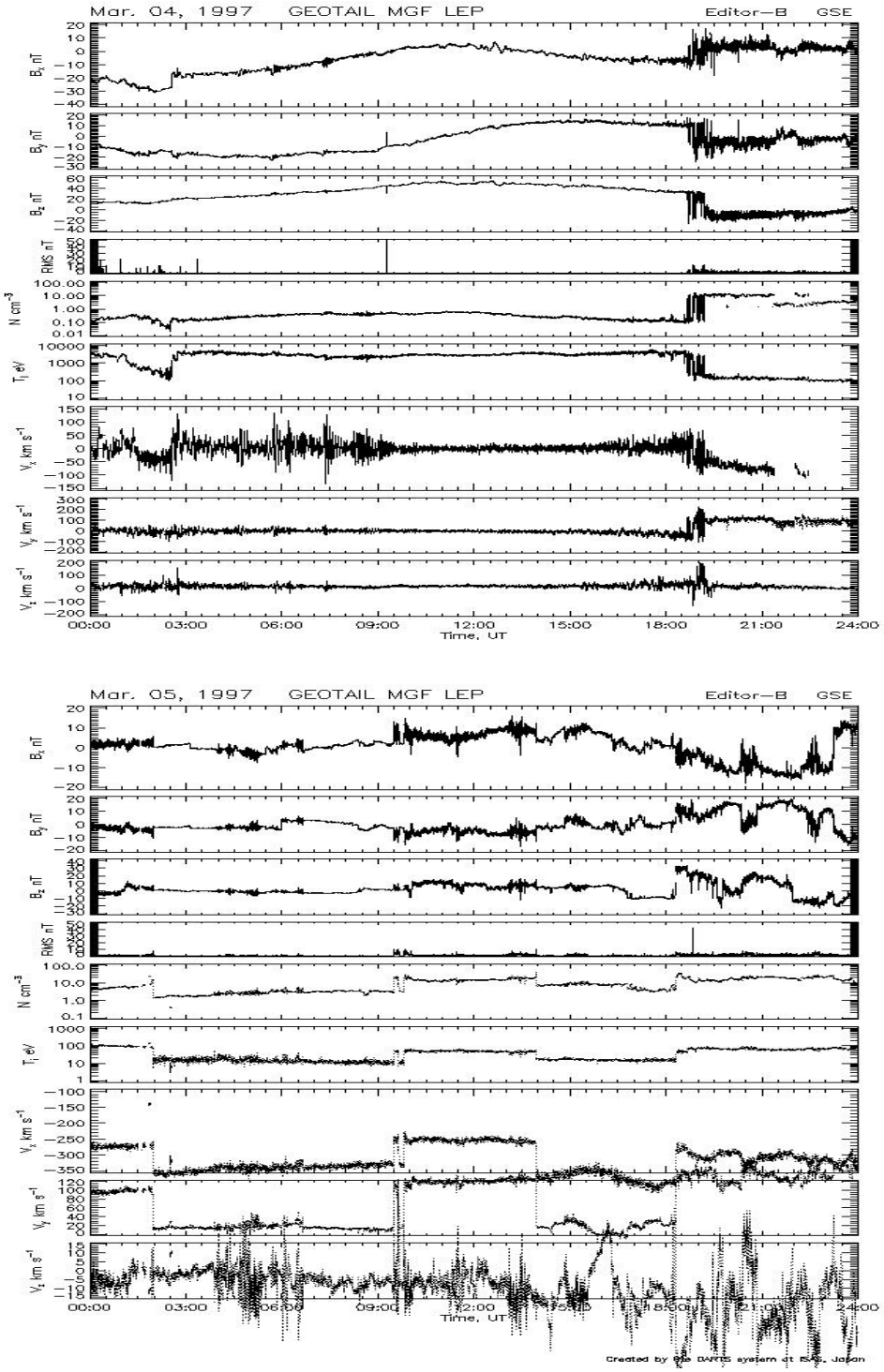

Figure 6.7: Showing the DARTS data plots for 4th and 5th March 1997. It is noted that the data shows the features of a traversal from magnetosphere through the magnetopause at around 19:00 on March 4th, and a crossing from magnetosheath through bow shock at around 02:00 on March 5th. On 5th March, it can also be seen that Geotail skims back through the bow shock into the magnetosheath between around 09:30 and 14:00 before re-entering finally at around 18:30 to complete the next traversal.

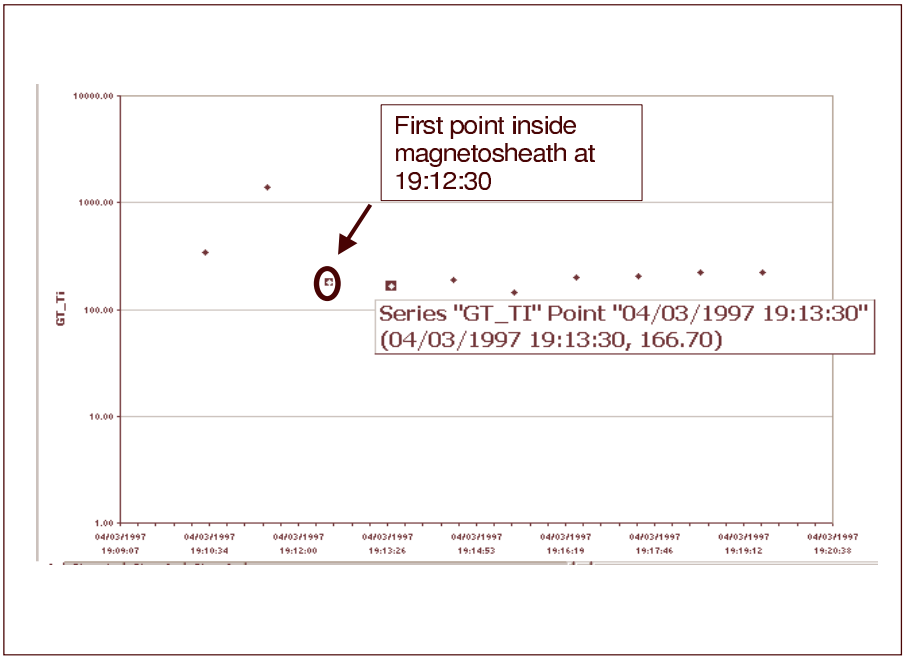

Figure 6.8: Showing the ion temperature data points immediately surrounding the magnetopause crossing from magnetosphere to magnetosheath. We selected 19:12:30 as being the first point inside the magnetosheath.

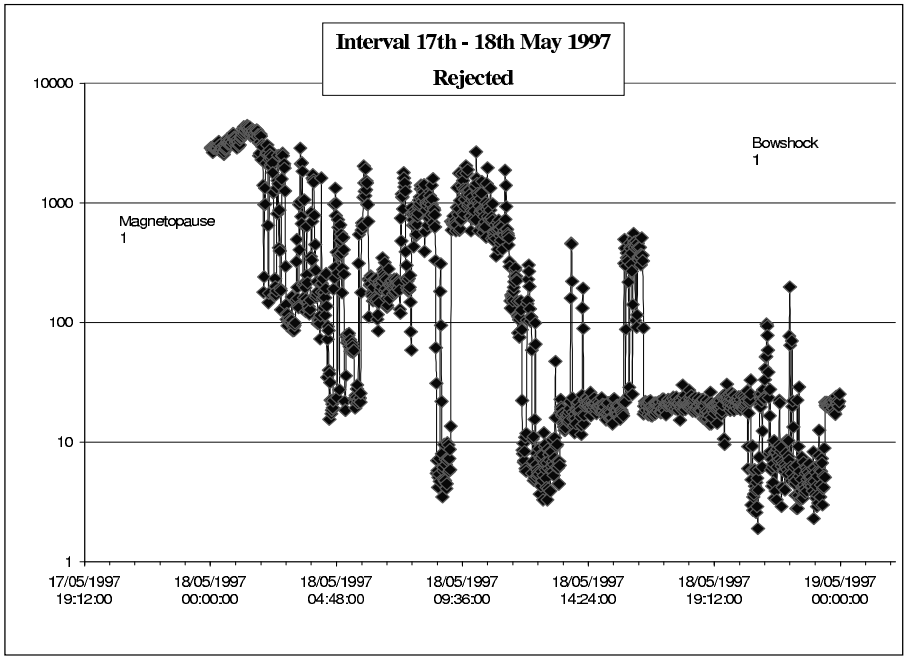

Figure 6.9: Rejected interval: Showing the interval from late 17th May to early hours of 19th May which was rejected because identificaton of crossing points was unclear, let alone the variability of data within the interval.

A number of potential intervals were discarded when the data showed too much variability to choose a crossing point, for example Figure 6.9, or where the data within an interval exhibited a great deal of variation. Additionally, some intervals were discarded when there was insufficient Wind data, particularly at the start and end of the intervals or where the Wind spacecraft was not in the solar wind. Data from a final 54 useable intervals was used and a total of 34 hours of minute-binned magnetosheath data remain. A list of these is given in Appendix D.

6.5 Comparison of Wind data with IMP8 data

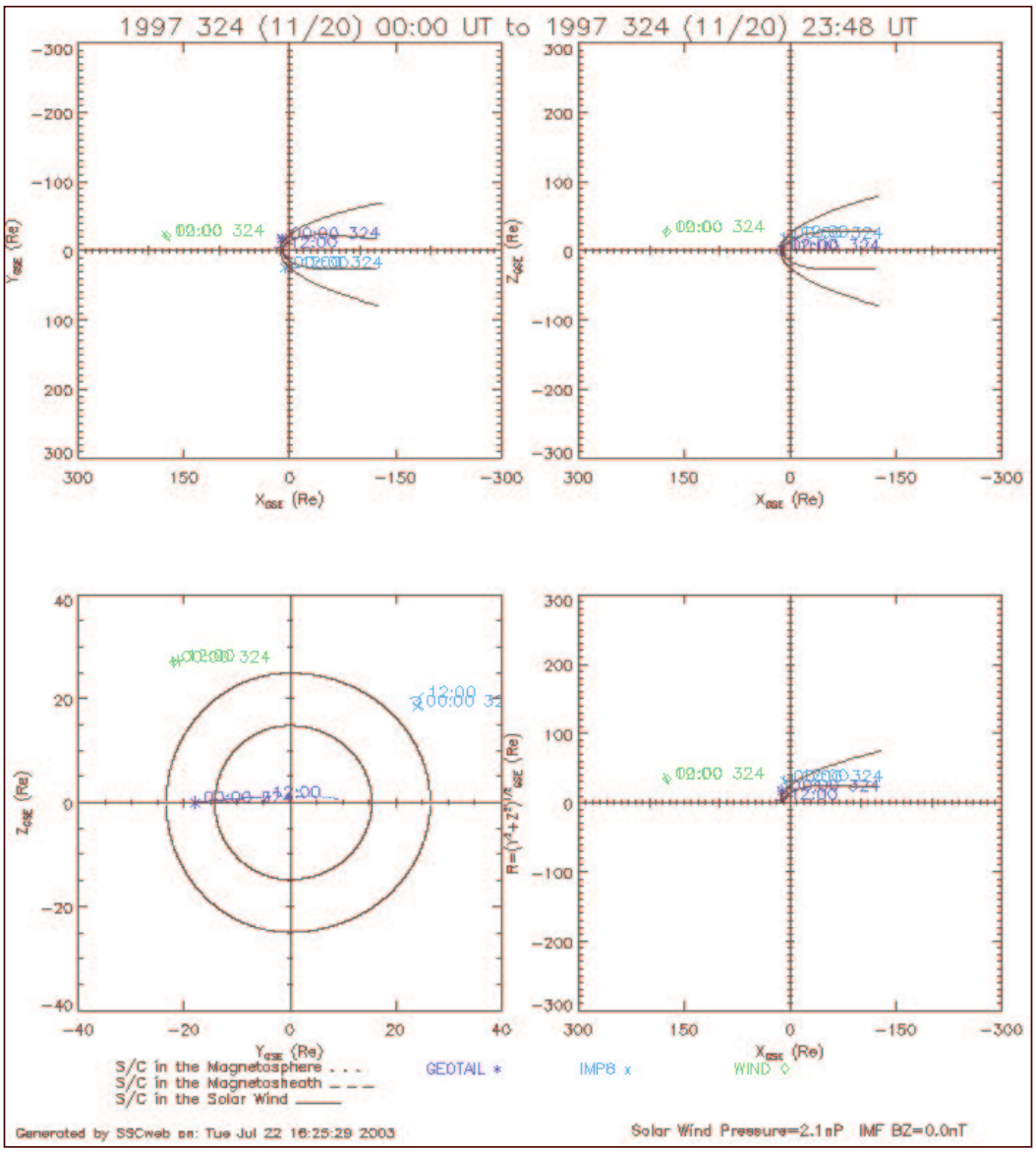

Figure 6.10: Comparison of Wind with IMP8: This figure from SSC Locator shows the relative positions of Wind (green), IMP8 (blue) and Geotail (violet) on March 20th 1997. IMP8 and Geotail are at approximately the same X, but IMP8 is in the solar wind and Geotail in the magnetosheath.

As a last test of reasonableness for using Wind as our solar wind monitor, we took three time intervals where IMP8 was at approximately the same X as Geotail, but in the solar wind as shown in Figure 6.10. The number density data from IMP8 is binned to the minute. We propagated the solar wind from Geotail to IMP8 using the method described in Section 6.3.3 and compared the results. From Figure 6.11 it can be seen that there is very good correspondence for two of the time intervals, the afternoon of March 20th and the time interval on November 20th. The IMP8 data for the morning of March 20th shows more variability than that of Wind, but has a similar average. We are satisfied, therefore, that using Wind data for number density measurements is reasonable.

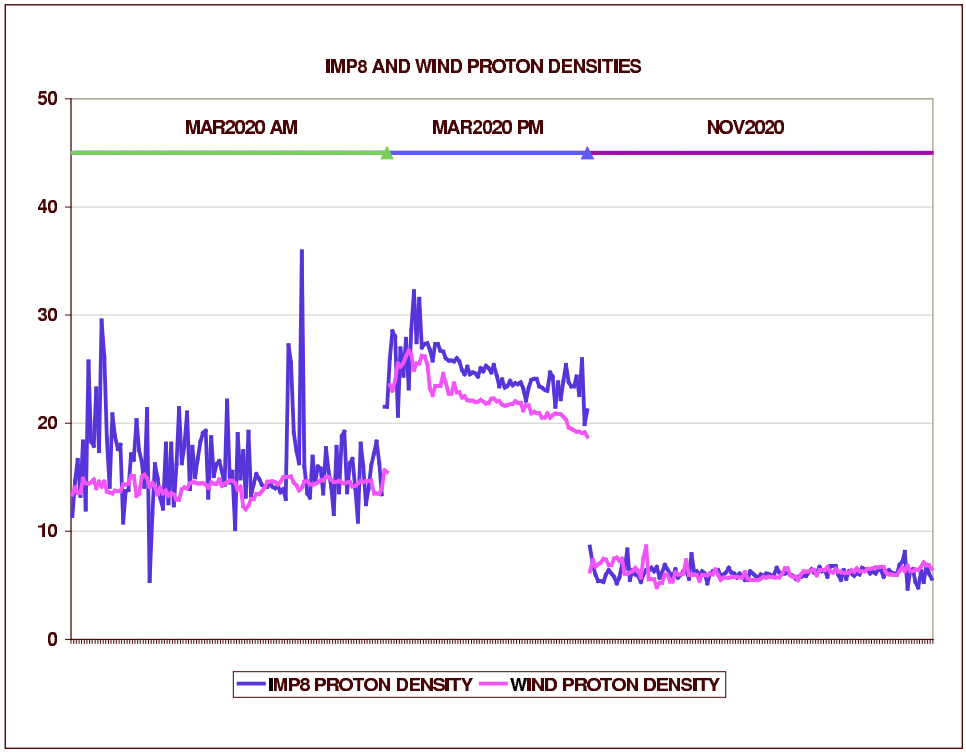

Figure 6.11: Comparison of Wind with IMP8: The figure compares the solar wind density at Wind with that propagated forward to IMP8 for two separate time spans on March 20th and a third time span on November 20th when IMP8 was also in a similar position relative to the other two spacecraft.

Chapter 7

Results

In this chapter we set out the results of our survey and compare them, where appropriate, with existing models, predictions, or other observations. We first present an overview of our results and follow this with two statistical investigations. In the first investigation (Section 7.3), we specifically compare our results with the predictions of S66. In the second (Section 7.4), we carry out a more detailed analysis of our data in order to identify whether there are any broad effects. We then suggest possible empirical models based on our results and compare their predictions with the existing models. Lastly, we compare the predicted locations for sub-Alfvénic flow using the existing and suggested new models.

7.1 General presentation of results

Throughout this discussion, X, Y and Z refer to GSE coordinates.

Data are binned to the nearest minute and quantities, including location, are averaged. Each location is normalized to the magnetopause stand-off distance, R_{mp}, calculated using Equation 5.8 and using the solar wind number density and velocity relevant to that minute. Our data is predominantly in the ecliptic plane thus we present our results on a scaled (GridX, GridY) space where GridX $= X/R_{mp}$ and GridY $= r/R_{mp}$ where $r = \sqrt{(Y^2 + Z^2)}$. From time to time we make use of the quantity Q (normalized radial distance) where Q $= \sqrt{(X^2 + Y^2 + Z^2)}/R_{mp}$.

For ease of comparison and reference, contour figures from S66 were transferred onto a grid. Between the sub-solar magnetopause and to just outside the sub-solar bow shock, i.e. 1.0 < GridX < 1.3, the grid was set at intervals of 0.05. Elsewhere it was set at intervals of 0.1. GridY was set at intervals of 0.1 throughout. If an actual contour line passed through the grid point, its value was noted, otherwise values were interpolated by comparison with the surrounding values. The results of the survey were similarly gridded, and the one-minute data values were further binned into the grid and quantities averaged.

Analysis was carried out using MS-Access 97, MS-Excel 97 or Minitab Version 13 as appropri-

ate.

7.2 Overview Results

Once we had removed data which had come from the Geotail 'SW' monitor (as advised by the DARTS team), and data which we were unable to link to suitable Wind data (either because it was missing or because Wind was not in the upstream solar wind), we were left with a total of 34 hours of data ranging over 54 intervals.

Figure 7.1 gives an overview of the locations and binned one-minute data counts included in each. The areas of the bubbles in this figure are proportional to the count. Small blue bubbles indicate only 1 or 2 minutes in the bin, the large red bubbles, over 100. It can be readily seen that we have a good quantity of data at the dayside and on the flanks, and somewhat less in the vicinity of the dawn-dusk meridian.

Figures 7.2 and 7.3 show the actual values of the speed, number density, ion (or mass) flux and magnetic field strength obtained in our survey. In the figures, the colours of the bubbles represent the values of the data while the area of the bubbles is proportional to $\sqrt{\text{count}}$ of minutes averaged into the bin.

No account has been taken here of the incoming solar wind values. There are some general features evident in the figures: slower speeds are found in the sub-solar region and higher speeds downtail. The reverse is true for the number density where we find higher densities in the subsolar magnetosheath and lower densities downtail.

The ion flux is simply the product of the speed and the number density (with units $\#cm^{-3}kms^{-1}$) and we may expect, therefore, a relatively even spread (high speed · low density moving to low speed · high density), possibly with a peak value somewhere in the middle. We see higher values on the dayside and lower on the flanks, with a peak at $X \sim 0$.

Lastly, we see higher magnetic fields concentrated on the dayside, but fairly constant values of 10-20nT downtail of the dawn-dusk meridian.

In the actual data, therefore, we do see some indication that the data set exhibits the gross features of gas dynamic flow around an obstacle.

In the next section, we consider in more detail how our results compare with S66 and in the following section, we look at our results in more detail.

7.3 Investigation 1 - Comparison of Results with S66

In this section, we normalize the data to the incoming solar wind values. Our grid of the S66 model covers $X/R_{MP} \geq -1$ and we have confined our comparison to actual data from the same region. For each of the ratios of velocity, density and mass flux, we show first our actual ratios and describe their features. Next we show the S66 model and describe its general features. Next,

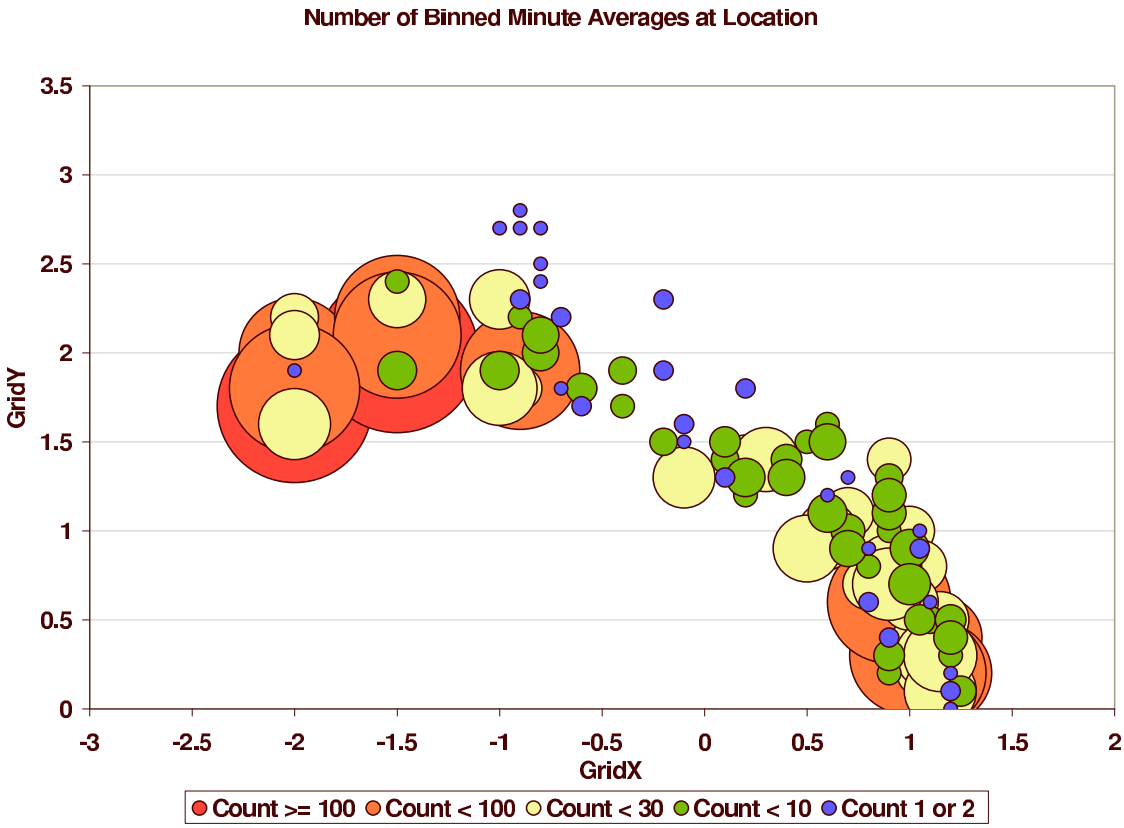

Figure 7.1: Showing the range of locations and number of minutes of data at each grid point for our survey. GridX is X/R_{mp} and GridY is r/R_{mp}. The area of the bubbles here is proportional to the count. For example the smallest blue bubbles represent 1 minute in the bin, and the largest red one represents 136 minutes in the bin.

we display the S66 and our actual results on the same grid. Lastly, for each ratio, we do a more detailed analysis including some regression analysis and t-tests on the model and actual ratios to assess whether the values are statistically different. In Appendix E we describe a number of the tests that we use.

The ratios are defined as follows: velocity ratio = V_{ms}/V_{∞}, density ratio = N_{ms}/N_{∞}, ion (mass) flux ratio = $N_{ms}V_{ms}/N_{\infty}V_{\infty}$ and magnetic field ratio = B_{ms}/B_{∞} where the subscript ms indicates the magnetosheath parameters, either derived from the S66 models or as measured at Geotail as appropriate.

Throughout, we have used the S66 models which assumed M_{∞}= 8 and $\gamma = 5/3$. For our data sample we calculated the sonic Mach number to lie in the range 6.7 to 10.5 (see Section 7.5 for how we calculated the sound speed), with a mean of 7.6 and median of 7.4. Our calculated γ varied very widely.

The actual magnetic field ratio is included at the end of this section. However, as it is not specifically addressed in S66, we compare it to the KF94 model used earlier in this work (Chapter 3.6.1).

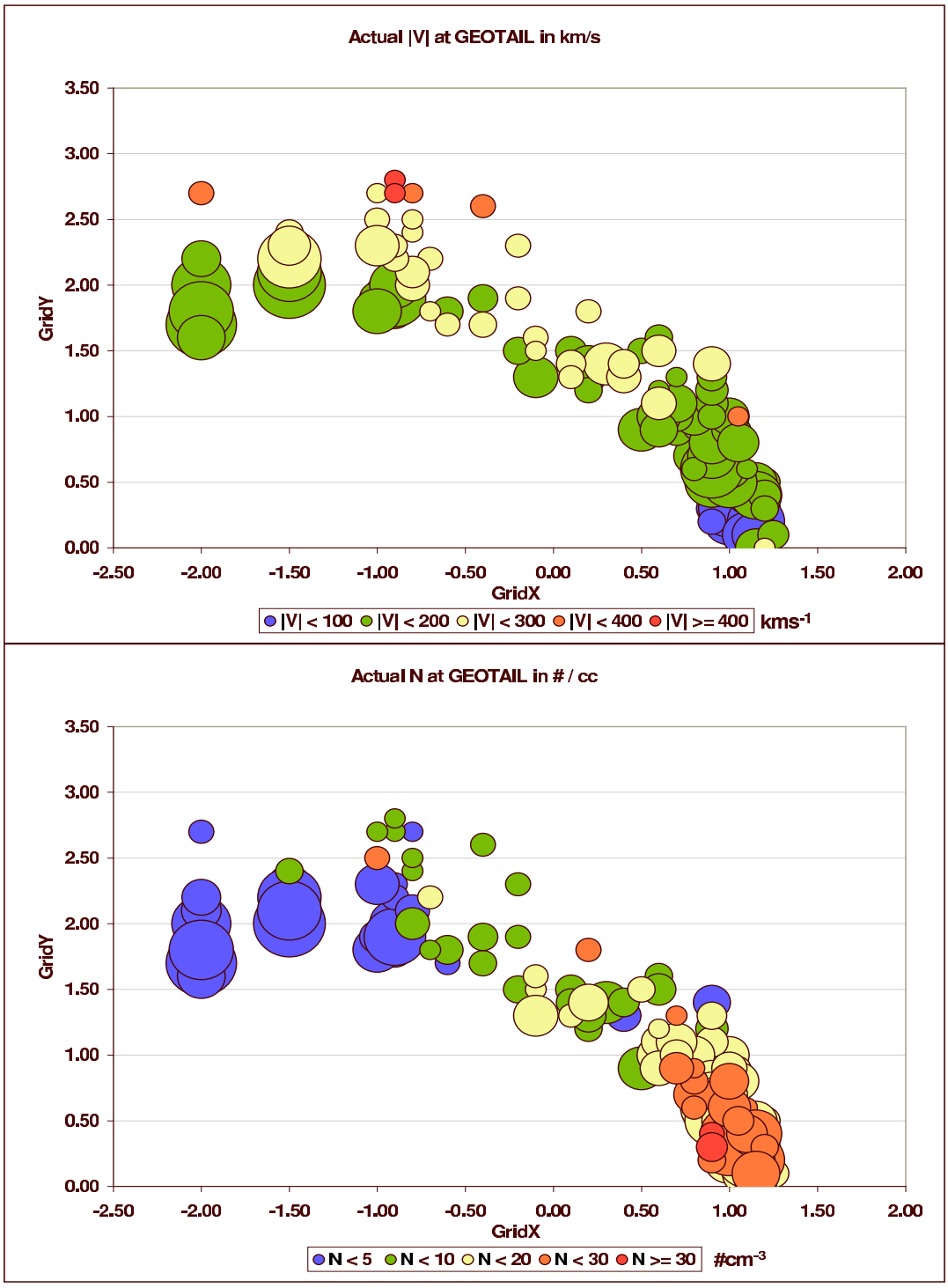

Figure 7.2: Overview of results from our survey. The top figure shows the actual speed and the lower figure that of number density which we obtained, binned into the grid. In these figures, the area of the bubbles is proportional to the $\sqrt{\text{count}}$ of minutes in the grid point. For example, in the top figure, the small orange bubble near (-0.5,2.5) means that a small amount of data were binned into the grid point and its average velocity was between $300 kms^{-1}$ and $400 kms^{-1}$.

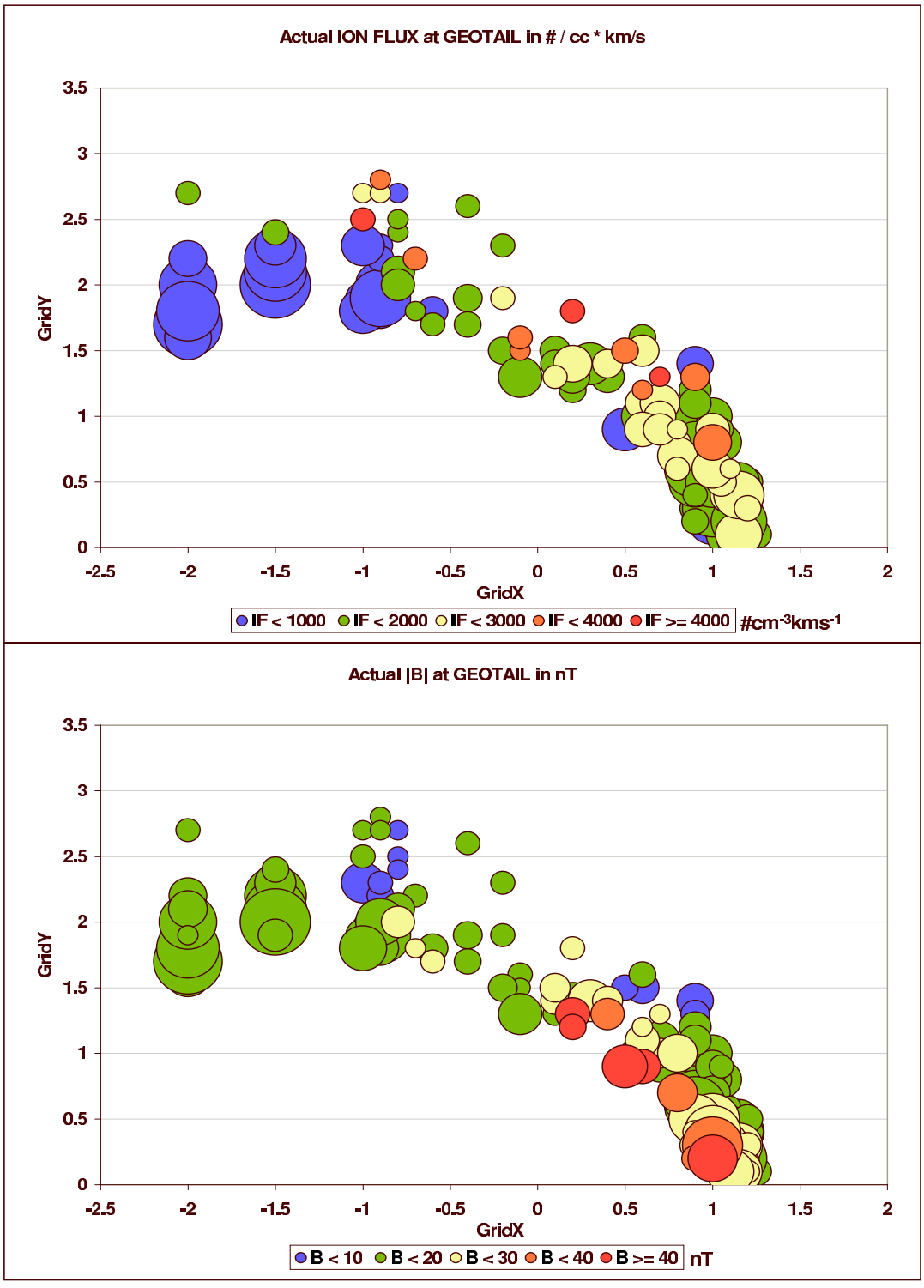

Figure 7.3: Overview of results from our survey. The top figure shows the actual ion flux (calculated as velocity · number density) and the lower figure that of the magnetic field intensity which we obtained, binned into the grid. In these figures, the area of the bubbles is proportional to the $\sqrt{\text{count}}$ of minutes in the grid point.

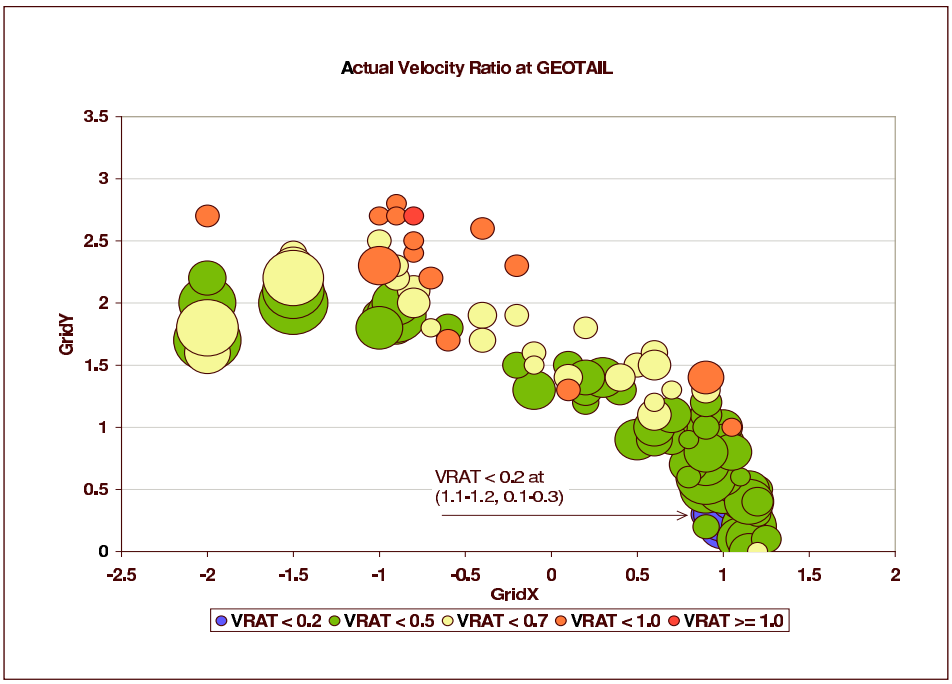

Figure 7.4: Shows the ratio of actual velocity at Geotail in the magnetosheath to that at Wind in the solar wind, lagged as described in the text. The bubble areas are proportional to the $\sqrt{\text{count}}$ of minutes binned in to the grid point.

7.3.1 The Velocity Ratio

Figure 7.4 shows the actual values of the velocity ratio which we obtained from our data. We see lower ratios on the dayside, and the lowest (< 0.2) at grid references (1.1-1.2,0.1-0.3).

S66 Velocity Ratio

Figure 7.5 shows the contours for the velocity and temperature (as ratios of the upstream values, subscripted ∞) for hydromagnetic flow around the magnetosphere as presented in S66.

The model has the following features: The solar wind speed slows on crossing the bow shock (hence a velocity ratio of less than 1). Within the magnetosheath, as we move tailwards there is an acceleration of the flow. Additionally, there is a gradient in the flow in the radial (GridY) direction with speeds just inside the bow shock being higher than those at the magnetopause for a given value of GridX. The position changes a little as we approach GridX $\sim$ -1.0 where the speeds are slower in the centre of the magnetosheath (again in the radial direction for given GridX). There is also slowing along the sub-solar stagnation line leading to a stagnation point at the sub-solar point of the magnetopause.

Comparison of Survey Velocity Ratio with S66

We see that our survey data does show the same basic structure as that of the S66 model. However, our ratios do not seem to get as high as the model predictions. There is also evidence of a stagnation

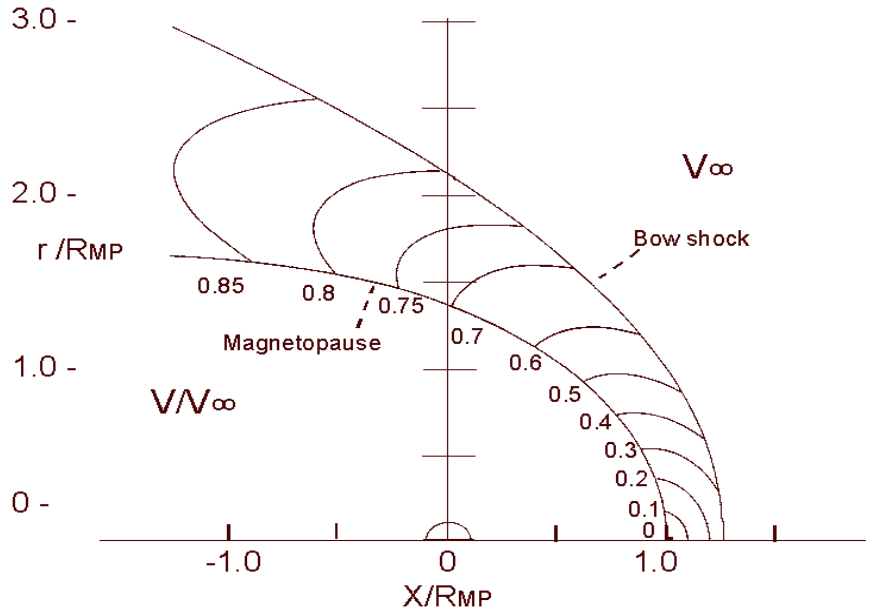

Figure 7.5: Velocity contours for supersonic flow past the magnetosphere for $M_\infty = 8$ and $\gamma = \frac{5}{3}$ adapted from Spreiter *et al.* [1966] (S66)

point or line (see Section 7.5.3). In addition to 'by the eye' comparisons between the figures, we also conducted a number of statistical tests (see Appendix E) to further assess whether the data from the survey is genuinely different from that of the model.

We performed a paired t-test on the model and actual data to see how the ranges of data compared statistically. While the box plot (Figure 7.6) appears to show broad similarity between the two data sets, the median is somewhat lower for the actual data and the paired t-test suggests that there is a statistically significant difference between the two in terms of their means.

The top two plots in Figure 7.7 shows how the model velocity ratio varies with projection on to the GridX axis and the GridY axis respectively. The lower plots show how our data compares for the same grid values. In the GridX direction, we see that the model predicts an increase in the velocity ratio as GridX decreases and GridY increases. Regression using a quadratic polynomial shows that the model values for velocity ratio are very well predicted by the values of GridX and GridY.

The gross features are exhibited in our actual data with the velocity ratio increasing as GridX decreases, and increasing as GridY increases. However, the fitting of quadratic polynomials in GridX and GridY respectively is rather less good that for the model. A very marginally improved result was obtained by using a model containing both $(\text{GridX})^2$ and GridY (not shown). The increase in the velocity ratio as GridX decreases is lower than that predicted by S66. GridY dependence is also much shallower in the actual data.

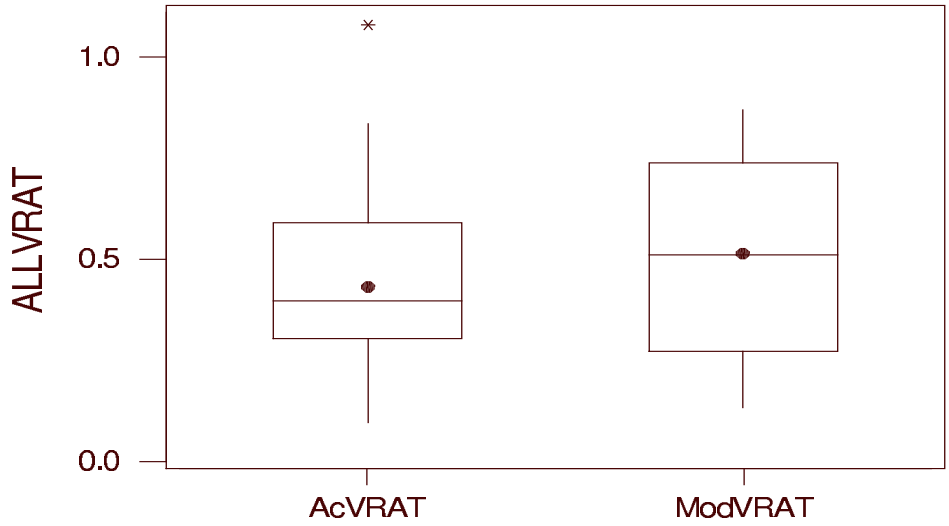

Figure 7.6: Compares the range of velocity ratios in the actual survey data and the model data (set on the same grid). The boxes show the 25th - 75th percentile range and the line in the box shows the median value. A * indicates an outlier. The dot indicates the location of the mean of the data sample. The range of values in the survey is broadly similar to but showing less variation and a slightly lower mean than that of the model. The paired t-test, however, suggests statistically significant differences between the means of the two data sets.

7.3.2 The Density Ratio

Figure 7.8 shows the actual values of the density ratio which we obtained from our data. The actual density ratio is highest on the dayside, especially in the sub-solar region, and lowest on the flanks.

S66 Density Ratio

Figure 7.9 shows the contours for the number density (as a ratio of the upstream value, subscripted ∞) for hydromagnetic flow around the magnetosphere as presented in S66.

Higher density ratios are concentrated in the sub-solar region, with the stagnation line (GridY = 0) showing a rising profile as we move in toward the sub-solar point where the density ratio reaches a maximum value of 4.23. As we move in the anti-Sun direction to around GridX $\sim$ 0.8, the profile changes from one which increases through the magnetosheath from bow shock to magnetopause to one which decreases. Likewise, the radial profile also changes. In the sub-solar region it decreases as GridY increases, but from the same GridX as mentioned previously, it changes to a profile where density ratio increases as GridY increases.

Comparison of Survey Number Density Ratio with S66

Again, we see that the actual data exhibits similar features to S66. However, our density ratios are lower, particularly on the flanks. As both our velocity and density ratios are lower than predicted by S66, the question of flux conservation is raised. We discuss this further in Section 7.3.6.

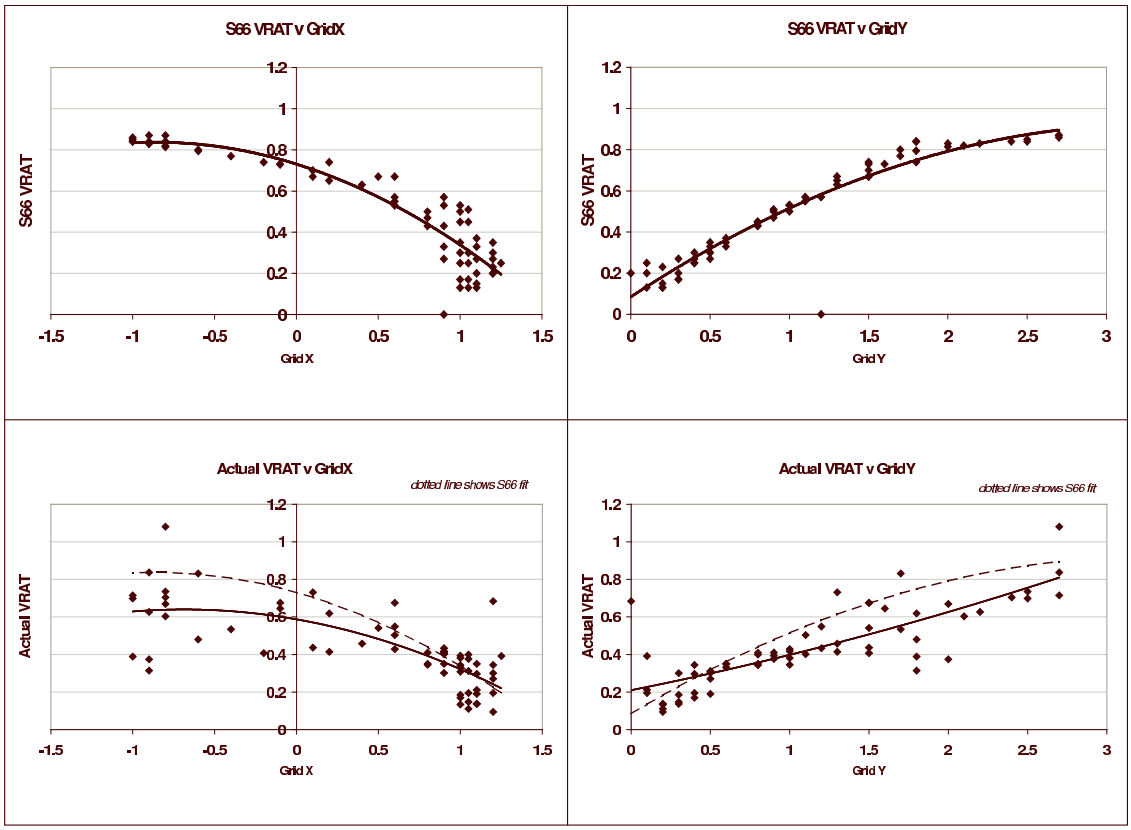

Figure 7.7: The top two figures show the variation of the velocity ratio projected onto GridX and GridY predicted by S66. We have fitted a quadratic regression equation to the predictions and obtain a good level of fit, particularly with GridY. The bottom figures compare our actual survey data for the same grid locations. The dotted lines in the lower plots show the relevant fit for the S66 values. Quadratic fits to the data involving only GridX and GridY terms were less good than for the model.

As with the velocity ratio, we performed a paired t-test on the model and actual data to see how the ranges of data compared. While the box plot (Figure 7.10) shows some overlap betwen the data ranges, the actual density ratio appears to be lower than that that predicted by the model. The paired t-test bears this out with a statistically significant difference between the two data sets.

The top two plots in Figure 7.11 shows how the model number density ratio varies with GridX and GridY respectively while the lower plots show our real data.

The model data shows density ratio decreasing as GridX decreases but with a flip up as GridX approaches -1.0. It also shows a decrease in density ratio as GridY decreases, again with an upturn as GridY approaches 2.5. Our real data shows the same general features apart from the size of the increases in the region (-1.0, 2.5).

In this case, we fitted cubic regression equations to the plots. The fits were reasonably good, giving R-Sq and R-Sq(adj) (see Appendix E) above or near the minimum 70% desirable for physical data. We were able to improve the regression equation for the model ratio by including both

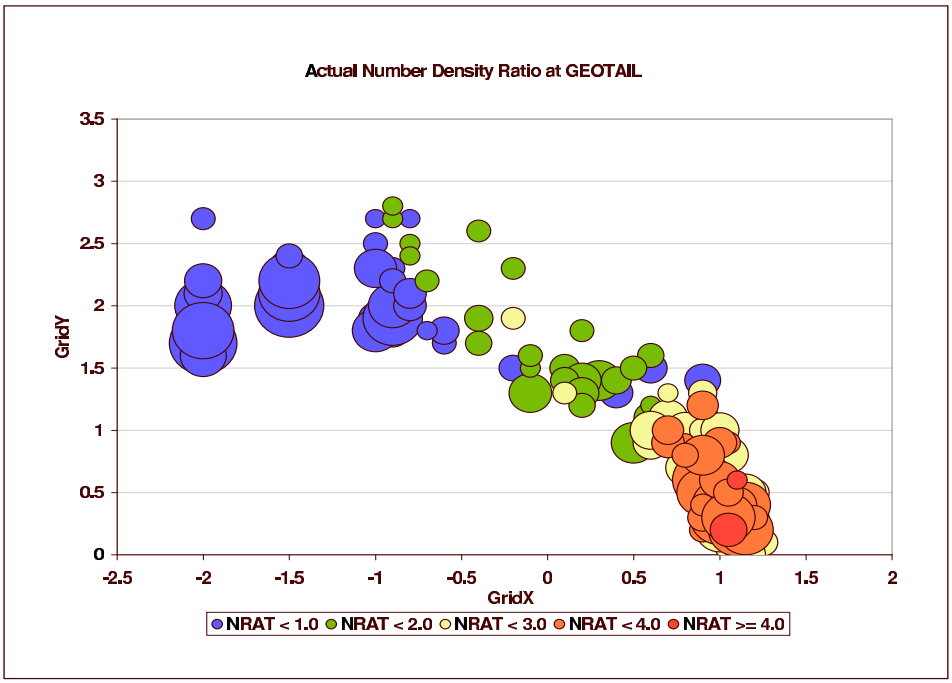

Figure 7.8: Shows the actual number density ratio at Geotail when compared with Wind data, lagged as described in the text. The bubble areas are proportional to the $\sqrt{\text{count}}$ of minutes binned in to the grid point.

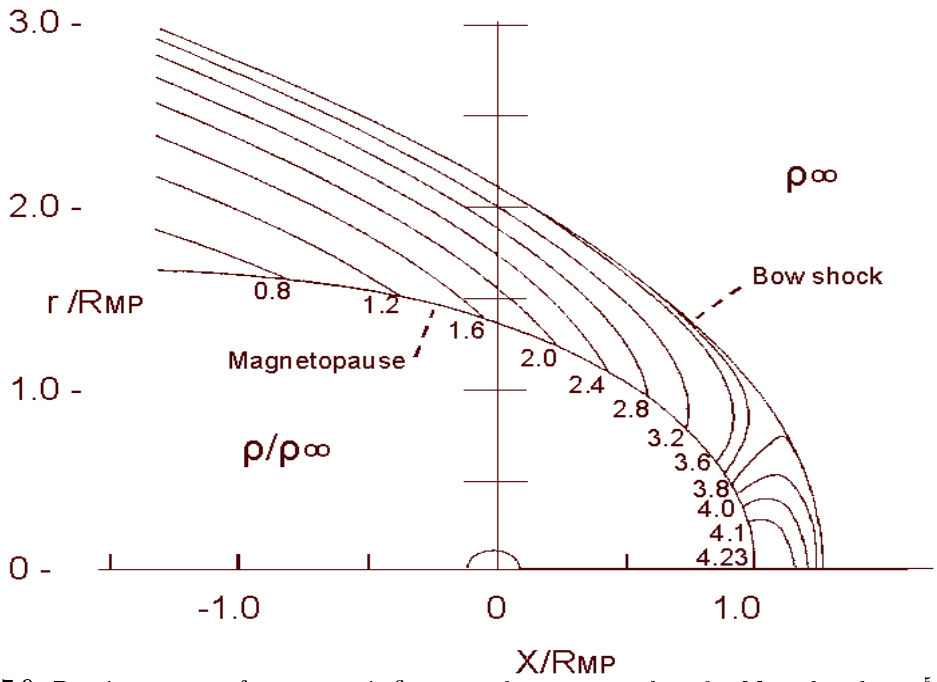

Figure 7.9: Density contours for supersonic flow past the magnetosphere for $M_\infty = 8$ and $\gamma = \frac{5}{3}$. Adapted from Spreiter *et al.* [1966] (S66)

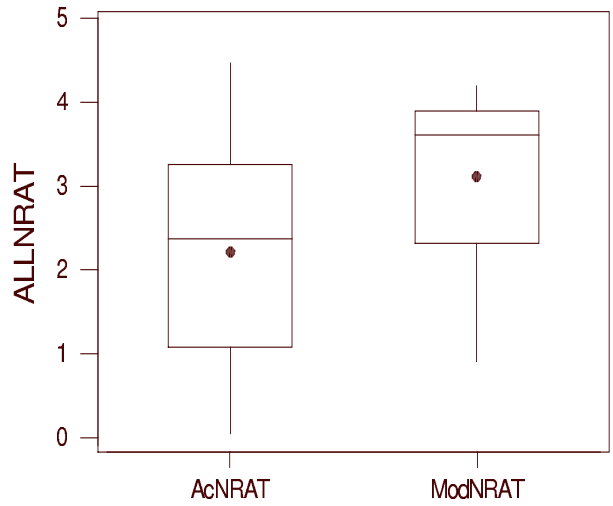

Figure 7.10: Compares the range of number density ratios in the actual survey data and the model data (on the same grid). The range of values in the survey is broadly similar (though lower) but showing greater variation than that of the model. The paired t-test revealed statistically significant differences between the means of the two data sets.

GridX, GridY and their squares and cubes to achieve an R-Sq and R-Sq(adj) of 97.6% and 97.4% respectively, however no such improvement was discerned for the real data.

7.3.3 The Mass Flux Ratio

Figure 7.12 shows the actual values of the mass flux ratio which we obtained from our data. Here we find higher ratios on the dayside and lower on the flanks. There is a peak at $X \sim 0.5$.

S66 Mass Flux Ratio

Figure 7.13 shows the contours for the mass flux (as a ratio of the upstream value, subscripted ∞) for hydromagnetic flow around the magnetosphere as presented in S66.

The model predicts the lowest mass flux values are found in the sub-solar region with a decreasing stagnation line profile leading to zero mass flux at the sub-solar point. The radial profile for given GridX is increasing for all values of GridX. However, as GridX decreases, the magnetopause values show an increase until we reach GridX ~ 0.5, and a decrease for lower GridX.

Comparison of Survey Mass Flux Ratio with S66

Once more, the actual data supports the S66 predictions, though again, with lower values for the mass flux ratio.

As with the velocity ratio and density ratio, we performed a paired t-test on the model and actual data to see how the ranges of data compared. The mass flux ratio was calculated simply as the product of the velocity ratio and density ratio. The box plot (Figure 7.14) shows that the range of real values, while overlapping the model a little, is somewhat lower than predicted by the

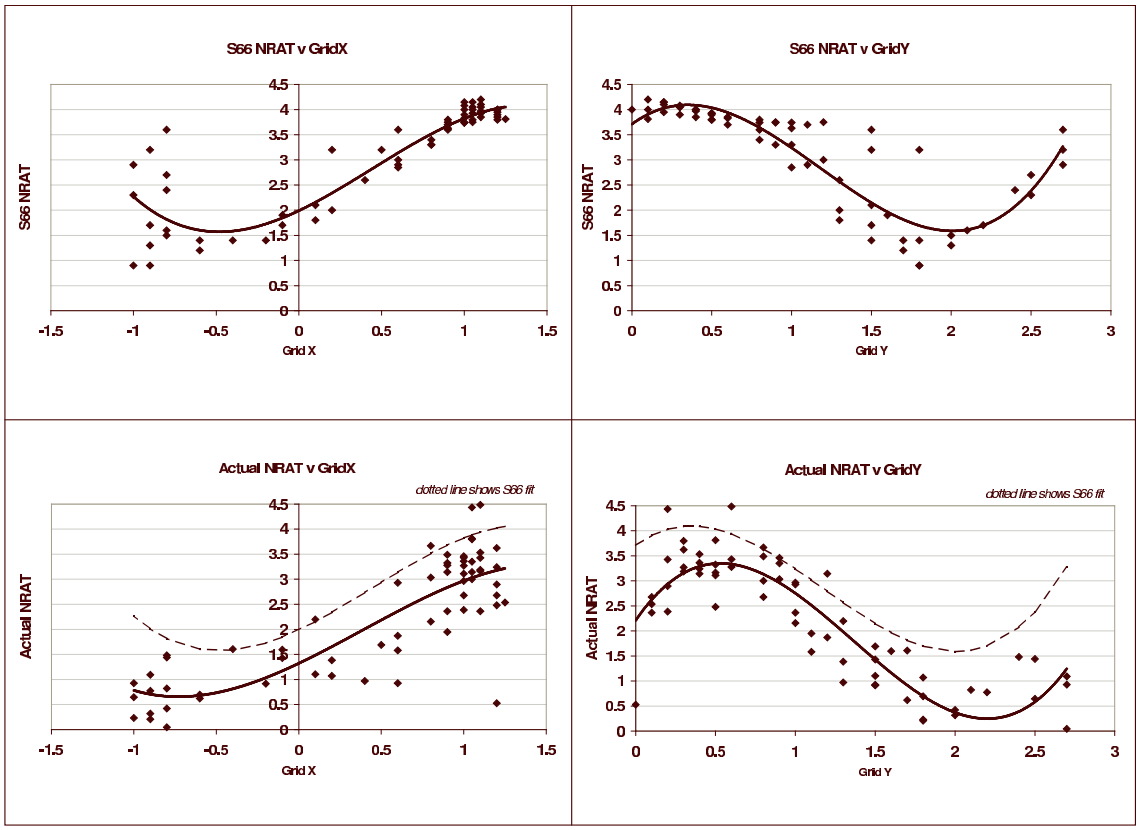

Figure 7.11: The top two figures show the variation of the density ratio with GridX and GridY predicted by S66. We have fitted a cubic regression equation to the predictions and obtain a reasonably good level of fit. The bottom figures compare our actual survey data for the same grid locations. The dotted lines in the lower plots show the relevant fits for the S66 values. The cubic fits to the data involving only GridX and GridY terms were not quite as good as for the model fits, but were nevertheless valuable.

model. It comes as little surprise, therefore, that the paired t-test shows a statistically significant difference between the two sets of data.

The top two plots in Figure 7.15 shows how the model mass flux ratio varies with GridX and GridY respectively while the lower plots show our real data.

The model shows a concentration of lower mass flux ratio in the sub-solar region, increasing as we move a little towards the Earth, say around GridX $\sim$ 0.75, but then dropping down until the final up turn at GridX $\sim$ -1.0. The ratio also shows an increase as GridY increases towards the Earth, but then this drops back a little for GridY $\sim$ 2.0 before again increasing.

The eye perceives some similarity between the model and actual results for both GridX and GridY. However, regression plots using only GridX or GridY and their squared and cubed values showed very low R-Sq and R-Sq(adj) and are probably therefore meaningless. A regression equation including all of the GridX, GridY and their squares and cubes terms did yield an improved prediction with R-Sq of 97.6% for the model, but for the actual data, the best achieved was 48.8%.

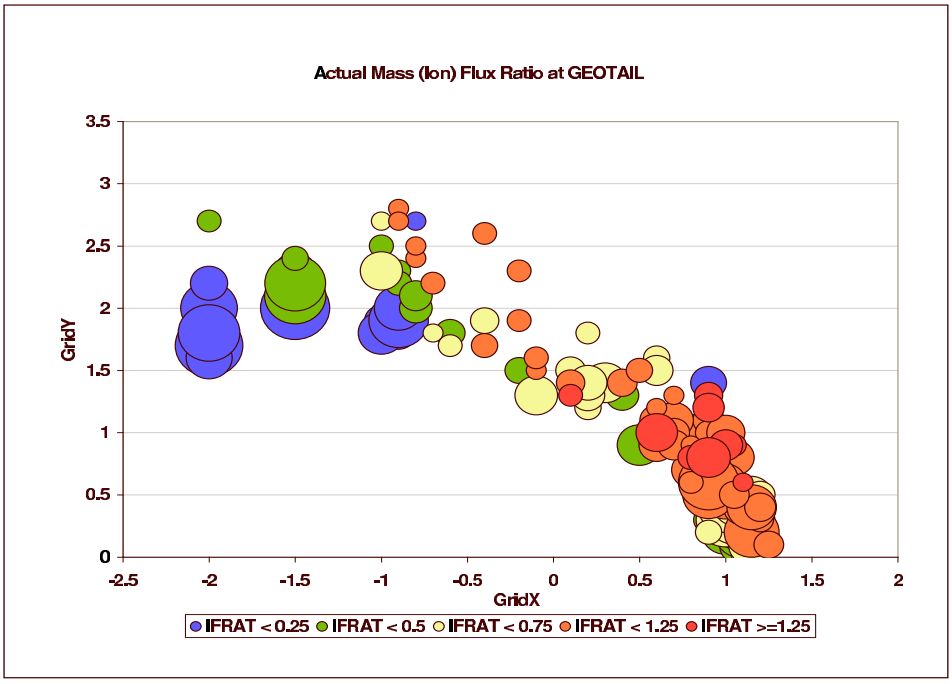

Figure 7.12: Shows the actual mass flux ratio at Geotail when compared with Wind data, lagged as described in the text. The bubble areas are proportional to the $\sqrt{\text{count}}$ of minutes binned in to the grid point.

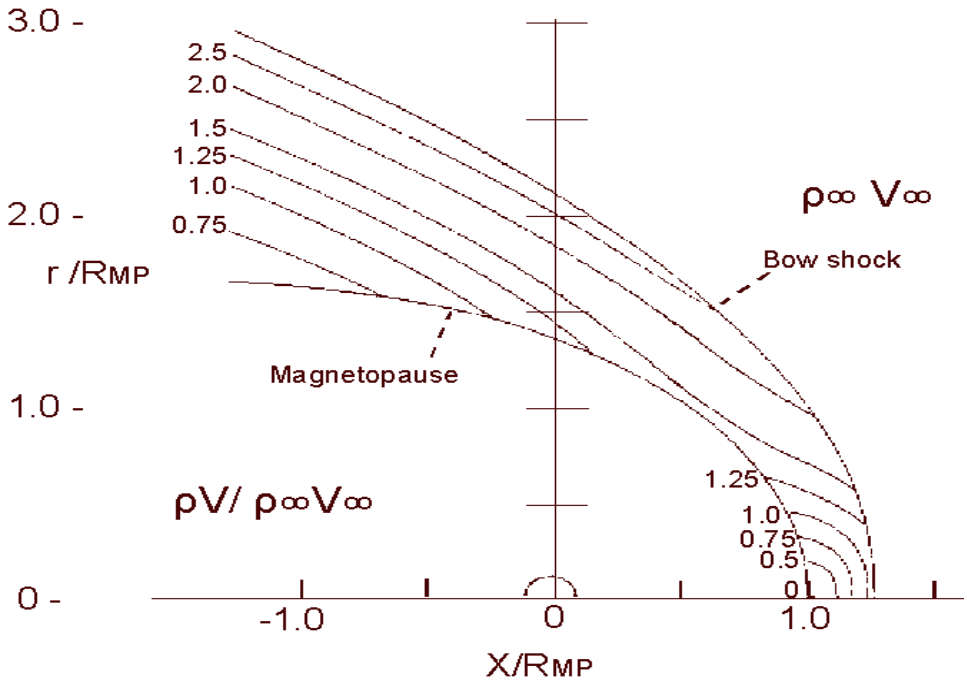

Figure 7.13: Mass flux contours for supersonic flow past the magnetosphere for $M_\infty = 8$ and $\gamma = \frac{5}{3}$ taken from Spreiter *et al.* [1966] (S66)

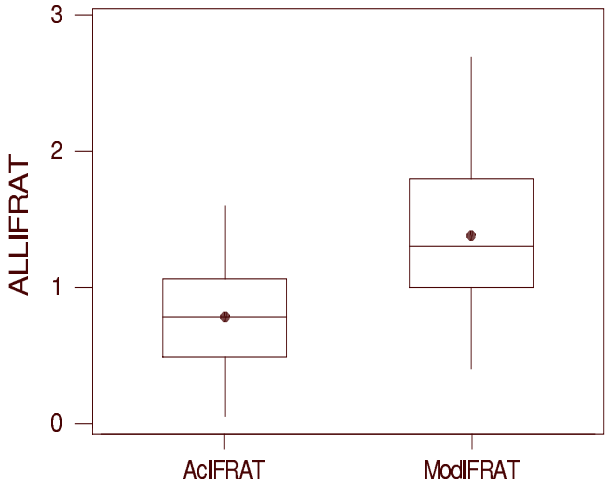

Figure 7.14: Compares the range of mass flux ratios in the actual survey data and the model data (on the same grid). The range of values in the survey is lower than that predicted by the model. The paired t-test revealed statistically significant differences between the means of the two data sets.

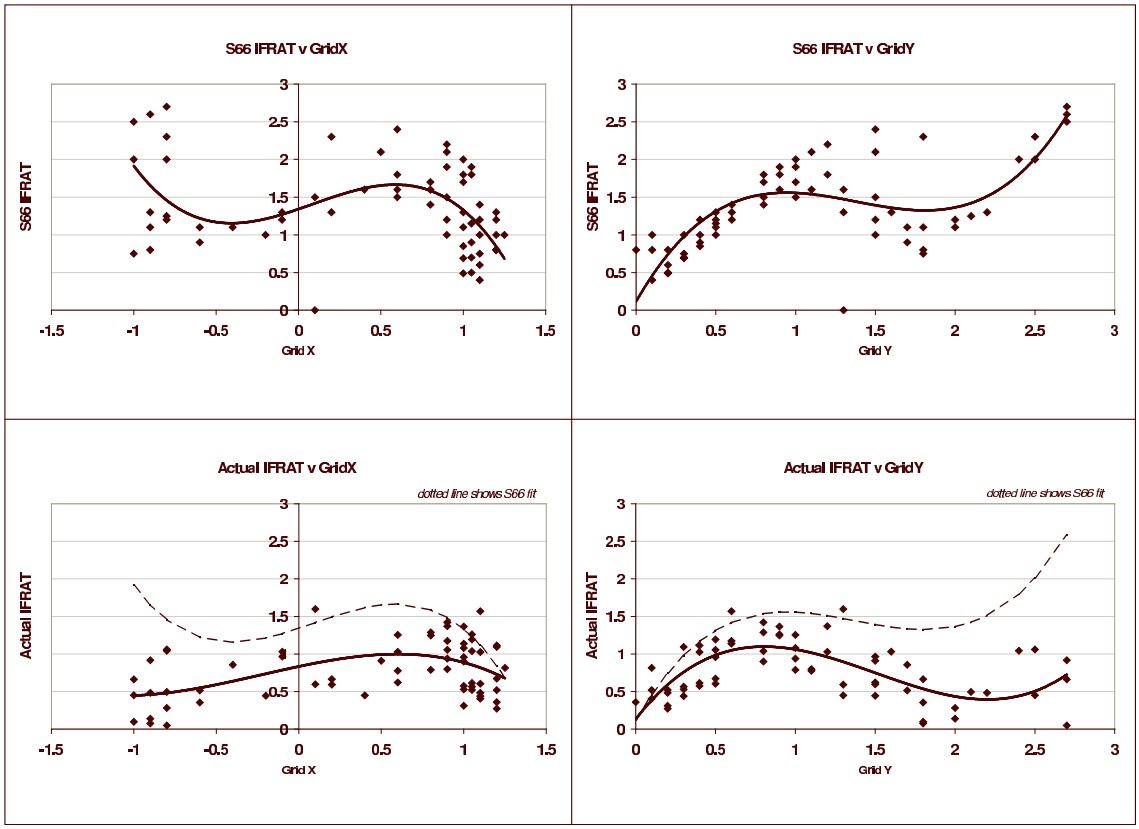

Figure 7.15: The top two figures show the variation of the mass flux ratio with GridX and GridY predicted by S66. We fitted cubic regression equations to the data for both the model and the actual data, but the fits are on the whole poor and almost certainly of little predictive value.

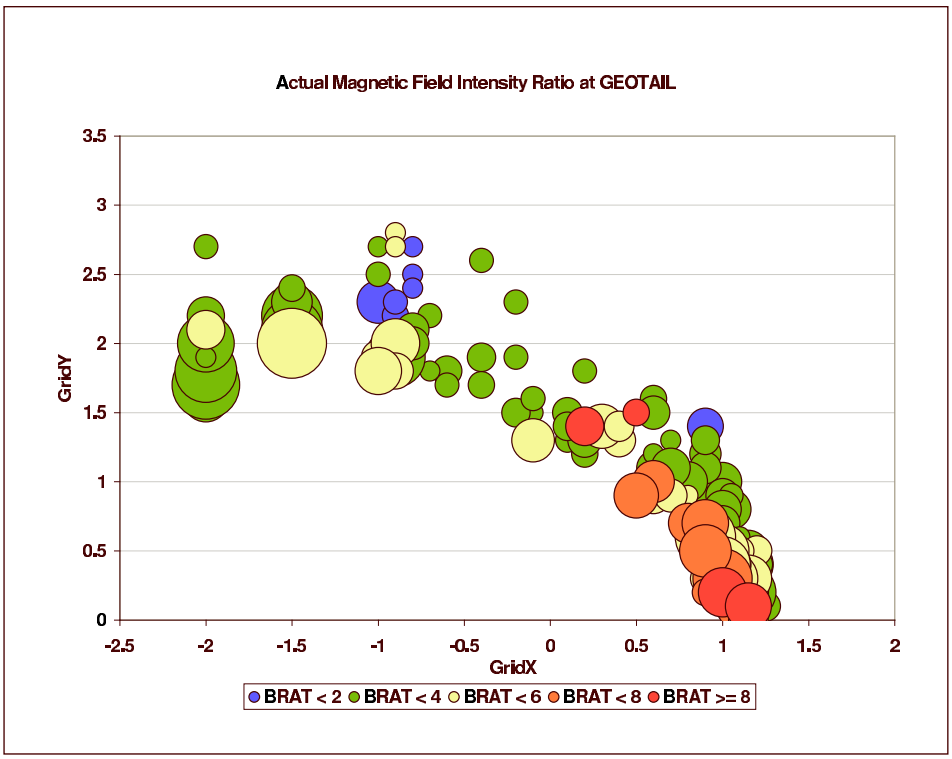

Figure 7.16: Shows the actual magnetic field intensity ratio at Geotail when compared with Wind data, lagged as described in the text. The bubble areas are proportional to the $\sqrt{\text{count}}$ of minutes binned in to the grid point.

7.3.4 The Magnetic Field Intensity Ratio

Figure 7.16 shows the actual values of the magnetic field strength ratio which we obtained from our data. The highest values are found in the sub-solar region, but tend to be fairly even for tailward X.

7.3.5 Comparison of Survey Magnetic Field Intensity with KF94

Because S66 do not explicitly discuss the magnetic field intensity, we chose to compare it with the KF94 model (see Section 3.6.1). In this case, we reverted to the original data (with full X, Y, Z coordinates and components of the IMF) in order to calculate the KF94 magnetic field magnitude (adjusting components to the KF94 coordinate system).

In Figure 7.17, we show for given solar wind magnetic field measured by Wind, the magnetic field measured by Geotail in the magnetosheath (blue diamonds) and the magnetic field predicted by KF94 (pink squares) for the same location in the magnetosheath. We also show the (green) line $4.5|B_{sw}|$. It is easily seen that the values predicted by KF94 are very close to this line. There is considerably more variation in the real survey data, hence there is little value in comparing the real ratio with the predicted ratio. We note, however, that the linear fit of $|B_{\text{Geotail}}| = 4.12|B_{\text{Wind}}| + 0.31$ is quite close to the line $4.5|B_{sw}|$. We conclude, therefore, that using a magnetic field ratio of 4.5 as a gross assumption throughout the magnetosheath is not unreasonable for general purposes.

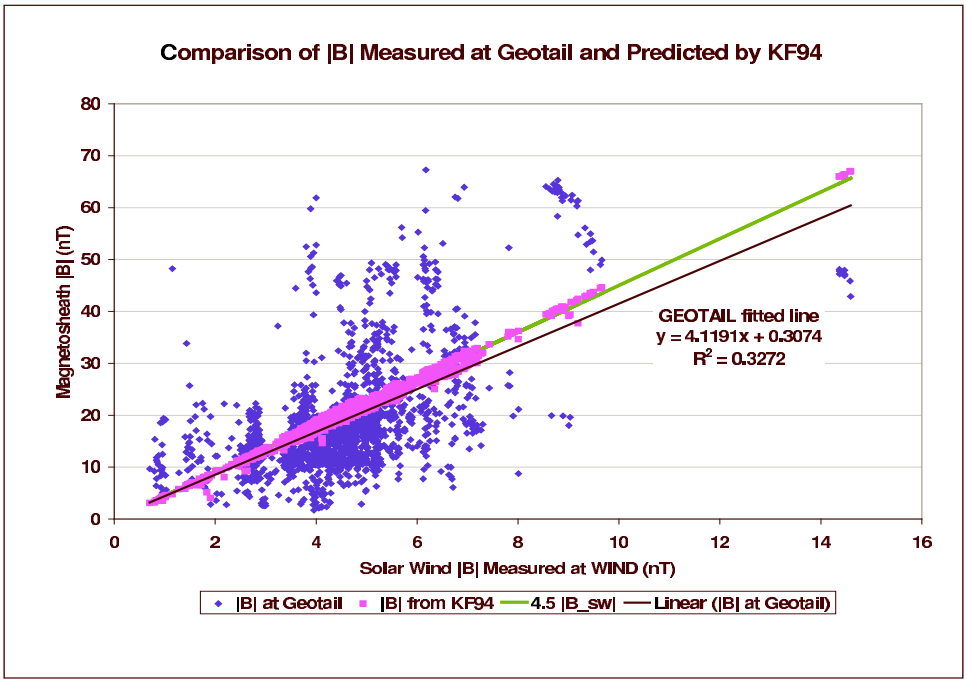

Figure 7.17: Shows the actual values of the magnetosheath magnetic field measured by Geotail (blue diamonds) compared with the predictions of KF94 (pink squares) for the solar wind magnetic field value measured by Wind. The green line is simply $4.5|B_{sw}|$. It can be seen that the predictions of KF94 for the magnetic field strength are very close to this. We have also fitted a regression line to the Geotail data (black) and while the correlation is low (R-Sq of 33%) the line is not too far from the green line.

Note that the KF94 also makes predictions about the orientation of the magnetosheath magnetic field vector which we have not attempted to address here.

7.3.6 Conclusions of Investigation 1

In this section we reviewed a subset of our data which, when binned, corresponded to gridded S66 models for hydromagnetic flow around the magnetosphere for $M_\infty = 8$ and $\gamma = 5/3$. Broadly speaking, we believe that our survey demonstrates that the magnetosheath profiles for velocity ratio and density do follow the predictions of the S66 models, at least in the ecliptic plane.

We have shown that our data confirms the following predictions:

- The interquartile range of velocity ratio values in the magnetosheath of ~ 0.25 to 0.75. All but one of our values gave a ratio of less than 1.
- The velocity ratio shows an increase with GridX.
- The velocity ratio increases with GridY.
- The lowest values of velocity ratio are in the sub-solar region.
- The interquartile range of density ratio values of ~ 1.0 to 3.5 is a little lower than the predictions but is in the same broad range.

- The density ratio decreases with GridX.
- The density ratio increases with GridY.
- The highest values of density ratio are in the sub-solar region.
- An increase in the mass flux ratio in the day-side region.

We do not convincingly show:

- An increase in density ratio at GridX ~ -1.
- An increase in the mass flux ratio at the same location.

Investigation of regression relationships based strictly on combinations of GridX, GridY and their squares and cubes fitted the model velocity ratio extremely well but not the actual velocity ratio . The model mass flux ratio was fitted very well but the real mass flux ratio not at all. Both the model and actual density ratio had reasonably good fits to such regression models.

The fact that our velocity and density (and consequently mass flux) ratios were all lower than predicted by S66 raises the problem of conservation of mass flux. The most probable reason why our survey appears to show non-conservation of mass flux is that we are taking average properties at different points in the magnetosheath at different times, rather than a snapshot (S.J.Schwartz, 2004, in correspondence). The magnetosheath is a non-linear system and therefore taking the average at each point may not be appropriate. More data would be required in order to explore this issue further and may be considered as further work.

For our comparison of the magnetic field intensity with that predicted by KF94, we found no correlation between the magnetic field ratios, but we did find that the best fit line through the real data were broadly similar to the KF94 predictions which we believe is sufficient to justify its use as a basic analytical predictive tool for actual magnetosheath magnetic field values.

In our second investigation (Section 7.4), we will analyse our full data set in more detail and attempt to construct empirical models for the velocity ratio and density ratio. We will also investigate the magnetic field which did not form a significant part of the S66 work.

7.4 Investigation 2 - Analysis of Survey Results

In this section we look at our data in more detail. We will consider only the velocity ratio, density ratio and magnetic field strength ratio. We continue to use the GridX, GridY binning and averaging of our data, but now we split it into various groupings in order to try to identify relevant factors in controlling the values.

The inputs which we will consider are: magnetosheath location as determined by GridX, GridY, solar wind velocity, density, magnetic field, pressure, temperature, beta, sonic Mach number, Alfvénic Mach number, the sign of Y (to test for dawn-dusk effects), the sign of B_Z (to test for northward or southward IMF effects), month and season of measurements.

7.4.1 Time Effects

The Sun-Earth system varies throughout the year. There is the motion of the Earth's dipole, the varying distance from the Sun, and the 29 day solar cycle. Here, we attempt to discern whether there are any time effects visible in the data when grouped by season or by month.

Season

Data were grouped into 4 season bins, March and April defined as season 1, May - July as season 2, August - October as season 3 and November - December as season 4. Figure 7.18 shows the data grouping.

We carried out a one-way ANOVA (Analysis of Variance - see Appendix E) of the velocity ratio, density ratio and magnetic field strength ratio by season and found that there was statistical evidence for a seasonal effect for the first two with p values of 0.018 and 0.012 respectively, but no evidence for a seasonal effect on the magnetic field strength ratio values (p value 0.28). The velocity ratio means were highest for season 3 (autumnal equinox) and lowest for season 4 (winter solstice). For density ratio, the means were highest for season 4 and lowest for season 2 (summer solstice).

Month

The data were sorted into monthly bins. Figure 7.19 shows the resulting data range. One way ANOVAs for velocity ratio, density ratio and magnetic field strength ratio were performed. There was statistical evidence for a monthly effect for the velocity ratio and density ratio which supported the findings above with highest velocity means and lowest density means during months 7, 8 and 9 (which do not correspond precisely to a season). The p values for the velocity ratio and density ratio were 0.007 and 0.001 respectively. Again, there was no evidence for a monthly effect on the magnitude of magnetic field strength ratio , as the p value was 0.576 (or 0.355 once an extreme outlier with a magnetic field strength ratio of 40 was removed).

Conclusion on Time Effects

The results appear to show evidence for a seasonal and/or monthly effect on the values of velocity ratio and density ratio. We need to consider, though, whether there is bias in our data - upon consideration of the orbit of Geotail, it may be that the sign of Y correlates strongly with the month or season.

While there are 1021 minutes with negative Y and 1020 with positive Y, they are not evenly spread throughout the year as shown in Figure 7.20. Our conclusion, therefore, is that the time effects displayed in the data need to be treated with some care as they may instead reflect bias in our samples.

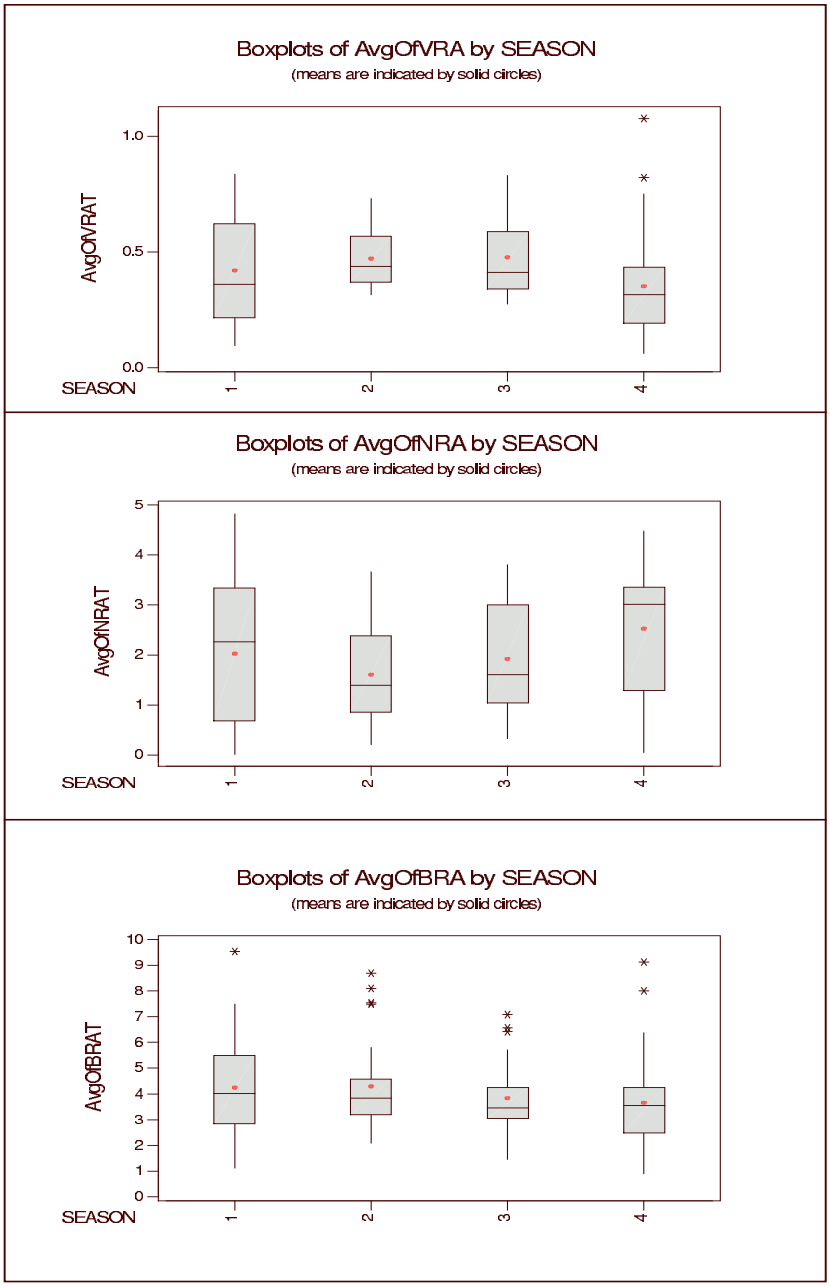

Figure 7.18: Showing the survey data grouped by season for velocity ratio, density ratio and magnetic field strength ratio respectively. ANOVA analysis indicates that there is evidence for a seasonal effect for velocity and density ratios, but not for the magnetic field.

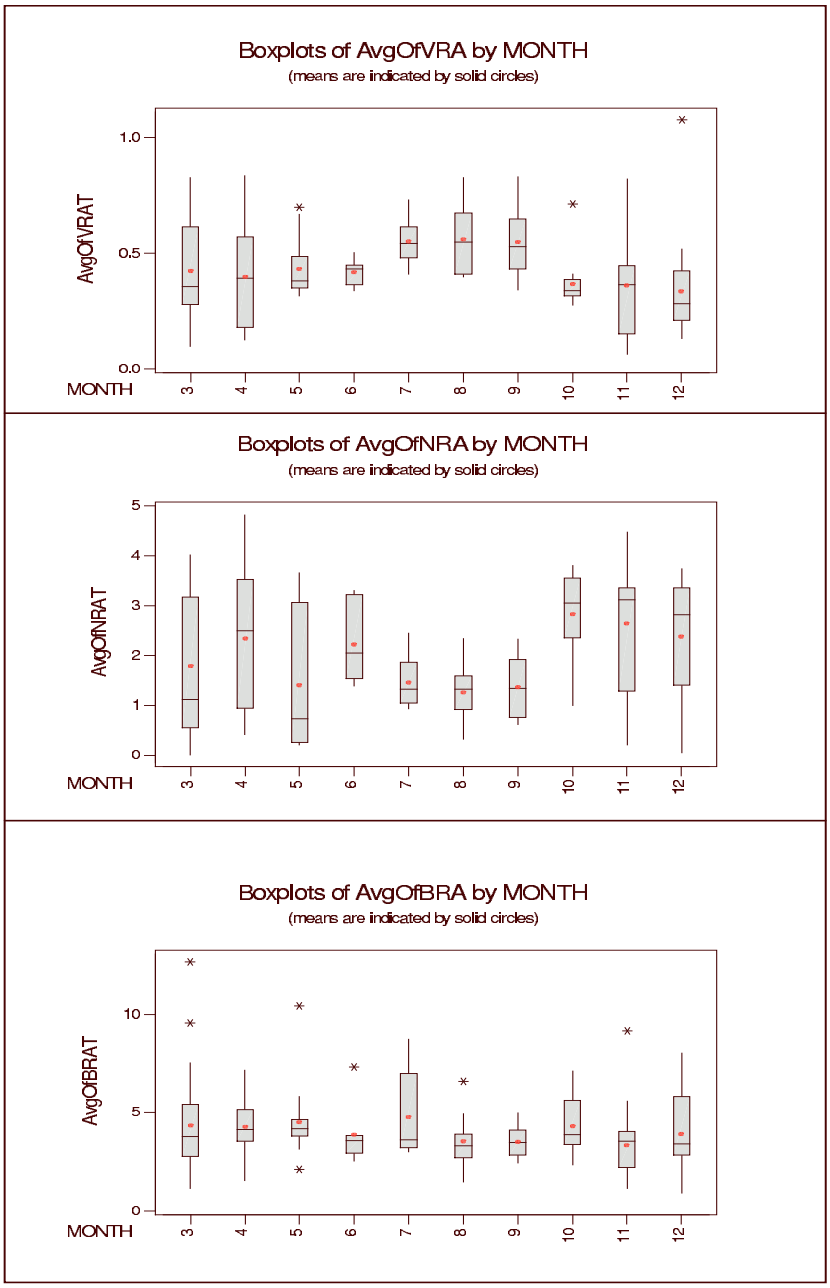

Figure 7.19: Showing the survey data grouped by month for velocity ratio, density ratio and magnetic field strength ratio respectively. ANOVA analysis indicates that there is evidence for a monthly effect for velocity and density ratios, but not for the magnetic field. Note that an extreme outlier with magnetic field strength ratio of 40 was removed from the dataset for this box plot.

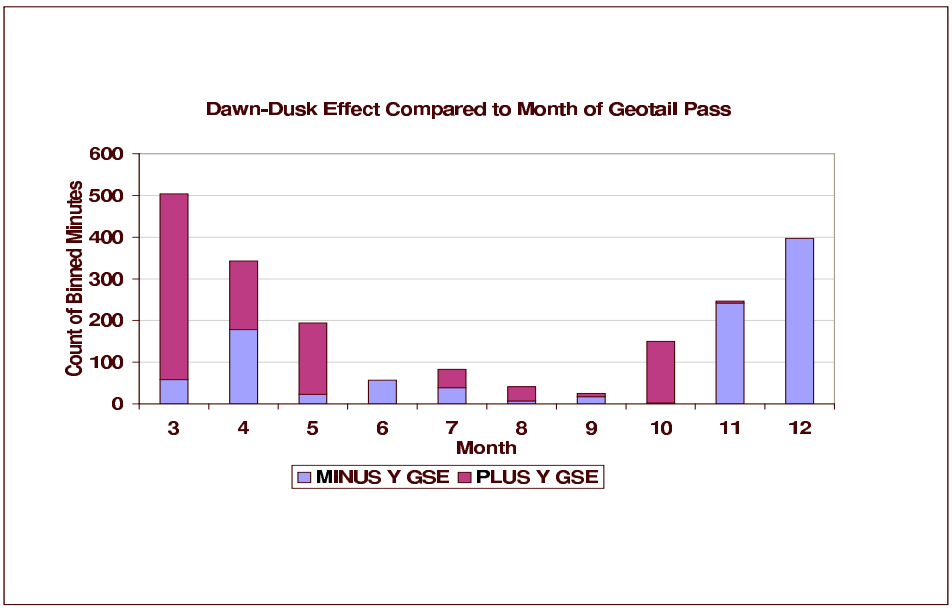

Figure 7.20: Shows the number of binned data minutes with either positive or negative Y value grouped by month.

7.4.2 Mach Number Effects

Sonic Mach Number

The data set has been grouped into low and high sonic Mach numbers, flag 0 for Mach number < 7.4 otherwise 1. Figure 7.21 does not suggest any real difference between the data sets when grouped in this manner, and this is supported by the two sample t-test for each of the ratios which all have high p values. As this result is somewhat surprising, we considered the spread of our sonic Mach numbers as shown in Figure 7.22. While the data ranges from 6.5 - 10.5, the bulk of it lies in the region of 7 - 8. It is likely therefore that the range is too small to discern any effects and more data would need to be considered.

Alfvén Mach Number

The data set has been grouped into four bands, Alfvén Mach number < 4 is band 1, from 4 to 10(-) is band 2, from 10 to 16(-) band 3 and 16 or over is band 4. Figure 7.23 shows the box plots for the three ratios. In the case of the velocity ratio and density ratio no variation between the bands is suggested, a conclusion that is supported by the one-way ANOVA p values which are high. However, the magnetic field strength ratio values do show a variation with Alfvén Mach number and this is supported by the extremely low p value.

Conclusion on Mach number effects

The sonic Mach number does not appear to have an effect on the data, though this may be because of the limited spread in our data. However, the Alfvénic Mach number does appear to affect the value of magnetic field strength ratio.

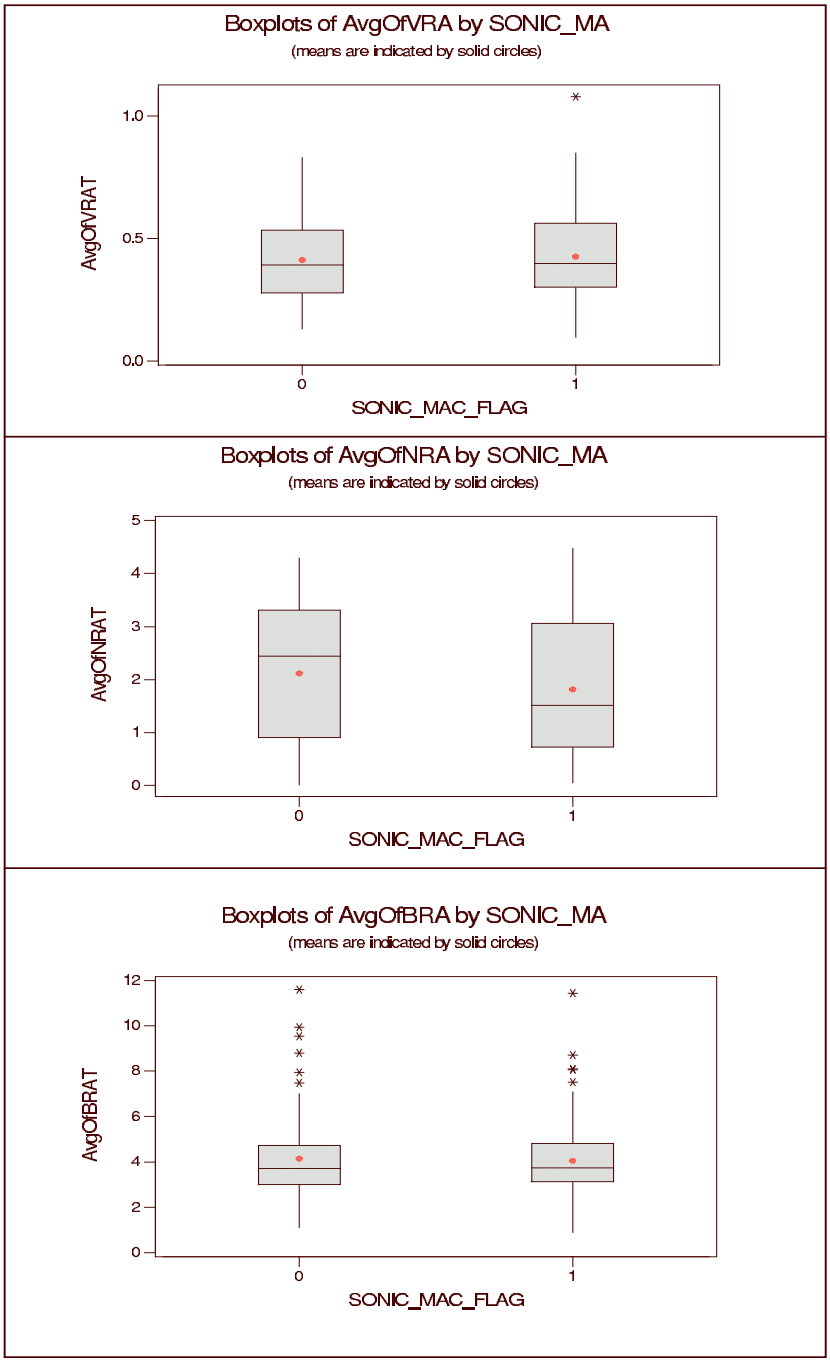

Figure 7.21: The boxplots for the velocity ratio, density ratio and magnetic field strength ratio when grouped by low (less than 7.4) and high sonic Mach number do not suggest a difference. (* indicate outliers in the data)

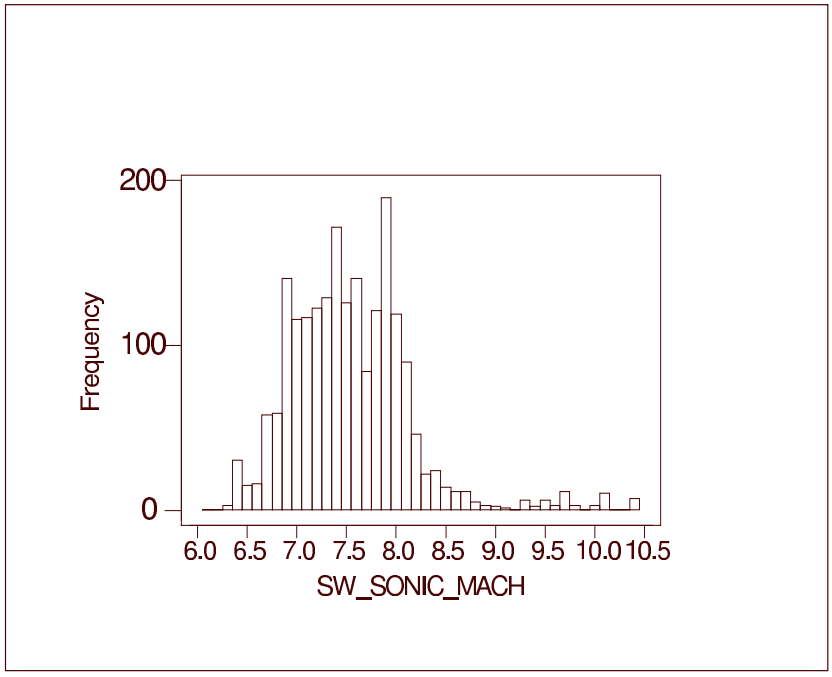

Figure 7.22: The spread of sonic Mach number values in our survey.

7.4.3 Plasma Beta

The data were grouped into two, low beta, coded '0', (for beta less than 1) and high beta, coded '1'. The box plots in Figure 7.24 do not suggest a variation for velocity ratio, for density ratio they are a little more ambiguous. The statistical p value is 0.099 which, as it is greater than 0.05, indicates no evidence for believing them to be different. In the case of magnetic field strength ratio, a difference is clearly suggested and this is backed up by the t-test which reveals an extremely low value of p.

Conclusion on plasma beta effects

There is no evidence for a plasma beta effect on the velocity ratio. The density ratio values do not give sufficient evidence to suggest that there is a plasma beta effect. Lastly, there is statistical evidence to support the claim that there is a beta effect on the value of the magnetic field strength ratio.

7.4.4 Sign of B_Z

Figure 7.25 shows that there is no discernible effect from the sign of B_Z on the data. This, too, is backed up by the 2 sample t-test which yields high p values.

7.4.5 Sign of Y - Dawn-Dusk Effect

The boxplots in Figure 7.26 indicate a dawn-dusk effect for both the velocity ratio and density ratio values. This is backed up by the two sample t-tests which yield low p values of less than

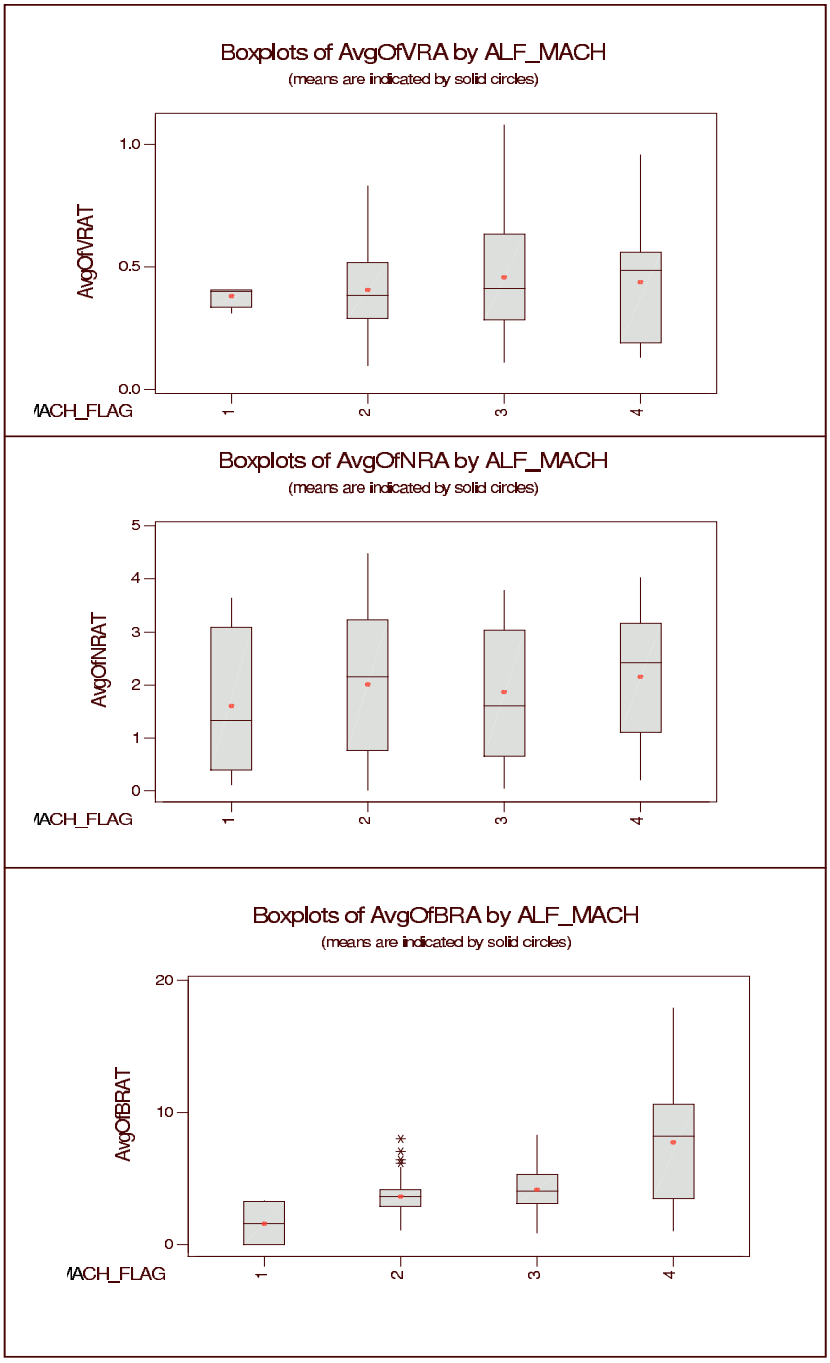

Figure 7.23: Boxplots for the velocity ratio, density ratio and magnetic field strength ratio are shown. No variation by Alfvén Mach number is indicated for the velocity ratio or density ratio, but is for the magnetic field strength ratio. This is supported by the ANOVA test.

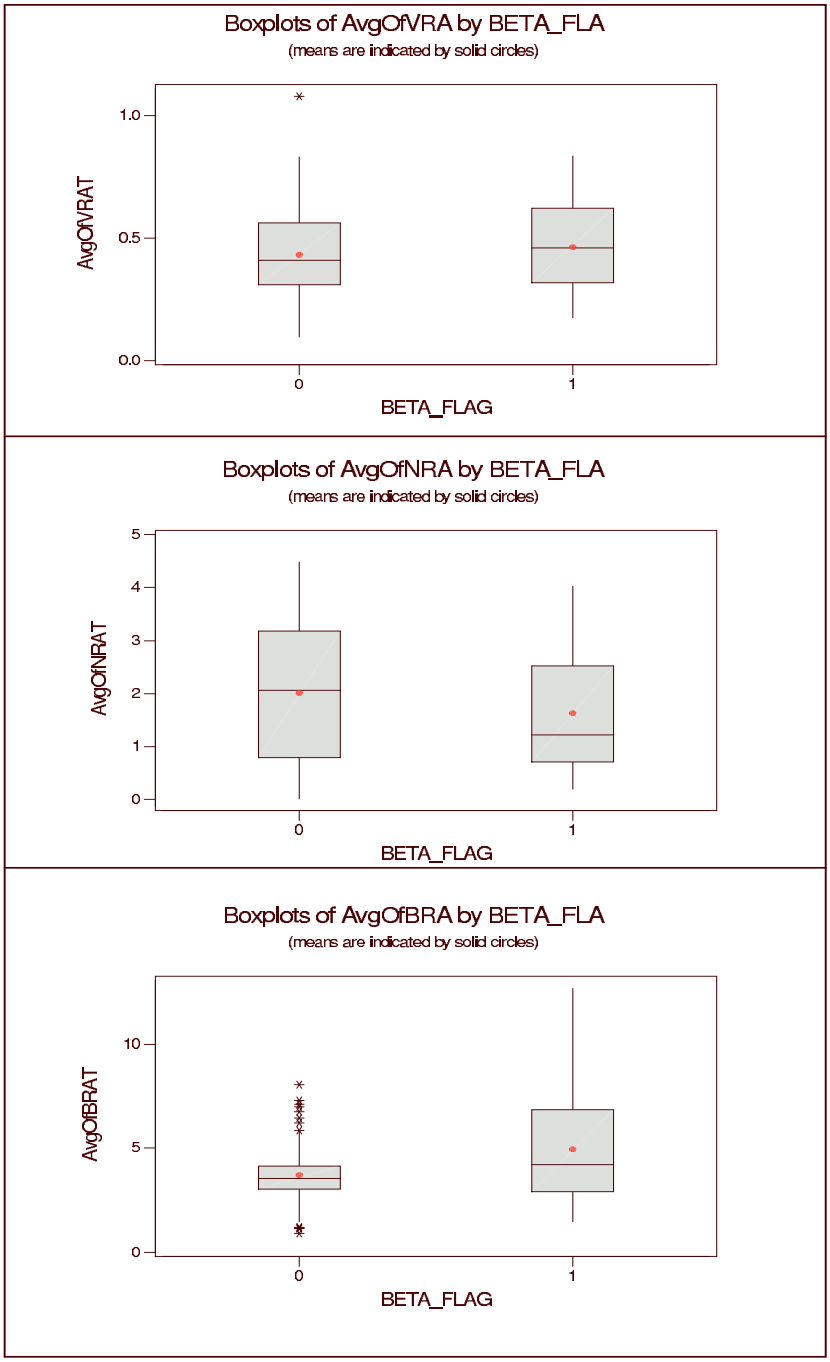

Figure 7.24: The figures suggest no variation due to the plasma beta for the velocity ratio and may possibly do so for density ratio values. A beta effect is indicated for the magnetic field strength ratio values. This is supported by the two sample t-test.

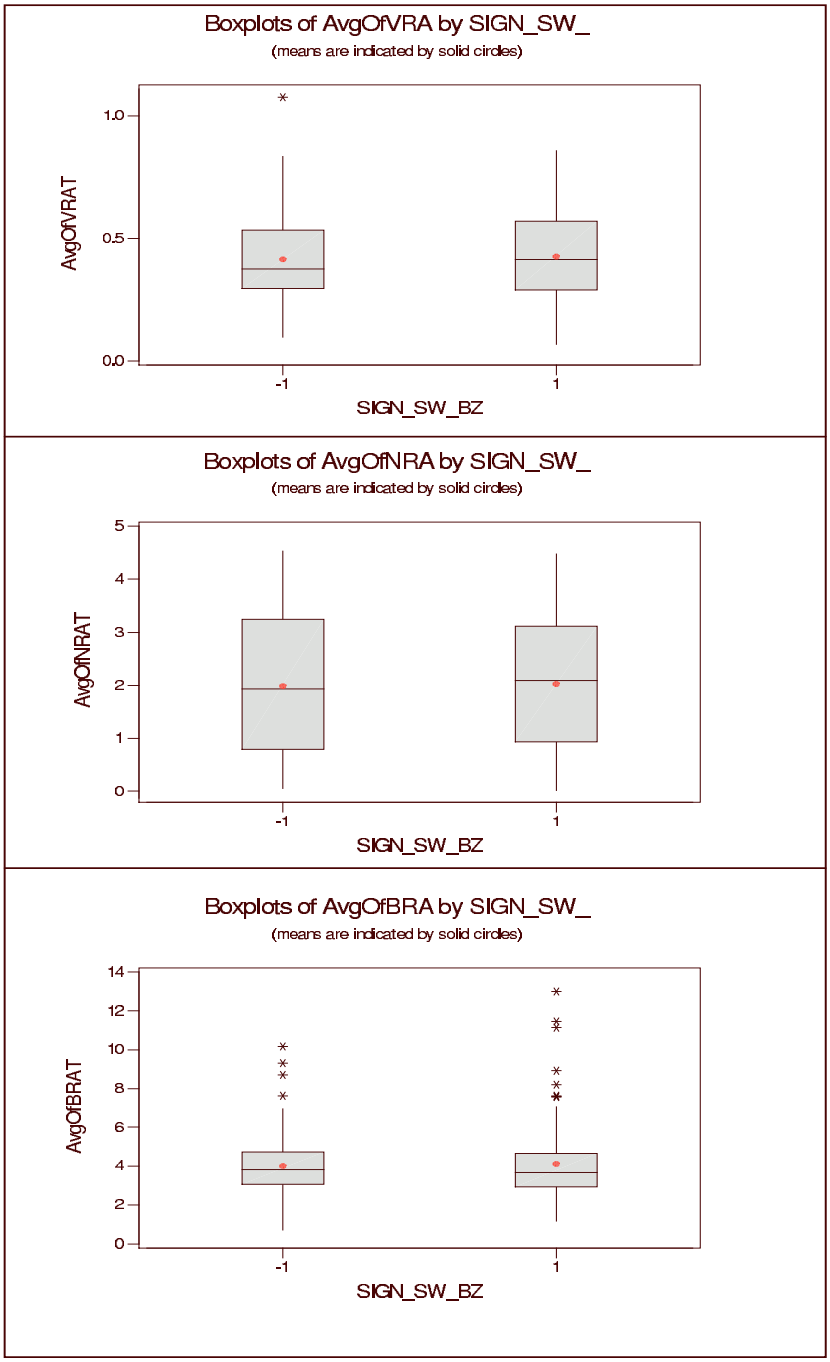

Figure 7.25: The figures suggest no variation due to the sign of B_Z . This is supported by the two sample t-tests.

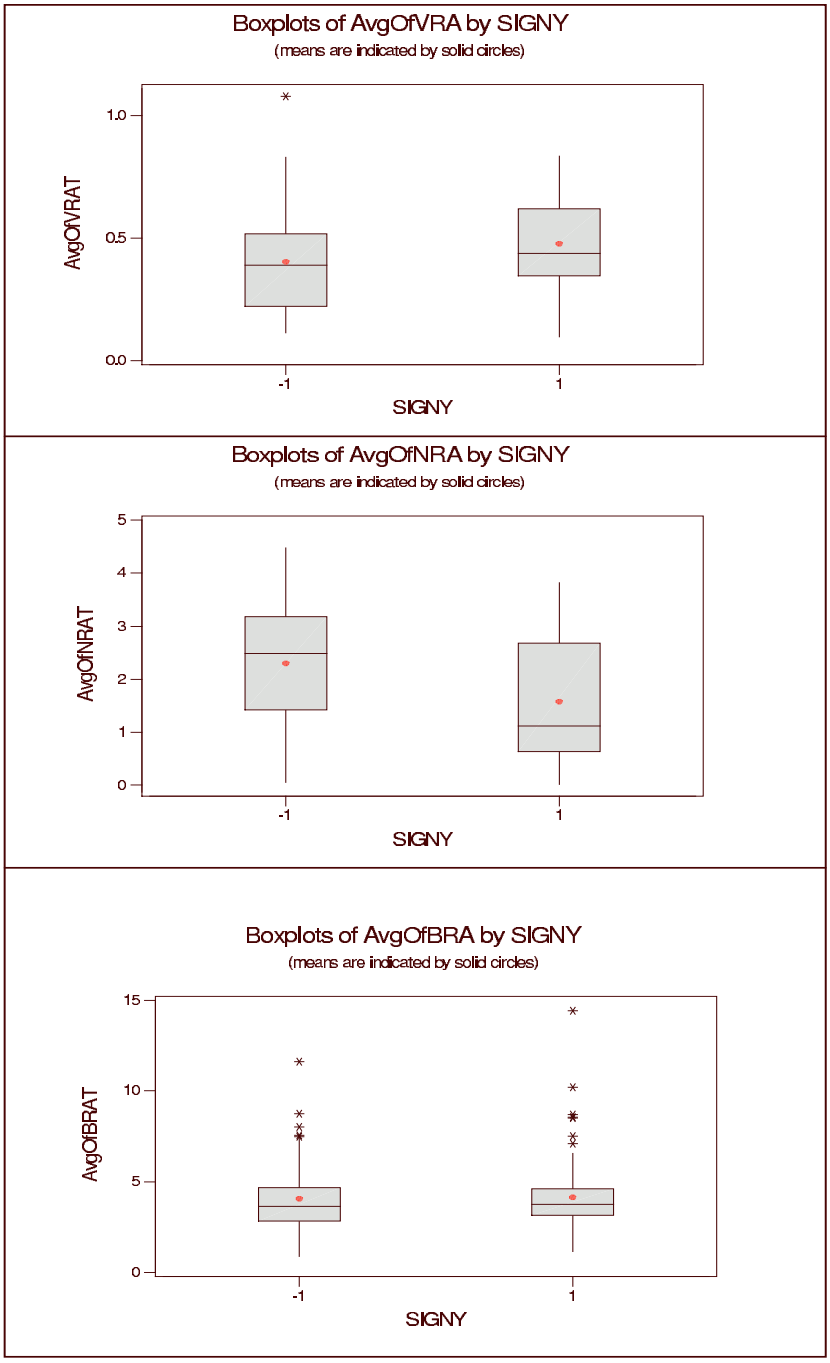

Figure 7.26: The figures suggest that there is variation due to the sign of Y for both the velocity ratio and density ratio values. No effect is apparent for the magnetic field strength ratio values. This is supported by the two sample t-tests.

Possible Factors	VRAT	NRAT	BRAT
Season*	Y	Y	N
Month*	Y	Y	N
Sonic Mach No.+	N	N	N
Alfvén Mach No.	N	N	Y
Plasma Beta	N	T	Y
Sign of B_Z	N	N	N
Sign of Y	Y	Y	N

Table 7.1: Summarizes the findings from the analysis. Y means statistical evidence for an effect was found, N that it was not found, and T for a tentative effect. The * by the season and month indicates that the effects we saw need to be treated with care as described in the text. The + by the Sonic Mach number indicates that we do not believe the range in our data were sufficient to discern an effect.

0.05. There is no evidence for a dawn-dusk effect on the magnetic field strength ratio values.

A possible explanation for a dawn-dusk effect is aberration due to the Earth's motion causing a deflection of the flow of plasma around the geomagnetic obstacle. We examined our data by plotting our binned minute data $|V|$ and N against Y_{GSE} (see Figure 7.33 for the former, the latter is not shown) and found that the minimum speeds and maximum densities, consistent with the location of a stagnation point, were at $\sim$ -2R_e. At this location, the M_A for our data were $\sim$ 1. Russell *et al.* [1981], taking an analytical and theoretical approach, use M_A as a predictor of the effect of the $\mathbf{j} \wedge \mathbf{B}$ forces which deflect the flow and predict that for this M_A, a dawnward shift of $12 - 14^o$ would be seen. We do see this in our data. The dawn-dusk effect is possibly the underlying cause of the seasonal and monthly effects seen in the data as the location of our Geotail survey data points through the magnetosheath does shift towards the dawn as 1997 progressed.

We chose not to take potential aberration into account when setting up our data as we did not wish to pre-judge whether an effect would be discernible or not, nor its magnitude or location. Aberration is discussed in more detail in Section 7.5.3.

7.4.6 Summary of Findings from Effects

Table 7.1 summarizes the findings from the above analysis.

We found a seasonal and monthly effect on both velocity ratio and density ratio which may be explained by the dawn-dusk effect (sign of Y) due to the bias of the Geotail sample data in the Y direction. The dawn-dusk effect itself may be explained by the Earth's motion and MHD effects which cause an aberration in the flow. We did not find any dependence on the sonic Mach number. However, this may be due to the small range in our survey and it may be that further samples with lower sonic Mach numbers than ours may reveal a difference. For magnetic field strength ratio we found evidence suggesting an effect from the Alfvén Mach number and the plasma beta.

7.5 Models

In this section, our intention is to develop simple empirical models based on our survey data of the three principle ratios V/V_{sw}, N/N_{sw}, B/B_{sw} . We plan to use a 'parsimonious' selection of input variables, i.e. the smallest quantity of input variables required to reach a reasonable model. In the models developed in this section, we used the original, ungridded data (2040 one-minute averaged items) though kept the scaling.

Because there will be no single unique model, and because the process could last indefinitely, stopping criteria for the model design were essential. These were set at: either a model achieving an R-Sq(adj) of greater than 70% (or failing that, the maximum achievable in 100 different set ups). Once an acceptable R-Sq was achieved, terms with the highest values of p (see Appendix E) were removed methodically and the effect on R-Sq checked. Where the removal of a term took R-Sq below 70%, it was put back in.

A two-pronged approach has been used in developing the models: firstly, throw every variable into the regression and see which can safely be eliminated while leaving the model more or less unchanged, and secondly, build the model from the ground up using those variables which we expect to have some bearing on the problem based on physical considerations.

The possible inputs are:

Solar wind velocity components and magnitude, magnetic field components and magnitude, number density, temperature, ion flux, beta, sound speed and sonic Mach number, Alfvén speed and Alfvén Mach number, sign of y, sign of B_Z, the X/R_{mp} and (signed) r/R_{mp} components (rather than the gridded values) and their squares and cubes, $X/R_{mp} \cdot r/R_{mp}$, square of solar wind speed. Despite having found a 'month' or 'season' effect above, we chose to leave this out of the models at this stage as we believe it is actually a Y bias in the data.

Each of the inputs should have as low a p value as possible. This means that there is a very high probability that their coefficients in the regression equation are not zero and hence, that they are important in the model. In most cases we have eliminated terms where the p value is greater than 0.05.

In the models below, V, V_X, V_Y, V_Z, B, B_X, B_Y, B_Z, N, T are the solar wind velocity magnitude and GSE coordinates in kms^{-1}, solar wind magnetic field magnitude and GSE coordinates in nT, solar wind number density in particles cm^{-3} and solar wind temperature in K respectively. X and $r = \sqrt{Y^2 + Z^2}$ are the location of the spacecraft in GSE coordinates. β is calculated from the interpolated Omni data as $2\mu_0 NkT/B^2$ where the terms are in SI units. Our calculated βs ranged from 0.01 to 6.2 with the bulk of them around the 0.5 - 0.7 mark.

R_{MP} is the calculated magnetopause stand-off distance in R_e (see Equation 5.8), C_s is the solar wind sound speed in kms^{-1} as calculated by the equation $C_s = 0.12 \cdot (T + 1.28\text{x}10^5)^{1/2}$ (originating from the IMP team), and V_A is the solar wind Alfvén speed in kms^{-1} as calculated by the equation $V_A = 21.8B/N^{1/2}$ [Kivelson, 1995a, p.530].

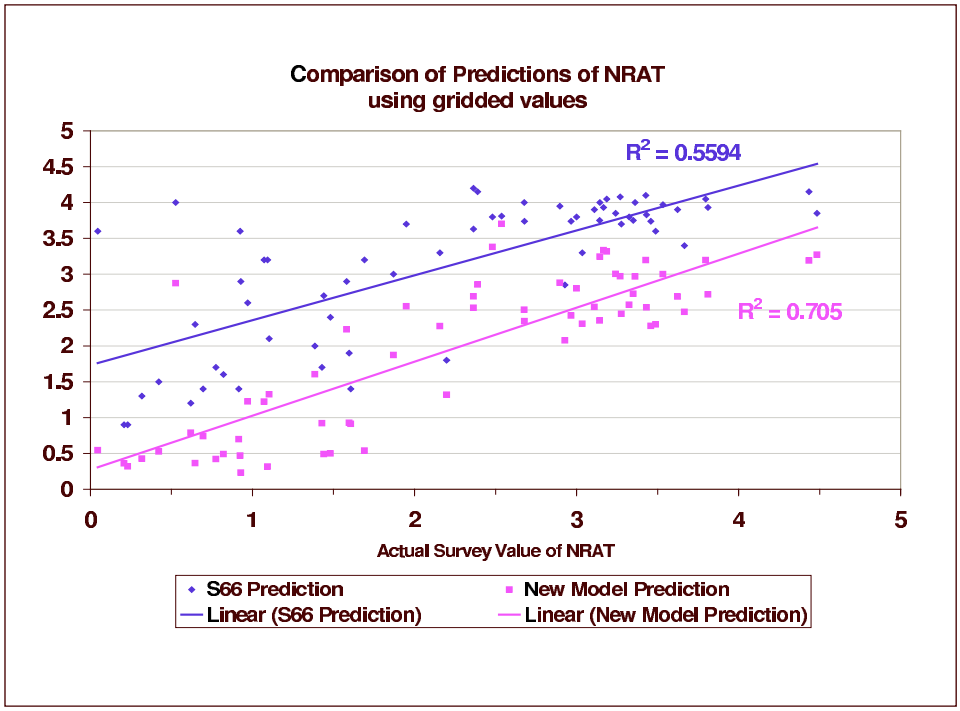

Figure 7.27: Density ratio model: This figure compares the fit from the empirical model (pink squares)(see Equation 7.2) with that of S66 (blue diamonds) for our survey data. As the empirical model is built from a data fit, then the R-Sq value is higher.

7.5.1 Number Density Model

Our first model was to fit the density ratio to the input variables and a model with quite high R-Sq of 81.5% was found. Inspection of the residuals, however, revealed 'funnelling', i.e. the size of the residual increased with the predicted size of density ratio (see Appendix E). We therefore chose to make a transformation of the data.

Using a Box-Cox transformation, an 'optimal' transformation using $(N_{Geotail}/N)^{0.337}$ was found. Using this transformation we found a model which had an R-Sq of 80.9% but which had a much more acceptable residual fit to predicted value. As this transformation was very close to taking the cube root of density ratio, we tried a transformation using this value. Using this transformation, we found a model with an R-Sq /R-Sq(adj) of 85.3% / 85.2% respectively and with acceptable residual plots.

$$\begin{aligned}\left(\frac{N_{Geotail}}{N}\right)^{1/3} = &-0.616 + 0.201\left(\frac{X}{R_{MP}}\right)\left(\frac{r}{R_{MP}}\right) + 0.157R_{MP} - 0.0168B_X - 0.0149B_Y \\ &+ 0.000511|V| + 0.00703N - 0.00107V_Y - 0.000657V_Z - 0.0681\left(\frac{X}{R_{MP}}\right)^3 \\ &- 0.124\left(\frac{X}{R_{MP}}\right)^2 + 0.333\left(\frac{X}{R_{MP}}\right) + 0.237\left|\left(\frac{r}{R_{MP}}\right)^3\right| \\ &- 0.0682(\text{signY})\left(\frac{r}{R_{MP}}\right) - 0.511\left(\frac{r}{R_{MP}}\right)^2 \end{aligned} \quad (7.1)$$

While this model has a high fit to the data, it is not easy to interpret. We therefore used physical considerations to build up a model which both made physical sense and which was also statistically

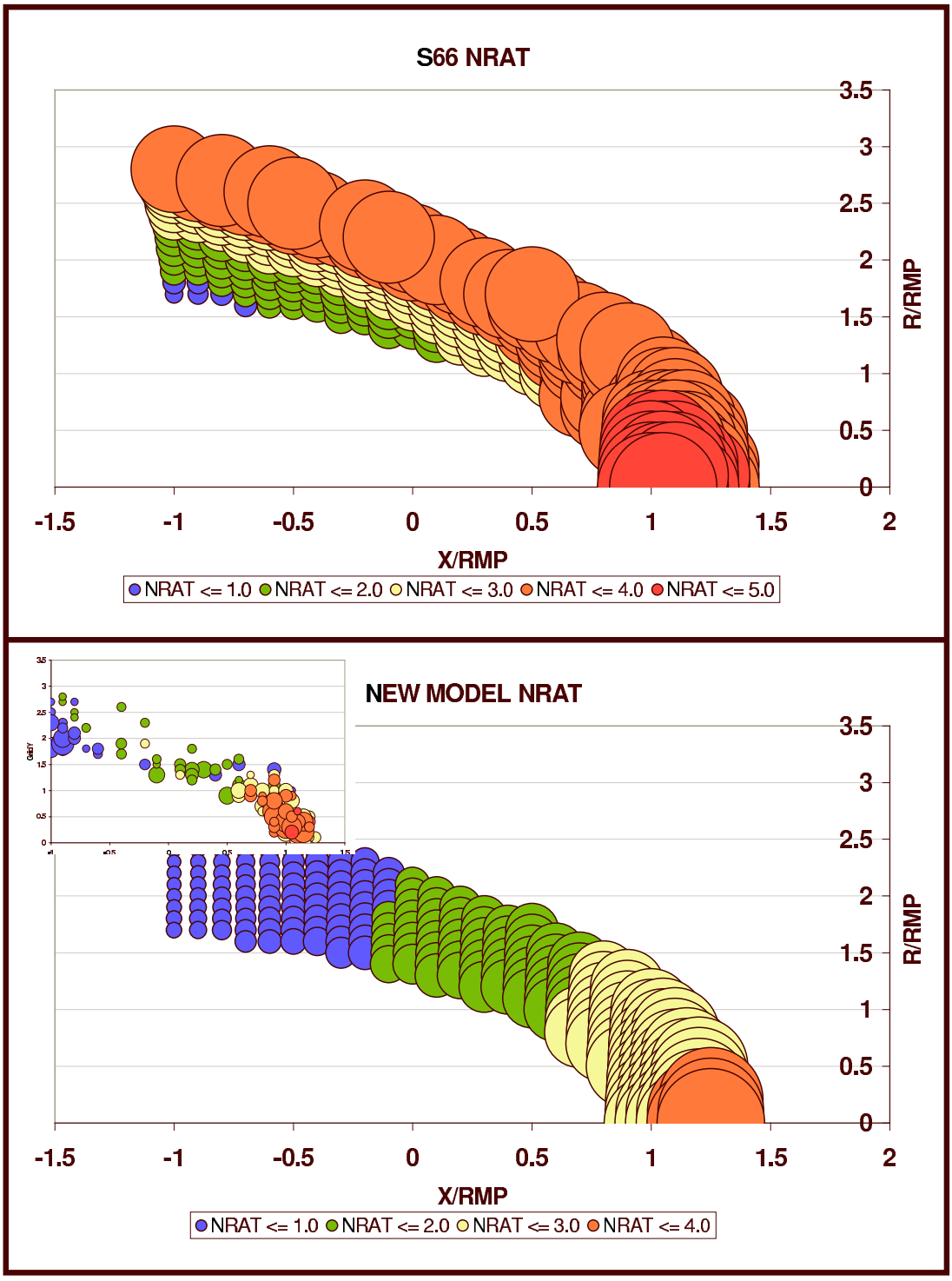

Figure 7.28: Density ratio model: The top figure shows the predictions of S66 for M_∞=8 and $\gamma = 5/3$. The lower figure shows the predictions of our new empirical model for a plasma β of 0.7 and $M_A = 10$ (average values of our actual data set). It is easily seen that generally, our densities decrease as we move away from the Sun, as do those of S66, the densities predicted by our model are lower than those of S66. The highest value predicted by our model at the sub-solar point is 3.14 which is somewhat lower than the actual survey result of 4.5. The small inset is a reminder of the actual survey values (see Figure 7.8).

sound.

A number of potential models involving X/R_{mp}, r/R_{mp}, β, Alfvénic Mach number and sonic Mach number were found. The coefficients of the terms were examined in order to come up with a final version.

There was a substantial correlation between X/R_{mp} on its own, achieving R-Sq of 74.5% using the model $\left(\frac{N_{Geotail}}{N}\right)^{1/3} = 1.11 + 0.292\left(\frac{X}{R_{MP}}\right)$. Additional terms improve the model slightly.

Our final suggested model, used for our comparisons, is:

$$\left(\frac{N_{Geotail}}{N}\right)^{1/3} = 1.18 - 0.1\beta + 0.00706M_A + 0.255\left(\frac{X}{R_{MP}}\right) - 0.0668\left(\frac{r}{R_{MP}}\right) - 0.035 \text{ signY} \quad (7.2)$$

This model fits the data with an R-Sq and R-Sq(Adj) of 77.6% / 77.5% respectively. In Figure E.1 in Appendix E we show the residual plots for this model, which are acceptable. Figure 7.27 compares the actual survey density ratio with the predictions of S66 and the new model where the values were calculated for each data minute before being binned into the grid. For our survey data, the new empirical model fits the results better than the S66 model (as it should).

Lastly, Figure 7.28 shows the values predicted by S66 compared to those predicted by Equation 7.2 for $\beta = 0.7$ and $M_A = 10$. Our predicted densities based on the empirical model are generally lower than those of S66 which is in line with the results of our survey. However, our model does not predict the higher values of the density ratio seen in the sub-solar region. This is probably because the actual data shows a wide range of Alfvénic Mach number and plasma β at the high X/R_{mp} values. As mentioned above, the predominant factor is the value of X/R_{mp} as evidenced in Figure 7.28. By contrast, S66 density ratios follow curved surfaces and it can be seen from Equation 7.2 that normally the contributions from the M_A and β almost cancel each other out, but possibly for our data set in the sub-solar region they do not. We have insufficient data to be able to test whether this variability in M_A and β in this area is usual or not.

7.5.2 Magnetic Field Model

This model was tackled in a similar manner to the density model. Given the high variability of the magnetic field measured at Geotail with that at Wind (see Section 7.3.5), in this case we fitted a model to the actual value of the magnetic field. The best fit we found with a reasonable quantity of variables is:

$$\begin{aligned} |B_{Geotail}| =& 179 + 3.86B_X + 0.709B_Z - 86.6Q + 0.0107V_X B_X + 0.0101V_Z B_Y \\ &+ 0.203Y - 0.0122X^2 - 0.187M_A - 1.20X \\ &+ 0.237V_A - 6.17R_{MP} + 15.2Q^2 \end{aligned} \quad (7.3)$$

The fit is R-Sq / R-Sq-Adj of 70.9% and 70.7% respectively.

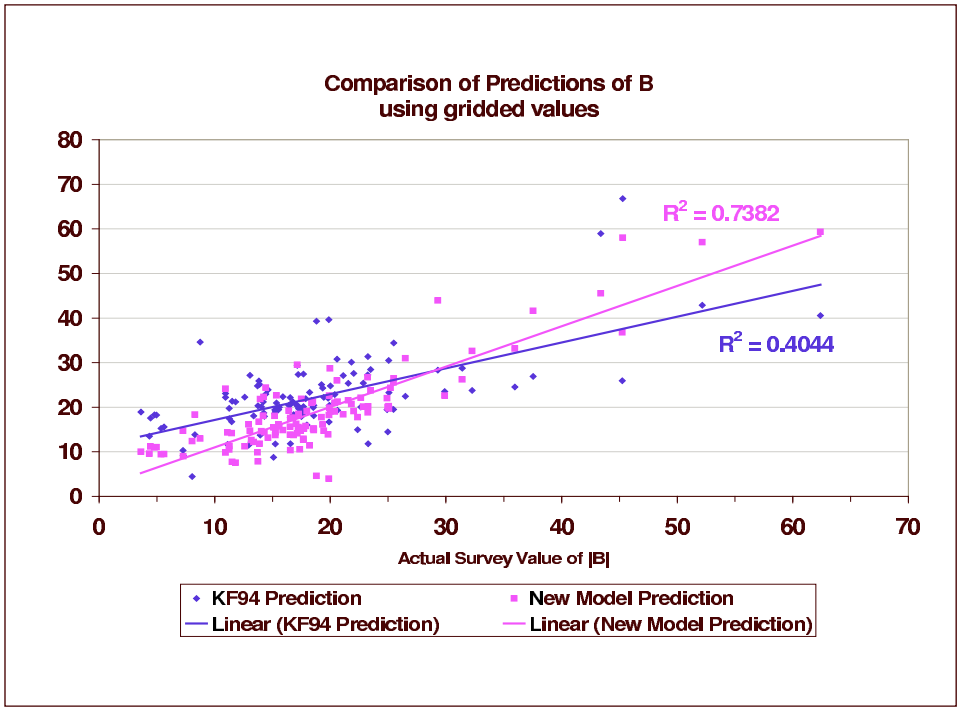

Figure 7.29: Magnetic field model: This figure shows how the fit from the empirical model (pink squares) is better than that predicted by KF94 (blue diamonds) for our survey data. On a point-by-point basis, the fits are not quite as good for both models.

As this equation is difficult to interpret dimensionally, we looked for a model using variables which were more readily understood. A model for the magnetic field intensity ratio proved to be somewhat elusive. Eventually, we settled on the following model which was the highest R-Sq / R-Sq(adj) of 68.7% / 68.6% which we could obtain using dimensionless variables. The model is heavily dependent on location and distance measurements and because of this, there is a high level of co-linearity between some of the predictors.

Our final suggested model is:

$$\begin{aligned} |B_{Geotail}| = &-4.42 - 54.8QB - 3.07Q^3B - 1.55\left(\frac{X}{R_{MP}}\right)B + 23.1\left(\frac{X}{R_{MP}}\right)^2 B \\ &+ 0.555\left(\frac{X}{R_{MP}}\right)^3 B - 1.32\left(\frac{r}{R_{MP}}\right)B + 26.5\left(\frac{r}{R_{MP}}\right)^2 B \\ &- 1.21\left|\frac{r}{R_{MP}}\right|^3 B + 0.290M_A B + 0.333\beta B + 40.70B \end{aligned} \tag{7.4}$$

Figure 7.29 compares the predictions of KF94 with those of our proposed new model with the actual survey data. The fit to our data is better from our model than that of KF94 when compared to the gridded data. The fit from both models is slightly less good for the minute-by-minute data.

Figure 7.30 shows the predictions of our model for the values of the magnetic field strength based on an initial solar wind value of $6nT$ and also the ratio when divided by that value.

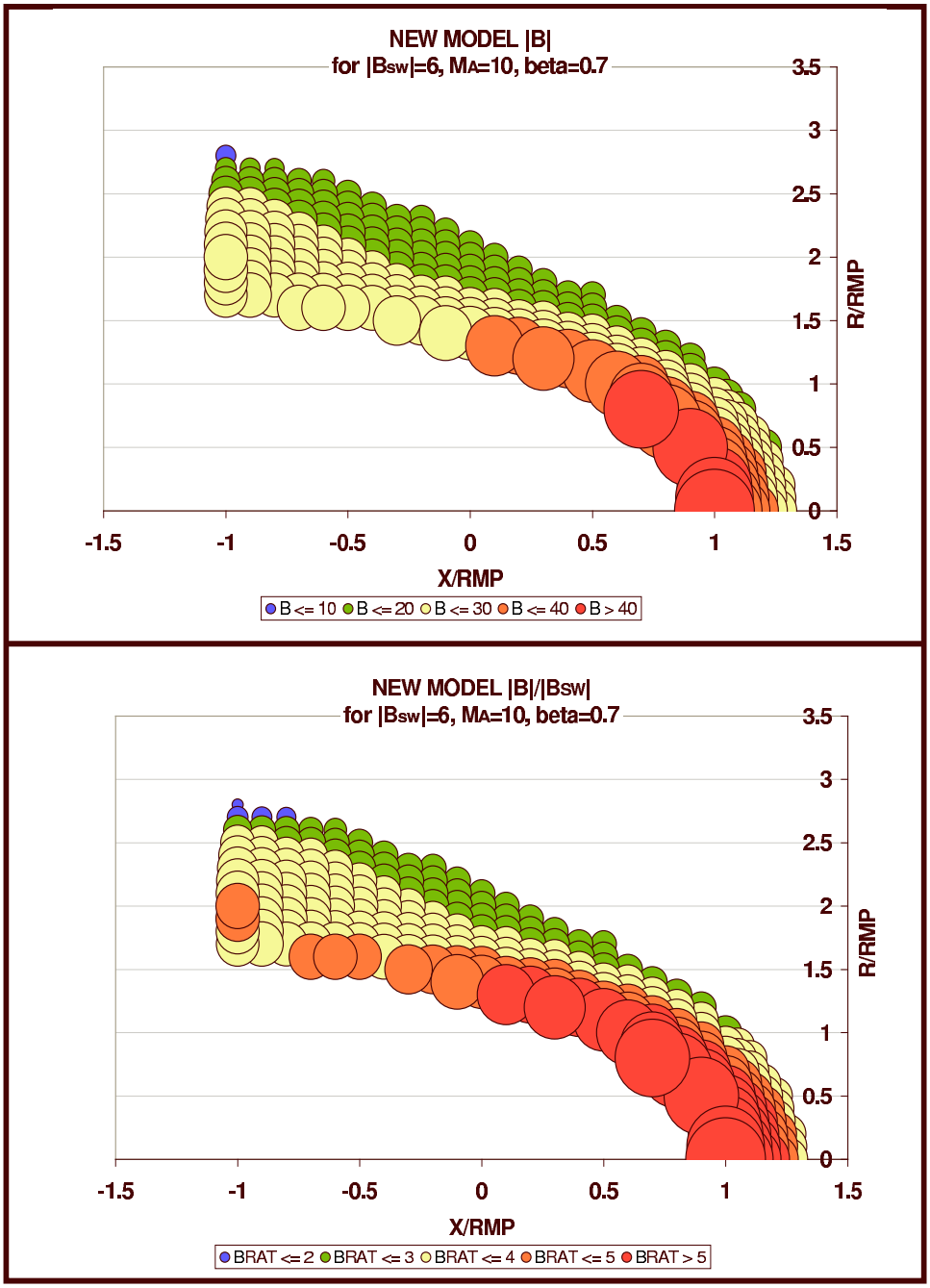

Figure 7.30: Magnetic field model: The model predicts highest values of $|B|$ and of the ratio in the sub-solar region, decreasing anti-Sunwards and also decreasing radially out from the magnetopause to the bow shock. This agrees with the findings of our survey.

7.5.3 Velocity Ratio Model

As with the density ratio, a trial and improvement process was used to identify the final model. The first model (Equation 7.9) fits the actual Geotail velocity magnitude. It was essential to add in cross products of **V** and **B** and differential terms of **V** with the location coordinates in order to get an R-Sq of over 70%.

$$V_{Geotail} = -17615 + 0.0303V_X B_Y - 0.108V_Y B_X + 0.121V_Z B_X + 13.2\frac{XY^*}{{R_{MP}}^2} - 0.000752NV^2 \quad (7.5)$$

$$+ \frac{52776}{\sqrt{T}} + 9.23\left(R_{MP} - \frac{X}{R_{MP}}\right)^2 - 136\sqrt{B} - 2489\sqrt{N} + 2024\sqrt{R_{MP}} - 20.1\sqrt{T} - 2.29\frac{V}{V_A} \quad (7.6)$$

$$+ 174\frac{V}{C_s} - 1.78V_A + 164T^{1/3} + 0.000003\left(\frac{VR_{MP}}{X}\right)^2 + 0.00139\frac{VR_{MP}}{Y^*} - 2.73B_X + 10.6B_Y \quad (7.7)$$

$$+ 0.471NV + 38.0B + 2.48V - 39.3N + 6238N^{1/3} + 0.0107T + 0.360V_Y - 21.4\left(\frac{X}{R_{MP}}\right)^3 \quad (7.8)$$

$$- 23.9\left(\frac{X}{R_{MP}}\right)^2 + 307\left(\frac{X}{R_{MP}}\right) + 67.0\left(\frac{Y^*}{R_{MP}}\right)^2 \quad (7.9)$$

where $Y^* = \text{signY}\sqrt{(Y^2 + Z^2)}$.

As with the first model for the magnetic field, this is somewhat cumbersome and difficult to interpret. We again sought a model which would make more sense physically. This was very difficult to achieve and our final suggested model only has an overall R-Sq and R-Sq(adj) of 59.9% / 59.7% respectively.

Our proposed model is:

$$\begin{aligned}\left(\frac{V_{Geotail}}{V}\right)^{1/2} =& 0.185 + 0.0453(\text{signY}) + 0.00811\beta + 0.234\left(\frac{X}{R_{MP}}\right) \\ &+ 0.00122\left(\frac{X}{R_{MP}}\right)^2 - 0.0353\left(\frac{X}{R_{MP}}\right)^3 + 0.215\left(\frac{r}{R_{MP}}\right) \\ &+ 0.0792\left(\frac{r}{R_{MP}}\right)^2 - 0.0171(\text{signY})\left|\frac{r}{R_{MP}}\right|^3\end{aligned} \quad (7.10)$$

In our original survey, an observation of $V_{Geotail}/V = 1.08$ was made. Data relating to this observation has been removed from the following graph (Figure 7.31). The location of the data were on the outer edge of the flank (-0.8, 2.7) and we suspect that this was 'rogue' unshocked plasma. The effect of removing this point was to increase the R-Sq value of our model quite substantially while barely affecting that of the S66 value.

Figure 7.32 shows the predictions of the S66 model compared with that proposed in Equation 7.10. Our predictions are broadly similar in that we predict a very low velocity ratio in the sub-solar region and an increasing ratio as we move in the anti-Sunwards direction. The overall values which we find are lower than those predicted by S66, as reported earlier in our survey data. Additionally, our model shows slightly more stratification from the inner to the outer magnetosheath with the lowest values abutting the magnetopause, than does the S66 model.

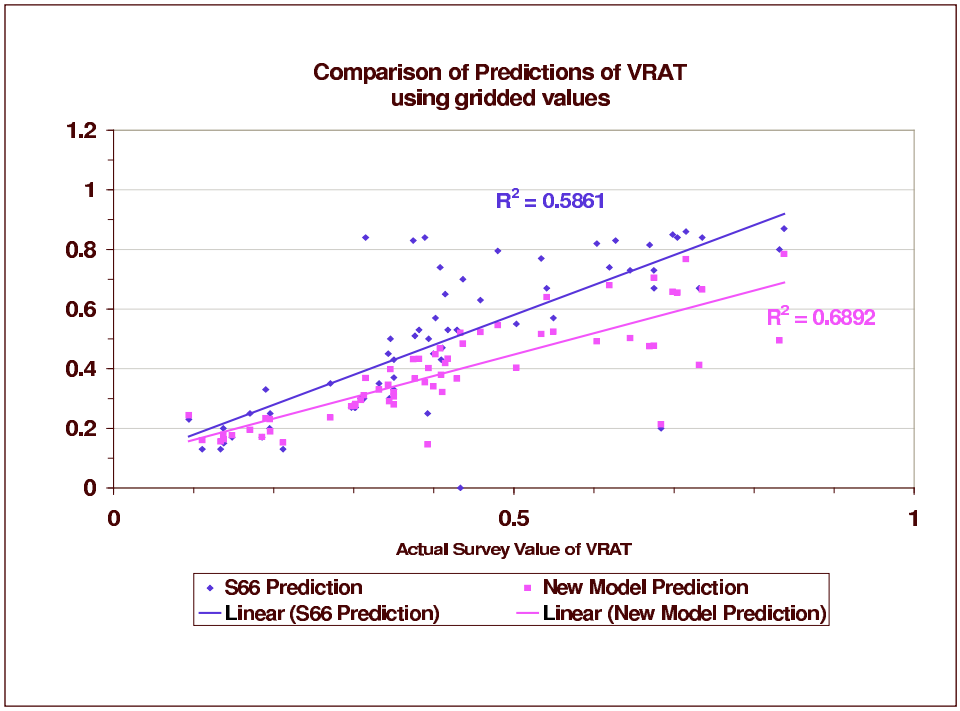

Figure 7.31: Velocity ratio model: This figure compares the fits from the S66 (blue diamonds) and new (pink squares) models against our survey data. A rogue survey data point giving a velocity ratio of 1.08 at location (-0.8,2.7) was removed from the data. The empirical model fits the data better than does that of S66. On a point-by-point basis, the predictions were worse for both models, S66 giving an R-Sq of 40% and the new model of 57%

Aberration of Stagnation Point

The data displayed in the figures in Section 7.2 support the notion of a stagnation point or line in the sub-solar region with lowered speeds. Higher densities and magnetic field intensities are also evident in the same location. Figure 7.33 displays the actual measured velocities against the YGSE (dawn-dusk) axis. The pink squares indicate all the values where we measured a flow of less than $40 kms^{-1}$. 138 binned minutes of data across eleven intervals contribute towards these low velocities. The data supports the existence of a stagnation point (or line) extending for approximately $1R_e$ across the magnetopause, centred around -2.6R_e . For a magnetopause stand-off distance of about $10R_e$, this would give an aberration of $\sim 14^o$ which is consistent with predictions of a dawnward shift in magnetosheath flow, for example Russell *et al.* [1981] and Crooker *et al.* [1984]. The figure shows 'wings' of lower velocity at ± 20 R_e in the Y_{GSE} direction. These are mainly located in the flanks at around -20R_e downtail in the X_{GSE} direction and from Figures 7.34 and 7.35 probably lie on the magnetopause side of the magnetosheath.

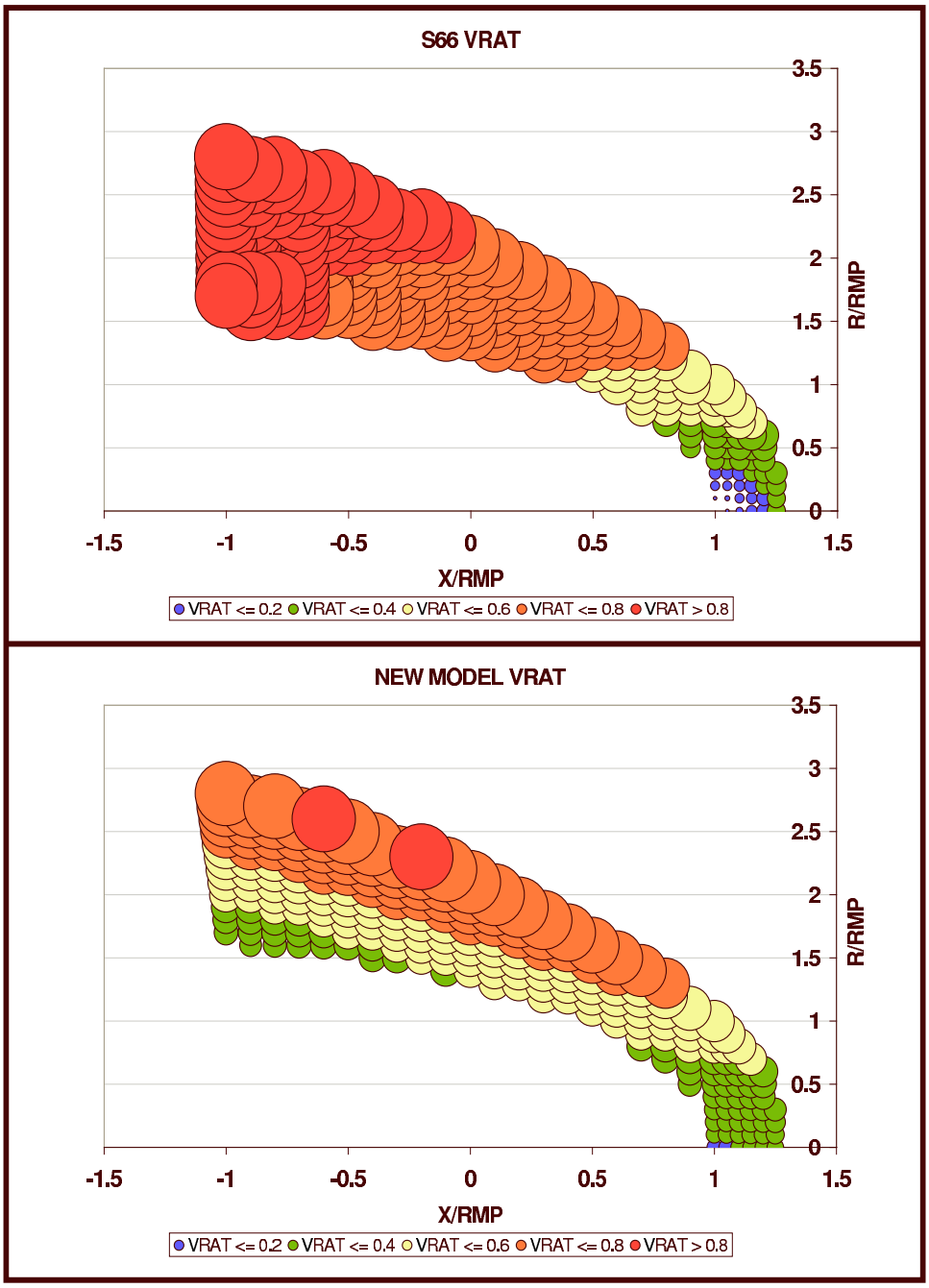

Figure 7.32: Velocity ratio model: The proposed model (shown here for $\beta = 0.7$) predicts generally lower velocity ratio values than that of S66, as seen in our survey data. On the whole, it is broadly similar in that there is a very low velocity ratio predicted in the sub-solar region (though less extensive than in the S66 model) and the ratio increases as we move anti-Sunwards. The new model shows more stratification within the magnetosheath than that of S66.

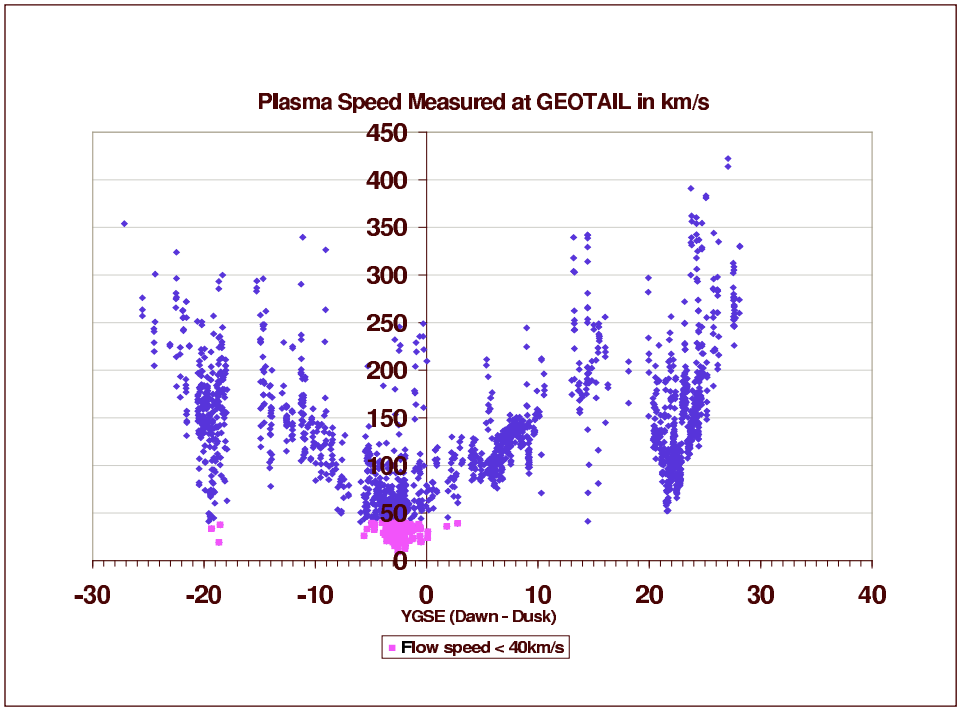

Figure 7.33: Stagnation point: the measured speed at Geotail is shown plotted against the actual YGSE coordinates of the spacecraft. The pink squares show the locations of all the speeds measured at under $40 kms^{-1}$. The data clearly demonstrates the existence of a stagnation point or line approximating to an aberration of $\sim 14^{\circ}$ as predicted by Russell *et al.* [1981] and Crooker *et al.* [1984]. The low speeds resembling wings at $\pm 20\ R_e$ in the Y_{GSE} direction are mainly located in the flanks near the magnetopause at around -$20R_e$ downtail in the X_{GSE} direction.

7.6 Sub-Alfvénic Flow

A key motivator in our reason for carrying out this survey was to look at the extent of sub-Alfvénic flow in the magnetosheath region, especially adjacent to the magnetopause. Observers claim to see steady-state reconnection poleward of the cusps (see Chapter 2.5) in a region where the sheath flow is traditionally expected to be super-Alfvénic. Such flow would carry reconnecting flux tubes and the rotational discontinuity downtail thus preventing a steady-state to take hold. The model which we developed earlier in this work (see Chapters 3 and 4) showed that the necessary condition for steady-state reconnection is:

$$| \mathbf{V}_{sh}.\hat{\mathbf{q}} | < | V_A \mathbf{b}_{ms}.\hat{\mathbf{q}} | \tag{7.11}$$

where $\hat{\mathbf{q}}$ is defined in Section 3.3. We arbitrarily reduced the density in order to demonstrate steady state reconnection poleward of the cusp.

We now consider whether the findings from our survey support a greater extent of sub-Alfvénic flow than traditionally predicted. We make two assumptions, firstly, for ease, that the magnetic fields are anti-parallel and we therefore do not have to consider the $\hat{\mathbf{q}}$ direction leading to the more familiar requirement that steady-state reconnection should occur where $V_{sh}/V_A < 1$. Secondly we assume that the system is cylindrically symmetric and that the results of our survey in the

ecliptic plane may be extended. We do not address the problem of the cusp. When calculating the Alfvén speed, we assumed only protons. If we add in alphas, then the density would increase, lowering the Alfvén speed and increasing M_A, making the flow more super-Alfvénic.

Figures 7.34 and 7.35 show the actual Alfvén speed and Alfvén Mach number respectively for the shocked flow where the value was calculated for each minute of binned data and then averaged into the grid. We see a reasonably even spread of Alfvén speeds, predominantly $\sim$ 100-200kms^{-1}, along X, with the lowest speeds in the sub-solar region. As expected, we see sub-Alfvénic flow in the sub-solar region. We also see it in the regions (0.2-0.4,1.2-1.3) and (0.5-0.6,0.9) together with a cluster downstream. If we are able to assume cylindrical symmetry then these results indicate that it may be possible to achieve sub-Alfvénic flow just poleward of the cusps, and also some way further back. It should be remembered that we have ignored the $\hat{\mathbf{q}}$ which may bring more of the flow within the steady-state condition.

We ran eight tests to compare the predicted locations of sub-Alfvénic flow using the traditional models and our suggested new ones. In the 'traditional' tests, we used a constant value for the magnetic field intensity ratio of 4.5, which is a typical value arising from the KF94 model and set $T = 30000K$ when calculating our plasma β. The values chosen were typical of our data set.

The results are shown in Figures 7.36 and 7.37. Predictably, the best conditions for sub-Alfvénic flow are low speed, low number density and high magnetic field strength. Using the S66 and KF94 models, only the test for V=300, N=4 and B=6 resulted in extensive sub-Alfvénic flow along the magnetopause. Our suggested new models predict this for all of the higher B=6 tests. It should be noted that the new models do not always predict more extensive regions of sub-Alfvénic flow than the traditional models. In particular, for the case where V=300, N=10 and B=2 we have only a very small region on sub-Alfvénic flow in the immediate sub-solar region, and in the case where V=450, N=10 and B=2 we predict no sub-Alfvénic flow using our empirical model.

From our survey, we found lower velocity and density ratios, and higher magnetic field ratios than predicted by traditional models. If, further, we assume cylindrical symmetry, then we propose that conditions favouring extensive sub-Alfvénic flow poleward of the cusps may occur.

Throughout our work, we have not discussed the cusps in any detail. The conditions at the cusps may lead to some localized variations in the magnetosheath flow and other parameters which we do not yet know. Experiments currently being carried out by Cluster II may lead to greater knowledge and understanding of the conditions in this area.

7.7 Summary

In this chapter we set out the results of our survey data. First, we directly compared them to the predictions of the S66 (and KF94) models and found that on the whole, the general predictions were supported, though values often differed. In particular we found the velocity and density ratios were lower than the predicted values, and that there was more variation in the magnetic

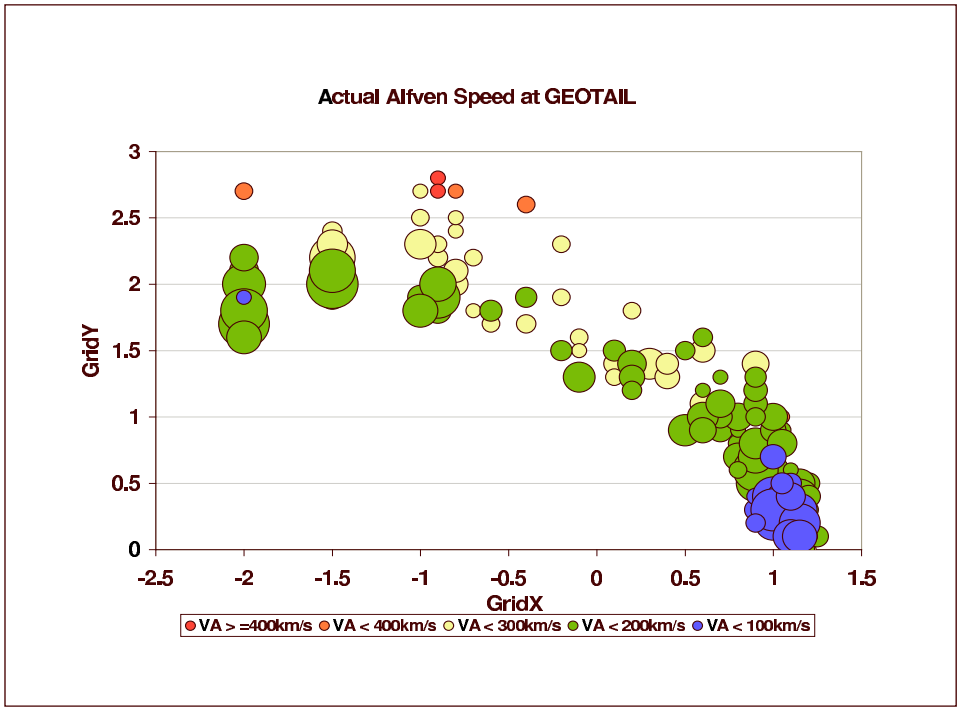

Figure 7.34: Alfvén speed.: The figure above shows the Alfvén speed for each minute of binned data further binned into the grid. In this figure, the width of the areas of the bubbles is proportional to $\sqrt{\text{count}}$. We used the equation $V_A(kms^{-1}) = 21.8B(nT)/N(cm^{-3})^{1/2}$ to calculate the Alfvén speed.

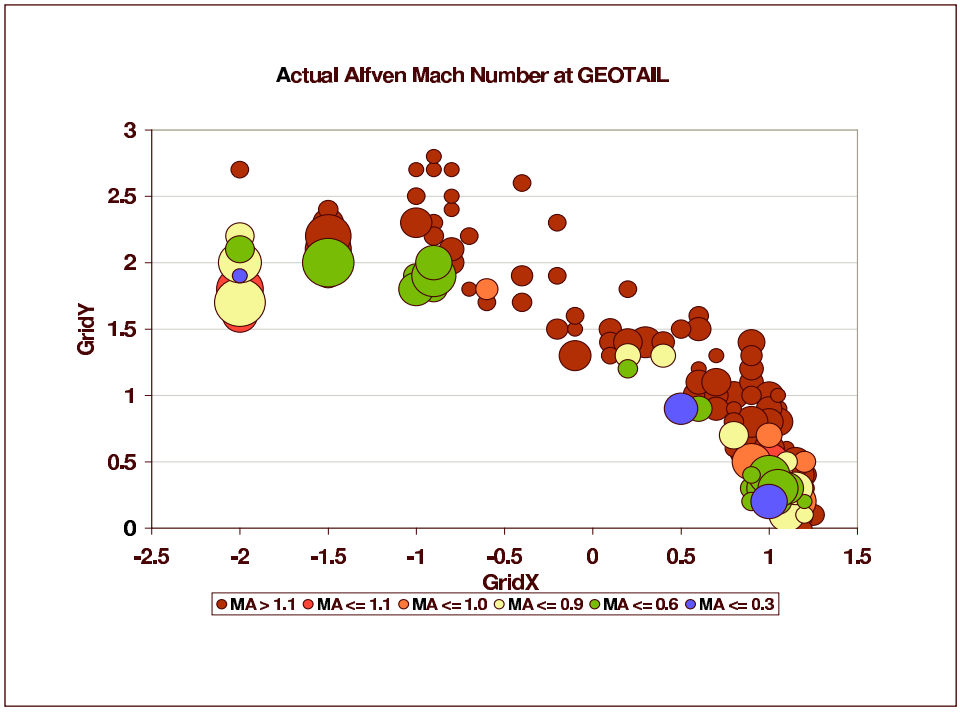

Figure 7.35: Alfvén Mach no.: The figure above shows the Alfvén Mach no. for each minute of binned data further binned into the grid.

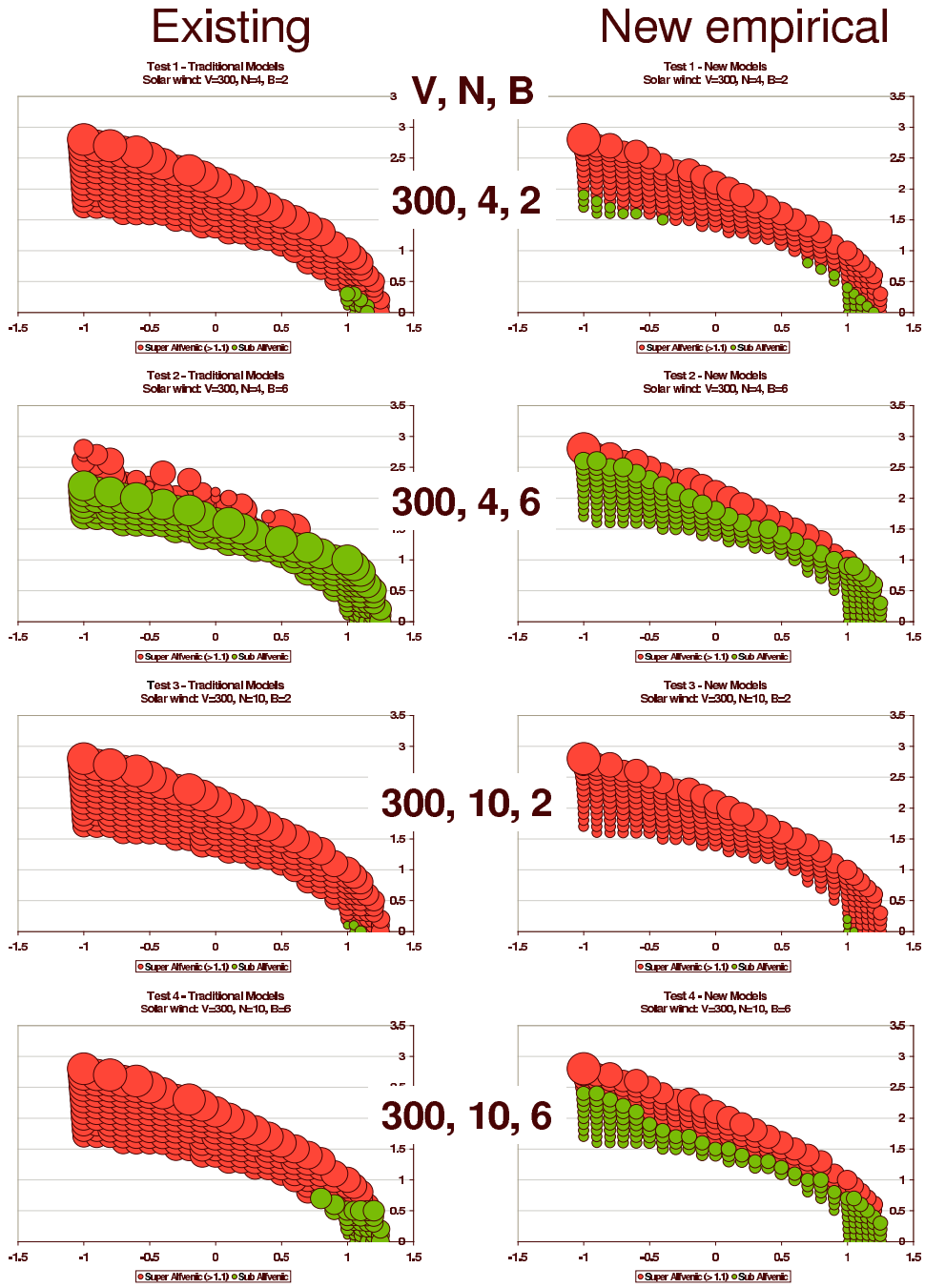

Figure 7.36: Sub-Alfvénic flow: Shows predictions for the location of sub-Alfvénic flow (green) resulting from the S66 and KF94 models on the left, and our suggested new models on the right. In this figure, all the results relate to a solar wind speed of $300 kms^{-1}$, and, moving down the figure, solar wind densities and magnetic field strengths of: $4cm^{-3}$ and $2nT$, $4cm^{-3}$ and $6nT$, $10cm^{-3}$ and $2nT$, and $10cm^{-3}$ and $6nT$. Figure 7.37 shows the results for solar wind speed of $450 kms^{-1}$. We have chosen to classify everything with an Alfvénic Mach number of up to 1.1 as sub-Alfvénic - this allows a notional 10% for other processes to encourage sub-Alfvénic flow, in particular $\hat{\mathbf{q}}$. See text for discussion of the results.

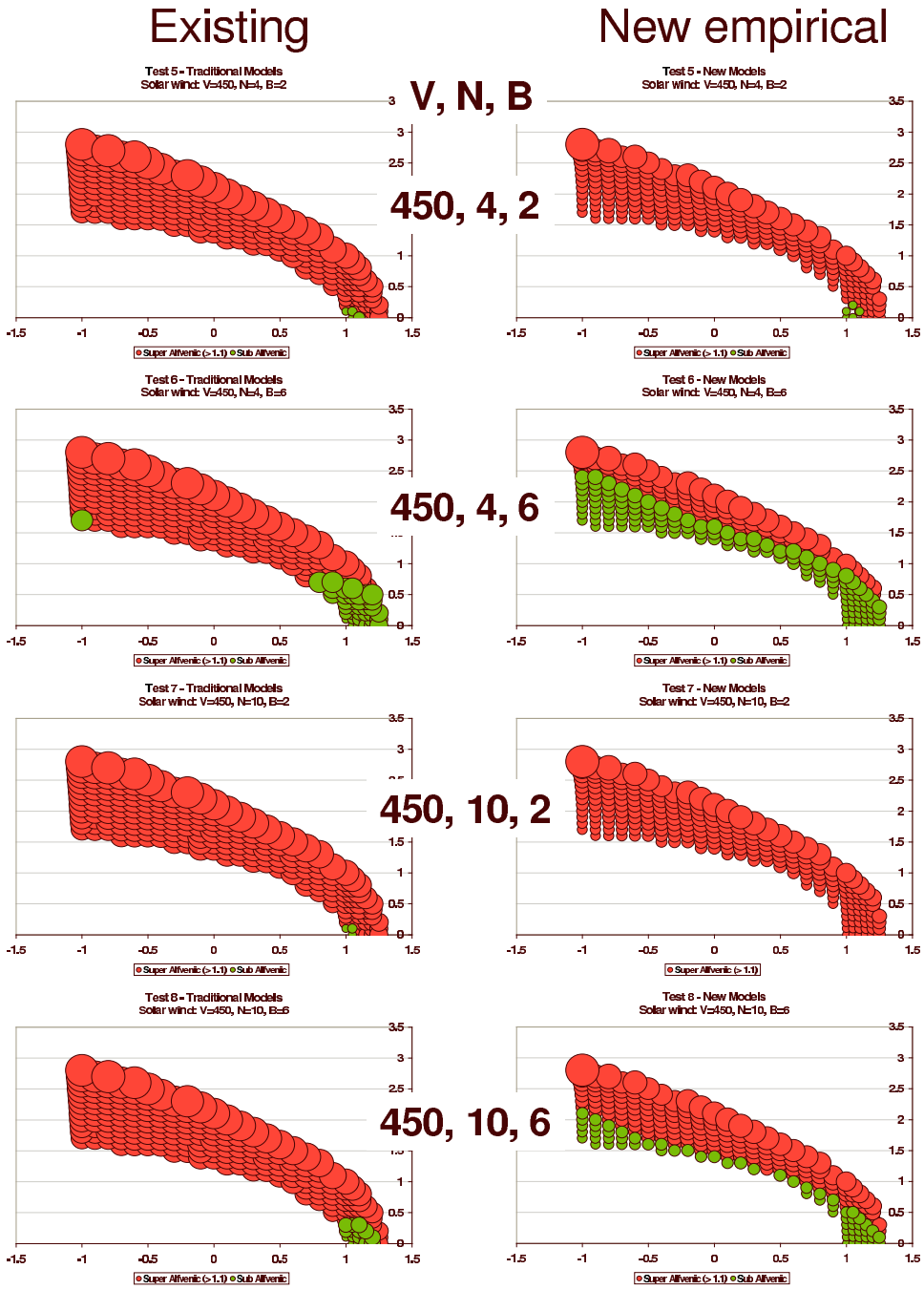

Figure 7.37: Sub-Alfvénic flow: Shows predictions for the location of sub-Alfvénic flow (green) resulting from the S66 and KF94 models on the left, and our suggested new models on the right. In this figure, all the results relate to a solar wind speed of $450 kms^{-1}$, and, moving down the figure, solar wind densities and magnetic field strengths of: $4cm^{-3}$ and $2nT$, $4cm^{-3}$ and $6nT$, $10cm^{-3}$ and $2nT$, and $10cm^{-3}$ and $6nT$. Figure 7.36 shows the results for solar wind speed of $300 kms^{-1}$. We have chosen to classify everything with an Alfvénic Mach number of up to 1.1 as sub-Alfvénic - this allows a notional 10% for other processes to encourage sub-Alfvénic flow, in particular $\hat{\mathbf{q}}$. See text for discussion of the results.

field intensity than predicted by KF94. Next, we performed a range of statistical tests on our data to identify general effects. We found some evidence of dawn-dusk effects, plasma β and Alfvénic Mach number. We did not find evidence for effects arising from sonic Mach number which was somewhat surprising. However, this may be because the range of sonic Mach numbers in our final data set was small, with the bulk lying within the range of 7-8.

Having looked in general at our results, we then sought to find three simple empirical models for the velocity, density and magnetic field ratios within the magnetosheath based upon our data. This was most straightforward for the density ratio and least straightforward for the velocity ratio. In each case, our proposed models fitted our survey data better than the existing models. Before applying these generally, though, it should be remembered that having started with a whole year of data, we were left with a useable 34 hours, and all of it in the ecliptic plane. We demonstrated that our data supports the existence of an aberrated stagnation point or line at the angles predicted in the literature.

Lastly, one of the main motivators for carrying out this survey was the search for a way in which sub-Alfvénic flow poleward of the cusps could be achieved in order for steady-state reconnection in that area to take place. Our survey showed sub-Alfvénic flow at an X/R_{mp} which would be slightly poleward of the cusp if we were able to assume cylindrical symmetry. We then used the existing models and our new models to compare the predicted locations of sub-Alfvénic flow along the magnetopause. We found that there were conditions (low upstream velocity and density and high magnetic field) where both models would predict extensive sub-Alfvénic flow, but that our empirical models also predicted it more often, including at higher upstream solar wind flow speed.

Chapter 8

Conclusions and Further Work

8.1 Conclusions

In Chapter 2 of this thesis we showed evidence that solar wind plasma enters the Earth's magnetosphere and described a number of mechanisms by which this process may be achieved.

The most successful paradigm for the transfer of the majority of transmitted plasma is believed to be that of magnetic reconnection. However, this mechanism is not universally accepted, nor is it well understood. Plasma from two separate regimes is separated by a current sheet (which is the magnetopause in the case of the solar-terrestrial interface) and will not mix under normal conditions. The plasma is 'tied' to the magnetic field lines of each regime (known as the 'frozen-in-flux' theorem) and magnetic reconnection requires the breakdown and reconfiguration of local magnetic field topology at a rotational discontinuity. A number of models for this process have been developed, from the Sweet-Parker model through the Petschek and Sonnerup models, to those proposed by Priest and Forbes, together with a range of computational models.

Magnetic reconnection is thought to be responsible for the transfer of solar wind energy, momentum and mass into the magnetosphere. Certain features such as accelerated plasma jets found inside the magnetopause boundary, the spectra of particles crossing the magnetopause boundary, global flow patterns and cleft currents are explained by the motion of open flux tubes (represented by the path of the rotational discontinuity) along the magnetopause. The flux tube motion is a result of the contraction of the reconnected magnetic field lines formed from the process coupled with the magnetosheath flow.

Understanding the motion of the open flux tubes can also contribute to the explanation of a number of other phenomena in the near-Earth environment such as polar ionosphere convection patterns and the entry of solar wind plasma at the polar caps.

Further, the conditions under which magnetic reconnection may occur would seem to mitigate against it occuring in the steady-state poleward of the cusp in the area where the local magnetosheath flow speed exceeds the local Alfvén speed. Despite this, a number of observers claim to

have seen evidence for steady-state reconnection in that region (Chapter 2.5).

In order to understand the motion of open flux tubes in more detail, we took as our starting point the work of CO89 which was based on a planar model of the dayside magnetopause, and which used simple models of the sheath flow to predict the motion of reconnecting flux tubes. We built a paraboloid surface to represent the magnetopause and used the models of S66 and KF94 to enable us to predict whether magnetic reconnection might occur for a wide range of magnetic field IMF conditions over the dayside and near-nightside magnetopause, and the motion of the open flux tubes formed by the reconnection.

We showed that the condition for steady-state reconnection was dependent not just on the ratio V_{sh}/V_A, but on the orientation of these velocities to the local reconnection line. We defined the perpendicular to the local reconnection line $\hat{\mathbf{q}}$ as being in the direction $\mathbf{B}_{ms} - \mathbf{B}_{gm}$ (see Chapter 3.3) and the condition thus became $\mid \mathbf{V}_{sh}.\hat{\mathbf{q}} \mid < \mid V_A \mathbf{b}_{ms}.\hat{\mathbf{q}} \mid$. One consequence of this definition is that rather than the limited oval region traditionally expected at $5R_e$ from the sub-solar point for sub-Alfvénic flow, a more sausage-shaped region may be possible (Chapter 4.1.5). We demonstrated how we may see a wider spread of sub-Alfvénic flow in regions poleward of the cusp by arbitrarily reducing the density.

Our model is also able to assist in identification of possible locations for the onset of reconnection and whether it will be steady-state or non-steady (for example FTEs).

From the experiments carried out using our model, we concluded that under conditions of northward B_Z, the model predictions were very sensitive to sub- or super-Alfvénic flow. Having reached this conclusion, we reviewed the literature for comparisons of the models of the magnetosheath parameters with survey data, in particularly S66. We found a number of specific surveys looking at, for example, crossings of the magnetopause, radial and stagnation line profiles (Chapter 5) but no more wide-ranging surveys.

We decided therefore to carry out a data survey in the dayside/near-nightside region using data from the Geotail satellite with the Wind satellite as the solar wind monitor. We took one year of Geotail data, filtered it as appropriate, binned it to the minute and linked it to the solar wind data. This is described more fully in Chapter 6.

In Chapter 7, we compared the resulting data directly with the S66 models and concluded that while the data followed the general predictions of the gas dynamic models, the measured velocity and density ratios were generally lower than predicted. We also looked at the KF94 magnetic field model and found more variation in our data than that predicted by their model.

We further analysed the data to examine a number of potential effects: seasonal, monthly, dawn-dusk, plasma β, sonic and Alfvénic Mach numbers. While we found evidence for seasonal and monthly effects, we concluded that these were an artefact reflecting a dawn-dusk bias in the Geotail data, where magnetosheath passes in our data set occurred more often on the afternoon/dusk side in the earlier part of the year, and dawn/morning side in the latter part of the year, and that there was no real evidence for a seasonal effect.

We found an Alfvénic Mach number effect for the magnetic field ratio, but not the velocity or number density ratios. We found a dawn-dusk effect for the velocity and number density ratios, the latter potentially supporting the work of Paularena *et al.* [2001]. We did not find a dawn-dusk effect for the magnetic field ratio. There was evidence for a plasma beta effect on the magnetic field ratio, none for the velocity ratio and slightly tentative for the number density ratio. We did not, however, find evidence for a sonic Mach number effect. As this was surprising, we reviewed our data set and found that almost of all of our data had a sonic Mach number of around 7-8 and hence there was insufficient spread to draw any conclusions about the sonic Mach number.

We then used regression techniques to draw up three simple, empirical models for the density ratio, velocity ratio and magnetic field strength within the magnetosheath.

An important motivation for our survey was the location of sub-Alfvénic flow at the magnetopause. We compared the predictions of the traditional models with those of our fitted empirical models for the potential location of such flow. We found that for solar wind of low speed, low density and high magnetic field strength, it was possible to find wide-spread sub-Alfvénic flow using the traditional models. However, using our empirical models, we found sub-Alfvénic flow could occur under a wider range of solar wind conditions.

We conclude therefore that if we may assume cylindrical symmetry and if our survey data is typical, then there are a range of solar wind conditions for which steady state reconnection poleward of the cusps may well occur. In Section 2.5 we presented observational evidence for sub-Alfvénic flow in high-latitude locations expected to be super-Alfvénic and we believe, therefore, that this conclusion is reasonable. Exploration of the cusps in greater detail is beyond the scope of this thesis.

8.2 Further Work

There are a number of ways in which the work carried out in this thesis could be extended.

Our model is intended to be fairly simple but some further development of the components could be carried out to enhance its use allowing, say, for different models of the magnetosheath flow, density and magnetic field. As it stands, the bow shock and magnetopause stand-off distances are inputs to the model, but a module to calculate these could be added. These improvements would not detract from the overall simplicity of the model, but may give a more accurate picture of flux tube motion or may allow for testing of different theories of the components.

The model itself is written in IDL but it may be useful to convert it into another programming language to allow it to be used more readily. Alternatively, a wide range of results could be catalogued and placed on the internet for reference.

With regard to the survey part of our work, we narrowly defined the range of data which we used, insisting that it should be confined to complete traversals of the magnetosheath. We had originally intended to scale the data between paraboloid representations of the bow shock and

magnetopause to try to gain a much more definitive picture of the contours of the parameters in the magnetosheath. However, we were left with insufficient data to make this worthwhile. It may be possible over time to build up data on enough passes to make this possible.

Our survey data were entirely in the ecliptic plane. While we have shown some evidence that similar results have been achieved out of this plane, it would be useful to carry out a similar survey using data from out-of-the-ecliptic magnetosheath passes to build up a more thorough picture of the magnetosheath region and whether, in fact, cylindrical symmetry is a reasonable assumption.

The cusps are an important physical region of the magnetopause, being the entry point for solar wind plasma into the Earth's magnetosphere. Recent developments, for example Cluster II may allow for investigations of magnetosheath parameters in this region and possible further development of our model.

Fresh data from a number of potential sources could be used to test whether the empirical models which we derived from our data set are more generally applicable, and also whether there are, for example, sonic Mach number effects which we could not discern.

Appendix A

Acronyms, Symbols, Subscripts

In this Appendix we list separately (1) Acronyms and Abbreviations, (2) Symbols, (3) Subscripts and Superscripts. Items are listed approximately in the order of introduction. A small number of symbols used only in a single section of the thesis and defined within that section have not been included.

A.1 Acronyms and Abbreviations

Chapter of First Use	Acronym	description
1	MHD	magnetohydrodynamic
	IMF	interplanetary magnetic field
	AU	astronomical unit (149.6 x 10^6 km) Earth - Sun distance
	R_e	Earth radius (6378 km)
2	LLBL	low latitude boundary layer
	PMAF	poleward moving auroral form
	KHI	Kelvin-Helmholtz instability
	FTE	flux transfer event
3	CO89	Cowley & Owen [1989]
	dHT	de Hoffmann Teller frame [de Hoffmann & Teller, 1950]
	GSM	Geocentric solar magnetospheric coordinate system
	GSE	Geocentric solar ecliptic coordinate system
	KF94	Kobel & Flückiger [1994]
5	GDCFM	gas dynamic convected field model
	AKR	auroral kilometric radiation
	S66	Spreiter *et al.* [1966] models for hydromagnetic flow
7	VRAT	ratio of magnetosheath velocity to solar wind velocity
	NRAT	ratio of magnetosheath density to solar wind density

IFRAT	ratio of magnetosheath ion (mass) flux to solar wind ion (mass) flux
BRAT	ratio of magnetosheath magnetic field strength to IMF strength
ANOVA	analysis of variance (see Appendix E)
t-test	statistical test (see Appendix E)

A.2 Symbols

Note that the majority of sub- and superscripts are listed separately in the next section.

Chapter of First Use	Symbol	description
1	$\mathbf{E}$	electric field
	$\mathbf{B}$	magnetic flux density (though often used for magnetic field intensity)
	$\mathbf{j}$	current density
	$\mathbf{V}$	fluid velocity
	μ_0	permeability of free space
	σ	conductivity
	R_M	magnetic Reynold's number
	L	characteristic length of spatial variation of magnetic field
	V	fluid speed
	ω	vorticity of hydrodynamic flow
	$\mathbf{n}$	unit normal vector
	P	fluid pressure
	ρ	density
	N	number density
	$\mathbf{V_{Amod}}$	modified Alfvén velocity for anisotropic plasma
	$\mathbf{V_A}$	Alfvén velocity
2	k	Boltzmann's constant (1.3807 x $10^{-23} J/K$)
	$\mathbf{V_{sh}}$	magnetosheath flow velocity in Earth (magnetopause) rest frame
	M	Mach Number (with appropriate relevant subscript e.g. M_A)
3	B_{sh}	magnetosheath field strength at magnetopause from Crooker *et al.* [1982]
	$\hat{\mathbf{q}}$	unit vector $\parallel$ to $\mathbf{B_{ms}} - \mathbf{B_{gm}}$
	$\hat{\mathbf{j}}$	unit vector $\parallel$ to local magnetopause current sheet and $\perp$ to $\hat{\mathbf{q}}$ and $\hat{\mathbf{n}}$
	$\hat{\mathbf{n}}$	unit vector outward normal to local current sheet $\perp$ to $\hat{\mathbf{q}}$ and $\hat{\mathbf{j}}$
	$\mathbf{V_{HT}}$	de Hoffmann Teller velocity
	$\mathbf{b}$	unit vector in direction of magnetic field
	$\mathbf{\Delta M}$	change in momentum flux
	ΔT	short time interval
	O	origin

Chapter of First Use	Symbol	description
	R_{mp}	stand-off distance from Earth to sub-solar point of magnetopause
	R_{bs}	stand-off distance from Earth to sub-solar point of bow shock
	X, Y, Z	X, Y or Z coordinates (subscripted to show GSE or GSM coordinates)
	ν	parameter used in KF94 model for definition of paraboloids
	x, y, z	x, y, z coordinates in KF94 system
	r	$\sqrt{x^2+y^2+z^2}$ in KF94 system
	l	distance from focus of paraboloid to magnetopause surface KF94
	A	constant used in KF94
	γ	ratio of specific heat capacities for a fluid
5	C_s	sound speed
	$\mathbf{H}$	magnetic field strength
	C_f	magnetosonic fast mode speed
	β	ratio of gas pressure to magnetic pressure for a plasma
	α	a constant
	$F(\rho, B, P_\parallel)$	a function used by Erkaev *et al.* [2000]
	ψ	angle between upstream flow and normal to the obstacle
6	eV/Q	measure of ion energy
	R-Sq	measure of correlation - see Appendix E
	Ti,YY	ion temperature in given direction
7	GridX	X/R_{mp}
	GridY	r/R_{mp}
	Q	$\sqrt{(X^2+Y^2+Z^2)}/R_{mp}$
	r	$\sqrt{Y^2+Z^2}$
	R-Sq(adj)	adjusted measure of correlation - see Appendix E
	p value	measure of the tail area of the normal curve - see Appendix E

A.3 Subscripts and Superscripts

Chapter of First Use	Symbol	example	description
1	n	v_n	normal component to surface under discussion
	t	v_t	tangential component
	$\perp$	$P_\perp$	perpendicular component
	$\parallel$	$P_\parallel$	parallel component
	1	ρ_1	upstream parameter
	2	ρ_2	downstream parameter

Chapter of First Use	Symbol	example	description
2	s	M_s	sonic or sound
3	$R1$, $R2$	V_{R1}	reconnected field line
	ms	$\mathbf{B_{ms}}$	magnetosheath parameter (but also see $\mathbf{V_{sh}}$)
	gm	$\mathbf{B_{gm}}$	geomagnetic parameter
	q, j, n	B_{msq}	components $\parallel$ to $\hat{\mathbf{q}}$, $\hat{\mathbf{j}}$ and $\hat{\mathbf{n}}$
	N, S	V_{HTN}	North-pole or South-pole connected component
	mp	O_{mp}	magnetopause
	bs	R_{bs}	bow shock
	imf	B_{imf}	IMF value
	X, Y, Z	B_X	X, Y, Z component
	GSE, GSM	B_{XGSE}	GSE or GSM component
	dis	$\mathbf{B^{dis}}$	distortion of magnetic field used by KF94
	KF	x_{KF}	KF94 component or value
	st	B_{st}	stagnation field
	sw	V_{sw}	solar wind component
5	∞	M_∞	alternative description for solar wind component
	f	M_f	fast mode (e.g. magnetosonic fast model)

Appendix B

Coordinates

GSM

X - axis from Earth to Sun

X-Z plane contains the Earth's magnetic dipole axis

+Z direction same sense as Earth's North pole

Y - perpendicular to Earth's magnetic dipole

+Y direction to dusk

GSE

X - axis from Earth to Sun

Y - axis in the ecliptic plan

+Y direction to dusk

Z - axis parallel to the ecliptic pole

GIPM

X - axis from Earth to Sun

XY plane contains the IMF

XY coordinates always opposite sign

Boundary Normal

A common notation is L, M, N where N is the normal to the relevant boundary e.g. the bow shock or the magnetopause (assumed to be infinitesimally thin), and the L and M coordinates are tangential to the boundary. One may be in the direction of maximum variance, and the other forming the third coordinate of a right-handed system. The system defined in Chapter 3.3 is such a system where:

$\hat{\mathbf{n}}$ is the outward normal to the local current sheet (magnetopause)

$\hat{\mathbf{q}}$ is tangential to the current sheet and parallel to the direction $\mathbf{B}_{ms} - \mathbf{B}_{gm}$ where $\mathbf{B}_{ms}$ and $\mathbf{B}_{gm}$ are respectively the draped magnetosheath and geomagnetic fields either side of the magnetopause

$\hat{\mathbf{j}}$ is also tangential to the local magnetopause current sheet and parallel to the current, i.e. in the direction $\nabla \wedge \mathbf{B}$

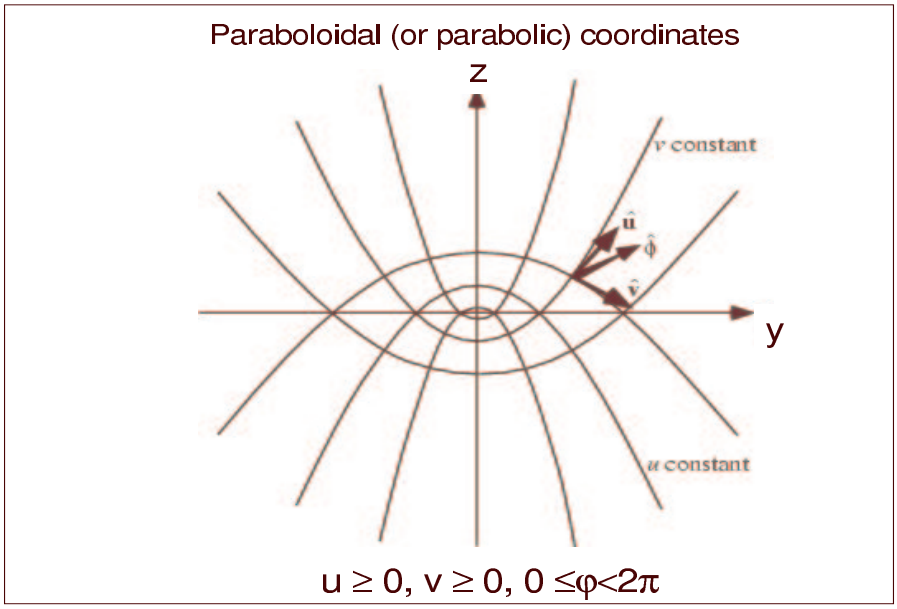

Figure B.1: Paraboloidal coordinates: two sets of coordinate surfaces are generated by revolving the parabolae about the z axis. Constant u and constant v will define a paraboloid surface. (Figure taken from http://mathworld.wolfram.com/ParabolicCoordinates.html)

Paraboloidal or Parabolic Coordinates

This coordinate system is used by KF94. This system has coordinates u, v, ϕ (see for example Spiegel [1974]) where:

$$x = uv\cos\phi,$$
$$y = uv\sin\phi \text{ and}$$
$$z = \tfrac{1}{2}(u^2 - v^2)$$

where $u \geq 0$, $v \geq 0$ and $0 \leq \phi < 2\pi$.

Alternatively:

$$u = \sqrt{r + z}$$
$$v = \sqrt{r - z}$$
$$r = \sqrt{x^2 + y^2 + z^2}$$
$$\tan\phi = \tfrac{y}{x}$$

Surfaces of constant u or v are paraboloid. KF94 use paraboloid surfaces generated by $\nu_{mp} = \sqrt{R_{mp}}$ and $\nu_{bs} = \sqrt{2R_{bs} - R_{mp}}$ to represent the magnetopause and bow shock surfaces respectively. The origin (and focus of the paraboloids) of the KF94 system is at $X_{GSM} = R_{mp}/2$.

The equivalent paraboloids in GSM coordinates are, for the magnetopause, $Y^2+Z^2 = 2R_{mp}(R_{mp}-X)$ and for the bow shock, $Y^2 + Z^2 = 2(2R_{bs} - R_{mp})(R_{bs} - X)$. The distance from the focus of the magnetopause paraboloid to a point on the magnetopause surface is given by $l = \frac{3R_{mp}}{2} - X$.

Appendix C

Catalogue

In this Appendix we display a range of the resulting features of the models which we used in Chapters 3 and 4 of this thesis.

- Section C.1
  Plots of the shear angles between KF94 and the geomagnetic field model used in our model development. The shears are shown in three blocks of nine clock angle orientations of the IMF. In each case we use an IMF of approximate strength $10nT$. The first set of plots shows the shear angles for IMFs with positive B_X, the second set shows IMFs with no B_X component, and the third set with negative B_X.

- Section C.2
  Plots of the magnetopause current strength calculated from our models. As above, three blocks of nine orientations are shown.

- Section C.3
  Plots of the current contours equating to threshold ΔB_q of $35nT$ and $50nT$, as described in Chapter 3, overplotted onto the shear angle contours. We show a single set of plots for negative B_X. Plots for positive B_X are a rotation of 180° for the same B_Y, B_Z clock angles.

- Section C.4
  Plots of the Alfvén speed calculated from our models. Note that these relate only to the work of Chapters 3 and 4 and not to the empirical models derived in Chapter 7. In these plots, we have used a density of 100% (see text) under northward IMF. As above, we have shown a single set of plots for negative B_X. Plots for positive B_X are a rotation of 180° for the same B_Y, B_Z clock angles.

We have chosen not to display the Alfvén Mach number (V_{sh}/V_A) contours. This is because our conclusions related not to this ratio but to the more subtle relationship with the reconnection line and we feel, therefore, that to display them would be misleading.

C.1 Shears

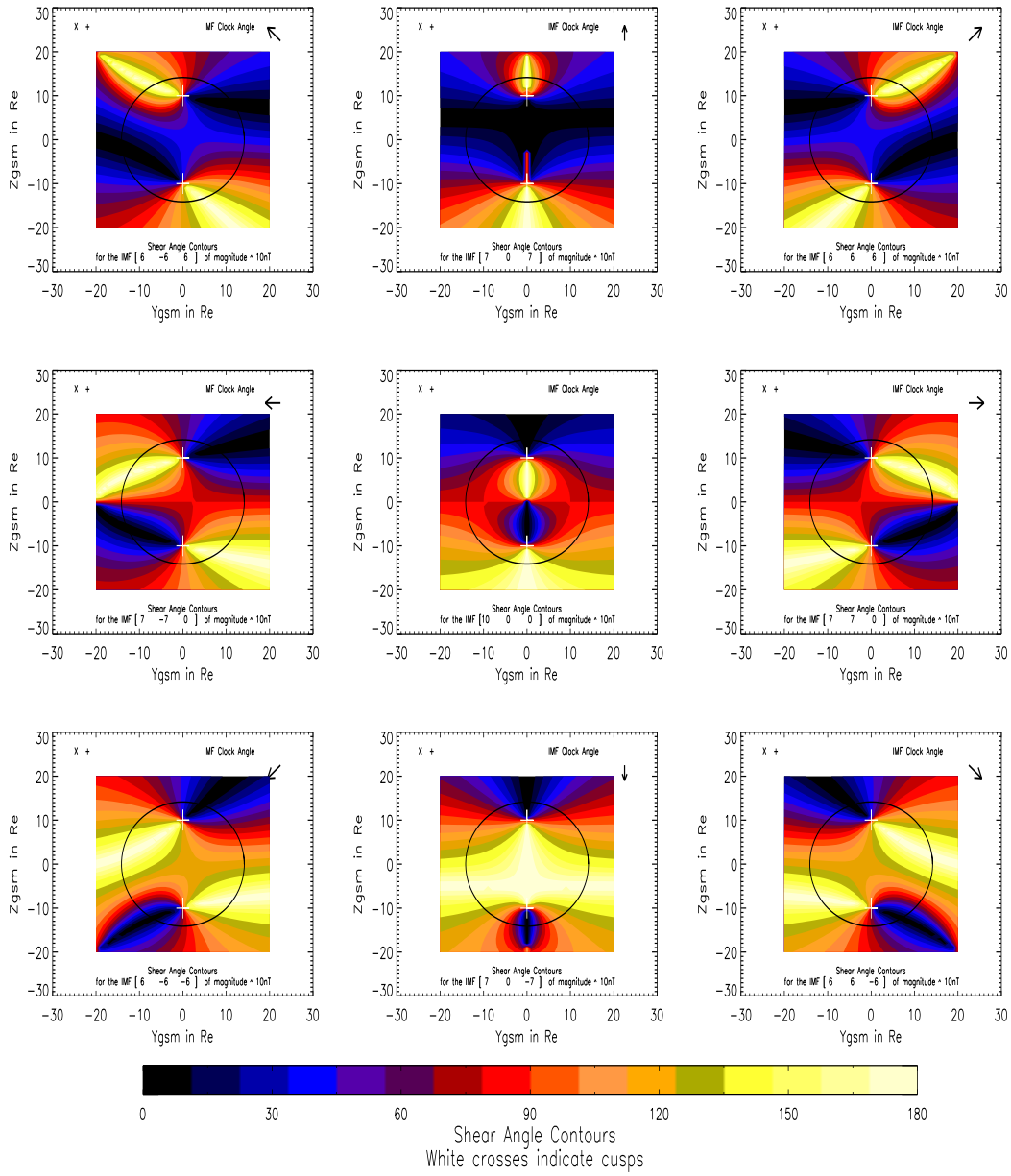

Figure C.1: This shows the shears for positive Bx.

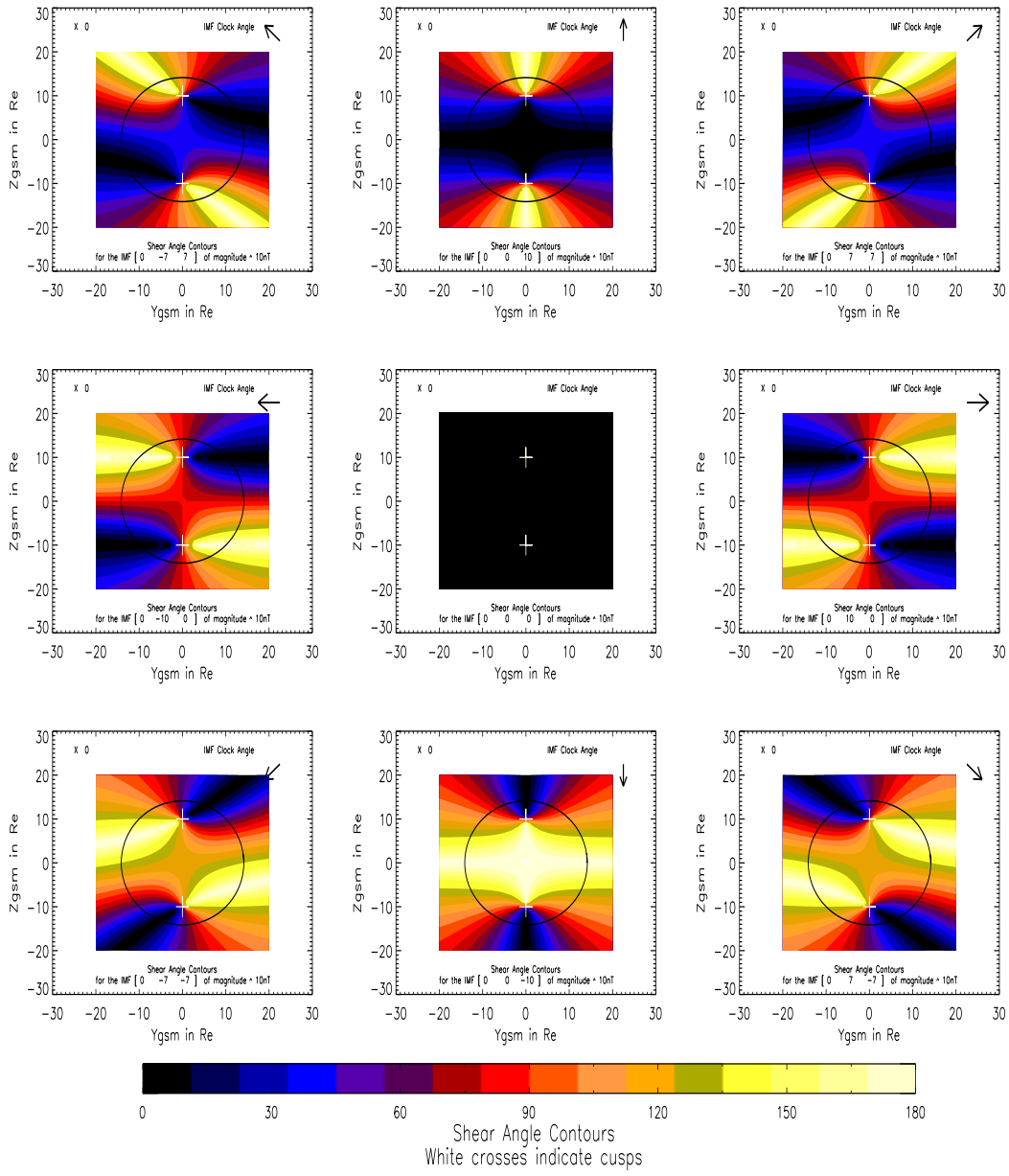

Figure C.2: This shows the shears for zero Bx.

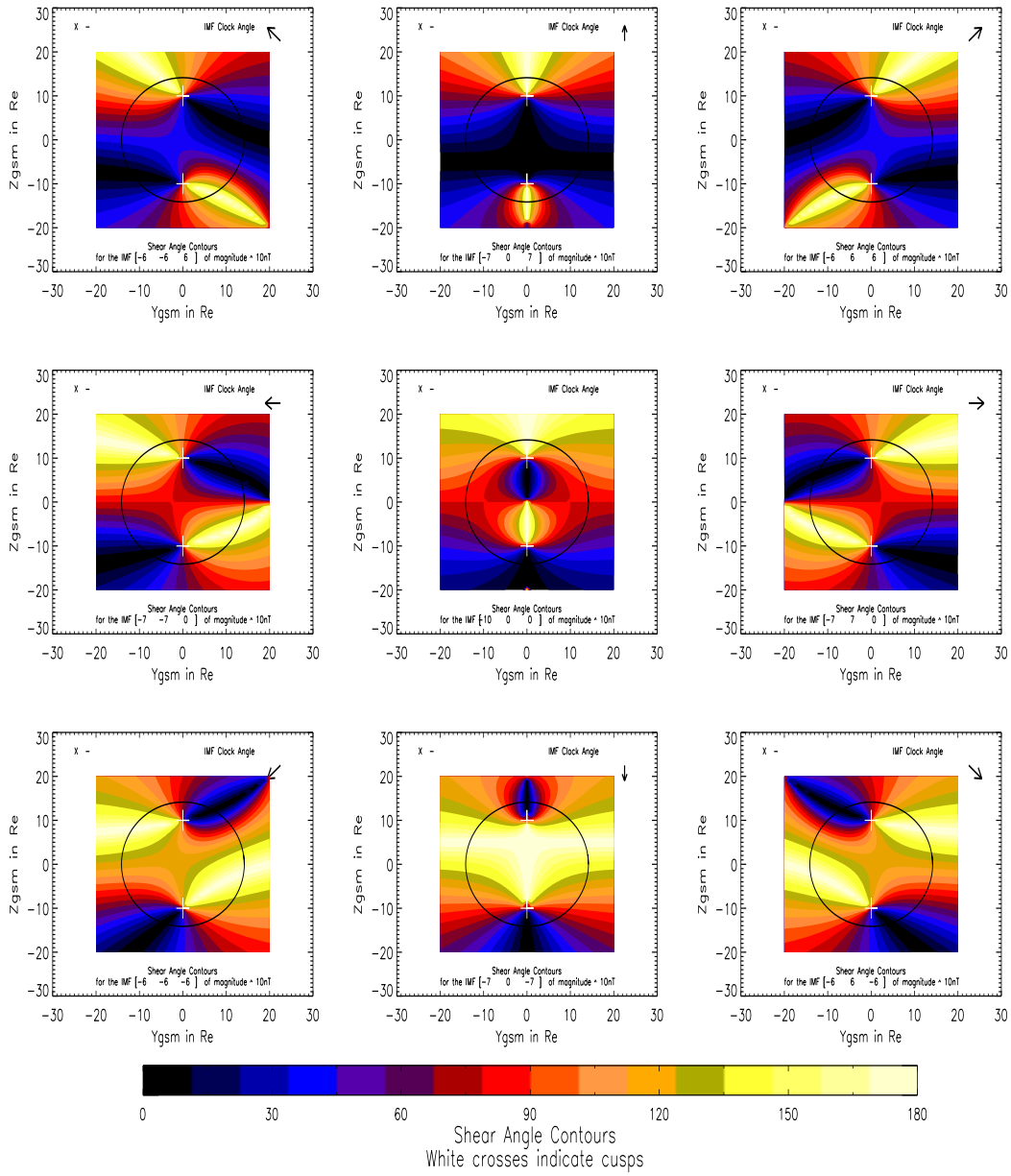

Figure C.3: This shows the shears for negative Bx.

C.2 Currents

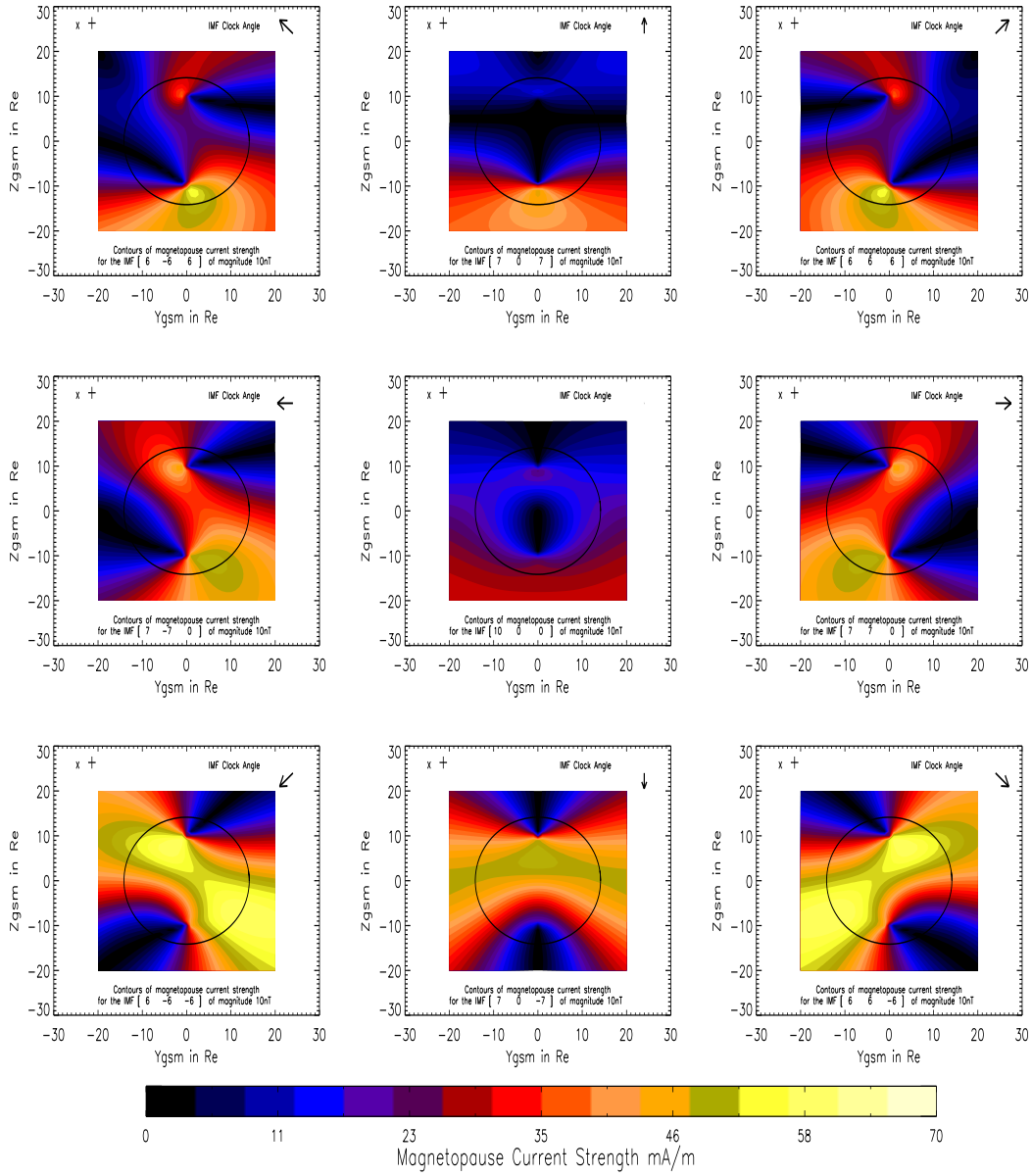

Figure C.4: Magnetopause current strength contours +X

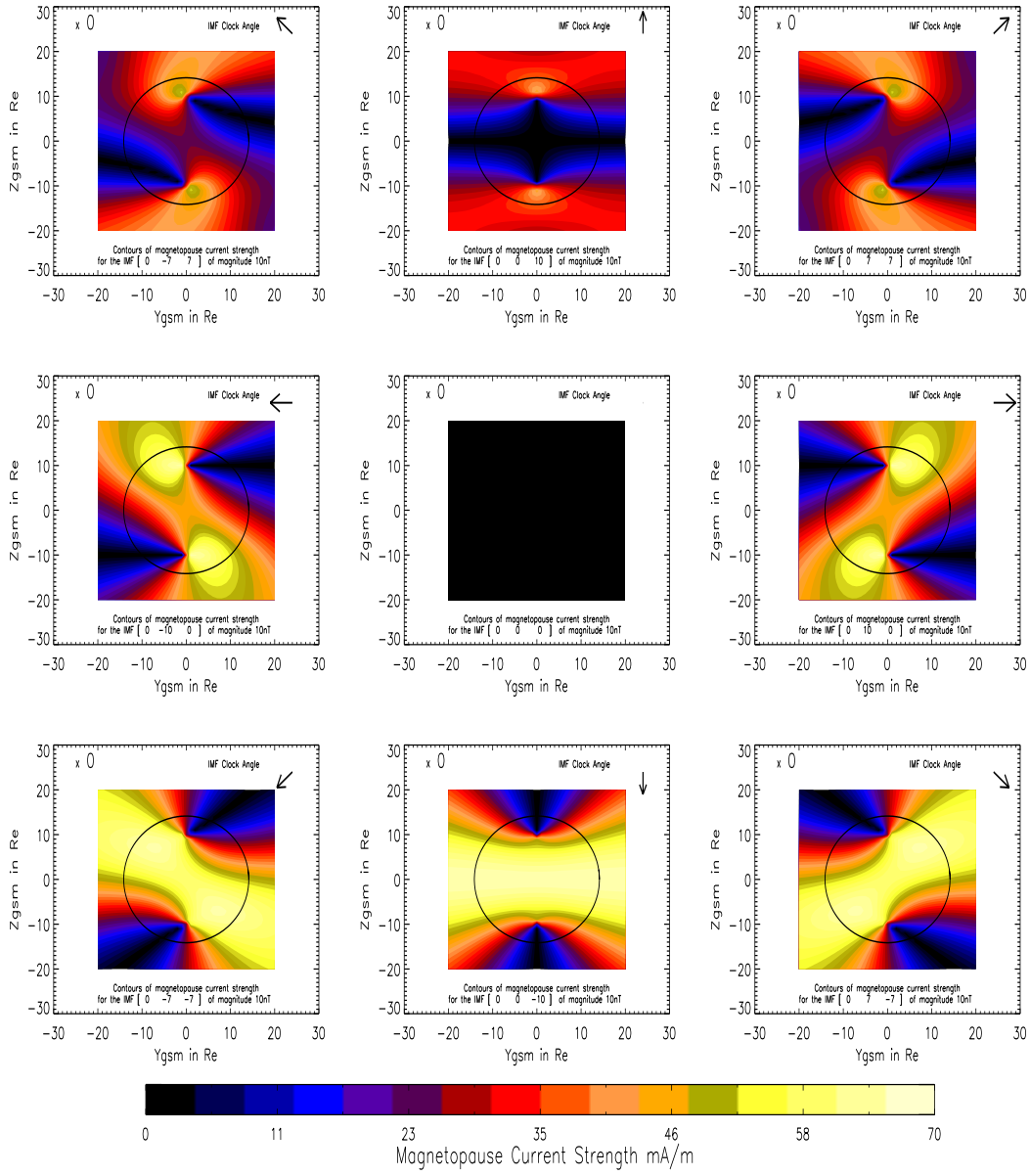

Figure C.5: Magnetopause current strength contours 0X

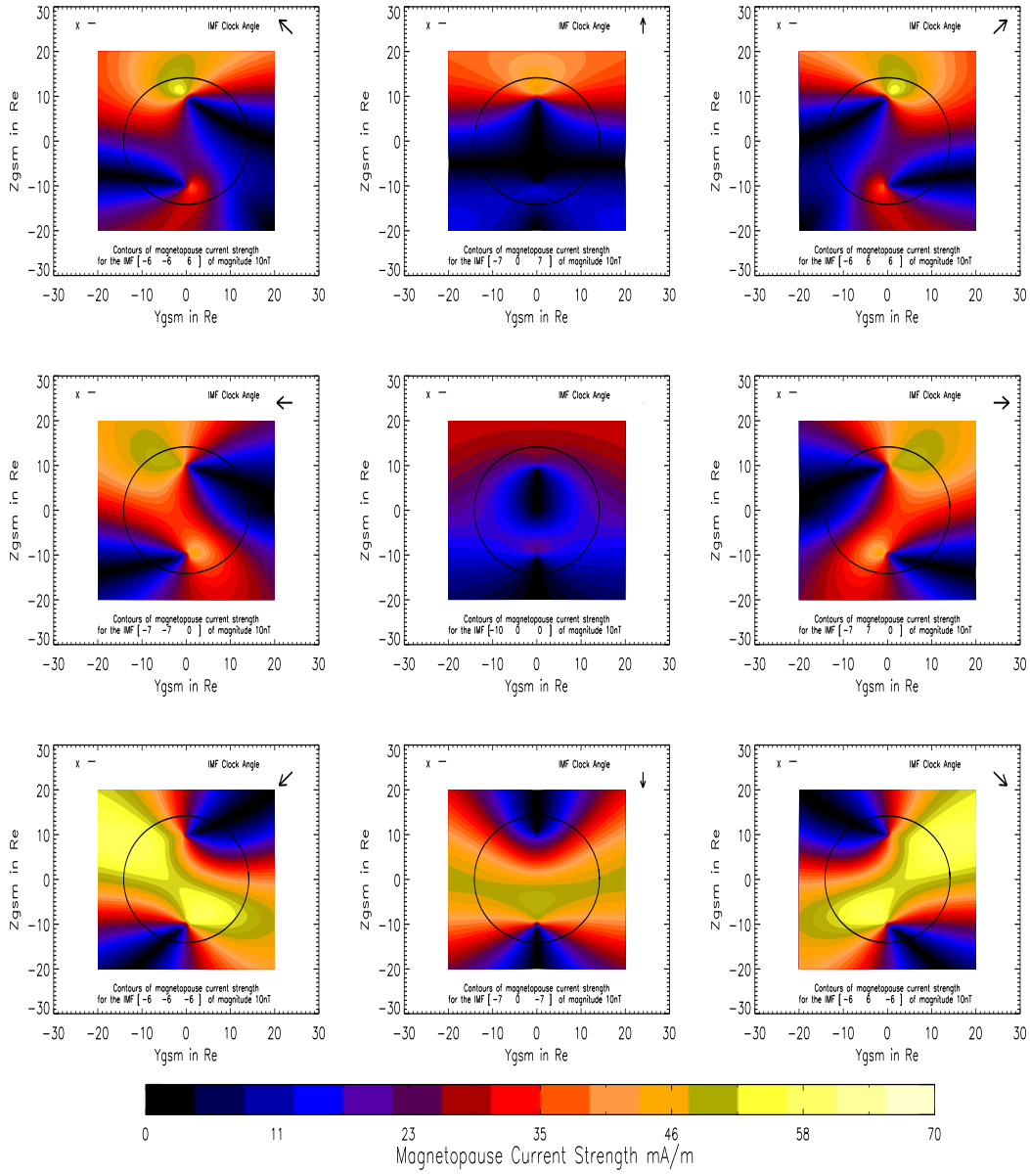

Figure C.6: Magnetopause current strength contours -X

C.3 Overplotting of shears with current contours

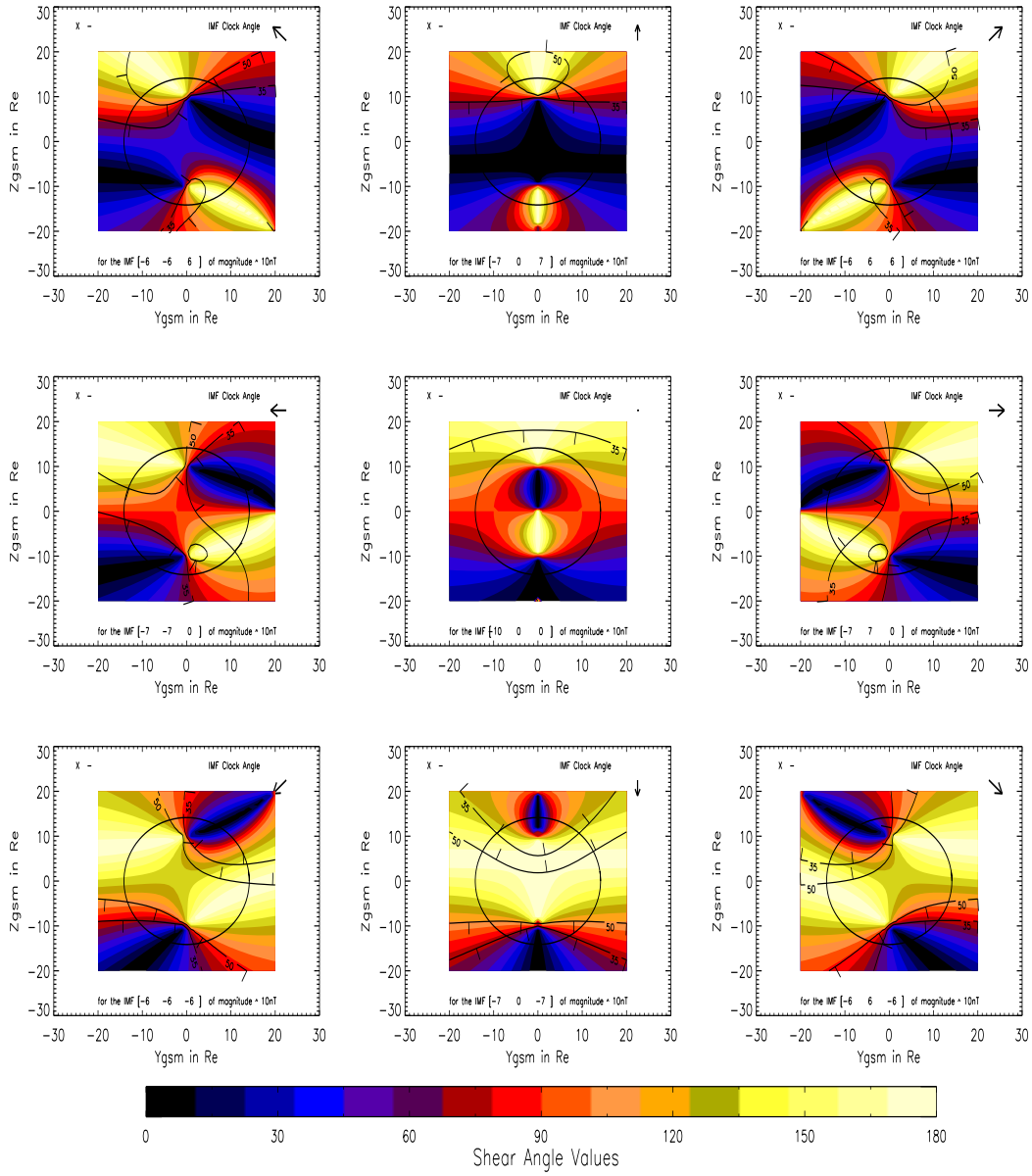

Figure C.7: Overplotting of shears with current contours -X

C.4 Alfvén speeds

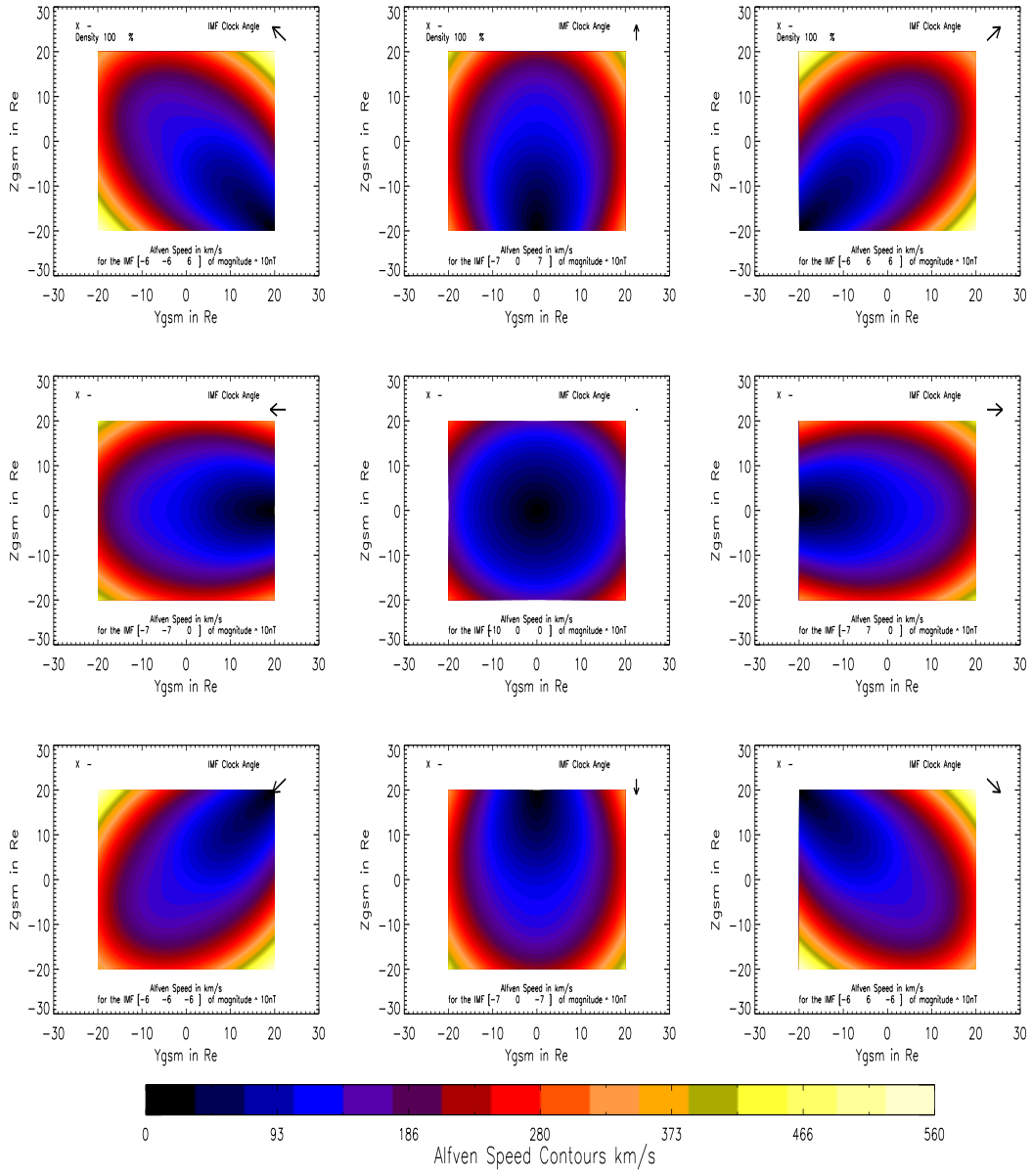

Figure C.8: Alfvén speeds at the magnetopause -X

Appendix D

Intervals

The next 2 pages show a list of the 54 useable intervals included in the analysis of Chapters 6 and 7 of this thesis.

INTERVAL	From	To
MAR0405	04/03/1997 19:13:30	05/03/1997 01:53:30
MAR0910	09/03/1997 21:43:30	10/03/1997 03:35:30
MAR1112	11/03/1997 03:30:30	12/03/1997 09:06:30
MAR1515	15/03/1997 04:45:30	15/03/1997 10:22:30
MAR2020	20/03/1997 12:30:30	20/03/1997 16:40:30
MAR2223	22/03/1997 01:42:30	23/03/1997 04:55:30
APR0203	02/04/1997 07:34:30	03/04/1997 07:16:30
APR0505	05/04/1997 14:21:30	05/04/1997 16:10:30
APR0708	07/04/1997 20:57:30	08/04/1997 18:54:30
APR1010	10/04/1997 17:17:30	10/04/1997 18:52:30
APR1616	16/04/1997 06:19:30	16/04/1997 10:11:30
APR1819	18/04/1997 18:24:30	19/04/1997 14:21:30
MAY0505	05/05/1997 09:31:30	05/05/1997 23:04:30
MAY0707	07/05/1997 10:37:30	07/05/1997 14:07:30
MAY1011	10/05/1997 15:43:30	11/05/1997 08:39:30
MAY1212	12/05/1997 17:45:30	12/05/1997 20:37:30
MAY2122	21/05/1997 15:21:30	22/05/1997 02:17:30
MAY2323	23/05/1997 10:01:30	23/05/1997 12:43:30
JUN0203	02/06/1997 22:30:30	03/06/1997 02:20:30
JUN0607	06/06/1997 16:41:30	07/06/1997 03:53:30
JUN0808	08/06/1997 05:41:30	08/06/1997 09:07:30
JUN1313	13/06/1997 12:42:30	13/06/1997 17:22:30
JUN1819	18/06/1997 22:06:30	18/06/1997 23:59:30

INTERVAL	From	To
JUL1313	13/07/1997 14:12:30	13/07/1997 20:27:30
JUL1415	14/07/1997 21:02:30	15/07/1997 00:40:30
JUL1819	18/07/1997 21:31:30	19/07/1997 02:29:30
JUL2020	20/07/1997 02:25:30	20/07/1997 05:27:30
JUL2424	24/07/1997 05:32:30	24/07/1997 08:47:30
JUL2929	29/07/1997 07:47:30	29/07/1997 12:03:30
JUL3030	30/07/1997 10:03:30	30/07/1997 15:12:30
AUG0303	03/08/1997 14:43:30	03/08/1997 18:18:30
AUG0808	08/08/1997 16:28:30	08/08/1997 22:07:30
AUG0910	09/08/1997 20:07:30	10/08/1997 01:03:30
AUG1314	13/08/1997 22:32:30	14/08/1997 03:55:30
AUG1919	19/08/1997 03:35:30	19/08/1997 06:52:30
SEP1414	14/09/1997 03:45:30	14/09/1997 07:41:30
SEP1515	15/09/1997 10:54:30	15/09/1997 19:06:30
SEP2021	20/09/1997 15:51:30	21/09/1997 00:11:30
OCT0606	06/10/1997 07:27:30	06/10/1997 19:10:30
OCT1010	10/10/1997 04:04:30	10/10/1997 07:34:30
OCT1515	15/10/1997 05:38:30	15/10/1997 10:13:30
OCT2020	20/10/1997 10:48:30	20/10/1997 14:42:30
OCT2525	25/10/1997 16:04:30	25/10/1997 18:38:30
NOV0405	04/11/1997 22:05:30	05/11/1997 05:13:30
NOV1010	10/11/1997 07:03:30	10/11/1997 08:41:30
NOV2020	20/11/1997 11:35:30	20/11/1997 15:09:30
NOV2525	25/11/1997 08:20:30	25/11/1997 18:51:30
NOV2829	28/11/1997 04:03:30	29/11/1997 07:46:30
NOV3030	30/11/1997 09:21:30	30/11/1997 19:42:30
DEC0304	03/12/1997 18:14:30	04/12/1997 15:00:30
DEC0506	05/12/1997 21:54:30	06/12/1997 04:52:30
DEC0808	08/12/1997 14:01:30	08/12/1997 19:40:30
DEC1616	16/12/1997 04:37:30	16/12/1997 14:15:30
DEC2121	21/12/1997 11:38:30	21/12/1997 19:19:30

Table D.1: List of 54 intervals from which useable data was obtained for the survey.

Appendix E

Statistics

In the first section, we give a brief overview of the statistical tests used in the survey part of this work. In the second section, we show the residual plots of our proposed empirical model for density ratio as an example of our process.

E.1 Statistics

E.1.1 Correlation and Regression

For a regression analysis between predictor X and variable Y, R measures the strength of the relationship. R^2 (R-Sq) measures the % of variation in Y explained by the regression model between X and Y.

$$R^2 = \frac{\text{explained variation}}{\text{total variation}} \text{ x } 100\% \tag{E.1}$$

R-Sq(adj) is R adjusted for degrees of freedom. If a variable is added to an equation, R will get larger even if the added variable is of no real value. To compensate for this, Minitab also prints R-Sq (adj), which is an approximately unbiased estimate of the population R that is calculated by the formula.

Assumptions are that the residuals are normally distributed, have a constant variance (i.e. do not increase as predicted Y increases - known as funnelling), that they are independent of X and that they are stable with time.

Just because R-sq is high, it does not necessarily mean that there is a causation (the principle that 'correlation does not mean causation') and just because there is a low R-sq, does not necessarily mean that there is no relationship. A number of factors can lead to this situation: small sample size, other factors not taken into consideration, range of data too small, data not stratified correctly.

The p value is the measure of the tail area of the normal curve, between the value of interest and the extreme. If the p value is small, it means that the probability that the value of interest

comes from the normal distribution by chance is small, and therefore something else may well be going on.

E.1.2 Central Limit Theorem

If X1, X2 ... Xn is a random sample of size n, from a population with mean μ and variance σ^2, i.e.

$$\overline{X} \sim N\left(\mu, \frac{\sigma^2}{n}\right) \tag{E.2}$$

then if n is large, $\overline{X}$ is approximately normal even if the population is not.

E.1.3 t-tests

t-tests may be used to compare, for example, data against a target where the population standard deviation is unknown. While there is an assumption of normality, t-tests are fairly robust to non-normality due to the 'central limit theorem'.

We assume independent, random, unbiased samples and continuous or pseudo-continous data. We have assumed that our grid is pseudo-continuous.

A 2-sample t-test may be used to examine differences between two groups of data to see if an observed difference is real. If we obtain a p value of < 0.05, we can assume that the two groups are probably different.

A paired t-test may be used where the data are matched. In our case, they are matched on the grid.

A 2-sample t-test tests the mean first, then the difference between the means. A paired t-test first takes the differences between the two sample and then examines the mean of the differences.

E.1.4 ANOVA

ANalysis Of VAriance is used for studying the statistical significance of relationships between the dependent variable Y and single or multiple independent variables organized into discrete groups or levels. It is used to determine whether or not mean responses at each level are the same. While it assumes equal variances and normal populations, it is robust to non-normality of uni-modal distributions because of the 'Central Limit Theorem'.

E.2 Statistical Background to Proposed Empirical Models

In this section we show the residuals plots for the density ratio model as an example of the analysis which we carried out on the proposed models.

We fitted the model:

$$\left(\frac{N_{Geotail}}{N}\right)^{1/3} = 1.18 - 0.1\beta + 0.00706M_A + 0.255\left(\frac{X}{R_{MP}}\right) - 0.0668\left(\frac{r}{R_{MP}}\right) - 0.035 \text{ signY} \tag{E.3}$$

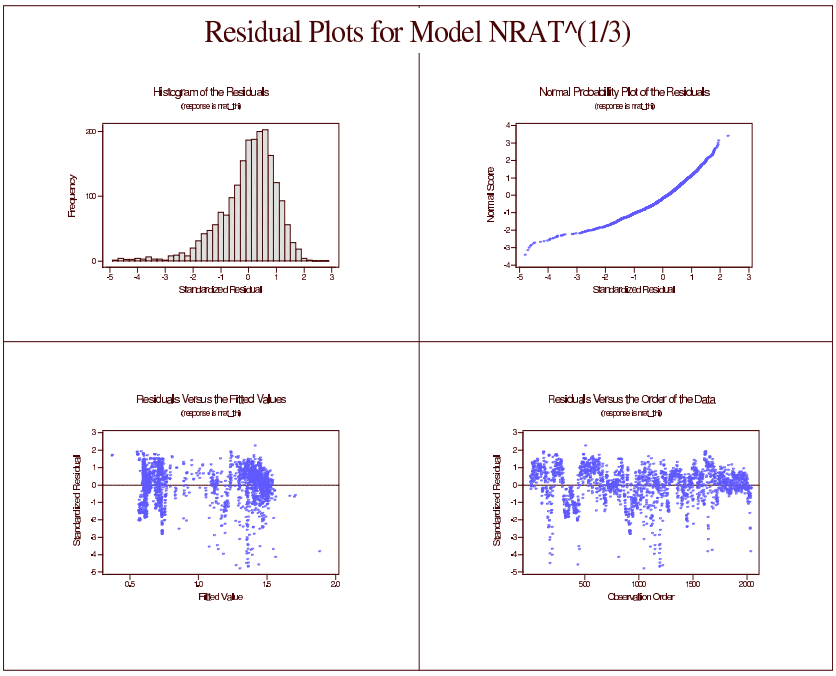

Figure E.1: The plots show a reasonable level of normality and acceptable (i.e. random) fits against the fitted data and the order of the data.

to the data with an R-Sq and R-Sq-Adj of 77.3%.

Figure E.1 shows the residual plots for the regression fit. These are acceptable in terms of normality and random distribution with fit and order.

Bibliography

Alexeev, I. I., Sibeck, D. G., & Bobrovnikov, S. Y. 1998. Concerning the location of magnetopause merging as a function of the magnetopause current strength. *J.Geophys.Res.*, **103**(A4), 6675–6684.

Alksne, A. Y. 1967. The steady-state magnetic field in the transition region between the magnetosphere and the bowshock. *Planet. Space Sci.*, **15**, 239.

Alksne, A. Y., & Webster, D. L. 1970. Magnetic and electric fields in the magnetosheath. *Planetary and Space Science*, **18**, 1203.

Angelopoulos, V., Phan, T. D., Larson, D. E., Mozer, F. S., Lin, R. P., Tsuruda, K., Hayakawa, H., Mukai, T., Kokubun, S., Yamamoto, T., Williams, D. J., McEntire, R. W., Lepping, R. P., Parks, G. K., Brittnacher, M., Germany, G., Spann, J., Singer, H. J., & Yumoto, K. 1997. Magnetotail flow bursts: association to global magnetospheric circulation, relationship to ionospheric activity and direct evidence for localization. *Geophysical Research Letters*, **24**(18), 2271–2274.

Avanov, L. A., Smirnov, V. N., Waite, Jr., J. H., Fuselier, S. A., & Vaisberg, O. L. 2001. High-latitude magnetic reconnection in sub-Alfvénic flow: Interball Tail observations on May 29,1996. *J.Geophys.Res.*, **106**(A12), 29491–502.

Axford, W. I. 1962. The interaction between the solar wind and the Earth's magnetosphere. *J.Geophys.Res.*, **67**, 3791.

Axford, W. I. 1984. Magnetic field reconnection. *In:* Hones, E. W. Jr. (ed), *Magnetic reconnection in space and laboratory plasmas.* Geophysical Monograph 30. AGU, Washington D. C.

Axford, W. I., & Hines, C. O. 1961. A unifying theory of high-latitude geophysical phenomena and geomagnetic storms. *Can. J. Phys.*, **39**, 1433.

Baum, P. J., & Bratenahl, A. 1980. Magnetic reconnection experiments. *Adv. Electronics and Electron Phys.*, **54**, 1.

Berchem, J., & Russell, C. T. 1984. Flux-transfer events on the magnetopause - spatial distribution and controlling factors. *J.Geophys.Res.*, **89**, 6689.

Berdichevsky, D., Thejappa, G., Fitzenreiter, R. J., Lepping, R. L., Yamamoto, T., Kokubun, S., McEntire, R. W., Williams, D. J., & Lin, R. P. 1999. Widely spaced wave-particle observations during GEOTAIL and Wind magnetic conjunctions in the Earth's ion foreshock with near-radial interplanetary magnetic field. *Journal of Geophysical Research*, **104**(A1), 463–482.

Besser, B. P., Pudovkin, M. I., Lebedeva, V. V., Zaitseva, S. A., & Meister, C-V. 2000. Magnetosheath structure in an anisotropic plasma model. *Astrophysics and Space Science*, **274**(1-2), 399–405.

Biermann, L. 1951. Kometschwerfe und solare Korpuskularstrahlung. *Z. Astrophys.*, **29**, 274.

Biernat, H. K., Heyn, M. F., Rijnbeek, R. P., Semenov, V. S., & Farrugia, C. J. 1989. The structure of reconnection layers: application to the Earth's magnetopause. *J.Geophys.Res.*, **94**(A1), 287–98.

Biskamp, D. 1982. Resistive MHD processes. *Physica Scripta*, **T2**(2), 405–9.

Biskamp, D. 1984a. Anomalous resistivity and viscosity due to small-scale magnetic turbulence. *Plasma Phys. & Controlled Fusion*, **26**(1B), 311–19.

Biskamp, D. 1984b. Magnetic reconnection across an X-type neutral point slow shocks versus current sheets. *Phys.Lett.A*, **105A**(3), 124–8.

Biskamp, D. 1986. Magnetic reconnection via current sheets. *Phys.Fluids*, **29**(5), 1520–31.

Bostik, W. H. 1956. Experimental study of ionized matter projected across a magnetic field. *Phys.Rev.*, **104**, 292.

Burgess, D. 1995. Collisionless Shocks. *Pages 129–163 of:* Kivelson, Margaret G., & Russell, Christopher T. (eds), *Introduction to Space Physics*. Cambridge, U.K.: Cambridge University Press.

Burlaga, L. F., Lemaire, J., & Turner, J. M. 1977. Interplanetary current sheets at 1 AU. *J.Geophys.Res.*, **82**, 3191.

Burns, A., & Mitchell, W. 1946. *Measuring Business Cycles*. National Bureau of Economic Research, New York.

Cahill, L. J. Jr., & Amazeen, P. G. 1963. The boundary of the geomagnetic field. *J.Geophys.Res.*, **68**, 1835.

Cameron, J. 1997. *The Speculator - How to Ride Cycles. Berkeley Futures Ltd, 38 Dover Street, London, UK, W1X 3RB*. internet:
www.consensus-inc.com/sample/spec-rep/spec3.htm, March 1997.

Chandler, M. O., Fuselier, S. A., Lockwood, M., & Moore, T. E. 1999. Evidence of component merging equatorward of the cusp. *J.Geophys.Res.*, **104**(A10), 22623–22633.

Chapman, S., & Ferraro, V. C. A. 1931. A new theory of magnetic storms. *Terr. Magn. Atmosph. Elec.*, **36**, 171–186.

Chen, S. H, *et al.* 1993. Anomalous aspects of magnetosheath flow and of the shape and oscillations of the magnetopause during an interval of strongly northward interplanetary magnetic field. *J.Geophys.Res.*, **98**(A4), 5727–5742.

Chen, S. H., Boardsen, S. A., Fung, S. F., Green, J. L., Kessel, R. L., Tan, L. C., Eastman, T. E., & Craven, J. D. 1997. Exterior and interior polar cusps: Observations from Hawkeye. *J.Geophys.Res.*, **102**(A6), 11335 – 11347.

Coleman, I. J., Pinnock, M., & Rodger, A. S. 2000. The ionospheric footprint of antiparallel merging regions on the dayside magnetopause. *Ann. Geophys.*, **18**(5), 511 – 516.

Coleman, I. J., Chisham, G., Pinnock, M., & Freeman, M. P. 2001. An ionospheric convection signature of antiparallel reconnection. *J.Geophys.Res.*, **106**(A12), 28995–9007.

Coleman, I. J., Chisham, G., Pinnock, M., & Freeman, M. P. 2003. Reply to comment by S. M. Petrinec and S. A. Fuselier on "An ionospheric convection signature of antiparallel reconnection". *J.Geophys.Res.*, **108**(A5), 10.1029/2002JA009568.

Cooling, B. M. A., Owen, C. J., & Schwartz, S. J. 2001. Role of the magnetosheath flow in determining the motion of open flux tubes. *J.Geophys.Res.*, **106**(A9), 18,763–18,775.

Coroniti, F. V., & Eviatar, A. 1977. Magnetic field reconnection in collisionless plasma. *Astrophys. J. Supple. Ser.*, **33**, 189.

Cowley, S. W. H. 1976. Comments on the merging on nonantiparallel magnetic fields. *J.Geophys.Res.*, **81**(19), 3455–3458.

Cowley, S. W. H. 1979. The formation and properties of boundary layers downstream from neutral lines in an open magnetosphere. *Magnetospheric Boundary Layers, ed Battrick, B. Rep. ESA SP-148, Noordwick, Netherlands*, 333.

Cowley, S. W. H. 1981. Magnetospheric asymmetries associated with the Y-component of the IMF. *Planet.Space Sci.*, **29**, 79.

Cowley, S. W. H. 1982. The causes of convection within the Earth's magnetosphere: a review of developments during the IMS. *Rev.Geophys.Space Phys.*, **20**, 531.

Cowley, S. W. H. 1985. Magnetic reconnection. *Pages 121–155 of:* Priest, E. R. (ed), *Solar System Magnetic Fields*. Geophysics and Astrophysics Monographs.

Cowley, S. W. H. 1995. Theoretical perspectives of the magnetopause: A tutorial review. *Pages 29–43 of:* Song, P., Sonnerup, B. U. Ö., & Thomsen, M. F. (eds), *Physics of the Magnetopause*. Geophysical Monograph Series, vol. 90. AGU, Washington D. C.

Cowley, S. W. H., & Owen, C. J. 1989. A simple illustrative model of open flux tube motion over the dayside magnetopause. *Planet. Space Sci.*, **37**(11), 1461–1475.

Cowley, S. W. H., Southwood, D. J., & Saunders, M. A. 1983. Interpretation of magnetic field perturbations in the Earth's magnetopause boundary layers. *Planet.Space Sci.*, **31**, 1237.

Cravens, Thomas E. 1997. *Physics of Solar System Plasmas.* Cambridge Atmospheric and Space Science Series. Cambridge, UK: Cambridge University Press.

Crooker, N. U. 1979. Dayside merging and cusp geometry. *J.Geophys.Res.*, **84**(A3), 951–959.

Crooker, N. U. 1985. A split separator line merging model of the dayside magnetopause. *J.Geophys.Res.*, **90**(A12), 12104–12110.

Crooker, N. U., Eastman, T. E., Frank, L. A., Smith, E. J., & Russell, C. T. 1981. Energetic magnetosheath ions and the interplanetary magnetic field orientation. *Journal of Geophysical Research*, **86**(A6), 4455–4460.

Crooker, N. U., Siscoe, G. L., & Mullen, P. R. 1982. Magnetic field compression at the dayside magnetopause. *Journal of Geophysical Research*, **87**(A12), 10407–10412.

Crooker, N. U., Siscoe, G. L., Eastman, T. E., Frank, L. A., & Zwickl, R. D. 1984. Large-scale flow in the dayside magnetosheath. *J.Geophys.Res.*, **89**(A11), 9711–9719.

Crooker, N. U., Luhmann, J. G., Russell, C. T., Smith, E. J., Spreiter, J. R., & Stahara, S. S. 1985. Magnetic field draping against the dayside magnetopause. *J.Geophys.Res.*, **90**(A4), 3505–3510.

Crooker, N. U., Siscoe, G. L., & Toffoletto, F. R. 1990. A tangent subsolar merging line. *J.Geophys.Res.*, **95**(A4), 3787–3793.

Daly, P. W., & Keppler, E. 1983. Remote sensing of a flux transfer event with energetic particles. *J.Geophys.Res.*, **88**, 3971.

Daly, P. W., Williams, D. J., Russell, C. T., & Keppler, E. 1981. Particle signature of magnetic flux transfer events at the magnetopause. *J.Geophys.Res.*, **86**, 1628.

Davydov, D. M. 1995. Heliophysical influences are modulating human autonomic and behavioural activities. *In:* Sokolov, E. N., Abramson, Ch., Bezdenezhnykh, B. N., Spinks, J. A., Balaban, P. M., & Nezlina, N. I. (eds), *Man, Neuron, Model: E-mail communications in psychophysiology*, vol. 6. Association of Psychophysiologists, Moscow.

de Hoffmann, F., & Teller, E. 1950. Magneto-hydrodynamic shocks. *Phys.Rev.*, **80**, 692.

Dorman, L. I. 2001. *Forecasting dangerous situations for spacecrafts and aircrafts caused by large solar energetic particle events.* Israel Cosmic Ray Center and Emilio Segre Observatory, March 2001.

Drake, J. F. 1995. Magnetic reconnection: A kinetic treatment. *Pages 155–165 of:* P., Song., Sonnerup, B. U. Ö., & Thomsen, M. F. (eds), *Physics of the Magnetopause*. Geophysical Monograph, vol. 90. American Geophysical Union, Washington DC 20009.

Drakou, E., Sonnerup, B. U. Ö., & Lotko, W. 1994. Self-consistent steady-state model of the low-latitude boundary-layer. *J.Geophys.Res.*, **99**(A2), 2351 – 2364.

Dubinin, E., Skalsky, A., Song, P., Savin, S., Kozyra, J., Moore, T. E., Russell, C. T., Chandler, M. O., Fedorov, A., Avanov, L., Sauvaud, J-A., & Friedel, R. H. W. 2002. Polar-Interball coordinated observations of plasma and magnetic field characteristics in the regions of the northern and southern distant cusps. *Journal of Geophysical Research*, **107**(A5), SMP2–1–2–16.

Dungey, J. W. 1954a. Electrodynamics of the outer atmosphere. *Pennsylvania State University Ionosphere Research Laboratory Report*, **69**.

Dungey, J. W. 1954b. The propagation of Alfvén waves through the ionosphere. *Pennsylvania State University Ionosphere Research Laboratory Report*, **57**.

Dungey, J. W. 1958. *Cosmic Electrodynamics*. New York: Cambridge University Press.

Dungey, J. W. 1961. Interplanetary field and the auroral zones. *Phys.Rev.Lett.*, **6**, 47–48.

Dungey, J. W. 1963. The structure of the exosphere or adventures in velocity space. *In: Geophysics, the Earth's environment*. New York: Gordon and Breach.

Durand-Manterola, Héctor Javier, & Mendoza, Blanca. 2001. A plausible physical mechanism for the interaction Sun-Biota. *Boletin de Investigacion Cientifica*, **1**(1), ariel.igeofcu.unam.mx/∼hdurand/bolinvcien/volumen1/solbiota.html.

Eastman, T., & Christon, S. 1995. Ion composition and transport near the Earth's magnetopause. *Pages 131–137 of:* P., Song., Sonnerup, B. U. Ö., & Thomsen, M. F. (eds), *Physics of the Magnetopause*. Geophysical Monograph, vol. 90. American Geophysical Union, Washington DC 20009.

Elsen, R. K., & Winglee, R. M. 1997. The average shape of the magnetopause: A comparison of three-dimensional global MHD and empirical models. *J.Geophys.Res.*, **102**(A3), 4799–4819.

Erkaev, N. V., Farrugia, C. J., & Biernat, H. K. 1999. Three-dimensional, one-fluid, ideal MHD model of magnetosheath flow with anisotropic pressure. *Journal of Geophysical Research*, **104**(A4), 6877–87.

Erkaev, N. V., Biernat, H. K., & Farrugia, C. J. 2000. Ideal magnetohydrodynamic flow around a blunt body under anisotropic pressure. *Physics of Plasma*, **7**(8), 3413–3420.

Fairfield, D. H. 1971. Average and unusual locations of the Earth's magnetopause and bow shock. *Journal of Geophysical Research*, **76**, 6700–6716.

Fairfield, D. H. 1979. Structure of the magnetopause: Observations and implications for reconnection. *Space Sci. Rev.*, **23**, 427.

Fairfield, D. H., & Cahill, Jr., L. J. 1966. Transition region magnetic field and polar magnetic disturbances. *J.Geophys.Res.*, **80**(4), 535–542.

Farrugia, C. J., Erkaev, N. V., Vogl, D. F., Biernat, H. K., Øieroset, M., Lin, R. P., & Lepping, R. P. 2001. Anisotropic magnetosheath: comparison of theory with Wind observations near the stagnation streamline. *Journal of Geophysical Research*, **106**(A12), 29373–85.

Feigin, V. L., Nikitin, Yu. P., & Vinogradova, T. E. 1997. Solar and geomagnetic activities: are there associations with stroke occurrence? *Cerebrovasc.Dis.*, **7**, 345–348.

Fennell, J. F. 1973. Access of solar protons to the Earth's polar cap. *J.Geophys.Res.*, **78**, 1036.

Forbes, T. G., & Priest, E. R. 1987. A comparison of analytical and numerical models for steadily driven magnetic reconnection. *Rev. Geophys.*, **25**, 1583.

Formisano, V. 1979. Orientation and shape of the Earth's bow shock in three dimensions. *Planet. Space Science*, **27**, 1151.

Fu, S. Y., Pu, Z. Y., Guo, S. C., & Liu, Z. X. 1995. Kinetic Alfvén Wave Instability and Wave-Particle Interaction at the Magnetopause. *Pages 73–76 of:* Ashour-Abdalla, Maha, Chang, Tom, & Dusenbery, Paul (eds), *Space Plasmas: Coupling between small and medium scale processes.* Geophysical Monograph 86. American Geophysical Union, Washington DC 20009.

Fu, Z. F., & Lee, L. C. 1986. Multiple X line reconnection. II. The dynamics. *J.Geophys.Res.*, **91**(A12), 13373–83.

Fuller, Mike, Laj, Carlo J., & Herrero-Bervera, Emilio. 1996. The reversal of the Earth's magnetic field. *American Scientist*, **84**(6).

Fuselier, S. A., Klumpar, D. M., Peterson, W. K., & Shelley, E. G. 1989a. Direct injection of ionospheric O^+ into the dayside low latitude boundary layer. *Geophys.Res.Lett.*, **16**, 1121–1124.

Fuselier, S. A., Trattner, K. J., & Petrinec, S. M. 2000a. Cusp observations of high- and low-latitude reconnection for northward interplanetary magnetic field. *J.Geophys.Res.*, **105**(A1), 253266.

Fuselier, S. A., Petrinec, S. M., & Trattner, K. J. 2000b. Stability of the high-latitude reconnection site for steady northward IMF. *Geophys.Res.Lett.*, **27**(4), 473–476.

Fuselier, S. A., Waite, J. H Jr., Avanov, L. A., Smirnov, V. M., Vaisberg, O. L., Siscoe, G., & Russell, C. T. 2002. Characteristics of magnetosheath plasma in the vicinity of the high-altitude cusp. *Planetary and Space Science*, **50**(5-6), 559–566.

Gonzalez, W. D. 1991. Comment on "A tangent subsolar merging line" by N.U.Crooker et al. *J.Geophys.Res.*, **96**(A2), 1873–1874.

Gonzalez, W. D., & Mozer, F. S. 1974. A quantitative model for the potential resulting from reconnection with an arbitrary magnetic field. *J.Geophys.Res.*, **79**(28), 4186–4194.

Gosling, J. T., Asbridge, J. R., Bame, S. J., Feldman, W. C., Paschmann, G., Sckopke, N., & Russell, C. T. 1982. Evidence for quasi-steady reconnection at the dayside magnetopause. *J.Geophys.Res.*, **87**, 2147.

Gosling, J. T., Thomsen, M. F., Bame, S. J., & Russell, C. T. 1986. Accelerated plasma flows at the near-tail magnetopause. *J.Geophys.Res.*, **91**, 3029.

Gosling, J. T., Thomsen, M. F., Bame, S. J., Elphic, R. C., & Russell, C. T. 1990. Cold ion-beams in the low latitude boundary-layer during accelerated flow events. *Geophys.Res.Lett.*, **17**(12), 2245 – 2248.

Gosling, J. T., Thomsen, M. F., Bame, S. J., Elphic, R. C., & Russell, C. T. 1991. Observations of reconnection of interplanetary and lobe magnetic field lines at the high-latitude magnetopause. *J.Geophys.Res.*, **96**, 14097.

Haerendel, G., & Paschmann, G. 1982. Interaction of the solar wind with the dayside magnetosphere. *Page 49 of:* Nishida, A. (ed), *Magnetospheric Plasma Physics.* D. Reidel, Norwell, Mass.

Haerendel, G., Paschmann, N., Sckopke, N., Rosenbauer, H., & Hedgecock, P. C. 1978. The frontside boundary layer of the magnetosphere and the problem of reconnection. *J.Geophys.Res.*, **83**, 3195–16.

Halberg, Franz, Cornélissen, Germaine, Otsuka, Kuniaki, Watanabe, Yoshihiko, S., Katinas George., Burioka, Naota, Delyukov, Anatoly, Gorgo, Yuri, Zhao, Ziyan, Weydahl, Andi, Sothern, Robert B., Siegelova, Jarmila, Fiser, Bohumil, Dusek, Jiri, Syutkina, Elena V., Perfetto, Federico, Tarquini, Roberto, Singh, R. B., Rhees, Brad, Lofstrom, Dennis, Lofstrom, Paula, Johnson, Paul William Cort, & Schwartzkopff, Othild & the International BIOCOS Study Group. 2000. Cross-spectrally coherent $\sim$ 10.5- and 21- year biological and physical cycles, magnetic storms and myocardial infarctions. *Neuroendocrinology Letters*, **21**, 233–258.

Hashimoto, K., Matsumoto, H., Murata, T., Kaiser, M. L., & Bougeret, J-L. 1998. Comparison of AKR simultaneously observed by the GEOTAIL and WIND spacecraft. *Geophysical Research Letters*, **25**(6), 853–856.

Heard, T. J., & Martin, D. R. 1978. *Extending Mathematics 2.* Oxford, U.K.: Oxford University Press.

Hedgecock, P. C. 1975. A correlation technique for magnetometer zero level determination. *Space Sci. Instr.*, **1**, 83–90.

Heikkila, W. J. 1982. Impulsive plasma transport through the magnetopause. *Geophys. Res. Lett.*, **9**(2), 159–162.

Heikkila, W. J., Jorgensen, T. S., Lanzerotti, L. J., & Maclenman, C. G. 1989. A transient auroral event on the dayside. *J.Geophys.Res.*, **94**, 291.

Heppner, J. P. 1972. Polar-cap electric field distributions related to the interplanetary magnetic field. *J.Geophys.Res.*, **77**(25), 4877–4887.

Heppner, J. P., & Maynard, N. C. 1987. Empirical high-latitude electric field models. *J.Geophys.Res.*, **92**(A5), 4467–4489.

Heyn, M. F., Biernat, H. K., Rijnbeek, R. P., & Semenov, V. S. 1988. The structure of reconnection layers. *J. Plasma Physics*, **40 Pt.2**, 235–52.

Hill, T. W. 1975. Magnetic merging in a collisionless plasma. *J.Geophys.Res.*, **80**, 4689.

Howe, H. C. Jr., & Binsack, J. H. 1972. Explorer 33 and 35 plasma observations of magnetosheath flow. *Journal of Geophysical Research*, **77**, 3334–3344.

Huba, J. D. N., Gladd, T., & Papadopoulos, K. 1977. The lower-hybrid-drift instability as a souce of anomalous resistivity for magnetic field reconnection. *Geophys. Res. Lett.*, **4**, 125.

Hudson, P. D. 1970. Discontinuities in an anisotropic plasma and their identification in the solar wind. *Planet. Space Sci.*, **18**, 1611–1622.

Hughes, W. J. 1995. The magnetopause, magnetotail and magnetic reconnection. *Pages 227–287 of:* Kivelson, Margaret G., & Russell, Christopher T. (eds), *Introduction to Space Physics.* Cambridge, U.K.: Cambridge University Press.

Hundhausen, A. J. 1995. The Solar Wind. *Pages 91–128 of:* Kivelson, Margaret G., & Russell, Christopher T. (eds), *Introduction to Space Physics.* Cambridge, U.K.: Cambridge University Press.

Illingworth, Valerie (ed). 1994. *Collins Dictionary of Astronomy.* Glasgow: HarperCollins.

Ivchenko, N. V., Sibeck, D. G., Takahashi, K., & Kokubun, S. 2000. A statistical study of the magnetosphere boundary crossings by the Geotail satellite. *Geophysical Research Letters*, **27**(18), 2881–4.

Jacob, J. D., & Cattell, C. 1993. High time resolution measurements of upstream magnetic-field and plasma conditions during flux-transfer events at the Earth's dayside magnetopause. *Geophys.Res.Lett.*, **20**, 2007.

Jardine, M. 1991. Magnetic Reconnection in Solar Flares. *Pages 203–220 of:* Priest, Eric R., & Wood, Alan W. (eds), *Advances in solar system magnetohydrodynamics*. Cambridge: Cambridge University Press.

Jokipii, J. R. 1997. Transport and Acceleration of Energetic Particles in Winds. *In:* Jokipii, J. R., Sonnett, C. P., & Giampapa, M. S. (eds), *Cosmic Winds in the Heliosphere*. Space Science Series. Arizona: The University of Arizona Press.

Kallio, E. J., & Koskinen, H. E. J. 2000. A semiempirical magnetosheath model to analyze the solar wind-magnetosphere interaction. *Journal of Geophysical Research*, **105**(A12), 27469–79.

Kan, J. R. 1988. A theory of patchy and intermittent reconnections for magnetospheric flux-transfer events. *J.Geophys.Res.*, **93**, 5613.

Kawano, H., Kokubun, S., & Takahashi, K. 1992. Survey of transient magnetic field events in the dayside magnetosphere. *J.Geophys.Res.*, **97**, 10677–692.

Kellogg, P. J. 1962. Flow of plasma around the Earth. *J.Geophys.Res.*, **67**, 3805.

Kennel, C. F. 1995. *Convection and Substorms - Paradigms of Magnetospheric Phenomenology*. International Series on Astronomy and Astrophysics. New York: Oxford University Press.

Kessel, R. L., Chen, S. -H., Green, J. L., Fung, S. F., Boardsen, S., Tan, L., Eastman, T., Craven, J., & Frank, L. A. 1996. Evidence of high-latitude reconnection during northward IMF: Hawkeye observations. *Geophys.Res.Letts.*, **23**(5), 583–586.

Kessel, R. L., Quintana, E., & Peredo, M. 1999. Local variations of interplanetary magnetic field at Earth's bow shock. *Journal of Geophysical Research*, **104**(A11), 24869–78.

Kim, K. -H., Lin, N., Cattell, C. A., Song, Y., & Lee, D. -H. 2002. Observations of GEOTAIL of accelerated plasma flow reversal near the subsolar magnetopause. *Geophys.Res.Lett.*, **29**(6), 4.1–3.

Kivelson, M. G. 1995a. Physics of Space Plasmas. *In:* Kivelson, Margaret G., & Russell, Christopher T. (eds), *Introduction to Space Physics*. Cambridge, U.K.: Cambridge University Press.

Kivelson, M. G. 1995b. Pulsations and magnetohydrodynamic waves. *Pages 330–355 of:* Kivelson, Margaret G., & Russell, Christopher T. (eds), *Introduction to Space Physics*. Cambridge, U.K.: Cambridge University Press.

Kobel, E., & Flückiger, E. O. 1994. A model of the steady state magnetic field in the magnetosheath. *J.Geophys.Res.*, **99**(A12), 23617–23622.

Kokubun, S., Yamamoto, T., Acuna, M. H., Hayashi, K., Shiokawa, K., & Kawano, H. 1994. The Geotail Magnetic Field Experiment. *J. Geomag. Geoelectr.*, **46**(1), 7–21.

Konik, R. M., Lanzerotti, L. J., Wolfe, A., MacLennan, C. G., & Venkatesan, D. 1994. Cusp latitude magnetic impulse events.2. Interplanetary magnetic-field and solar-wind conditions. *J.Geophys.Res.*, **99**(A8), 14831 – 14853.

Korotova, G. I., & Sibeck, D. G. 1995. A case-study of transient event motion in the magnetosphere and in the ionosphere. *J.Geophys.Res.*, **100**(A1), 35 – 46.

Kozlovsky, A., Koustov, A., Lyatsky, W., Kangas, J., Parks, G., & Chua, D. 2002. Ionospheric convection in the postnoon auroral oval: Super Dual Auroral Radar Network (SuperDARN) and polar ultraviolet imager (UVI) observations. *J.Geophys.Res.*, **107**(A12), SIA6–1–16.

Kuznetsova, M. M., Roth, M., & Zelenyi, L. M. 1995. Kinetic structure of the magnetopause: Equilibrium and percolation. *Pages 99–108 of:* P., Song., Sonnerup, B. U. Ö., & Thomsen, M. F. (eds), *Physics of the Magnetopause*. Geophysical Monograph, vol. 90. American Geophysical Union, Washington DC 20009.

Labelle, J., Treumann, R. A., Haerendel, G., Bauer, O. H., Paschmann, G., Baumjohann, W., Lühr, H., Anderson, R. R., Koons, H. C., & Holzworth, R. 1987. AMPTE/IRM observations of waves associated with flux transfer events in the magnetosphere. *J.Geophys.Res.*, **92**, 5827.

Lattice Financial. 2001. *Goals at Risk. Stochastic Scenario Generation System.* Lattice Financial, Princeton Junction, NJ 08550 www.latticefinancial.com/riskmanagementa.html, 2001.

Le, G., Russell, C. T., Gosling, J. T., & Thomsen, M. F. 1996. ISEE observations of low-latitude boundary layer for northward interplanetary magnetic field: Implications for cusp reconnection. *J.Geophys.Res.*, **101**(A12), 27239–27249.

Lee, L. C. 1995. A review of magnetic reconnection: MHD models. *Pages 139–153 of:* P., Song., Sonnerup, B. U. Ö., & Thomsen, M. F. (eds), *Physics of the Magnetopause*. Geophysical Monograph, vol. 90. American Geophysical Union, Washington DC 20009.

Lee, L. C., & Fu, Z. F. 1985. A theory of magnetic flux transfer at the Earth's magnetopause. *Geophys.Res.Lett.*, **12**, 105–8.

Lee, L. C., & Fu, Z. F. 1986a. Multiple X line reconnection, I. A criterion for the transition from a single X line to a multiple X line reconnection. *J.Geophys.Res.*, **91**, 3311.

Lee, L. C., & Fu, Z. F. 1986b. A simulation study of magnetic reconnection: transition from a fast mode to a slow mode expansion. *J.Geophys.Res.*, **91**(A4), 4551–6.

Lemaire, J., & Roth, M. 1978. Penetration of solar wind plasma elements into the magnetosphere. *J.Atmos.Terr.Phys.*, **40**, 331.

Lepping, R. P., Acuña, M. H., Burlaga, L. F., Farrell, W. M., Slavin, J. A., Schatten, K. H., Mariani, F., Ness, N. F., Neubauer, F. M., Whang, Y. C., Byrnes, J. B., Kennon, R. S., Panetta, P. V., Scheifele, J., & Worley, E. M. 1995. The WIND Magnetic Field Investigation. *The Global Geospace Mission*, 207.

Levy, R. H., Petschek, H. E., & Siscoe, G. L. 1964. Aerodynamic aspects of the magnetospheric flow. *AIAA J.*, **2**, 2065.

Lin, R. P., & Anderson, K. A. 1966. Evidence for connection of geomagnetic tail lines to the interplanetary magnetic field. *J.Geophys.Res.*, **71**, 4213.

Lockwood, M. 1995. Location and characteristics of the reconnection x-line deduced from low-altitude satellite and ground-based observations.1. Theory. *J.Geophys.Res.*, **100**(A11), 21791 – 21802.

Lockwood, M. 1997. Energy and pitch-angle dispersions of LLBL/cusp ions seen at middle altitudes: Predictions by the open magnetosphere model. *Ann. Geophys.*, **15**(12), 1501 – 1514.

Lockwood, M., & Davis, C. J. 1995. Occurrence probability, width and number of steps of cusp precipitation for fully pulsed reconnection at the dayside magnetopause. *J.Geophys.Res.*, **100**(A5), 7627 – 7640.

Lockwood, M., & Smith, M. F. 1994. Low and middle altitude cusp particle signatures for general magnetopause reconnection rate variations. 1. Theory. *J.Geophys.Res.*, **99**(A5), 8531 – 8553.

Lockwood, M., & Wild, M. N. 1993. On the quasi-periodic nature of magnetopause flux-transfer events. *J.Geophys.Res.*, **98**, 5935.

Lockwood, M., Chandler, M. O., Horwitz, J. L., Waite, J. H. Jr., Moore, T. E., & Chappell, C. R. 1985. The cleft ion fountain. *J.Geophys.Res.*, **90**, 9736–9748.

Lu, G., Holzer, T. E., Lummerzheim, D., Ruohoniemi, J. M., Stauring, P., Troshichev, O., Newell, P. T., Brittnacher, M., & Parks, G. 2002. Ionospheric response to the interplanetary magnetic field southward turning: fast onset and slow reconfiguration. *J.Geophys.Res.*, **107**(A8), SIA2–1–9.

Luhmann, J. G., Walker, R. J., Russell, C. T., Crooker, N. U., Spreiter, J. R., & Stahara, S. S. 1984a. Patterns of magnetic field merging sites on the magnetopause. *Pages 156–157 of:* Hones, E. W. Jr. (ed), *Magnetic reconnection in space and laboratory plasmas.* Geophysical Monograph 30. AGU, Washington D. C.

Luhmann, J. G., Walker, R. J., Russell, C. T., Crooker, N. U., Spreiter, J. R., & Stahara, S. S. 1984b. Patterns of potential magnetic field merging sites on the dayside magnetopause. *J.Geophys.Res.*, **89**(A3), 1739–1742.

Lühr, H., & Klocker, N. 1987. AMPTE-IRM observations of magnetic cavities near the magnetopause. *Geophys.Res.Letts.*, **14**(3), 186–9.

Lundin, R., & Dubinin, E. 1985. Solar wind energy transfer regions inside the dayside magnetopause: Accelerated heavy ions as tracers for MHD-processes in the dayside boundary layer. *Planet. Space Sci.*, **33**, 891.

Lundin, R., Sauvaud, J. -A., Rème, H., Balogh, A., Dandouras, I., Bosqued, J. M., Carlson, C., Parks, G. K., Möbius, E., Kistler, L. M., Klecker, B., Amata, E., Formisano, V., Dunlop, M., Eliasson, L., Korth, A., Lavraud, B., & McCarthy, M. 2003. Evidence for impulsive solar wind plasma penetration through the dayside magnetopause. *Ann. Geophysicae*, **21**(2), 457–472.

Lysack, Rover L., Song, Yan, & Griefer, John C. 1995. Coupling of the magnetopause to the ionosphere by means of Alfvén waves and field-aligned currents. *Pages 385–393 of:* P., Song., Sonnerup, B. U. Ö., & Thomsen, M. F. (eds), *Physics of the Magnetopause*. Geophysical Monograph, vol. 90. American Geophysical Union, Washington DC 20009.

Mansurov, S. M. 1969. New evidence of a relationship between magnetic fields in space and on Earth. *Geomagn.Aeron.*, **9**, 622.

Matsuoka, A., Southwood, D. J., Mukai, T., Kokubun, S., & Matsumoto, H. 2002. A Walen test of low-frequency MHD waves in the magnetosheath observed by Geotail. *Planetary and Space Science*, **50**(5-6), 613–618.

Maxwell. 2003. *RAD-PAK Technology Overview.* internet: www.maxwell.com/microelectronics/products/technologies/radpak-overview.html.

Maynard, Nelson C. 1995. Space weather prediction U.S. National Report to IUGG, 1991-1994. *Rev. Geophys.*, **33 Suppl.**

McPherron, R. L. 1995. Magnetospheric Dynamics. *Pages 400–458 of:* Kivelson, Margaret G., & Russell, Christopher T. (eds), *Introduction to Space Physics*. Cambridge, U.K.: Cambridge University Press.

McPherron, R. L., Russell, C. T., & Aubry, M. 1973. Satellite studies of magnetospheric substorms on August 15, 1978 9. Phenomenological model for substorms. *J.Geophys.Res.*, **78**, 3131–3149.

McPherron, R. L., Nakamura, R., Kokubun, S., Kamide, Y., Shiokawa, K., Yumoto, K., Mukai, T., Saito, Y., Hayashi, K., Nagai, T., Ables, S., Baker, D. N., Friis-Christensen, E., Fraser, B., Hughes, T., Reeves, G., & Singer, H. 1997. Fields and flows at GEOTAIL during a moderate substorm. *Advances in Space Research*, **20**(4-5), 923–931.

Mei, Y., Crooker, N. U., & Siscoe, G. L. 1995. Cusp currents from ionospheric vorticity generated by gasdynamic and merging flow-fields at the magnetopause. *J.Geophys.Res.*, **100**(A5), 7641 – 7647.

Mendoza, B., & Diaz-Sandoval, R. 2001. Relationship between Forbush descreases and myocardial infarctions in Mexico. *Proceedings of ICRC 2001*, 3527–3530.

Moore, T. E., Fok, M. C., & Chandler, M. O. 2002. The Dayside Reconnection X-Line. *J.Geophys.Res.*, **107**(A10), 1332.

Morfill, G., & Scholer, M. 1973. Study of the magnetosphere using energetic particles. *Space Sci. Rev.*, **15**, 267.

Mozer, F. S. 1984. Electric field evidence for viscous interaction at the magnetopause. *Geophys.Res.Lett.*, **11**, 135.

Mukai, T., Machida, S., Saito, Y., Hirahara, M., Terasawa, T., Kaya, N., Obara, T., Ejira, M., & Nishida, A. 1994. Low Energy Particle LEP Experiment. *J. Geomag. Geoelectr.*, **46**(8), 669–692.

NASA. 1996. *Space storms affect life on Earth.* internet: science.nasa.gov/newhome/headlines/plasma-plume/bullet6.htm.

Němeček, Z., Šafránková, J., Prech, L., Zastenker, G. N., Paularena, K. I., & Kokubun, S. 2000a. Magnetosheath study: Interball observation. *Advances in Space Research*, **25**(7-8), 1511–16.

Němeček, Z., Šafránková, J., Zastenker, G. N., Pišoft, P., Paularena, K. I., & Richardson, J. D. 2000b. Observations of the radial magnetosheath profile and a comparison with gasdynamic model predictions. *Geophysical Research Letters*, **27**(17), 2801–2804.

Nishida, A. 1989. Can random reconnection on the magnetopause produce the low latitude boundary layer. *Geophys.Res.Lett.*, **16**, 227–230.

Nykyri, K., & Otto, A. 2001. Plasma transport at the magnetospheric boundary due to reconnection in Kelvin-Helmholtz vortices. *Geophys.Res.Let.*, **28**(18), 3565.

Ogilvie, K. W., Chornay, D. J., Fitzenrieter, F. J., Hunsaker, F., Keller, J., Lobell, J., Miller, G., Scudder, J. D., Sittler, Jr., E. C., Torbert, R. B., Bodet, D., Needell, G., lazarus, A. J., Steinberg, J. T., Tappan, J. H., Mavretic, A., & Gergin, E. 1995. SWE, a comprehensive plasma instrument for the WIND spacecraft. *Space Science Review*, **71**, 55–77.

Øieroset, M., Phan, T. -D., Fujimoto, M., Lin, R. P., & Lepping, R. P. 2001. In situ detection of collisionless reconnection in the Earth's magnetotail. *Nature*, **412**(July 26), 414.

Onsager, T. G., Chang, S. W., Perez, J. D., Austin, J. B., & Janoo, L. X. 1995. Low-altitude observations and modeling of quasi-steady magnetopause reconnection. *J.Geophys.Res.*, **100**(A7), 11831 – 11843.

Oulu. 1998. *Space Physics Text Book, Department of Physical Sciences, University of Oulu.* internet: http://www.oulu.fi/~spaceweb/textbook/.

Owen, C. J., & Cowley, S. W. H. 1991. Heikkila mechanism for impulsive plasma transport through the magnetopause - a reexamination. *J.Geophys.Res.*, **96**(A4), 5565 – 5574.

Owen, C. J., Slavin, J. A., Richardson, I. G, Murphy, N., & Hynds, R. J. 1995. Average motion, structure and orientation of the distant magnetotail determined from remote sensing of the edge of the plasma sheet boundary layer with E>35keV ions. *J.Geophys.Res.*, **100**, 185.

Owen, C. J., Fazakerley, A N., Carter, P. J., Coates, A. J., Krauklis, I. C., Szita, S., Taylor, M. G. G. T., Travnicek, P., Watson, G., Wilson, R. J., Balogh, A., & Dunlop, M. W. 2001. Cluster PEACE observations of electrons during magnetospheric flux transfer events. *Ann. Geophys.*, **19**, 1509–1522.

Papitashvili, V. O., Christiansen, F., & Neubert, T. 2001. Field-aligned currents during IMF $\sim$ 0. *Geophys.Res.Lett.*, **28**(15), 3055–3058.

Parker, E. N. 1957. Sweet's mechanism for merging magnetic fields in conducting fluids. *J.Geophys.Res.*, **62**, 509.

Parker, E. N. 1958. Dynamics of the interplanetary gas and magnetic fields. *Astrophys. J.*, **128**, 664–676.

Parks, George. K. 1991. *Physics of Space Plasmas - An Introduction.* Redwood City: Addison-Wesley.

Paschmann, G., & Daly, P. W. (eds). 1998. *Analysis methods for multi-spacecraft data.* ISSI Scientific Report, nos. SR–001. Germany: International Space Science Institute.

Paschmann, G., Sonnerup, B. U. Ö., Papamastorakis, I., Sckopke, N., Haerendel, G., Bame, S. J., Asbridge, J. B., Gosling, J. T., Russell, C. T., & Elphic, R. C. 1979. Plasma acceleration at the earth's magnetopause: evidence for reconnection. *Nature*, **282**, 243.

Paschmann, G., Papamastorakis, I., Baumjohann, W., Sckopke, N., Carlson, C. W., Sonnerup, B. U. Ö., & Luhr, H. 1986. The magnetopause for large magnetic shear: AMPTE/IRM observations. *J.Geophys.Res.*, **91**, 11099.

Paularena, K. I., Richardson, J. D., Kolpak, M. A., Jackson, C. R., & Siscoe, G. L. 2001. A dawn-dusk density asymmetry in Earth's magnetosheath. *Journal of Geophysical Research*, **106**(A11), 25377–94.

Peredo, M., Slavin, J. A., Mazur, E., & Curtis, S. A. 1995. Three-dimensional position and shape of the bow shock and their variation with Alfvénic, sonic and magnetosonic Mach numbers and interplanetary magnetic field orientation. *Journal of Geophysical Research*, **100**(A5), 7907–7916.

Perreault, P., & Akasofu, S. -I. 1978. A study of geomagnetic storms. *Geophys. J. Roy. Astron. Soc.*, **54**, 547.

Petrinec, S. M., & Fuselier, S. A. 2003. Comment on "An ionospheric convection signature of antiparallel reconnection" by Coleman et al. *J.Geophys.Res.*, **A5**(A5), 10.1029/2002JA009421.

Petrinec, S. M., & Russell, C. T. 1997. Investigations of hydrodynamic and magnetohydrodynamic equations across the bow shock and along the outer edge of planetary obstacles. *Advances in Space Research*, **20**(4-5), 743–746.

Petrinec, S. M., Mukai, T., Nishida, A., Yamamoto, T., Nakamura, T. K., & Kokubun, S. 1997. GEOTAIL observations of magnetosheath flow properties, with simultaneous observations of the solar wind by the WIND spacecraft. *Advances in Space Research*, **20**(4/5), 767–776.

Petschek, H. E. 1964. Magnetic Field Annihilation. *In:* Hess, W. N. (ed), *The Physics of Solar Flares*. Proceedings of the AAS-NASA Symposium held at Goddard Space Flight Center, NASA SP-50.

Petschek, Harry E. 1995. The concept of rapid magnetic field reconnection: A retrospective view. *Pages 21–28 of:* P., Song., Sonnerup, B. U. Ö., & Thomsen, M. F. (eds), *Physics of the Magnetopause*. Geophysical Monograph, vol. 90. American Geophysical Union, Washington DC 20009.

Peymirat, C., & Fontaine, D. 1994. Relationships between field-aligned currents and convection observed by EISCAT and implications concerning the mechanism that produces region-2 currents: statistical study. *Ann.Geophys.*, **12**, 304–315.

Phan, T., Frey, H. U., Frey, S., Peticolas, L., Fuselier, S., Carlson, C., Rème, H., Bosqued, J. -M., Balogh, A., Dunlop, M., Kistler, L., Mouikis, C., Dandouras, I., Sauvaud, J. -A., Mende, S., McFadden, J., Parks, G., Moebius, E., Klecker, B., Paschmann, G., Fujimoto, M., Petrinec, S., Marcucci, M. F., Korth, A., & Lundin, R. 2003. Simultaneous Cluster and IMAGE observations of cusp reconnection and auroral proton spot for northward IMF. *Geophys.Res.Letts.*, **30**(10), 10.1029/2003GL016885.

Phan, T. D., Kistler, L. M., Klecker, B., Haerendel, G., Paschmann, G., Sonnerup, B. U. Ö., Baumjohann, W., Bavassano-Cattaneo, M. B., Carlson, C. W., DiLellis, A. M., Fornacon, K-H., Frank, L. A., Fujimoto, M., Georgescu, E., Kokubun, S., Möbius, E., Mukai, T., Øieroset, M., Paterson, W. R., & Rème, H. 2000. Extended magnetic reconnection at the Earth's magnetopause from detection of bi-directional jets. *Nature*, **404**, 848–850.

Phan, T. D., Freeman, M. P., Kistler, L. M., Klecker, B., Haerendel, G., Paschmann, G., Sonnerup, B. U. Ö., *et al.* 2001. Evidence for an Extended Reconnection Line at the Dayside Magnetopause. *Earth Planets Space*, **53**(6), 619–625.

Pinnock, M., Chisham, G., Coleman, I. J., & Freeman, M. P. 2003. The location and rate of dayside reconnection during an interval of steady southward IMF. *Annales Geophys.*, **21**, 1467–1482.

Priest, E. R., & Forbes, T. G. 1986. New models for fast steady state magnetic reconnection. *J.Geophys.Res.*, **91**, 5579.

Priest, E. R., & Forbes, T. G. 2001. *Role of Sun's Magnetic Field – Workshop on Magnetic Fields – Santiago - January 15 2001.* internet: http://www-solar.mcs.st-andrews.ac.uk/∼eric/TALKS/CHILE/10/index4.html.

Pu, Z. Y., Wei, C. Q., & Liu, Z. X. 1986. Drift kinetic instabilities at the magnetopause. *Proceedings of International Symposium on Space Physics in Beijing, 4-066.*

Pudovkin, M. I., & Semenov, V. S. 1977. Stationary frozen-in co-ordinate system. *Ann. Geophys.*, **33**, 429–433.

Pudovkin, M. I., & Semenov, V. S. 1985. Magnetic field reconnection theory and the solar wind - magnetosphere interaction: A review. *Space Science Reviews*, **41**, 1–89.

Pudovkin, M. I., Zaitseva, S. A., & Besser, B. P. 1995. Magnetopause magnetic barrier parameters in dependence on the solar wind magnetic field orientation. *Ann. Geophysicae*, **13**, 828–835.

Pudovkin, M. I., Besser, B. P., Zaitseva, S. A., Lebedeva, V. V., & Meister, C-V. 2001. Magnetic barrier in case of a southward interplanetary magnetic field. *Journal of Atmospheric and Solar-Terrestrial Physics*, **63**(10), 1075–83.

Pulkkinen, T. I., Baker, D. N., Walker, R. J., Raeder, J., & Ashour-Abdalla, M. 1995. Comparison of empirical magnetic field models and global MHD simulations: The near-tail currents. *Geophysical Research letters*, **22**, 349–352.

Rijnbeek, R. P., Cowley, S. W. H., Southwood, D. J., & Russell, C. T. 1984. A survey of dayside flux transfer events observed by ISEE-1 and ISEE-2 magnetometers. *J.Geophys.Res.*, **89**, 786.

Rijnbeek, R. P., Biernat, H. K., Heyn, M. F., Semenov, V. S., Farrugia, C. J., Southwood, D. J., Paschmann, G., Sckopke, N., & Russell, C. T. 1989. The structure of the reconnection layer observed by ISEE 1 on 8 September 1978. *Ann. Geophys.*, **7**(3), 297–310.

Rodger, A. S., Coleman, I. J., & Pinnock, M. 2000. Some comments on transient and steady-state reconnection at the dayside magnetopause. *Geophys.Res.Lett.*, **27**(9), 1359–1362.

Roederer, J. G. 1988. Tearing down disciplinary barriers. *Astrophysics and Space Science*, **144**(1-2), 659–667.

Roelof, E. C., & Sibeck, D. G. 1993. Magnetopause shape as a bivariate function of interplanetary magnetic field B_z and solar wind dynamic pressure. *J.Geophys.Res.*, **98**, 21421.

Roelof, E. C., & Sibeck, D. G. 1994. Correction to "Magnetopause shape as a bivariate function of interplanetary magnetic field B_Z and solar wind dynamic pressure". *J.Geophys.Res.*, **99**, 8787.

Roth, M. 1995. Impulsive transport of solar wind into the magnetosphere. *Pages 343–348 of:* P., Song., Sonnerup, B. U. Ö., & Thomsen, M. F. (eds), *Physics of the Magnetopause*. Geophysical Monograph, vol. 90. American Geophysical Union, Washington DC 20009.

Russell, C. T. 1995. A Brief History of Solar-Terrestrial Physics. *Pages 1–26 of:* Kivelson, Margaret G., & Russell, Christopher T. (eds), *Introduction to Space Physics*. Cambridge, U.K.: Cambridge University Press.

Russell, C. T., & Elphic, R. C. 1978. Initial ISEE magnetometer results: Magnetopause observations. *Space Sci. Rev.*, **22**, 681–715.

Russell, C. T., & Elphic, R. C. 1979. *ISEE* observations of flux transfer events at the dayside magnetopause. *Geophys.Res.Lett.*, **6**, 33.

Russell, C. T., & McPherron, R. L. 1973. The magnetotail and substorms. *Space Science Review*, **11**, 111.

Russell, C. T., Zhuang, H-C., & Walker, R. J. 1981. A note on the location of the stagnation point in the magnetosheath flow. *Geophysical Research Letters*, **8**(9), 984–986.

Russell, C. T., Fedder, J. A., Slinker, S. P., Zhous, X. -W., Le, G., Luhmann, J. G., Fenrich, F., Chandler, M. O., Moore, T. E., & Fuselier, S. A. 1998. Entry of the POLAR spacecraft into the polar cusp under northward IMF conditions. *Geophys.Res.Lett.*, **25**, 3015–3018.

Russell, C. T., Le, G., & Petrinec, S. M. 2000. Cusp observations of high- and low-latitude reconnection for northward IMF: An alternate view. *J.Geophys.Res.*, **105**, 5489–5495.

Šafránková, J., Němeček, Sibeck, D. G., Pech, L., Měrka, J., & Santolik, O. 1998. Two point observation of high-latitude reconnection. *Geophys.Res.Lett.*, **25**, 4301.

Samsonov, A. A., Pudovkin, M. I., Gary, S. P., & Hubert, D. 2001. Anisotropic MHD model of the dayside magnetosheath downstream of the oblique bow shock. *Journal of Geophysical Research*, **106**(A10), 21689–99.

Samsonova, A. A., & Hubert, D. 2002. Temporal variations in the magnetosheath: comparison between MHD calculations and observations for one event on September 17, 1978. *Planetary and Space Science*, **50**(5-6), 619–625.

Saunders, Mark. 1991. The Earth's Magnetosphere. *Pages 357–397 of:* Priest, Eric R., & Wood, Alan W. (eds), *Advances in solar system magnetohydrodynamics*. Cambridge: Cambridge University Press.

Schindler, K., & Birn, J. 1987. On the generation of field-aligned plasma flow at the boundary of the plasma sheet. *J.Geophys.Res.*, **92**(A1), 95–107.

Schmidt, G. 1991. Plasma motion across magnetic fields. *Phys.Fluids*, **3**, 961.

Scholer, M. 1988. Magnetic flux transfer at the magnetopause based on single X-line reconnection. *Geophys.Res.Lett.*, **15**, 291.

Scholer, M. 1989. Undriven reconnection in an isolated current sheet. *J.Geophys.Res.*, **94**, 8805.

Schwartz, S. J., Burgess, D., & Moses, J. J. 1996. Low-frequency waves in the Earth's magnetosheath: present status. *Annales Geophysicae*, **14**, 1134–1150.

Scudder, J. D. 1997. Theoretical approaches to the description of magnetic merging: the need for finite β_e, anisotropic, ambipolar Hall MHD. *Space Science Rev.*, **80**(1-2), 235–267.

Semenov, V. S., & Pudovkin, M. I. 1985. Localization and features of the development of the processes of interconnection at the magnetopause. *Geomagn.Aeron. (Engl. Transl.)*, **25**(N4), 494–498.

Senior, C., Cerisier, J-C., Thorolfsson, A., & Lester, M. 2002. Propagation in the ionosphere of convection changes following a sharp interplanetary magnetic field B_Y transition. *J.Geophys.Res.*, **107**(A10), SMP20–1–9.

Seon, J., Park, S. M., Min, K. W., Frank, L. A., Paterson, W. R., & Ogilvie, K. W. 1999. Observations of density fluctuations in Earth's magnetosheath with Geotail and Wind spacecraft. *Geophysical Research Letters*, **26**(7), 959–962.

Shay, M. A., Drake, J. F., Rogers, B. N., & Denton, R. E. 2001. Alfvénic collisionless magnetic reconnection and the Hall term. *J.Geophys.Res.*, **106**, 3759.

Shi, Y., Wu, C. C., & Lee, L. C. 1991. Magnetic field reconnection patterns at the dayside magnetopause: an MHD simulation study. *J.Geophys.Res.*, **96**(A10), 17627–50.

Sibeck, D. G. 1990. A model for the transient magnetospheric response to sudden solar wind dynamic pressure variations. *J.Geophys.Res.*, **95**, 3755–3771.

Sibeck, D. G. 1992. Transient events in the outer magnetosphere - boundary waves or flux-transfer events? *J.Geophys.Res.*, **97**, 4009.

Sibeck, D. G. 1995. The magnetospheric response to foreshock pressure pulses. *Pages 293–302 of:* Song, P., Sonnerup, B. U. Ö., & Thomsen, M. F. (eds), *Physics of the Magnetopause.* Geophysical Monograph Series, vol. 90. AGU, Washington D. C.

Sibeck, D. G., & Smith, M. F. 1992. Magnetospheric plasma flows associated with boundary waves and flux-transfer events. *Geophys.Res.Lett.*, **19**, 1903.

Sibeck, D. G., Lopez, R. E., & Roelof, E. C. 1991. Solar wind control of the magnetopause shape, location, and motion. *Journal of Geophysical Research*, **96**, 5489–5495.

Siscoe, G. L., Erickson, G. M., Sonnerup, B. U. Ö., Maynard, N. C., Siebert, K. D., Weimer, D. R., & White, W. W. 2000. Deflected magnetosheath flow at the high-latitude magnetopause. *J.Geophys.Res.*, **105**(A6), 12851 – 12857.

Slavin, J. A., & Holzer, R. E. 1981. Solar wind flow about the terrestrial planets 1. Modeling bow shock position and shape. *J.Geophys.Res.*, **86**, 11401–11418.

Slavin, J. A., Smith, E. J., Sibeck, D. G., Baker, D. N., Zwickl, R. D., & Akasofu, S. I. 1985. An ISEE3 study of average and substorm conditions in the distant magnetotail. *J.Geophys.Res.*, **90**, 10875–10895.

Smets, R., Delcourt, D., Chanteur, G., & Moore, T. E. 2002. On the incidence of Kelvin-Helmholtz instability for mass exchange process at the Earth's magnetopause. *Ann. Geophysicae*, **20**(6), 757–769.

Snyder, C. S., Neugebauer, M., & Rao, V. R. 1963. The solar wind velocity and its correlation with cosmic ray variations and with solar magnetic activity. *J.Geophys.Res.*, **68**, 6361.

Song, P. 2000. Forecasting Earth's magnetopause, magnetosheath, and bow shock. *IEEE Transactions of Plasma Science*, **28**(6), 1966–1975.

Song, P., & Russell, C. T. 1992. Model of the formation of the low-latitude boundary-layer for strongly northward interplanetary magnetic-field. *J.Geophys.Res.*, **97**(A2), 1411 – 1420.

Song, P., Russell, C. T., Gosling, J. T., Thomsen, M., & Elphic, R. C. 1990. Observations of the density profile in the magnetosheath near the stagnation streamline. *Geophysical Research letters*, **17**(11), 2035–2038.

Song, P., Russell, C. T., Gombosi, T. I., Spreiter, J. R., Stahara, S. S., & Zhang, X. X. 1999a. On the processes in the terrestrial magnetosheath 1. Scheme Development. *Journal of Geophysical Research*, **104**(A10), 22345–22355.

Song, P., Russell, C. T., Zhang, X. X., Stahara, S. S., Spreiter, J. R., & Gombosi, T. I. 1999b. On the processes in the terrestrial magnetosheath 2. Case Study. *Journal of Geophysical Research*, **104**(A10), 22357–22373.

Sonnerup, B. U. Ö. 1970. Magnetic field reconnection in a highly incompressible fluid. *J. Plasma Phys.*, **4**, 161.

Sonnerup, B. U. Ö. 1979. Transport mechanisms at the magnetopause. *Page 77 of:* Akasofu, S-I (ed), *Dynamics of the Magnetosphere*. D.Reidel, Dordrecht, Netherlands.

Sonnerup, B. U. Ö. 1984. Magnetic reconnection at the magnetopause: An overview. *Page 92 of:* Hones, E. W. Jr. (ed), *Magnetic reconnection in space and laboratory plasmas*. Geophysical Monograph 30. AGU, Washington D. C.

Sonnerup, B. U. Ö., & Ledley, B. G. 1979. OGO5 Magnetopause structure and reconnection. *J.Geophys.Res.*, **84**, 399.

Sonnerup, B. U. Ö, Paschmann, G., Papamastorakis, I., Sckopke, N., Haerendel, G., Bame, S. J., Asbridge, J. R., Gosling, J. T., & Russell, C. T. 1981. Evidence for magnetic field reconnection at the Earth's magnetopause. *J.Geophys.Res.*, **86**, 10049.

Sonnerup, B. U. Ö., Paschmann, G., & Phan, T. D. 1995. Fluid aspects of reconnection at the magnetopause: In situ observations. *Pages 167–180 of:* P., Song., Sonnerup, B. U. Ö., & Thomsen, M. F. (eds), *Physics of the Magnetopause*. Geophysical Monograph, vol. 90. American Geophysical Union, Washington DC 20009.

Southwood, D. J., & Kivelson, M. G. 1990. The magnetohydrodynamic response of the magnetospheric cavity to changes in solar wind pressure. *J.Geophys.Res.*, **95**, 2301.

Southwood, D. J., & Kivelson, M. G. 1995. Magnetosheath flow near the subsolar magnetopause: Zwan-Wolf and Southwood-Kivelson theories reconciled. *Geophysical Research letters*, **22**, 3275–3278.

Southwood, D. J., Farrugia, C. J., & Saunders, M. A. 1988. What are flux transfer events? *Planet.Space Sci.*, **36**(5), 503–8.

Soward, A. M., & Priest, E. R. 1986. Magnetic field-line reconnection with jets. *J.Plasma Phys.*, **35**(pt. 2 April), 333–50.

Spiegel, M. R. 1974. *Theory and problems of vector analysis, SI Edition*. Schaum's Outline Series. McGraw Hill.

Spreiter, J. R., & Stahara, S. S. 1980. A new predictive model for determining solar wind-terrestrial planet interactions. *J. Geophys. Res.*, **85**(A12), 6769–6777.

Spreiter, J. R., Summers, A. L., & Alksne, A. Y. 1966. Hydromagnetic flow around the magnetosphere. *Planet.Space Sci.*, **14**, 223–253.

Stern, David P. 1973. A study of the electric field in an open magnetospheric model. *J.Geophys.Res.*, **78**(31), 7292–7305.

Stubbs, T. J., Lockwood, M., Cargill, P., Fennell, J., Grande, M., Kellett, B., Perry, C., & Rees, A. 2001. Dawn-dusk asymmetry in particles of solar wind origin within the magnetosphere. *Annales Geophysicae*, **19**, 1–9.

Sturrock, Peter A. 1994. *Plasma Physics - An introduction to the theory of astrophysical, geophysical and laboratory plasmas*. Cambridge: Cambridge University Press.

Svalgaard, L. 1968. Sector structure of the interplanetary magnetic field and daily variation of the geomagnetic field at high latitudes. *Geophys. Pap. R-6, Danish Meteorol. Inst., Copenhagen.*

Svalgaard, L. 1973. Polar cap magnetic variations and their relationship with the interplanetary magnetic sector structure. *J.Geophys.Res.*, **78**, 2064.

Sweet, P. A. 1958. The neutral point theory of solar flares. *In:* Lehnert, B. (ed), *Electromagnetic phenomena in cosmical physics.* Cambridge University Press.

Taguchi, S., Sugiura, M., Winningham, J. D., & Slavin, J. A. 1993. Characterization of the IMF B_y -dependent field-aligned currents in the cleft region based on de-2 observations. *J.Geophys.Res.*, **98**(A2), 1393 – 1407.

Takashima, T., Doke, T., Hayashi, T., Kikuchi, J., Kobayashi, M., Shirai, H., Takehana, N., Ehara, M., Yamada, Y., Yanagita, S., Hasebe, N., Kashiwagi, T., Kato, C., Munakata, K., Kohno, T., Kondoh, K., Murakami, H., Nakamoto, A., Yanagimachi, T., Reames, D. V., & von Rosenvinge, TT. 1997. The first observation of sulfur in anomalous cosmic rays by the Geotail and the Wind spacecrafts. *Astrophysical Journal*, **477**(No.2 Pt.2), L111–113.

Terasawa, T., Shimada, N., Tsuboubouchi, K., Hoshino, M., Mukai, T., Saito, Y., Yamamoto, T., Nishida, A., Machida, S., Kokubun, S., Matsumoto, H., Kojima, H., Sanderson, T. R., Lazarus, A. J., Steinberg, J. T., & Lepping, R. P. 1997. Particle acceleration at the interplanetary shock ahead of a large magnetic cloud on October 18, 1995: Geotail-Wind collaboration. *Advances in Space Research*, **20**(4-5), 641–644.

Thomsen, M. F., Stansberry, J. A., Bame, S. J., Fuselier, S. A., & Gosling, J. T. 1987. Ion and electron velocity distributions within flux transfer events. *J.Geophys.Res.*, **92**, 12127–12136.

Treumann, Rudolph A., LaBelle, James, & Bauer, Thomas, M. 1995. Diffusion Processes: An Observational Perspective. *Pages 331–341 of:* P., Song., Sonnerup, B. U. Ö., & Thomsen, M. F. (eds), *Physics of the Magnetopause.* Geophysical Monograph, vol. 90. American Geophysical Union, Washington DC 20009.

Tsurutani, B. T., & Thorne, R. M. 1982. Diffusion processes at the magnetopause boundary layer. *Geophys. Res. Lett.*, **9**, 1247–1250.

Tsyganenko, N. A. 1995. Modelling the Earth's magnetospheric magnetic field confined within a realistic magnetopause. *J.Geophys.Res.*, **100**(A4), 5599–5612.

Vasyliunas, V. M. 1975. Theoretical models of magnetic field line merging. *Rev.Geophys.Space Phys.*, **13**, 303.

Villoresi, G., Kopytenko, Y. A., Ptitsyna, N. G., Tyasto, M. I., Kopytenko, E. A., Iucci, N., & Voronov, P. M. 1994a. The influence of geomagnetic storms and man-made magnetic field disturbances on the incidence of myocardial infarction in St. Petersburg (Russia). *Physica Medica*, **10**, 107–117.

Villoresi, G., Breus, T. K., Iucci, N., Dorman, L. I., & Rapoport, S. I. 1994b. The influence of geophysical and social effects on the incidences of clinically important pathologies Moscow 1979-1981. *Physica Medica*, **10**, 79–91.

Walker, R. J., & Russell, C. T. 1995. Solar-wind interactions with magnetized planets. *Pages 164–182 of:* Kivelson, Margaret G., & Russell, Christopher T. (eds), *Introduction to Space Physics.* Cambridge, U.K.: Cambridge University Press.

Watt, C. E. J., Horne, R. B., & Freeman, M. P. 2002. Ion-acoustic resistivity in plasmas with similar ion and electron temperatures. *Geophys.Res.Lett.*, **29**(1), 10.1029/2001GLO13451.

Winglee, R. M., Menietti, J. D., Peterson, W. K., Burch, J. L., & Waite, Jr., J. H. 1994. Temporal and spatial signatures in the injection of magnetosheath plasma into the cusp/cleft. *Pages 171–181 of:* Burch, J. L., & Waite, Jr., J. H. (eds), *Solar System Plasmas in Space and Time.* Geophysical Monograph, vol. 84. American Geophysical Union, Washington DC 20009.

Winningham, J. D., & Heikkila, W. J. 1974. Polar cap auroral electron fluxes observed with ISIS 1. *J.Geophys.Res.*, **79**, 949.

Woch, J., & Lundin, R. 1991. Temporal magnetosheath plasma injection observed with Viking: a case study. *Ann. Geophys.*, **9**, 133.

Wu, C. C. 1992. MHD flow past an obstacle: large-scale flow in the magnetosheath. *Geophysical Research Letters*, **19**(2), 87–90.

Yamada, M. 1999. Review of controlled laboratory experiments on physics of magnetic reconnection. *J.Geophys.Res.*, **104**(A7), 14529–41.

Zastenker, G. N., Nozdrachev, M. N., Němeček, Z., Šafránková, J., Paularena, K. I., Richardson, J. D., Lepping, R. P., & Mukai, T. 2002. Multispacecraft measurements of plasma and magnetic field variations in the magnetosheath: Comparison with Spreiter models and motion of the structures. *Planetary and Space Science*, **50**(5-6), 601–612.

Zhuang, H. C., & Russell, C. T. 1981. An analytic treatment of the structure of the bow shock and magnetosheath. *J. Geophys. Res.*, **86**, 2191–2205.

Zwan, B. J., & Wolf, R. A. 1976. Depletion of solar wind plasma near a boundary layer. *J.Geophys.Res.*, **81**(10), 1636–1648.

Aurora of 19th March 2001 at 21:00 UT near Oulu, Finland.

Photo: Jouni Jussila – University of Oulu, Finland.

———————

"I used to watch them as a kid. My granny told me about 'em. Some cold nights you see them dancin' in the sky over the Hub, burnin' green and gold..."

"Oh, you mean the aurora coriolis," said Oats, trying to make his voice sound matter of fact. "But actually that's caused by magic particles hitting the – "

"Dunno what it's *caused* by," said Granny sharply, "but what it *is* is the phoenix dancin'."

Carpe Jugulum – Terry Pratchett